به نام خدا

مرکز دانلود رایگان
مهندسی متالورژی و مواد

www.Iran-mavad.com

WOODHEAD PUBLISHING IN MATERIALS

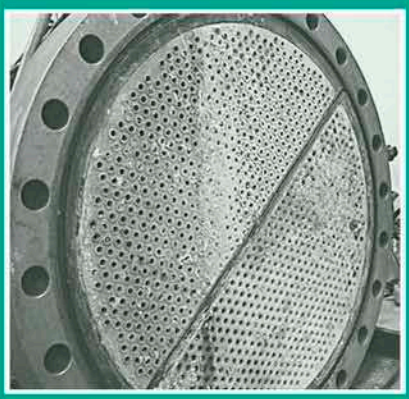

European Federation of
Corrosion Publications
Number 50

Corrosion behaviour and protection of copper and aluminium alloys in seawater

Edited by D. Féron

CRC

WP

ISSN 1354-5116

Corrosion behaviour and protection of copper and aluminium alloys in seawater

European Federation of Corrosion Publications
NUMBER 50

Corrosion behaviour and protection of copper and aluminium alloys in seawater

Edited by
D. Féron

**Published for the European Federation of Corrosion
by Woodhead Publishing and Maney Publishing
on behalf of
The Institute of Materials, Minerals & Mining**

**CRC Press
Boca Raton Boston New York Washington, DC**

WOODHEAD PUBLISHING LIMITED
Cambridge England

Published by Woodhead Publishing Limited, Abington Hall, Abington
Cambridge CB21 6AH, England
www.woodheadpublishing.com

Published in North America by CRC Press LLC, 6000 Broken Sound Parkway, NW,
Suite 300, Boca Raton, FL 33487, USA

First published 2007 by Woodhead Publishing Limited and CRC Press LLC

British Library Cataloguing in Publication Data
A catalogue record for this book is available from the British Library.

Library of Congress Cataloging in Publication Data
A catalog record for this book is available from the Library of Congress.

Woodhead Publishing ISBN 978-1-84569-241-4 (book)
Woodhead Publishing ISBN 978-1-84569-308-4 (e-book)
CRC Press ISBN 978-1-4200-5409-5
CRC Press order number: WP5409
ISSN 1354-5116

The publishers' policy is to use permanent paper from mills that operate a sustainable forestry policy, and which has been manufactured from pulp which is processed using acid-free and elementary chlorine-free practices. Furthermore, the publishers ensure that the text paper and cover board used have met acceptable environmental accreditation standards.

Typeset by Replika Press Pvt Ltd, India
Printed by TJ International Ltd, Padstow, Cornwall, England

Contents

PART II Copper alloys

Contributor contact details

(* = main contact)

Editor

D. Féron
CEA-Saclay
DPC/SCCME
Bât. 458, P.C. 50
91191 GIF-SUR-Yvette Cedex
France

Email: damien.feron@cea.fr

Chapter 1

Jerzy Birn and Igor Skalski*
Ship Design and Research Centre
Research and Development Division
Ship Materials, Corrosion and Environment Protection Division
80–369 Gdansk
Al. Rzeczypospolitej 8
Poland

Email: jbirn@cto.gda.pl
skalgo@cto.gda.pl

Chapter 2

Robert J. K. Wood
Surface Engineering and Tribology Group
School of Engineering Sciences
University of Southampton
Southampton
SO17 1BJ
UK

Email: rjw3@soton.ac.uk

Chapter 3

Anton Klassert* and Ladji Tikana
Deutsches Kupferinstitut e.V.
Am Bonneshof 5
40474 Düsseldorf
Germany

Email: AKlassert@kupferinstitut.de
LTikana@kupferinstitut.de

Chapter 4

Roy Johnsen
Norwegian University of Science and Technology
NO-7491 Trondheim
Norway

Email: roy.johnsen@ntnu.no

Chapter 5

Wilhelm Schleich*
Technical Advisory Service
KM Europa Metal AG
Klosterstr. 29
49074 Osnabrück
Germany

Email: wilhelm.schleich@kme.com

Carol Powell
Consultant to Copper Development Association UK
Square Covert
Caynham
Ludlow
Shropshire
SY8 3BJ
UK

Email: carol.powell@btinternet.com

Chapter 6

Hervé Le Guyader and Anne-Marie Grolleau*
DCN Cherbourg
Département 2EI
50115 Cherbourg Naval
France

Email: anne-marie.grolleau@dcn.fr

Edward Lemieux
Naval Research Laboratory
Key West
Fl 33040
USA

Keith Lucas
Naval Research Laboratory
Washington
DC 20375
USA

Theresa Wolejsza
Geo Centers
Key West
Fl 33040
USA

Chapter 7

R. S. Oakley*, J. C. Galsworthy and G. S. Fox
QinetiQ Ltd
Cody Technology Park
Farnborough
Hampshire
GU14 0LX
UK

Email: rsoakley@qinetiq.com

K. R. Stokes
Defence Science and Technology Laboratory
Porton
Salisbury
Wiltshire
SP4 0JQ
UK

Chapter 8

R. C. Barik, J. A. Wharton and
R. J. K. Wood*
Surface Engineering and Tribology
Group
School of Engineering Sciences
University of Southampton
Highfield
Southampton
SO17 1BJ
UK

Email: rjw3@soton.ac.uk

K. R. Stokes
Defence Science and Technology
Laboratory
Porton
Salisbury
Wiltshire
SP4 0JQ
UK

Chapter 9

Kemal Ni ancıo lu
Department of Materials Science
and Engineering
Norwegian University of Science
and Technology
N-7491 Trondheim
Norway

Email: kemaln@nt.ntnu.no

Chapter 10

R. Orozco-Cruz*
Unidad AntiCorrosión
Instituto de Ingeniería
Universidad Veracruzana
UV. S. S. Juan Pablo II
Zona Universitaria. Fracc. Costa
Verde
94294 Boca del río
Veracruz
México

Email: rorozco@uv.mx

J. Genesca
Dpto. Ingenieria Metalurgica
Facultad Quimica
Universidad Nacional Autonoma
México, UNAM
Ciudad Universitaria
04510
México D. F.

Email: genesca@servidor.unam.mx

J. A. Juarez-Islas
Instituto de Investigacion en
Materiales
Universidad Nacional Autonoma
México, UNAM
Ciudad Universitaria
04510
México D. F.

Email: julioalb@servidor.unam.mx

Chapter 11

Hervé Le Guyader, Valérie Debout and Anne-Marie Grolleau*
DCN Cherbourg
Département 2EI
50115 Cherbourg Naval
France

Email: anne-marie.grolleau@dcn.fr

Jean-Pierre Pautasso
DGA/CTA
16 bis, avenue Prieur de la Côte D'Or
94114 Arcueil
Cedex
France

European Federation of Corrosion (EFC) publications: Series introduction

The EFC, incorporated in Belgium, was founded in 1955 with the purpose of promoting European co-operation in the fields of research into corrosion and corrosion prevention.

Membership of the EFC is based upon participation by corrosion societies and committees in technical Working Parties. Member societies appoint delegates to Working Parties, whose membership is expanded by personal corresponding membership.

The activities of the Working Parties cover corrosion topics associated with inhibition, education, reinforcement in concrete, microbial effects, hot gases and combustion products, environment-sensitive fracture, marine environments, refineries, surface science, physico-chemical methods of measurement, the nuclear industry, the automotive industry, computer-based information systems, coatings, tribo-corrosion and the oil and gas industry. Working Parties and Task Forces on other topics are established as required.

The Working Parties function in various ways, e.g. by preparing reports, organising symposia, conducting intensive courses and producing instructional material, including films. The activities of Working Parties are co-ordinated, through a Science and Technology Advisory Committee, by the Scientific Secretary. The administration of the EFC is handled by three Secretariats: DECHEMA e.V. in Germany, the Société de Chimie Industrielle in France, and The Institute of Materials, Minerals and Mining in the United Kingdom. These three Secretariats meet at the Board of Administrators of the EFC. There is an annual General Assembly at which delegates from all member societies meet to determine and approve EFC policy. News of EFC activities, forthcoming conferences, courses, etc., is published in a range of accredited corrosion and certain other journals throughout Europe. More detailed descriptions of activities are given in a Newsletter prepared by the Scientific Secretary.

The output of the EFC takes various forms. Papers on particular topics, for example, reviews or results of experimental work, may be published in scientific and technical journals in one or more countries in Europe. Conference

proceedings are often published by the organisation responsible for the conference.

In 1987 the, then, Institute of Metals was appointed as the official EFC publisher. Although the arrangement is non-exclusive and other routes for publication are still available, it is expected that the Working Parties of the EFC will use The Institute of Materials, Minerals and Mining for publication of reports, proceedings, etc., wherever possible.

The name of The Institute of Metals was changed to The Institute of Materials on 1 January 1992 and to The Institute of Materials, Minerals and Mining with effect from 26 June 2002. The series is now published by Woodhead Publishing and Maney Publishing on behalf of The Institute of Materials, Minerals and Mining.

P. McIntyre
EFC Series Editor,
The Institute of Materials, Minerals and Mining, London, UK

EFC Secretariats are located at:

Dr B. A. Rickinson
European Federation of Corrosion, The Institute of Materials, Minerals and Mining, 1 Carlton House Terrace, London, SW1Y 5DB, UK

Dr J. P. Berge
Fédération Européenne de la Corrosion, Société de Chimie Industrielle, 28 rue Saint-Dominique, F-75007 Paris, FRANCE

Professor Dr G. Kreysa
Europäische Föderation Korrosion, DECHEMA e. V., Theodor-Heuss-Allee 25, D-60486, Frankfurt, GERMANY

Volumes in the EFC series

1 **Corrosion in the nuclear industry**
Prepared by the Working Party on Nuclear Corrosion

2 **Practical corrosion principles**
Prepared by the Working Party on Corrosion Education (Out of print)

3 **General guidelines for corrosion testing of materials for marine applications**
Prepared by the Working Party on Marine Corrosion

4 **Guidelines on electrochemical corrosion measurements**
Prepared by the Working Party on Physico-Chemical Methods of Corrosion Testing

5 **Illustrated case histories of marine corrosion**
Prepared by the Working Party on Marine Corrosion

6 **Corrosion education manual**
Prepared by the Working Party on Corrosion Education

7 **Corrosion problems related to nuclear waste disposal**
Prepared by the Working Party on Nuclear Corrosion

8 **Microbial corrosion**
Prepared by the Working Party on Microbial Corrosion

9 **Microbiological degradation of materials – and methods of protection**
Prepared by the Working Party on Microbial Corrosion

10 **Marine corrosion of stainless steels: chlorination and microbial effects**
Prepared by the Working Party on Marine Corrosion

11 **Corrosion inhibitors**
Prepared by the Working Party on Inhibitors (Out of print)

12 **Modifications of passive films**
Prepared by the Working Party on Surface Science and Mechanisms of Corrosion and Protection

13 **Predicting CO_2 corrosion in the oil and gas industry**
Prepared by the Working Party on Corrosion in Oil and Gas Production (Out of Print)

14 **Guidelines for methods of testing and research in high temperature corrosion**
Prepared by the Working Party on Corrosion by Hot Gases and Combustion Products

15 **Microbial corrosion (Proc. 3rd Int. EFC Workshop)**
Prepared by the Working Party on Microbial Corrosion

16 **Guidelines on materials requirements for carbon and low alloy steels for H_2S-containing environments in oil and gas production**
Prepared by the Working Party on Corrosion in Oil and Gas Production

17 **Corrosion resistant alloys for oil and gas production: guidance on general requirements and test methods for H_2S Service**
Prepared by the Working Party on Corrosion in Oil and Gas Production

18 **Stainless steel in concrete: state of the art report**
Prepared by the Working Party on Corrosion of Reinforcement in Concrete

19 **Sea water corrosion of stainless steels – mechanisms and experiences**
Prepared by the Working Parties on Marine Corrosion and Microbial Corrosion

20 **Organic and inorganic coatings for corrosion prevention – research and experiences**
Papers from EUROCORR '96

21 **Corrosion – deformation interactions**
CDI '96 in conjunction with EUROCORR '96

22 **Aspects on microbially induced corrosion**
Papers from EUROCORR '96 and the EFC Working Party on Microbial Corrosion

23 **CO_2 corrosion control in oil and gas production – design considerations**
Prepared by the Working Party on Corrosion in Oil and Gas

24 **Electrochemical rehabilitation methods for reinforced concrete structures – a state of the art report**
Prepared by the Working Party on Corrosion of Reinforced Concrete

25 **Corrosion of reinforcement in concrete – monitoring, prevention and rehabilitation**
Papers from EUROCORR '97

26 **Advances in corrosion control and materials in oil and gas production**
Papers from EUROCORR '97 and EUROCORR '98

27 **Cyclic oxidation of high temperature materials**
Proceedings of an EFC Workshop, Frankfurt/Main, 1999

28 **Electrochemical approach to selected corrosion and corrosion control**
Papers from 50th ISE Meeting, Pavia, 1999

29 **Microbial Corrosion (proceedings of the 4th international EFC workshop)**
Prepared by the Working Party on Microbial Corrosion

30 **Survey of literature on crevice corrosion (1979–1998): mechanisms, test methods and results, practical experience, protective measures and monitoring**
Prepared by F. P. Ijsseling and the Working Party on Marine Corrosion

31 **Corrosion of reinforcement in concrete: corrosion mechanisms and corrosion protection**
Papers from EUROCORR '99 and the Working Party on Corrosion of Reinforcement in Concrete

32 **Guidelines for the compilation of corrosion cost data and for the calculation of the life cycle cost of corrosion – a working party report**
Prepared by the Working Party on Corrosion in Oil and Gas Production

33 **Marine corrosion of stainless steels: testing, selection, experience, protection and monitoring**
Edited by D Féron on behalf of Working Party 9 on Marine Corrosion

34 **Lifetime modelling of high temperature corrosion processes**
Proceedings of an EFC Workshop 2001. Edited by M. Schütze, W. J. Quadakkers and J. R. Nicholls

35 **Corrosion inhibitors for steel in concrete**
Prepared by B. Elsener with support from a Task Group of Working Party 11 on Corrosion of Reinforcement in Concrete

36 **Prediction of long term corrosion behaviour in nuclear waste systems**
Edited by D. Féron and Digby D. Macdonald on behalf of Working Party 4 on Nuclear Corrosion

37 **Test methods for assessing the susceptibility of prestressing steels to hydrogen induced stress corrosion cracking**
Prepared by B. Isecke on behalf of Working Party 11 on Corrosion of Reinforcement in Concrete

38 **Corrosion of reinforcement in concrete: mechanisms, monitoring, inhibitors and rehabilitation techniques**
Edited by M. Raupach, B. Elsener, R. Polder and J. Mietz on behalf of Working Party 11 on Corrosion of Steel in Concrete

39 **The use of corrosion inhibitors in oil and gas production**
Edited by J. W. Palmer, W. Hedges and J. L. Dawson

40 **Control of corrosion in cooling waters**
Edited by J. D. Harston and F. Ropital

41 **Metal dusting, carburisation and nitridation**
Edited by M. Schütze and H. Grabke

42 **Corrosion in refineries**
Edited by J. Harston

43 **The electrochemistry and characteristics of embeddable reference electrodes for concrete**
Prepared by R. Myrdal on behalf of Working Party 11 on Corrosion of Steel in Concrete

44 **The use of electrochemical scanning tunnelling microscopy (EC-STM) in corrosion analysis: reference material and procedural guidelines**
Prepared by R. Lindström, V. Maurice, L. Klein and P. Marcus on behalf of Working Party 6 on Surface Science

45 **Local probe techniques for corrosion research**
Edited by R. Oltra, V. Maurice, R. Akid and P. Marcus on behalf of Working Party 8 on Physico-Chemical Methods of Corrosion Testing

46 **Amine unit corrosion survey**
Edited by J. Harston and F. Ropital on behalf of Working Party 15 on Corrosion in the Refinery Industry

47 **Novel approaches to the improvement of high temperature corrosion resistance**
Edited by M. Schütze and W. Quadakkers on behalf of Working Party 3 on Corrosion in Hot Gases and Combustion Products

48 **Corrosion of metallic heritage artefacts: investigation, conservation and prediction of longterm behaviour**
Edited by P. Dillmann, G. Béranger, P. Piccardo and H. Matthiessen on behalf of Working Party 4 on Nuclear Corrosion

49 **Electrochemistry in light water reactors: reference electrodes, measurements, corrosion and tribocorrosion issues**
Edited by R. W. Bosch, D. Féron and J. P. Celis on behalf of Working Party 4 on Nuclear Corrosion

50 **Corrosion behaviour and protection of copper and aluminium alloys in seawater**
Edited by D. Féron on behalf of Working Party 9 on Marine Corrosion

51 **Corrosion issues in light water reactors: stress corrosion cracking**
Edited by D. Féron and J-M. Olive on behalf of Working Party 4 on Nuclear Corrosion

Preface

The Marine Corrosion Working Party of the EFC (EFC WP9) organised an international workshop on the behaviour of copper and aluminium alloys in natural and treated seawaters during EUROCORR 2004 in Nice (France). One of the major objectives of this 'Marine Corrosion Workshop on Copper and Aluminium Alloys in Seawater' was to present evidence and gather together the results of research and development carried out on the seawater applications of these alloys during recent years. The workshop brought together scientists and engineers involved in assessing the behaviour of copper and aluminium in seawater, with particular emphasis on Long-Term Behaviour and Testing and on Mechanisms and Modelling.

Following the scientific and technical success of this event, a selection of papers presented at the workshop and during Eurocorrs have been collected together, updated by their authors and reviewed by a selection and review committee composed of:

- Bård Espelid, DNV (Norway), Past-Chairman of the EFC WP9 'Marine corrosion'
- Damien Féron, CEA (France)
- Gabrielle Ferrari, TNO (The Netherlands)
- Manfred Jasner, consultant to KME (Germany)
- Willy Schleich, KME (Germany)
- Jerzy Birn, retired from CTO (Poland)

The resulting book is divided into five parts, starting with overviews on the corrosion and the erosion–corrosion of copper and aluminium alloys in seawater. Next the behaviour of copper alloys and copper–nickel alloys in seawater is investigated. The third part deals with aluminium bronzes and their coupling with other materials in seawater or in brackish seawater and this is followed by the corrosion and protection of aluminium alloys in seawater. The last part is related to the aluminium-based materials used as anodes for the cathodic protection of structures in marine environments.

The editor and the chairman of the EFC WP9 hope that this book will be useful to engineers using copper and aluminium alloys in seawater and to

scientists working towards an understanding of and the resolution of the corrosion phenomena that we have to face in seawater.

Ulf Kivissak
Chairman of the EFC Working Party 9 on Marine Corrosion

Damien Féron
Editor of this volume

Part I

Overview of copper and aluminium alloys

1

Corrosion behaviour of non-ferrous alloys in seawater in the Polish marine industry

JERZY BIRN and IGOR SKALSKI, Ship Design and Research Centre, Poland

1.1 Introduction

Copper, aluminium and titanium alloys are the most important of the alloys belonging to the group of non-ferrous metals generally used in marine engineering. Titanium alloys are usually sufficiently resistant to corrosion in sea water, so in this chapter only the corrosion behaviour of copper and aluminium alloys is discussed. Copper alloys are mainly used for pipelines, heat exchangers, screw propellers, valves, gate valves, clad plates for steel hulls of small ships, clad plates for drilling rigs' splash zones, etc. Aluminium alloys are used for hulls of fast ships and superstructures of other ships to improve their stability, for construction of liquefied natural gas (LNG) cargo tanks, and also for construction of yachts, sport boats, police boats, etc. The following copper alloys are discussed in this chapter: aluminium and tin brasses, cupro–nickels 90/10 and 70/30, aluminium–nickel, tin and silicon bronzes as well as Al–Mg and Al–Mg–Zn aluminium alloys.

Copper alloys belong to the group of alloys having sufficient resistance to corrosion in seawater. However, they corrode under specific conditions, for instance in fast flowing seawater or when exposed to some pollutants existing in water, and also when requirements of an adequate chemical composition of the alloy are not fulfilled. Generally, copper alloys are not protected with paint coatings. Anticorrosion protection of pipes involves dosing Fe^{2+} ions into the seawater cooling system. An important feature of copper alloys is their antifouling activity. However, in mixed metal systems antifouling protection of these alloys may be necessary. This protection is provided by copper ions or biocides (including chlorine) dosing.

The types of corrosion that copper alloys are usually susceptible to are:

- selective corrosion (dezincification, denickelification and dealuminiumfication);
- stress corrosion and corrosion fractures;
- impingement attack;

- corrosion erosion and cavitation erosion;
- galvanic corrosion occurring when in contact with a more noble alloy;
- pitting corrosion.

Aluminium alloys, although self-passivating, do not have high resistance to chlorides contained in seawater. Some aluminium alloys, after an unfavourable heat treatment, e.g. welding, lose their corrosion resistance totally. So the use of aluminium alloys in seawater requires protection by means of paint coatings and cathodic protection.

Aluminium alloys are subject to the following kinds of corrosion:

- pitting corrosion;
- exfoliation corrosion;
- galvanic corrosion occurring when in contact with more noble alloys.

Later in this chapter, several kinds of corrosion and the main causes of their occurrence will be discussed. In conclusion, the research tasks which, in the authors' opinion, should improve the corrosion resistance of the alloys discussed and decrease the number of corrosion failures, will be presented. The topic is so extensive that in this chapter it will be possible to present only an outline rather than a detailed or profound demonstration. Particular attention is paid to the problems of modelling corrosion processes on aluminium and copper alloys and to the long-term prediction of life for these alloys. A significant part of the material is based on a literature survey 'Corrosion of Copper and Aluminium Alloys in Sea Water' [1].

1.2 Corrosion behaviour of copper alloys in seawater

1.2.1 Brasses

Brasses (together with bronzes) are the oldest alloys used in marine technology. Hence, corrosion of these alloys has been more studied and is better understood than that of other alloys. Brasses are the alloys most susceptible to selective corrosion and to stress corrosion cracking. An example of an intensive dezincification process is shown in Fig. 1.1 [2].

Selective corrosion of the brass was caused by an insufficient content of arsenic as an alloying component preventing dezincification. Additions of arsenic or tin are necessary to prevent this selective corrosion. De-alloying occurs when the arsenic content is lower than 0.07% [3].

However, additions of arsenic and of phosphorus should be limited due to the possibility of an increase in susceptibility to stress corrosion cracking. The arsenic content should not be higher than 0.06% and that of phosphorus no higher than 0.04% [4].

A second cause of serious corrosion damage of copper alloys may be high

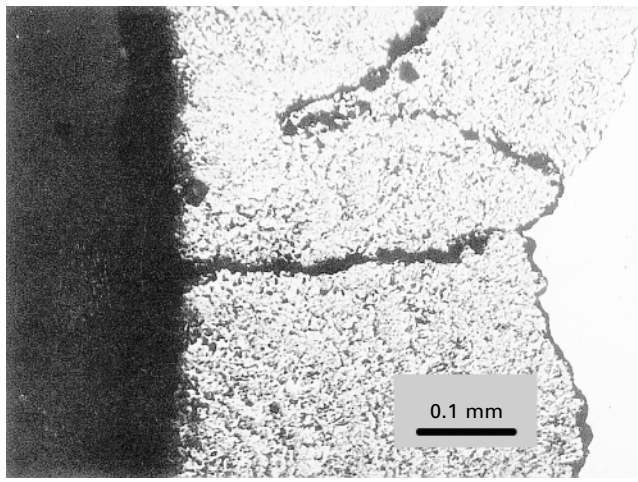

1.1 Metallographic cross-section through the wall of a pipe after 12 months of service in seawater. Dezincification of M70 alloy (Cu 69–71 %, rest Zn) reaches half of the wall thickness [2].

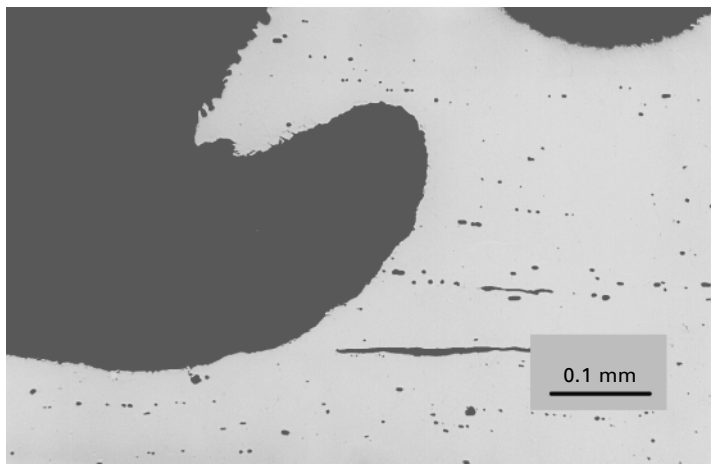

1.2 Wall of a pipe. Cross-section. Shape of the pit is characteristic for damage caused by an impingement attack [2].

seawater flow rates occurring mainly in pipelines, heat exchangers and ship propellers. Three kinds of corrosion damage can be distinguished: impingement attack, corrosion erosion and cavitation erosion. An example of impingement attack is shown in Fig. 1.2 [2].

Impingement attack occurs most often when the velocity of well-aerated sea water increases (for instance at pipe inlets, as a result of choking of a significant number of other pipes in the heat exchanger). Recommended seawater flow velocities are as follows [5]:

- pipes of diameters up to 20 mm inclusive, made of aluminium brass: between 0.8 and 1.75 m/s;
- pipes of diameters over 20 mm, made of aluminium brass: between 0.8 and 2.5 m/s;
- pipes of cupro–nickel 90/10: between 0.8 and 3.2 m/s;
- pipes of cupro–nickel 70/30: between 0.8 and 4.5 m/s.

BS MA 18 [6] gives examples of recommended seawater flow velocities as follows:

- pipes of diameter 20 mm: 0.98–1.15 m/s for Al–brass, CuNiFe 90/10 and CuNiFe 70/30;
- pipes of diameters 200 mm: Al–brass max 3.0 m/s; CuNiFe 90/10 max 3.5 m/s; CuNiFe 70/30 max 4 m/s.

Products made of aluminium, tin or other brasses may also suffer galvanic corrosion when incorrectly assembled in a system made of more noble material [2]. Corrosion damage of a thermometer casing made of brass mounted in a cupro–nickel pipeline is presented in Fig. 1.3 [7].

Corrosion of brasses in polluted seawater and microbiological corrosion will be discussed in a separate section of this chapter.

As can be seen from the examples given of corrosion of brasses, those alloys have the lowest resistance to corrosion of all the copper alloys used in the marine environment. Their wide use may be ascribed to their relatively low price.

1.2.2 Cupro–nickels

90/10 and 70/30 cupro–nickels have been widely used since around 1940, at first mainly for battleships but later also on merchant vessels. Their corrosion

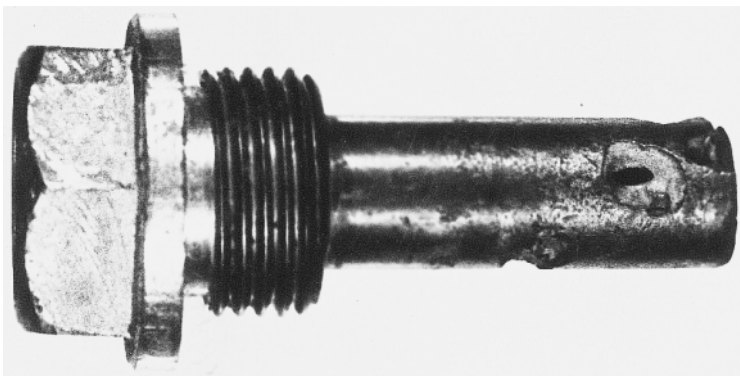

1.3 Thermometer casing made of 63Cu–37Zn brass placed in 90/10 copper–nickel pipe [7].

resistance in seawater is better than that of brasses, and they are not susceptible to stress corrosion. Selective and galvanic corrosion (except for contact with titanium alloys) do not create such a serious problem as they do in brasses. They are more resistant than brasses to corrosion erosion in flowing seawater and may be used at higher velocities of seawater flow. However, as alloys showing better passivation in seawater than brasses, they may be subject to more intensive pitting corrosion processes [8]. Denickelification is no longer a problem when 1–2 % of iron is added to these alloys.

North and Pryor [9], Mathiyarasu *et al*. [10], Milošev and Metikoš-Huković [11] as well as Shibad *et al*. [12] have shown that the main component of the protective film is Cu_2O. The iron as a component of cupro–nickels increased the electronic resistance of the Cu_2O oxide. North and Pryor [9] hypothesized that nickel and iron are incorporated into the Cu_2O film, occupy cation vacancies and, thus, reduce the cation vacancy concentration, which increases resistance. Mathiyarasu *et al*. [10] have investigated the role of chloride ions on the passivation of cupro–nickels. Chloride ions adsorb on the surface and occupy the oxygen vacancies in the film.

Cupro–nickels are subject to galvanic corrosion caused by contact with titanium (Fig. 1.4) [13]. They are also subject to localized corrosion processes usually caused by the presence of inorganic deposits and fouling [8]. Corrosion of this type may also be caused by the presence of carbon deposits not removed after a process of annealing of oiled pipes. This can also occur on brasses.

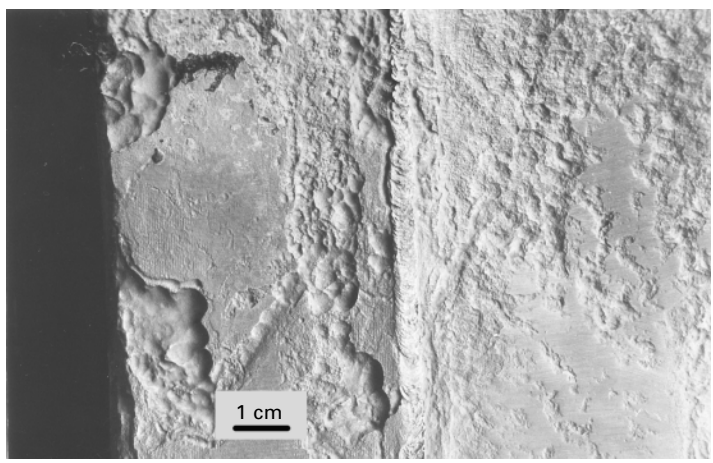

1.4 Galvanic corrosion of 90/10 cupro–nickel pipe connected with connector made of titanium.

1.2.3 Bronzes

Of all the copper alloys, the bronzes may be included in the group showing the highest corrosion resistance in fast flowing seawater. Bronzes are mainly used as cast materials. Atsumi *et al*. [14] studied service reports from 25 power plants, showing that the average failure rate over 17 years of AP bronze (Cu; 6–8 % Sn; 1 % Al; 0.1 % Si) is 0.30 tubes per 10^4 tubes per year, while that of aluminium brass tubes over 21 years is 5.46 tubes per 10^4 tubes per year. Corrosion resistance in polluted seawater is attributed to the inner surface film composed mainly of SnO_2.

However, not all kinds of bronzes have sufficient corrosion resistance in flowing sea water. Some ejector pump casings show heavy erosion–corrosion damage. One of the causes of intensive erosion–corrosion of these casings is inadequate chemical composition of bronze (Cu; 2.91 % Sn; 6.98 % Pb; 5.4 % Zn; 0.13 % Ni). Bronzes of 88/10/2 type or nickel bronzes should be used for pump casings [15].

Singh *et al*. [16] investigated the role of silicon in the corrosion resistance of cast silicon bronzes in natural seawater. Four alloys with different silicon contents (1, 3, 5, 10 %) were used for the investigations. Tests showed that the corrosion rates increase with increasing content of silicon, except for the alloy containing 10 % silicon. The Cu–1Si alloy shows lower corrosion current density because its optimum silicon–copper ratio allows the formation of a non-brittle alloy as well as a protective Cu–silicide layer.

Schüssler and Exner [17] investigated the corrosion of nickel–aluminium bronzes (Cu; Al 9.41 %; Ni 4.77 %; Fe 4.32 %; Mn 2.60 %) in seawater. The results showed that on the surface of the nickel-aluminium bronzes in seawater, protective layers are formed. A decrease of both anodic and cathodic reaction rate was found. Anodic passivation is due to the formation of an aluminium-oxide phase, which hampers ionic transport through the corrosion products. Therefore, corrosion in the passive state does not depend on the velocity of seawater flow. Decrease of the oxygen reaction is caused by formation of copper (Cu I) oxide in the outer part of the protective layer.

1.2.4 Modelling of corrosion processes of copper alloys and long-term prediction of life for the alloys

Lush and Carr [18] have presented a model for the dissolution of copper in seawater under mixed activation and diffusion control. A series of potentiostatic measurements of the current for a short annular electrode in a substitute seawater flow cell has been made at a variety of potentials between –0.25 and –0.15 V (SCE) and with fluid velocity between 0.16 and 1.6 m/s. The theoretical model enables the total current to be separated into two components, conveniently named the diffusion-affected and activation-affected currents,

and it allows the variation of each component with velocity to be determined. It was shown that the activation-affected component of the total current was independent of fluid velocity, as expected, and the diffusion-affected component varied with velocity to a power of about 0.65, again as expected, for turbulent flow over an electrode.

Wood *et al.* [19] have investigated the mass transfer influence of non-cavitating seawater on the corrosion of copper and 70/30 cupro–nickel alloy. The work presented is concerned with the prediction of corrosion rates of copper and cupro–nickel in flowing seawater (up to 16 m/s) and for filmed copper and cupro–nickel (up to 3.5 m/s). The effect of flow on corrosion currents of filmed and polished samples that allow the surface behaviour of old and newly fitted components to be modelled is discussed. Equations describing the flow velocity dependence of these currents are developed and used to determine the mechanism controlling the copper dissolution and to identify the dissolution reactions. Several important features of the anodic dissolution reaction have been established:

- the dissolution rate of unfilmed surfaces is determined by the surface concentrations of Cu(I);
- when the metal becomes covered by an oxide, it is a clear indication of a change in the rate-determining step from surface diffusion to ion transfer across the metal–oxide interface;
- the anodic film can be further oxidized at sufficiently positive potentials to yield Cu(II) – this reaction can indeed be caused by oxygen to yield atacamite.

An exact long-term prediction of the life expectancy of copper alloy products is not yet possible, although in 1962 [20] this was determined as follows:

- brass pipes: 9.7 years;
- cupro–nickel pipes 90/10 and 70/30 > 20 years;
- galvanized steel pipes: 5.7 years;

but these data were obtained from observations gained during service on ships rather than being based on calculations. Further studies should be performed in this field which would complement current knowledge regarding the long-term prediction of the service life of alloys.

1.2.5 Effect of pollutants and sulphate-reducing bacteria on the corrosion of copper alloys in seawater

Hydrogen sulphide and ammonia are the most common pollutants which may cause an intensive corrosion of copper alloys in seawater. However, since the 1980s most attention has been paid to sulphides generated from the

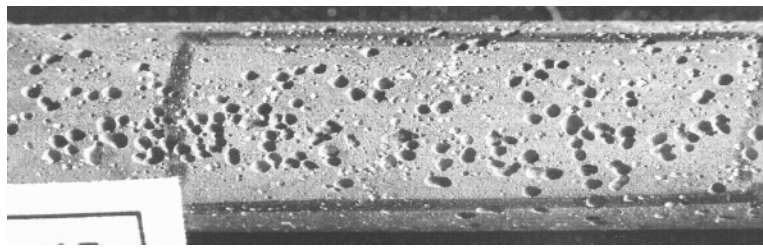

1.5 Pitting corrosion on aluminium brass pipe exposed in seawater containing SRB. Diameter of pipe = 12 mm.

reaction of hydrogen sulphide with components present in seawater. Intensity of corrosion in sulphide-polluted seawater (see Fig. 1.5) depends on the sulphides' concentration and the sequence of exposure: first in the polluted water then in a clean water. Syrett [21], Schiffrin and De Sanchez [22] and Kato *et al*. have described [23] the mechanism of accelerated corrosion of cupro–nickel in seawater polluted with sulphides. The presence of sulphide ions leads to modification of the oxide layer on copper-based alloys. Acceleration of corrosion is due to enhancement of the cathodic process. One of the most important parameters playing a major part in the processes of corrosion of copper alloys in seawater polluted with sulphides is their concentration. Traverso *et al*. [24] have found that the most intensive corrosion is caused by sulphides at initial levels of 4 ppm. Gudas and Hack [25] stated that wrought 90/10 Cu–Ni is susceptible to accelerated attack in seawater containing only 0.01 ppm of sulphides. Efird and Lee [26] have found that corrosion of cupro–nickel 90/10 is severely accelerated only during exposure to unpolluted seawater after long exposure to putrid seawater. Gudas and Hack [27] stated that for sulphide concentrations of 0.01 ppm, severe accelerated corrosion occurs until after the first 30 days of sulphide exposure. Mukhopadhyay and Baskaran [28] and Chauhan and Gadiyar [29] determined the chemical composition of corrosion products created on 70/30 copper–nickel in sulphide-polluted seawater. Instead of Cu_2O and green $CuCl_2 \cdot 3Cu(OH)_2 \cdot 3H_2O$, a grey layer of $Cu_2S(NiFe)_3S_4$ and Cu_2O was created.

Only a few publications regarding the effect of ammonia present in seawater on the corrosion of copper alloys have been found. One of them was Rajagopalan *et al*.'s publication [30]. Contamination of seawater with 1 ppm ammonia has a pronounced effect on the acceleration of corrosion of Admiralty brass, aluminium brass and 90/10 cupro–nickel. 70/30 cupro–nickel showed no observable effect.

Biocorrosion of copper alloys in sea water was described by de Saravia *et al*. [31]. Modifications in the metal/solution interface properties of Cu/Ni alloys can be induced by microbial attachment:

- through the generation of diffusional barriers;

- by changing the structural characteristic of the corrosion products beneath bacterial colonies;
- through the formation of layer-by-layer structures in which biological films are mixed with corrosion products and alter the adhesion of the latter;
- through the production of aggressive metabolites, which reduce the protective characteristics of the oxide layer.

Macdonald *et al*. [32] stated that accelerated corrosion of the cupro–nickel alloys in sulphide-polluted seawater is caused by a shift in the corrosion potential to active values.

1.2.6 Anticorrosion and antifouling protection of ship seawater cooling installations made of copper alloys

One of the methods of anticorrosion protection of copper alloys is dosing $FeSO_4$ solution or anodic dissolution of iron or aluminium. The inhibitive effect of $FeSO_4$ solution has been attributed to the generation of a film consisting of lepidocrocite (γ-FeO.OH) [33]. This film reduces oxygen transport to the cathode, thereby increasing the cathodic control. Lenard *et al*. [34] investigated the effect of Fe^{2+} ions on corrosion of cupro–nickel alloys and Naval brass in sulphide-polluted seawater. Sulphides delayed or prevented the development of a protective film during subsequent exposure to clean seawater. When using Fe^{2+} ions, a quick oxidation of these ions should be taken into consideration. Dosing should be carried out at such a rate that the Fe^{2+} ions have no time to oxidize. The oxidation of Fe^{2+} ions in aerated seawater occurs practically during the 3 min after generation [35].

Syrett and Coit [36] described other prevention methods such as: keeping the tubes clean (control of biofouling by chlorination, cleaning system by driving sponge rubber balls through the tubes), installing vanes and diffusers to reduce turbulence in the inlet region of the tubes, and cathodic protection. During the application of cathodic protection of condenser tubes, the authors stated, cathodic protection does not provide significant benefit beyond about 6 in. from the end of a copper alloy condenser tube because of limited ‘throw’ of the current down the tube. Some specialists are of the opinion that copper alloys do not need antifouling protection. However, shipowners require antifouling protection for seawater pipes on new ships, particularly on those which operate in tropical waters.

Chlorine is the only known biocide which can cause corrosion of copper alloys in seawater. Other biocides (quaternary ammonium chlorides, copper ions) do not increase the corrosion rate of copper alloys but, instead, act sometimes as corrosion inhibitors. Francis [37] stated that the safe chlorine concentration is 0.5 ppm, at which no significant change in the electrochemical

properties of the protective film occurred. Birn [38] has found that aluminium brass and 90/10 cupro–nickel show the first insignificant peak of corrosion rate at a very low chlorine concentration of 0.01 ppm. At higher chlorine concentration the alloys passivate, and further rapid increase of corrosion rate is observed at a chlorine concentration of 2.5 ppm. According to de Romero *et al*. [39], chlorinated compounds increased the corrosion rate of the 90/10 cupro–nickel alloy by increasing the medium's oxidizing capacity. This promoted greater Cu_2O oxidation to non-adherent compounds such as paratacamite. Furthermore, Goodman [40] stated that chlorine causes the formation of a different or modified film which can lead to the stimulation of attacks at sites of film damage as a result of a large potential difference between filmed and bare metal surface. Protection against galvanic corrosion is ensured by isolation of two sections of a pipeline made of different metals from each other (Fig. 1.6). [41].

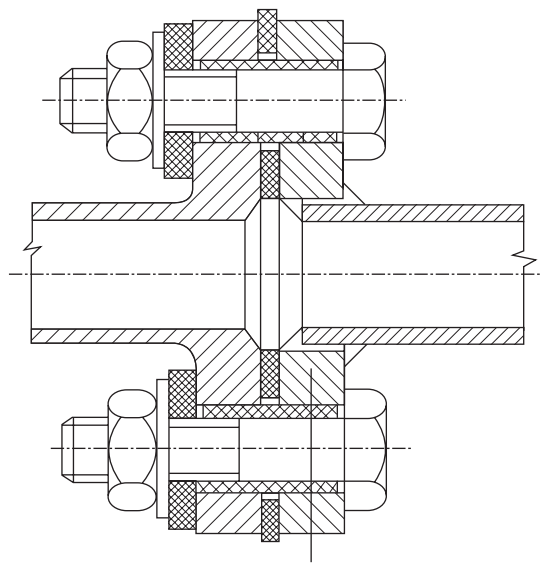

1.6 Example of insulation to prevent galvanic corrosion of galvanized carbon steel pipe attached to bronze pump casing. Galvanic insulation is one method of preventing galvanic corrosion. As insulating materials, rubber, PTFE or Textolit may be applied.

1.3 Corrosion behaviour of aluminium alloys in seawater

1.3.1 Description of various corrosion types of aluminium alloys

One of the most important types of corrosion of aluminium alloys in seawater is localized corrosion: pitting and crevice corrosion. There are many theories

concerning corrosion causes, and only basic problems are discussed here. Davis [42] described pitting and crevice corrosion as corrosion which arises from the creation of a localized, aggressive environment that breaks down the normal corrosion-resistant passive layers of metal. Pits are formed at local discontinuities in the oxide film on aluminium exposed to seawater. Szklarska-Śmiałowska [43] presents the following four stages of the pitting corrosion process:

1. processes occurring on the passive film;
2. processes occurring within the passive film, when no visible changes occur in the film;
3. formation of so-called metastable pits which initiate and grow below critical pitting potential and then repassivate;
4. stable pit growth, above a critical pitting potential.

Due to the susceptibility of aluminium alloys to localized corrosion, products made of these alloys and used in seawater should be protected against corrosion by paint coatings and cathodic protection.

Another type of corrosion, typical for aluminium alloys, is galvanic corrosion. The corrosion potential of aluminium alloys is usually more negative than that of other metals. Reboul [44] investigated the galvanic corrosion of aluminium alloys with other metals in seawater. The galvanic currents of different cells created between aluminium alloy and other metals were measured. For example, these currents for 1050 aluminium alloy after 15 days are as follows:

- plain steel: 1.3 $\mu A/cm^2$
- stainless steel: 1.6 $\mu A/cm^2$
- titanium: 0.3 $\mu A/cm^2$

Another type of corrosion typical for aluminium alloys, is exfoliation corrosion (Fig. 1.7) [45]. The aluminium alloy most susceptible to this type of corrosion is Al–Mg–Zn. This alloy, as supplied after an adequate heat treatment, is not attacked by exfoliation corrosion although it occurs in welded constructions in dimensions which do not enable heat treatment after welding. Robinson [46] described the role of wedging stresses in the exfoliation corrosion of high-strength aluminium alloys. For their investigations, an aluminium alloy L95 (Zn 5.8 %; Mg 2.5 %; Cu 1.6 %; Cr 0.15 %) was used. Wedging stress measurements, profile of surface blisters by a Taylor-Hobson TALYMIN 4-10, and double cantilever beam stress corrosion tests were carried out. The aim of the investigations was to answer the question of what is the main cause of exfoliation corrosion: intergranular corrosion or stress corrosion. The results showed that the lowest value of stress intensity at the tip of the developing corrosion product K_1 for a propagating crack in alloy L95 was 2.6 MN $m^{-3/2}$. The maximum stress generated by exfoliation corrosion

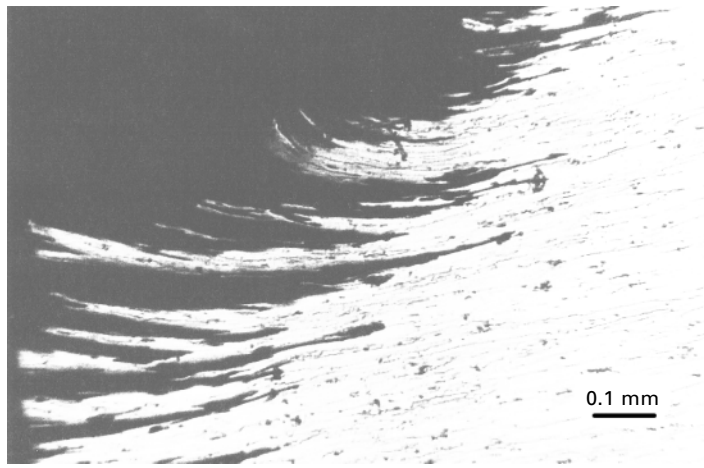

1.7 Exfoliation corrosion of Al–Mg–Zn alloy after welding.

products was 4.8 MN $m^{-3/2}$. The author stated that exfoliation had been effectively prevented by applying compressive loading. From this it is concluded that degradation occurs by a stress corrosion mechanism. The stress intensity at the developing corrosion front K_1 has been estimated by COD measurements and by mathematical modelling to be comparable with K_{ISCC}. If the stress intensity K_1 at the tip of the developing corrosion product is not significantly less than K_{ISCC} it would be additional evidence that stress corrosion is responsible for exfoliation corrosion. Poniewierska *et al*. [45] investigated welded joints of aluminium alloy similar to 7015–T6 alloy. They stated that in the heat-affected zone (HAZ) intensive exfoliation corrosion had occurred.

Low resistance to alkali of aluminium alloys requires a separate discussion. Corrosion risk in seawater in the presence of alkalis occurs only when a construction made of aluminium alloys is cathodically protected; meaning that, at sites adjacent to anodes, alkalization of seawater can occur. Aballe *et al*. [47] performed investigations of localized alkaline corrosion of aluminium alloy AA5083 in an aerated neutral 3.5 % NaCl solution. The localized corrosion is caused by the process of alkalization around the cathodic precipitations existing in the alloy. The pits show a hemispherical morphology. This problem has not been sufficiently studied as yet and should be a subject of further investigations.

Finally, aluminium alloys used as anodes should be mentioned. The properties of these alloys have to be quite different from those of materials used for construction. The anodic materials need not have good mechanical properties, but they should dissolve uniformly in contact with more noble materials and should not passivate in seawater. As anodic materials, aluminium alloys containing zinc, indium, gallium and mercury are applied. Mercury appears to be the most reactive of the mentioned activators. Zinc has no

activation effect but, when added with other activators, has a synergistic action [48].

1.3.2 Modelling of corrosion processes of aluminium alloys and long-term prediction of life for these alloys

Masters *et al*. [49] worked out a mathematical model for crevice corrosion of aluminium alloys in seawater. Seawater exposure tests were carried out, and a mechanism of crevice corrosion initiation was derived and modelled. Input data for the model were generated and model predictions were made which agreed with exposure test observations. Model predictions were also made to highlight the sensitivity of certain parameters as to whether or not corrosion would occur. The following aluminium alloys were used for the investigations: 1050A, 2024, 5083, 6061, 6082, 7010, 8090-T3 and 8090-T851. Crevice corrosion tests were conducted. The alloys 1050A, 5083 and 6082 did not suffer crevice corrosion, while the remainder did to varying degrees.

Robinson [50] worked out mathematical modelling of exfoliation corrosion in high-strength aluminium alloys. The elongated grain shape is an important feature for this form of corrosion. Active corrosion paths along grain boundaries resulting from the electrochemical action between age-hardening precipitates and adjacent solute denuded zones is another cause of exfoliation corrosion. If the volume of corrosion products exceeds the volume of the metal from which they are formed, wedging stresses arise which lift the surface grains. The model described allows the calculation of the internal pressure of the blisters together with a range of dimensions defining the extent of the attack.

Exfoliation damage may be minimised either by reducing the aspect ratio of the grains or by over-ageing the alloy to reduce its susceptibility to intergranular corrosion. Below a particular grain aspect ratio or grain boundary susceptibility to spalling, flaking or powdering of the surface will occur rather than blister formation. The depth of penetration of exfoliation corrosion is dependent on the susceptibility to intergranular corrosion but not upon the grain shape. For both copper alloys and aluminium alloys it is as yet impossible to calculate the alloys' life expectancy. Research in this area should be continued.

1.4 Recommendations on the use of non-ferrous alloys in seawater

In short, the following recommendations can be given for the application of non-ferrous alloys in seawater:

1. Al–brass for pipes and tubes of heat exchangers in seawater of small aggressivity;
2. Sn–brass for tube plates of heat exchangers;
3. cupro–nickels 90/10 and 70/30 for pipes and tubes of heat exchangers in seawater of greater aggressivity and in polluted seawater;
4. Sn bronzes as cast materials for pumps and valves;
5. Al, Mn, Ni, Fe bronzes as cast materials for propellers and other elements in seawater flowing at high velocity;
6. aluminium alloys Al–Mg and Al–Mg–Zn (without welding) for the hulls of fast ships.

1.5 Areas of future study

The following areas of study are proposed:

- development of new copper alloys with increased resistance to seawater flow and of moderate price as compared to 90/10 and 70/30 alloys;
- investigation of the causes of microbiological corrosion of aluminium alloys and newly developed copper alloys, and working out corrosion prevention methods;
- investigation of the problem of corrosion of aluminium alloys in seawater with high pH value in over-protected zone of cathodically protected constructions, and development of prevention methods;
- continuation of research on mathematical modelling of corrosion processes on copper and aluminium alloys, enabling development of a basis for calculation of long-term predictions of the service life of these alloys.

1.6 Acknowledgements

Work using the literature survey ‘Corrosion of Copper and Aluminium Alloys in Sea Water’ was financed by the Marine Corrosion Working Party of the European Federation of Corrosion.

1.7 References

1. J. Birn, Literature Survey ‘Corrosion of Copper and Aluminium Alloys in Sea Water’, 2002; unpublished.
2. J. Birn, ‘Corrosion damages of hulls and ship installations caused by improper choice of materials or wrong technology of shipbuilding and service’, *Internat Conference, Choice and Service of Engineering Materials.* Jurata, Poland, 22–25 Sept., 1997, 215–220 (in Polish).
3. F. Mazza, S. Torchio, *Corr. Sci.* **23** (1983) 10, 1053–1072.
4. S. Torchio *Corr. Sci.* **21** (1981) 6, 425–437.
5. Standard of Polish shipbuilding industry ZN-83/101125, Gdańsk, Ship Design and Research Centre S.A.

6. BSI, BS MA 18 *Salt Water Piping Systems in Ships*, London, British Standards Institution.
7. A Working Party Report 'Illustrated Case Histories of Marine Corrosion', European Federation of Corrosion Publications Number 5, London, The Institute of Metals, 1990.
8. Report of Ship Design and Research Centre No RO-94/B-115 (internal publication).
9. R. F. North, M. J. Pryor, *Corr. Sci.* **10** (1970) 297–311.
10. Mathiyarasu, N. Palaniswamy, V. S. Muralidharan, *Eurocorr 2000*, EFC, London, Sept. 2000.
11. I. Milošev, M. Metikoš-Huković, *Corrosion* **48** (1992) 3, 185–193.
12. P. R. Shibad, P. R. Singh, H. S. Gadiyar, *J. Electrochem. Soc. India*, **38** (1989) 3, 206–209.
13. Report of Ship Design and Research Centre No RO-00/T-054 (internal publication).
14. T. Atsumi, A. Ogiso, K. Nagata, S. Sato, *Sumitomo Light Metal Technical Reports* **29** (1988) 4, 23–31.
15. Report of Ship Design and Research Centre No RO-01/B-082 (internal publication).
16. I. Singh, D. K. Basu, M. N. Singh, A. K. Bhattamishra, S. C. Dev, *Anticorr. Meth. Mater.* **44** (1977) 3, 195–199.
17. A. Schüssler, H. E. Exner, *Corr. Sci*., **34** (1993) 11, 1793–1802.
18. P. A. Lush, M. J. Carr, *Corr. Sci.* **19** (1979) 1079–1088.
19. R. J. K. Wood, S. P. Hutton, D. J. Schiffrin, *Corr. Sci.* **30** (1990) 12, 1177–1201.
20. F. L. Laque, A. H. Tuthill, *Hansa* **99** (1962) 20, 2077–2086.
21. B. C. Syrett, *Corr. Sci.* **21** (1981) 3, 187–209.
22. D. J. Schiffrin, S. R. De Sanchez, *Corrosion* **41** (1985) 1, 31–37.
23. C. Kato, H. W. Pickering, J. E. Castle, *J. Electrochem. Soc.* **131** (1984) 6, 1225–1229.
24. P. Traverso, A. M. Beccaria, B. Poggi, *Br. Corr. J.* **29** (1994) 2, 110–114.
25. J. P. Gudas, H. P. Hack, *Corrosion* **35** (1979) 2, 67–73.
26. K. D. Efird, T. S. Lee, *Corrosion* **35** (1979) 2, 79–83.
27. J. P. Gudas, H. P. Hack, *Corrosion* **35** (1979) 6, 259–264.
28. N. Mukhopadhyay, S. Baskaran, *Corrosion* **42** (1986) 2, 113–117.
29. P. K. Chauhan, H. S. Gadiyar, *Corr. Sci.* **25** (1985) 1, 55–68.
30. K. S. Rajagopalan, M. Raghavan, N. S. Rengaswamy, T. M. Balasubramanian, V. S. Muralidharan, *Mater. Perform.* **26** (1981) 1, 19–27.
31. S. G. Gomez de Saravia, M. F. L. de Mele, H. A. Videla, *Corrosion* **46** (1990) 4, 302–306.
32. D. D. Macdonald, B. C. Syrett, S. S. Wing, *Corrosion* **35** (1979) 8, 367–378.
33. H. P. Hack, J. P. Gudas, *Mater. Perform.* **18** (1979) 3, 25–28.
34. D. R. Lenard, J. G. Moores, G. E. Morin, *Br. Corr. J.* **24** (1989) 1, 19–24.
35. H. P. Hack, J. P. Gudas, *Mater. Perform.* **19** (1980) 4, 49–54.
36. B. C. Syrett, R. L. Coit, *Mater. Perform.* **22** (1983) 2, 44–50.
37. R. Francis, *Corr. Sci.* **26** (1986) 3, 205–212.
38. J. Birn, *Ochrona przed Korozja* ('Protection against Corrosion' in Polish) **46** (2003) 11, 298–303.
39. M. de Romero, Z. Duquet, O. de Rincon, O. Perez, I. Araujo, A. Martinez, *Corrosion* **56** (2000) 8, 867–876.
40. P. D. Goodman, *Br. Corr. J.* **22** (1987) 1, 56–62.
41. Standard of Polish shipbuilding industry BN-87/3702-06. Requirements concerning protecting ship constructions connections against galvanic corrosion, Gdańsk, Ship Design and Research Centre S.A.

42. J. R. Davis, *Corrosion of Aluminium and Aluminium Alloys*, Materials Park, OH, ASM International, 1999.
43. Z. Szklarska-Śmialowska, *Corr. Sci.* **41** (1999) 1743–1767.
44. M. C. Reboul, *Corrosion* **35** (1979) 9, 423–428.
45. C. Poniewierska, J. Birn, A. Narozniak-Luksza, I. Skalski, *Przeglad Spawalnictwa* ('Review of Welding Technology' in Polish) **61** (1999) 6, 17–19.
46. M. J. Robinson, *Corr. Sci.* **22** (1983) 8, 887–889.
47. A. Aballe, M. Bethencourt, F. J. Botana, M. J. Cano, M. Marcos, *Corr. Sci.* **43** (2001) 1657–1674.
48. W. M. Caroll, C. B. Breslin, *Corr. Sci.* **33** (1992) 7, 1161–1177.
49. G. L. Masters, J. W. Oldfield, K. R. Strokes, *Eurocorr 96*, Paper no. XIV OR 12-1-12-4, EFC, Nice, France XIV OR 12-1 to 12-4, Sept. 1996.
50. M. J. Robinson, *Corr. Sci.* **22** (1982) 8, 775–790.

2

Erosion–corrosion interactions of copper and aluminium alloys

ROBERT J. K. WOOD, University of Southampton, UK

2.1 Introduction

The need to minimise costs associated with modern fluid handling and propulsion equipment demands increasing flow rates with the inherent risk of flow-dependent corrosion and, if solids are entrained or cavitation occurs, the erosion–corrosion of the engineering equipment involved. This is especially true for offshore and marine technologies and other industries that transport slurries and other particle-laden liquids in pipes or seawater propulsion systems. These industries expend the equivalent of millions of pounds every year to repair erosion–corrosion damage caused by solid particle impingement or cavitation. Typical examples of this kind of material destruction are erosion–corrosion damage to pumps, impellers, propellers, valves, heat exchanger tubes and other fluid handling equipment. In a recent survey, erosion–corrosion was rated in the top five most prevalent forms of corrosion damage in industry [1].

2.1.1 Material selection

Material selection for erosion–corrosion duty tends to be based on the following systems of aluminium, copper, zinc and nickel due to their relative cheapness or:

- stainless steels;
- polymers (where applicable);
- Co-based alloys;
- Ni-based alloys (e.g.UNS N06625);
- hard metals (e.g. sintered WC);
- ceramics.

Coatings of these materials are also applied onto substrates of carbon steel or low corrosion-resistant alloys [2–9]. Surface degradation control techniques other than surface selection may well include the use of inhibitors as well as

careful component design to avoid cavitation and solid particle impingement or to at least control the angle of impingement of the solid particle onto the surface [10]. Process parameters should also be reviewed to minimise erosion and sand removal (screens and cyclone separators) techniques and monitoring systems (acoustic) are deployed, where practicable, to reduce the potential for erosion–corrosion [11–14].

Figure 2.1 shows the pure erosion resistance of a range of typical engineering surfaces obtained from a free slurry jet impingement rig, described in [15] at 27 m/s, 90°, 235 μm sand, room temperature, after 5 hours of testing. However, for most marine service applications, erosion resistance should not be considered on its own. Flow corrosion resistance is likely to be of equal importance together with the materials response to combined erosion–corrosion.

For resistance to flow corrosion, corrosion-resistant alloys are used. Figure 2.2 shows the trend for a passive system as a function of flow velocity and its vulnerability to mechanical processes which accelerate corrosion loss rates. In general, corrosion-resistant alloys do not resist erosion well; nor are the interactions (synergies and additive effects) that exist between corrosion and erosion well understood. Also, cost reduction considerations favour coatings on mild steel instead of expensive solid alloy components. Organic coatings tend to perform relatively poorly under high-energy solid particle impingement but have a use within low-energy flow components [16]. Ceramic materials are usually too expensive to use, except in particularly critical applications. Sprayed metallic coatings are a relatively unexplored possibility for this duty. The most likely metallic coating materials for thermal spray systems, on cost grounds, are aluminium, copper, nickel and zinc, their alloys and possibly composite materials based on them. For highly aggressive (very energetic flows) WC–CoCr cermets are used either in sintered form or thermally sprayed by detonation type or High-Velocity Oxy-Fuel (HVOF) guns [17–19].

For corrosion resistance, the important distinction is between anodic and cathodic coatings. For example, zinc and aluminium are both anodic to carbon steel, i.e. they will protect steel galvanically in seawater, and they are indeed used in offshore applications for this purpose [1, 20]. Copper and nickel are both cathodic coatings, i.e. they are not protective to steel. Where defects in the coating occur, exposed steel is likely to be rapidly corroded adding to erosion–corrosion attack. It would be a condition for using copper or nickel (or their likely alloys), that the coating is initially guaranteed to be defect-free or that a sealant is used to protect the defects. This assumes that defects interconnect through the coating thickness, which is unlikely. A cautionary note should be made here as defect-free coatings are rarely achievable and, even if defects are minimised, erosion–corrosion processes can readily generate defect sites through induced stress systems which exploit imperfections, inclusions and any anisotropy in the near or sub-surface

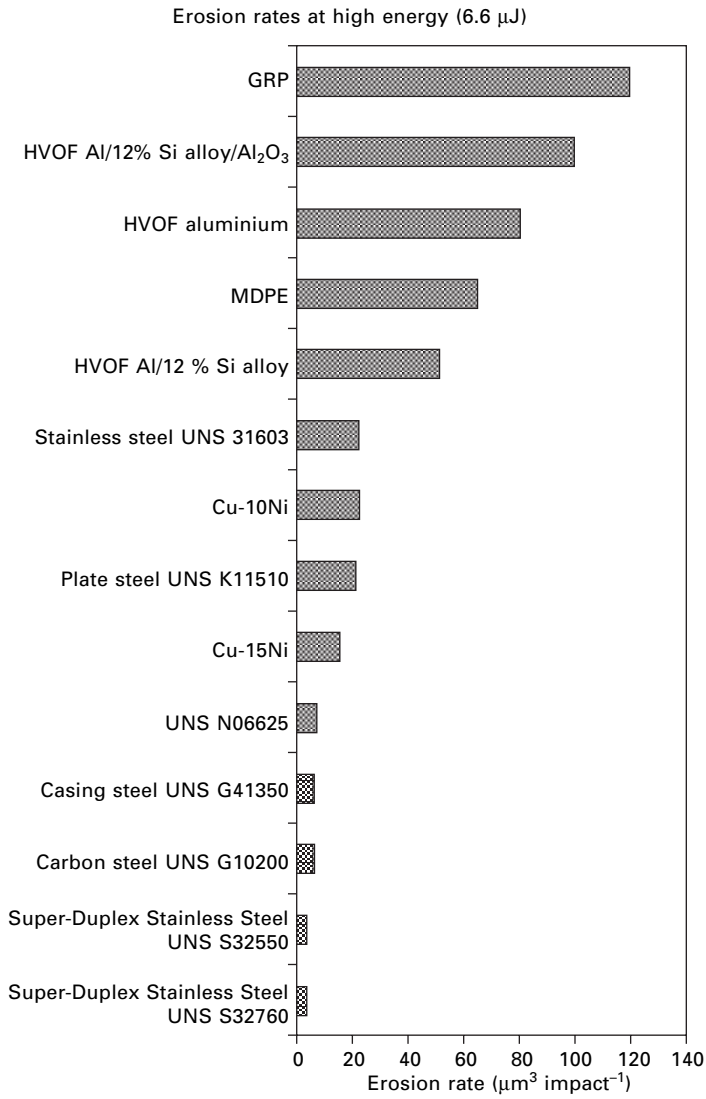

2.1 Pure erosion resistance of a range of typical engineering surfaces obtained from a free slurry jet impingement rig, described in [15] at 27 m/s, 90°, 235 μm sand, room temperature, after 30 min of testing. GRP = glass reinforced plastic, HVOF = High Velocity Oxy-Fuel spray deposited, MDPE = medium density polyethylene. Erosion rate is plotted in cubic microns per impact.

microstructure. For erosion resistance, a wide range of carbides are deposited along with the above metal binder elements with the aim of achieving good adhesion between carbide and binder and, therefore, successfully combining corrosion- and erosion-resistant elements together.

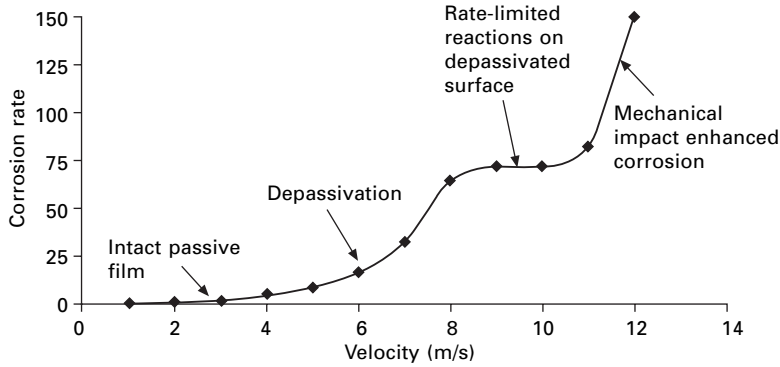

2.2 Illustration of possible corrosion trends for a passive metallic surface. Corrosion rates are arbitrary units and are not 'realistic'.

2.1.2 Seawater flow enhanced erosion–corrosion and erosion–corrosion of aluminium and copper alloys

Aluminium

In general, the degradation of aluminium is expected to depend on flow velocity. In potable/distilled water, very small mass losses occur, slowly increasing with flow velocity. In seawater, mass losses are larger, but may be (more than) balanced by mass gains from precipitation of corrosion products. In general, the latter dominate at low velocities, but mass losses dominate at higher flow rates. When sand is present, insoluble corrosion products are swept away; mass losses are always positive and increase rapidly with flow rate (approximately $\propto v^2$ if erosion dominates).

Li *et al*. [21] suggest that pitting corrosion has a marked influence on solid particle erosion–corrosion behaviour of commercially pure aluminium AA1100 in NaCl-containing slurries. Further studies by Li *et al*. [22], at open circuit, show that erosion rates of aluminium in NaCl slurries are much higher than those in an aqueous slurry without electrolyte additives, even though the pure corrosion component was very small. In pure aqueous slurry erosion, the basic mechanism leading to mass loss was the ductile fracture of flakes formed on the eroded surface. In corrosive slurries, however, the mass loss was enhanced by cracking of the flakes induced by stress and corrosion.

Some research has centred on increasing erosion resistance of aluminium alloys, and thereby hopefully erosion–corrosion resistance, by using a composite surface with hard particles dispersed within an aluminium binder matrix. The erosion–corrosion behaviour of a squeeze cast aluminium alloy (Al–Cu) dispersed with either 10 % v/v SiC particles or SiC fibres was investigated by Modi *et al*. [23], in slurry environments of 3 % NaCl (aqueous) + 40 % w/w sand and water + 40 % w/w sand over a range of test durations at a

linear speed of 7 ms^{-1}. Test results indicated higher weight loss for the SiC composites than for the matrix alloy in 3 %NaCl + 40 % w/w sand while the reverse trend was noted when the tests were conducted in water + 40 % w/w sand. Severe attack around the dispersoid/matrix and precipitate/matrix interfaces by the NaCl environment caused loosening of the dispersoid phase followed by the subsequent removal of the dispersoids.

The ability to deposit metal matrix composite (MMC) coatings on the surface of aluminium alloys has the potential to expand the engineering applications of these materials. Composite coatings reinforced with discontinuous ceramic particles enhance the tribological properties of the substrate. In applications where low-stress abrasive wear processes predominate, these coated aluminium alloy components could provide superior wear resistance when compared to aluminium alloys. Deuis *et al*. [24] report the abrasion–corrosion performance of MMC coatings formed using AA5083 aluminium alloy using a plasma transferred arc (PTA) surfacing technique. Various composite coatings reinforced with discontinuous ceramic particles of Al_2O_3, SiC and TiC (70 μm) of varying volume fractions have been tested. They found the composition of reinforcement altered the corrosion behaviour, with the highest corrosion rates being recorded for TiC and the lowest for Al_2O_3 reinforcements.

The hydrodynamic cavitation erosion resistance of aluminium has been extensively studied by Selim [25] while very limited studies have focused on cavitation erosion–corrosion of aluminium alloys. Passivated electrode surfaces of aluminium have been employed to investigate individual cavitation erosion–corrosion events produced by ultrasound. The extent of surface damage, as the result of individual cavitation events, is calculated from the current time transients recorded on passivated lead electrodes, see Birkin *et al*. [26].

Copper alloys

Protective layers (copper–chloride complexes) are assumed to be removed when the shear force is greater than the binding force between the film and the substrate. However, Wojcik *et al*. [27] observed that enhanced corrosion is not due to shear-induced removal of films for 99.9 % copper and Cu–30Ni alloy but may be due to destabilisation of the film by a potential gradient across the electrode surface generated by flow impingement. Also, the author suggested that film stability on copper in synthetic sea water appeared sensitive to oxygen levels. Melchers [28] reviewed the corrosion rates for Cu–10Ni in sea water and showed that the ratio of corrosion at 0.6 ms^{-1} to tidal (quiet) conditions reduces slowly with length of exposure, demonstrating the long-term requirements (seven years) to grow a fully protective film of corrosion product layers and associated biofilms under flow.

Bulk Nickel–Aluminium Bronze (NAB) under quiet, tidal or flowing

conditions below the critical velocity achieves a long-term corrosion rate of 0.015–0.05 mm y^{-1} [29]. Ault [30] reported that the seawater corrosion rate of typical cast NAB alloys varied as a function of the velocity. The minimum rate was reported to be 0.5 mm y^{-1} at 8 ms^{-1}, rising to 0.8 mm y^{-1} at 30 ms^{-1}. However, areas of localised corrosion were found with rates up to 2 mm y^{-1}. These findings are similar to those obtained by Tan [31] from HVOF NAB coatings under jet impingement conditions. Tan reports that a slight increase in the NAB coating corrosion rate at 6.7 ms^{-1} indicates that the surface film might be affected by turbulence intensity in the electrolyte jet. It should also be noted that the operational recommendation for cast bulk NAB alloys in flowing seawater is below 4.3 ms^{-1} [32]. Syrett [33] suggested that increased flow corrosion rates of NAB alloys at high velocity can occur in two steps: (1) increasing the velocity leads to an increased oxygen supply and mass transfer reactions; and (2) when the velocity exceeds the critical range, local turbulence of the flowing electrolyte can shear off the protective film on the material surface thus increasing the corrosion rate. However, other workers have also reported a much higher critical velocity (23 ms^{-1}) for the NAB alloys [34], although this reference relates to peripheral velocity in pumps and propellers rather than a system velocity. This suggests that the critical velocity could be dependent on actual service conditions, component geometry and hydrodynamics of the flow.

Tan [31] compares the flow corrosion rate of Aluminium Bronze (AB) and NAB coatings with other commonly used marine materials for various test geometries in seawater (see Table 2.1). The coatings were found to be comparable to or superior to the tungsten carbide-based HVOF coatings; they are also comparable to or slightly less resistant than marine alloys such as cupro–nickel and duplex stainless steels.

Table 2.1 Comparison of flow corrosion rates between the AB and NAB coatings and other materials in seawater

Material	Flow corrosion rate (mm y^{-1})	Reference
Bulk alloys		
Duplex SS (UNS 31803), 14 ~ 30 ms^{-1}	0.01 ~ 0.2	[35]
Duplex SS (UNS 32205), 14 ms^{-1}	0.06 ~ 0.2	[36]
Carbon steel, 14.3 ms^{-1}	2.6	[36]
Cupronickel alloy, 5 ~ 7 ms^{-1}	0.12 ~ 3.5	[37]
NAB alloy, 7.6 ~ 30.5 ms^{-1}	0.5 ~ 0.76	[30]
Coatings		
HVOF WC–Co alloyed, 14 ~ 30 ms^{-1}	7 ~ 10	[35]
HVOF 83WC–17Co, 14.3 ms^{-1}	1.9 ~ 2.5	[36]
HVOF AB, 5 ms^{-1}	2.0	[31]
HVOF NAB, 3 ~ 7 ms^{-1}	0.8 ~ 1.3	

A review of the detailed electrochemical responses of NAB in seawater can be found in Wharton *et al*. [38]. The effects of surface films on the anodic and cathodic kinetics of NAB under various flow and erosion–corrosion conditions are reviewed. These findings confirm that NAB is the most seawater corrosion–erosion resistant of the available copper-based alloys. Some work has been published that evaluates the corrosive wear resistance of copper-based alloys and other materials used for sliding parts in seawater to clarify their damage behaviour [39].

Hodgkiess *et al*. [40] observed the galvanic interactions on the surface of copper-based alloys during jet impingement erosion–corrosion tests with and without entrained solids. A two-electrode sample geometry was used with an outer ring electrode surrounding an inner disc electrode. The galvanic effects, in Cu–10Ni alloys between an actively corroding zone subject to relatively intense hydrodynamic conditions and the nearby more quiescent regions where a protective film can form on the surface, are significant. It is interesting to note that, in the solids-free jet impingement test, the inner electrode of the stagnation zone was cathodic to the outer electrode of the jet zone. With solids present in the jet, the converse was true.

2.1.3 Cavitation erosion–corrosion

The cavitation erosion and corrosion characteristics of various engineering alloys including grey cast iron, steels, copper alloys (brass, bronze and copper) and stainless steels were studied by Kwok and Cheng [41] using a 20 kHz ultrasonic cavitation horn in distilled water and in 3.5 % NaCl solution at 23 °C. The alloys studied were ranked in terms of cavitation erosion–corrosion resistance as follows:

UNS 32760 > UNS 30400 > UNS 31603 > UNS G10500 > tool steel > bronze > brass > grey cast iron > Cu

The authors link this ranking to the microstructure, mechanical strength, work hardenability, martensitic transformability, stacking fault energy and also corrosion resistance of these surfaces. For the copper alloys, corrosion was found to play only a minor role in the overall cavitation erosion–corrosion (0.1–1.8 %). For the steels and cast iron, corrosion/erosion synergism was very significant, amounting to 78 % of the overall cavitation erosion–corrosion loss. Corrosion and corrosion/erosion synergism played a negligible role for the stainless steels.

Cavitation erosion–corrosion of Cu and Cu–30Ni has been studied by Wood *et al*. [42–46] in a hydrodynamic cavitation tunnel. The tunnel was instrumented with a three-electrode electrochemical cell to allow corrosion measurements and to apply cathodic protection to determine the pure erosion rate. The proportions of corrosion-related and erosion-related damage vary

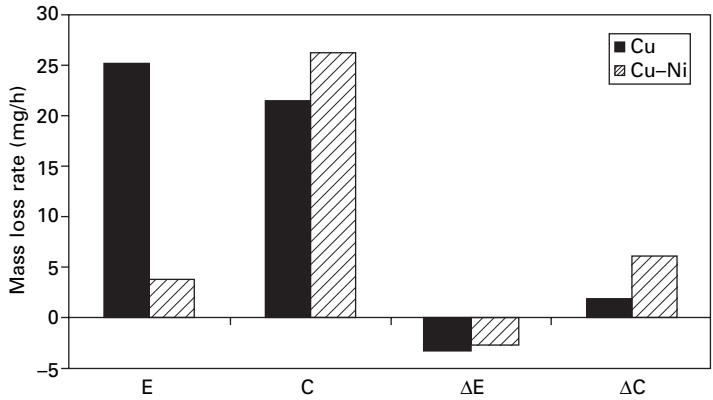

2.3 Erosion–corrosion components for copper and 70/30 cupro–nickel under peak noise cavitation (cavity length over width ratio = 1.6) at an anodic overpotential of 50 mV [42–44]. E = erosion rate, C = corrosion, ΔE = interactions (enhanced erosion due to corrosion) and ΔC = interactions (enhanced corrosion due to erosion).

as conditions (chemical and hydrodynamic cavitation intensity) change or if the target material is changed. These effects are shown in Fig. 2.3. Interactions (ΔC and ΔE) between erosion (E) and corrosion (C) are seen to increase the expected wastage rates ($E + C$) by 30 %. The Cu–30Ni alloy was found to have superior resistance to erosion–corrosion than commercially pure copper.

The aims of current research in this field are to deploy gravimetric and electrochemical techniques to understand erosion–corrosion surface loss mechanisms for surface selection of aluminium and copper-based alloys in marine service, quantify erosion–corrosion interaction factors (synergy) and obtain information on localised corrosion processes.

2.1.4 Pipe materials

Seawater handling systems used in the marine and offshore industries, can be fabricated with Cu–Ni castings (Navy applications) and wrought pipes, nominally containing 1–2 % Fe for erosion–corrosion resistance. However, during welding, iron can precipitate from solid solution onto grain boundaries in the heat-affected zones (HAZ). During seawater service, these iron-rich precipitates can dissolve preferentially (galvanically), leading to intergranular corrosion of the HAZ, see Burleigh and Waldeck [47].

The pipes and fittings of sewerage systems and storm drains as well as those used for high-density sludge transportation under high purging pressure are exposed not only to a corrosive environment, but also to the impact of solid particles that are contained in solid residues, resulting in an erosion of the surface. Traditional iron and steel used in these pipes are being replaced

by polymeric materials such as polyethylene, which have excellent corrosion resistance properties [48].

Non-metallic solutions to control erosion of pipes have focused on polyethylene and polyurethane surfaces. Slurry erosion tests of various pipe materials have been carried out by Hocke and Wilkinson [49], who showed that the damage to polyethylene was nearly half that of carbon steel at a flow velocity of 3.7 ms^{-1} and a particle concentration of 25 %. The damage was, however, over twice that of carbon steel at a particle concentration of 40 %. The correlation between erosion damage and the impact conditions has been discussed for various polymeric materials [50–52]. Polyurethane coatings on carbon steel offer a potential solution to control erosion–corrosion of carbon steel pipes; however, they are vulnerable to high-energy particle impact at 30° jet impingement angle erosion with kinetic energy around $E_k = 0.07$ μJ [53]. However, copper and aluminium alloys are still very popular selection options for seawater-handling pipework and associated process machinery and fittings.

2.1.5 Tribo-corrosion

Erosion–corrosion is a subject area within the broader topic of tribo-corrosion which covers all aspects of tribologically (mainly mechanically) induced interactions with electrochemical processes. Material selection for tribo-corrosion systems is extremely challenging and is based on optimising performance against the combined degradation processes. Tribo-corrosion covers a range of material degradation processes where there is relative motion between contacting surfaces or abrasives/erodents and a surface in conjunction with electrochemical corrosion. Published research has tried to deal with the synergistic effects between erosion and corrosion processes which result in accelerated material loss and, in some cases, in decelerated material loss [54–56]. A wide range of corrosion-resistant materials rely on a relatively thin surface film to provide a barrier (of high impedence) to charge transfer between the relatively active bulk material and the corrosive environment. This film renders the surface passive but, for fluid machinery handling flows where solid particles have been entrained or cavitation is induced, the passive film will be removed by mechanical wear or bubble collapse/microjet/shock wave impingement processes. Where the film is mechanically removed, charge transfer can occur at the interface without retardation from the barrier film [57]. This interaction between tribological and electrochemical corrosive effects is referred to as tribo-corrosion and causes materials to corrode at a substantially higher rate than those experienced under static or quiescent conditions.

When the corrosion rate is partially or wholly controlled by mass transfer of reactant to or product from the surface, then local conditions under erosion

may well influence mass transfer kinetics (measured by the mass transfer coefficient k_m). Under such conditions the corrosion will be controlled by the mass-transfer and the driving concentration gradient (relative concentrations of active species near surface compared to free stream concentrations) [58]. Both the mass transfer and concentration gradient will be affected by solid particle impingement, and the influence such impingements have on the local fluid flow field and the roughness caused by impacts which result in plastic deformation. Figure 2.2 illustrates possible corrosion trends for a passive metallic surface. Therefore, the standard models used to describe flow corrosion current densities, such as the modified Koutecky–Levich equation [44] given in Equation [2.1] where k_m can be derived from equations [2.2–2.4], may not be applicable.

$$\frac{1}{i} = \frac{1}{i_a} + \frac{1}{i_d} = \frac{1}{nFk_1} + \frac{k_{-1}}{k_1 nFk_m} \quad [2.1]$$

$$Sh = aRe^x Sc^y \quad [2.2]$$

and

$$k_m = aD^{1-y}L^{x-1}v^{y-x}u^x \quad [2.3]$$

Taking typical values for the exponents as $x = 0.6$ and $y = 0.33$, gives:

$$k_m = au^{0.6}\left(\frac{D^{0.66}}{V^{0.27}L^{0.4}}\right) \quad [2.4]$$

where i = corrosion current density, i_a = activation current density, i_d = diffusion current density, n = number of electrons, F = Faraday's constant, k_1 = forward reaction rate, k_{-1} = backward reaction rate, k_m = mass transfer coefficient, D = diffusion coefficient, u = flow velocity, v = kinematic viscosity, L = characteristic length, a = scaling constant, Sh = Sherwood number = (K_mL/D), Re = Reynolds number = (uL/v), Sc = Schmidt number = (v/D).

Erosion–corrosion results from the effects of turbulent flow corrosion and mechanical effects (erodent impacts) stripping away surface passive films and/or the inhibition of passive film regrowth. Erodent impacts that can generate fresh (nascent) reactive surfaces invoke cathode to anode area effects and accelerate corrosion at these sites.

The damage under erosion–corrosion can be represented as:

$$T = E + C + S \quad [2.5]$$

where E is the pure erosion material loss, C is the solids-free flow corrosion rate, possibly derived from the corrosion current density i in Equation [2.1]. The synergistic effect (interactive term), S, is referred to as ΔE_c or (ΔC_e + ΔE_c), depending on the literature source, where ΔE_c is the enhanced erosion loss due to corrosion and ΔC_e is the enhanced corrosion due to erosion. The ASTM G119-93 standard is a useful guide for researchers wishing to evaluate synergy [59]. Table 2.2 attempts to give an overview of the physical significance

Table 2.2 Overview of processes that could lead to positive and negative interactive effects between mechanical and electrochemical processes present under erosion–corrosion conditions. Partly taken from reviews by Wood [46] and Wang and Stack [62]

	Positive interaction	Negative interaction
Critical impact energy	For impacts above a critical energy, damage and/or penetration of passive films or corrosion product coverage will result in increased charge transfer at the liquid/metal interface.	Below critical impact energy. Results in reduced charge transfer at the liquid/metal interface as film composition could be influenced by impact.
Surface roughness, R_a	Roughening effects on mass transfer coefficients unknown but k_m likely to increase with increasing R_a. (Silverman review suggests mass-transfer sensitivities with Reynolds number is affected by surface roughness as $k_m \propto Re^{0.9}$ with solids compared to $k_m \propto Re^{0.65}$ solids free flows for rotating cylinder work due to roughening effects on the surface [57].) Roughness may promote microturbulence affecting the local double layer. Roughness could also promote local microelectrode behaviour at the tips of impact craters.	Roughness influences the contact mechanics of angular solid particle impingement. Increased roughness could reduce contact stresses and thereby the near and far field stress distributions.
Plastic deformation/strain	Plastically deformed and stressed surfaces possibly enhance corrosion processes. Corrosion causes premature detachment of plastically deformed or strain-hardened impact crater lips.	Strain-hardened surface increases hardness and reduces erosion rate and could reduce corrosion due to change in microstructure/grain lattice distortion.
Increased or unsteady hydrodynamics or turbulence	Unstable double layers (non-steady state) and unsteady driving concentration gradients of active species.	High concentrations of solid particles could block pores.

Table 2.2 Continued

	Positive interaction	Negative interaction
Contact temperature	Local surface (flash) temperatures could be significantly higher around and within impact craters which could accelerate corrosion rates.	Local surface (flash) temperatures could influence oxide film composition and microstructure and thus could be more erosion resistant.
Localised corrosion	Pitting and micro-galvanic corrosion cells due to localised defects in the passive layers induced by erosion or exposure of inclusions or voids. Crack systems would be vulnerable to crevice corrosion attack and accelerate crack propagation. Micro-galvanic corrosion cells could be formed.	
Passive film state	Depassivation: removal of air-formed oxides or oxide layers produced by passivation. Oxide layer could increase friction between impacting solid particle and the bulk substrate material.	Repassivation: fast and adherent oxide layers formed by passivation. Oxide layer could decrease friction between impacting solid particle and target.

of the interactive processes that could lead to positive and negative effects between mechanical and electrochemical processes present under erosion–corrosion conditions.

The possibility of synergy between erosion and corrosion was apparently first recognised by Zelders [60], who studied metal wastage in a coal washing plant. Zelders was unable to alter either the materials in the system or its geometry. Nevertheless, he correctly deduced that in the absence of solids, the important factors were oxygen concentration in the mine water, water conductivity, flow rates, turbulence and the porosity/adhesion characteristics of surface oxide layers. Flow corrosion of carbon steel could be as much as 20 times greater than static corrosion under otherwise similar conditions. In the presence of coal slurries (about 5 % w/v) mass losses were increased considerably further. While attributing most of this to direct erosion and (particularly) corrosion losses, Zelders recognised that his data could not be modelled without a further quantity, which would subsequently be termed 'synergy'. In practice, some of Zelders' corrosion loss under these circumstances was undoubtedly erosion-enhanced, so the various contributions to his mass loss are not cleanly separated.

Neville *et al*. have shown that the corrosion current density increases with increasing solid loading (200, 400 and 600 mg l^{-1}) for UNS S31603 under an impinging jet of 3.5 % NaCl at 17 ms^{-1} [2]. It has been shown [e.g. 2, 3] that synergistic or additive effects, which result in the damage due to separate corrosion and erosion processes, are normally greater than the sum of the individual damage processes and can accelerate material removal significantly (50 times for grey cast iron), see reference [46]. Synergistic effects have also been shown to be a function of impinging solid particle energy for UNS S31603, UNS S32100, UNS S32250 and UNS S32760 [61]. A combination of approaches may be fruitful in the future where erosion–corrosion performance or interactive terms, such as synergy, are mapped against total incident kinetic energy (TIKE), as illustrated by Fig. 2.4, where the alloy surfaces of interest in this chapter are plotted. TIKE is given by the summation of particle energies of all impacts (N) on the surface:

$$TIKE = \sum_{N} E_{k} \qquad [2.6]$$

2.2 Erosion–corrosion testing of marine alloys and coatings

Current work on copper and aluminium alloys at Southampton will now be used to demonstrate the erosion–corrosion performance of these alloys and the usefulness of advanced electrochemical techniques to help understand the interactive processes between erosion and corrosion activated on surfaces

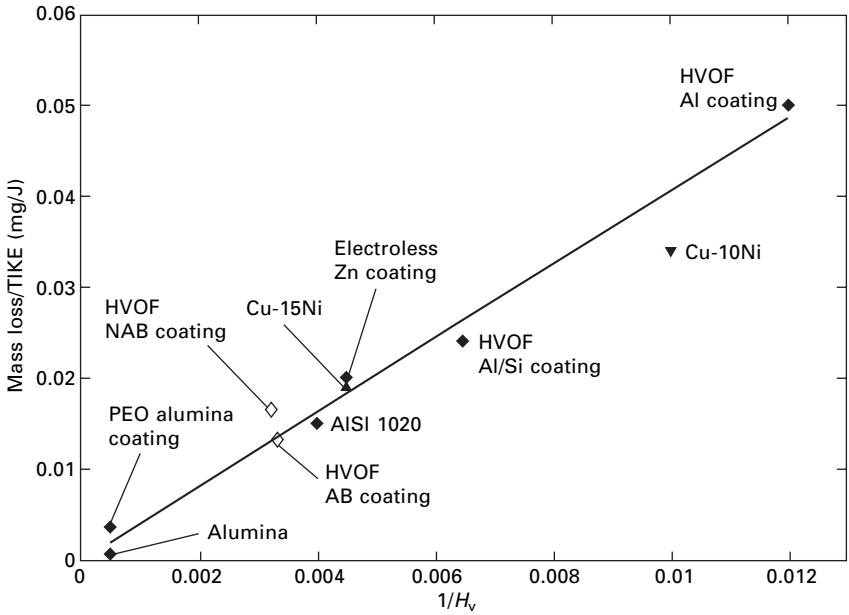

2.4 The trend between the ratio of erosion or erosion–corrosion mass loss to total incident sand kinetic energy (mass loss/TIKE) versus inverse surface hardness, $1/H_v$. Solid diamond symbols represent erosion-only mass loss data while open diamond symbols represent erosion–corrosion mass loss data. Solid upright and inverted triangles represent erosion-only mass loss data obtained on the rig used in [15]. PEO = plasma electrolytic oxidation.

of the alloys. Several candidate HVOF coatings have been considered for erosion–corrosion applications. In order that these thermal spray and plasma coatings can be exploited to their full potential, their resistance to combined erosion and corrosion needs to be quantified. Of particular concern is the level of porosity within the coatings which can accelerate crack propagation and coating removal under erosion, and can also be interconnected such that electrolyte can permeate into the coating/substrate interface.

2.2.1 Solid particle erosion

The rig used has been detailed elsewhere [63, 64]. The jet angle was set at 90° and the jet nozzle stand-off distance was 37 mm. The temperature was ambient (plus effects of heating by the circulating pump) and the test duration was six hours. Before and after each test, specimens were rinsed in tap water, dried and weighed with a precision balance with a range of 200 g and an accuracy of ± 0.2 mg.

Details of coatings tested

Details of the experimental HVOF coatings that have been tested at Southampton are given in Table 2.3 along with details of UNS K11510 (BS 4360 [65]) steel and the hot dipped zinc coating used for comparison purposes. Compositions of the NAB surfaces are given in Table 2.4.

Test conditions

A range of test conditions have been studied at 0, 3 and 5 % w/w sand loadings in 3.5 % NaCl solutions to measure T rates (combined erosion–corrosion rates) and in distilled water or 3.5 % NaCl solution with cathodic protection to measure E rates (erosion only rates). Solids-free flow tests with 3.5 % NaCl allowed the C rates (flow corrosion rates) to be measured. Four combinations of jet velocity and sand sizes have been used (see Table 2.5).

2.3 Results and discussion

Figure 2.5 shows the erosion–corrosion rates (T) of the cast NAB, Cu–10Ni, HVOF NAB coating and the UNS K11510 steel substrate plotted against

Table 2.3 Surface roughness, R_a and hardness, H_v, data for samples (N/A = not applicable)

Sample	R_a (μm) as received	R_a (μm) ground	Thickness (μm)	H_v	Porosity (%)
UNS K11510 Steel	N/A	0.13	8000	149	–
MDPE (medium density polyethylene)	0.1	N/A	8000	< 6	–
Copper (CP)	N/A		8000		N/A
Cu–30Ni	N/A	0.1	8000		N/A
Cu–10Ni	N/A	0.1	8000	98	N/A
HVOF NAB	7.0–9.0	0.01	300	290	2.00
HVOF aluminium on steel	9.0	< 0.1	200	83	0.67
Cast NAB	N/A	< 0.1	N/A	235	N/A
Hot-dipped zinc on steel	1.3	N/A	80	220	–

Table 2.4 Standard chemical composition of HVOF NAB and cast NAB coatings

Element	Al	Ni	Fe	Cr	Mo	Si	C	Cu
HVOF NAB	8.71	5.55	4.50	1.02	0.15	0.06	0.01	Bal
Cast NAB	9	5	4.5	–	–	–	–	Bal

Table 2.5 Slurry erosion–corrosion jet conditions at 90° jet impingement angle

Velocity (ms^{-1})	Mean sand size (μm)	Impingement energy (μJ)
3.1	135	0.016
3.1–3.5	235	0.086–0.110
5.0	235	0.224
6.7	235	0.402

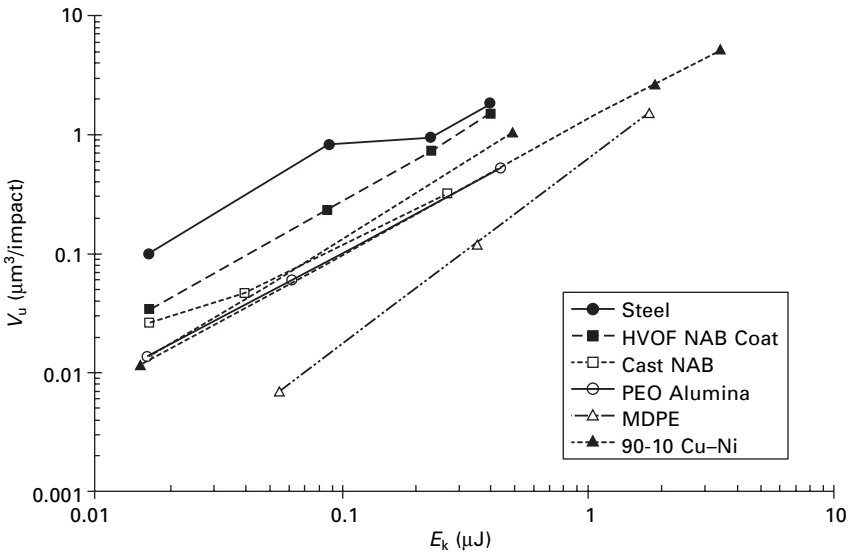

2.5 Relationship between erosion-corrosion rate, V_u, and kinetic energy, E_k.

energy. The carbon steel was shown to have the highest material rate over the range of energies (0.01–1 μJ); its erosion–corrosion rate is up to four times that of the NAB coating in the low-energy region. This is possibly due to the NAB coating being a harder material. However, the erosion–corrosion rates between the steel substrate and the NAB coating appears to converge at higher energies (0.4 μJ), due to the erosion–corrosion behaviour of the NAB coating being influenced by cracking at splat boundaries at these energies. The HVOF NAB under erosion–corrosion conditions and at low energy offers similar resistance to the cast, with both eroding by predominately ductile mechanisms of deformation and cutting wear. With increased energies the coating offers increasingly less resistance relative to the cast NAB due to crack propagation and splat ejection.

For comparison, some data for polyethylene pipe material (MDPE), taken

Table 2.6 Erosion rate, V_u, dependencies on impact energy, E_k, and correlation coefficients, R^2, for the various surfaces tested under slurry jet erosion-corrosion conditions at 90° impact angle (see Fig. 2.5). PEO = plasma electrolytic oxidation, N/A = not applicable

Material/coating	Power law	R^2
Carbon steel UNS G10200	$V_u = 4.06\ E_k^{0.87}$	0.93
Cast NAB	$V_u = 1.06\ E_k^{0.93}$	0.97
HVOF NAB coating	$V_u = 4.11\ E_k^{1.18}$	0.99
PEO alumina coating	$V_u = 2.66\ E_k^{1.44}$	N/A
MDPE	$V_u = 0.59\ E_k^{1.52}$	0.99
Cu–10Ni	$V_u = 1.48\ E_k^{1.12}$	0.99

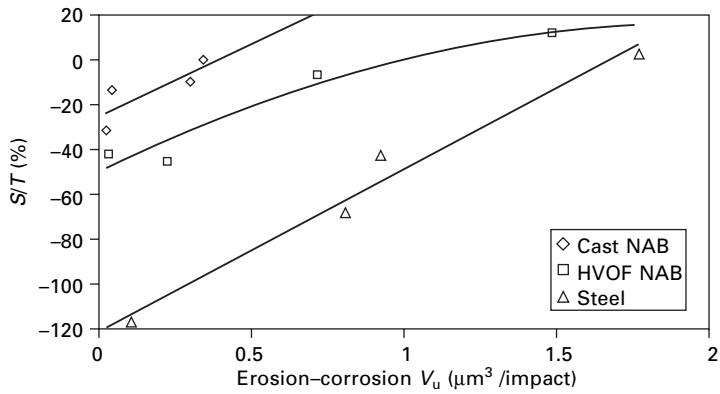

2.6 Relationship of synergy percentage with erosion–corrosion V_u. S/T = synergistic effect/combined erosion–corrosion = $[T - (E + C)]/T$.

from [66], are also plotted on Fig. 2.5. These results show that MDPE outperforms all the other surfaces tested and is an attractive option for resisting slurry erosion–corrosion where fluid temperatures permit selection. However, it has a high sensitivity to impact energy with an energy exponent over 1.5, see Table 2.6. Results for Cu–10Ni under erosion–corrosion conditions (same sand sizes as Table 2.5 and jet velocities with a 3.5 % NaCl solution and 2.1 % w/w solids loading) have been included, and it has a similar resistance and erosion–corrosion sensitivity to impact energy compared to the cast NAB, Table 2.6, although the NAB is twice as hard as the Cu–10Ni.

In order to quantify the amount of the synergy, the synergy percentage (S/T %) for cast NAB, HVOF NAB coating and the steel, was plotted against erosion–corrosion rate V_u, see Fig. 2.6. Negative synergy was found at all kinetic energies for cast NAB, reflecting an 'in-built' safety factor. Positive synergy was found for the HVOF NAB coating at high energy, suggesting a greater sensitivity to energy and/or increased corrosion activity. This is

consistent with the HVOF NAB coating suffering additional damage mechanisms related to crack propagation at the splat boundary and/or splat ejection at high energy compared to those seen on the cast NAB. Negative synergy is beneficial, and not all engineering surfaces demonstrate this property. This implies that the contributions of C and ΔC_e towards the total material loss under erosion–corrosion conditions are minimal. This is especially true when substantially thick oxide films or corrosion products are formed on erosion–corrosion surfaces, affecting the contact mechanics and thus the erosivity of the sand and yielding a negative ΔE_c. However, it is the influence of the NAB coating microstructure that affects performance at high energy where the mixed mode of micro-cutting and splat removal allows increased corrosion resulting in a positive synergy.

Figure 2.7 shows the same data set as in Fig. 2.6, but plots electrochemical mass loss (C) versus mechanical mass loss (T–C). Unlike Fig. 2.6, which shows the level of synergy, the plot in Fig. 2.7 allows the dominant mechanisms of wall wastage to be shown as zones. When T–C/C is above 10 the process is mechanically controlled, while for ratios between 1 and 10 it is erosion–corrosion controlled, for values above 0.1–1 it is corrosion–erosion controlled and below 0.1 it is electrochemically controlled. Plotting the data this way allows the dominant degradation processes to be recognised and should help inform surface improvements/modifications and thus change how to optimise the surface composition for highest resistance. Steel is an especially interesting example as at low-energy particle impacts, the wastage is electrochemically

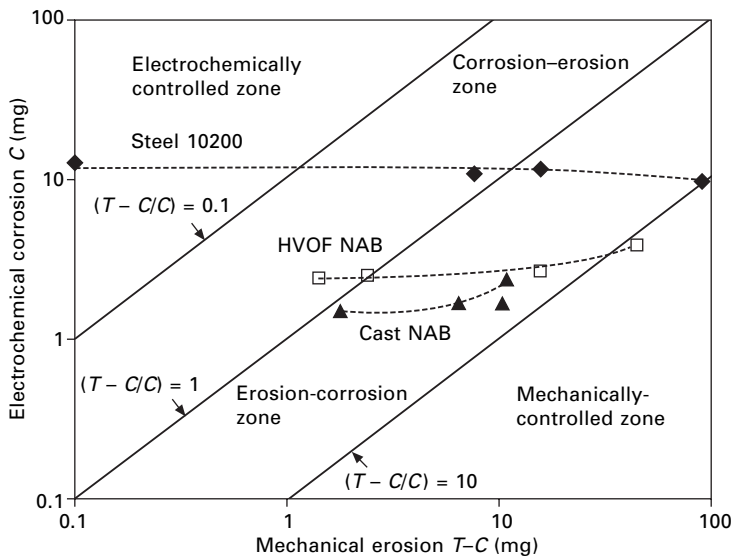

2.7 Electrochemical mass loss (C) versus mechanical mass loss (TC) for data plotted in Fig. 2.6.

dominated but as energy is increased, it moves through the corrosion–erosion zone and erosion–corrosion zone to the mechanically dominated zone. Cast and HVOF NAB, on the other hand, remain mainly in the erosion–corrosion zone for the same energy range as the steel.

In order to gain a further understanding of the effects of erosion-enhanced corrosion, electrochemical current noise (ECN) measurements were taken. These measurements allow current perturbations about the mean corrosion current to be analysed. These perturbations are thought to provide valuable information on the extent of passive film rupture and repassivation during erosion–corrosion. Table 2.7 lists the possible influences on the depassivation and repassivation kinetics.

Sasaki and Burstein show current transients for single particle impacts [67] on passive stainless steels, illustrating that monitoring such transients can provide direct information on the erosion–corrosion processes. Based on this principle the present work will take the standard deviation of ECN to provide information on the impact damage to the surface passive film. It should be noted that the fluctuations in the present work result from multiple impacts rather than single impacts as recorded by Sasaki and Burstein. The standard deviation ratios of the ECN measurements are plotted against synergy (S) in Fig. 2.8 for HVOF NAB and aluminium alloy coatings. As the standard deviation ratios indicate the addition of electrochemical activity (corrosion rate) on the surface under solid particle impingement, its increase will result in a similar increase in the levels of synergy. At lower kinetic energy conditions, sand particles might not have sufficient energy to cause surface film rupture. Sasaki and Burstein reported that the threshold kinetic energy required to cause passive film rupture for stainless steels is in the order of 0.03 μJ [67]. The protective layer on NAB alloys is approximately 800 nm [27], as opposed to 10 nm for stainless steels, indicating that a higher sand kinetic energy is required to cause film damage. If protective films are sustained on the surface under erosion–corrosion, standard deviation values will be similar to that under flow corrosion conditions. This can result in a negative synergy and

Table 2.7 Possible influences on the depassivation and repassivation kinetics

Depassivation	Repassivation
Solid particle impact	High mass transport
High velocities/wall shear stresses	Film growth kinetics (monolayer coverage plus lateral film growth)
Crack/occluded geometries/pitting	Crack/occluded geometries/pitting
Local temperature	Local temperature
Turbulent flow features	Rougher/larger surface area

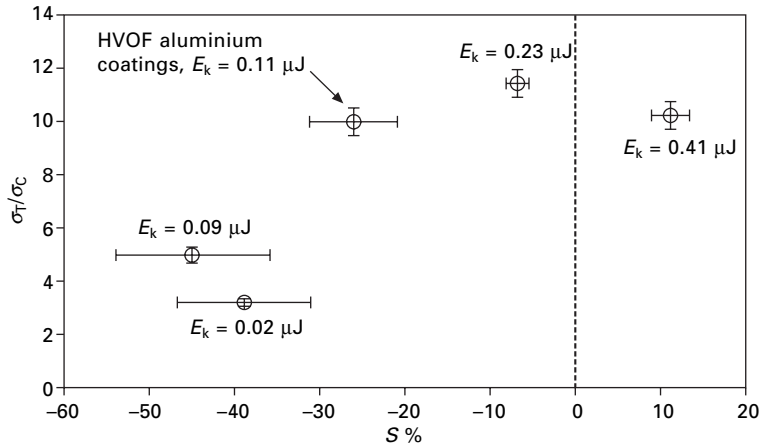

2.8 Relationship between the standard deviation ratio and synergy (*S*) percentage for HVOF NAB coatings and for HVOF aluminium alloy based coating [68].

both erosion and corrosion processes are then considered as antagonistic. It should be noted that the erosion–corrosion performance of the NAB surfaces which out-perform stainless steels is contrary to flow corrosion experience where stainless steels are selected in preference due to their higher flow corrosion resistance than NAB.

The sand particles will have higher damage efficiencies as their kinetic energy increases. This will result in unsustainable protective films, leading to higher standard deviation ratios and mass losses. A possible transition region is shown in Fig. 2.8 [68], at the vicinity where the electrochemical standard deviation ratio values are close to 10; synergy levels were shown to shift from negative to positive. This transition can be caused by the following processes: (i) Increased surface film removal by higher energy particles, leading to more exposed surfaces and an increase in corrosion rate. This is a result of erosion-enhanced corrosion (ΔC_e) processes; (ii) Higher kinetic energy sand particles can remove any work-hardened and corroded plastic deformation lips at a higher efficiency, leading to corrosion-enhanced erosion (ΔE_c) processes.

The erosion-enhanced corrosion process can be resolved electrochemically by obtaining the differences between erosion–corrosion standard deviation and flow corrosion standard deviation ($\sigma_T - \sigma_C$). Figure 2.9 shows the effects of ΔC_e on the percentage of synergy for the NAB coating within the range of kinetic energy tested. It is clear that ΔC_e increases with kinetic energy, subsequently leading to a positive synergy.

Other issues that make ECN analysis and its comparison to synergy difficult include the possibility of local film currents between anodes/cathodes [69]

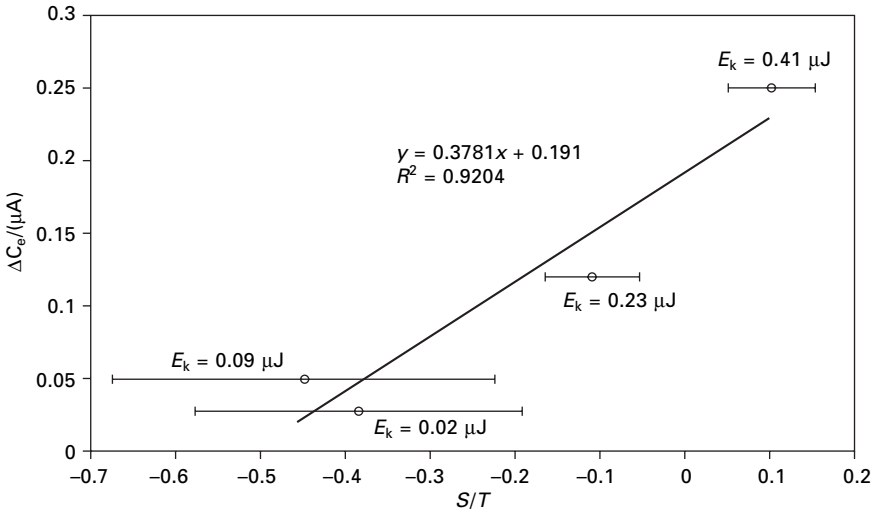

2.9 The effects of erosion-enhanced corrosion (ΔC_e) in affecting the synergy for the HVOF NAB coating [68].

which will not be seen by ECN measurements, and the effects of charging/recharging double-layer currents due to local events.

2.3.1 Influence of solid particle impingement angle

To further complicate surface performance under erosion–corrosion conditions there appears to be a dependence of S (Equation [2.5]) on the angle of solid particle impingement as well as on solid particle energy and loading. This is demonstrated by the results of erosion and erosion–corrosion tests on the HVOF aluminium alloy coatings seen in Fig. 2.10 from [70]. It is evident that the aluminium/12 % silicon alloy is slightly less angle sensitive than the pure aluminium coating.

The erosion mechanisms are not well understood even under laboratory conditions. Such work often ignores industrial experience, and so in the future a possible way forward will be to map this industrial experience. Such an attempt is shown in Fig. 2.11 which is based on particle energies as evaluated in Table 2.8, where types of damage are plotted on a total incident energy per unit area versus temperature map. This is a mechanistic map of industrial components subjected to erosion–corrosion from [71, 72 and 46].

2.4 Conclusions

The erosion–corrosion performance of materials for use in fluid handling and propulsion systems must be better understood if service lives are to be

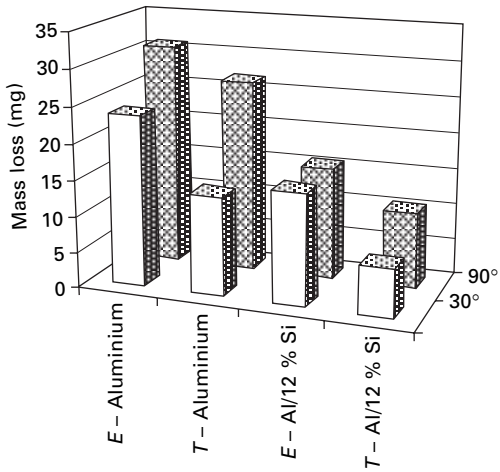

2.10 The influence of jet angle on erosion (*E*) and erosion–corrosion (*T*) rates for HVOF aluminium and HVOF aluminium/12 %Si coatings at 3.5 m/s with 5 % w/w of 235 μm sand [70].

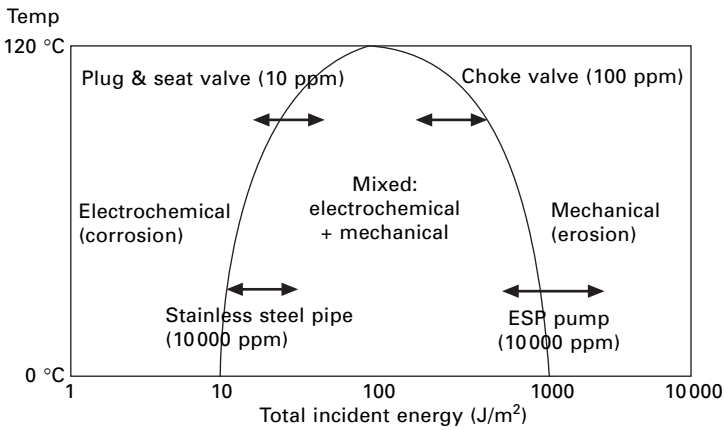

2.11 Mechanistic map of industrial components subjected to erosion–corrosion [46,71,72]. (ESP = electric submersible pump.)

Table 2.8 Potential particle kinetic energies for marine components

	Marine component			
	Pipe	Valve	Pump	Propulsor
Velocity (ms^{-1})	0–3	5	10	25
Particle diameter (μm)	100	100	100	100
Particle kinetic energy (μJ)	0–0.007	0.02	0.07	0.44

extended and erosion–corrosion control techniques better deployed. Valuable scientific insight into erosion–corrosion mechanisms can be gained by reproducing service conditions in the laboratory. Gravimetric and electrochemical measurements are both useful in assessing erosion–corrosion performance of bulk and coated surfaces. This chapter shows that there is a place for copper and aluminium alloys in marine applications where erosion–corrosion may occur. Along with other alloys, the presence of solids in corrosive flows which impinge on the alloy surfaces increases the wall wastage significantly over flow corrosion rates. For higher particle energies, the surface modification of aluminium is available through a plasma electrolytic oxidation (PEO) process to a harder layered alumina.

Research into experimental HVOF aluminium bronze and aluminium coatings shows the value of careful experimentation that reproduces service conditions while allowing electrochemical and gravimetric measurements to quantify wastage rates and thus increase the prediction accuracy of component life. Electrochemical noise measurements show promise as a technique for quantifying synergistic levels present under erosion–corrosion. Synergy between erosion and corrosion processes on the passivating HVOF coatings is sensitive to sand energy. These coatings show good erosion–corrosion resistance at low impact energies with surface films formed by coating–electrolyte contact reducing the contact mechanics (or erosivity) of sand impingement. Improvements in coating quality (reduced voids and stress raisers) are required if they are to match the erosion–corrosion resistance of bulk Cu–Ni and NAB surfaces subjected to high-energy erosion in marine environments.

Surface films can reduce mechanical loss to give negative synergy. Under low kinetic energy, cast NAB has good erosion–corrosion performance, but at a higher kinetic energy results imply a positive synergy and, hence, some vulnerability. Therefore, the option of using HVOF NAB coatings for refurbishment for erosion–corrosion protection of marine components is viable for low kinetic energy applications, but further improvements in coating integrity are required before these options can be subjected to high energy.

However, more insight is required to allow refined maps to be produced and thereby improve surface design and selection. Also, more effort should be made to record industrial failures and experience to allow service-based maps to be built up as a function of the environment.

2.5 Acknowledgements

The author would like to acknowledge the financial support of dstl (Defence Science and Technology Laboratory). He also thanks the University of Barcelona for spraying the HVOF NAB coatings, TWI for spraying the HVOF aluminium coatings and Meighs Ltd for supplying the cast NAB

samples. The contents of this chapter include material subject to © Crown copyright 2005 dstl.

2.6 References

1. P. McIntyre, Corrosion and associated costs in the UK offshore sector, Marine, Corrosion Club Meeting, April 1999.
2. A. Neville, M. Reyes, H. Xu, *Tribol. Int.*, 2002, **35** (10), 643–650.
3. R.J.K. Wood, A.J. Speyer, *Wear*, 2004, **256** (5), 545–556.
4. Y. Puget, R.J.K. Wood, K.R. Trethewey, *Wear*, 1999, **233–235**, 552–567.
5. A. Scrivani, S. Ianelli, A. Rossi, R. Groppetti, F. Casadei, G. Rizzi, *Wear*, 2001, **250** (1), 107–113.
6. B.F. Levin, J.N. Dupont, A.R. Marder, *Wear*, 1995, **181** (2), 810–820.
7. M.G. Gee, C. Phatak, R. Darling, *Wear*, 2005, **258** (1–4), 412–425.
8. A.J. Gant, M.G. Gee, A.T. May, *Wear*, 2004, **256** (9–10), 954–962.
9. A.J. Gant, M.G. Gee, A.T. May, *Wear*, 2004, **256** (5), 500–516.
10. J.H. Gerretsen, A. Visser, *Corr. Sci.*, 1993, **34** (8), 1299.
11. H.C. Meng, K.C. Ludema, *Wear*, 1995, **181–183** (Part 2), 443–457.
12. D.N. Madge, J. Romero, W.L. Strand, *Minerals Eng*., 2004, **17** (5), 625–636.
13. S. Mylvaganam, *Particulate Sci. Technol.*, 2003, **21** (3), 293–301.
14. A.I. Al-Shamma'a, R. Tanner, A. Shaw, J. Lucas, *Proc. 33rd European Microwave Conference*, 2003, Vols 1–3, 535–538.
15. R.J.K. Wood, *Materials and Design*, 1999, **20**, 179–191.
16. R.J.K. Wood, Y. Puget, Slurry Handling and Pipeline Transport – Hydrotransport 14, Conference Series Publication, PEP Suffolk, 1999, Series No 36, BHR Group 455–474.
17. R.J.K. Wood, B.G. Mellor, M.L. Binfield, *Wear*, 1997, **211** (1), 70–83.
18. D.W. Wheeler and R.J.K. Wood, *Wear*, 2005, **258** (1–4), 526–536.
19. C. Allen, A. Ball, *Tribology International*, 1996, **29** (2), 105–116.
20. R.J. Percy, BP Engineering, Risers and Subsea Equipment group, 1990 BPE.90.ER152 (unpublished).
21. Y. Li, G.T. Burstein, I.M. Hutchings, *Wear*, 1995, **181–183** (1), 70–79.
22. Y. Li, G.T. Burstein, I.M. Hutchings, *Wear*, 1995, **186** (2), 515–522.
23. O.P. Modi, B.K. Prasad, R. Dasgupta, A.K. Jha, D.P. Mondal, *Materials Sci. Technol*., 1999, **15** (8), 933–938.
24. R.L. Deuis, C. Subramanian, J.M. Yellup, *Wear*, 1997, **203**, 119–128.
25. S.M.A. Selim, PhD Thesis, Department of Mechanical Engineering, University of Southampton, UK, 1981.
26. P.R. Birkin, R. O'Connor, C. Rapple, S.S. Martinez, *J. Chem. Soc. – Faraday Trans*. 1998, **94** (22), 3365–3371.
27. P.T. Wojcik, E. Charriere, M.E. Orazem, *Tri-Service Conference on Corrosion*, North Carolina, Naval Surface Warfare Centre, November, 1997, 1–15.
28. R.E. Melchers, *Corrosion*, 2001, **57** (5), 440–451.
29. H. J. Meigh, *Cast and wrought aluminium bronzes properties, processes and structure*, London, IOM Communications Ltd, 2000.
30. J.P. Ault, *Corrosion* 1995; paper no. 281, NACE International, Houston, TX, 1990.
31. K.S. Tan, PhD Thesis, School of Engineering Sciences, University of Southampton, 2003.

32. J.W. Oldfield, G.L. Masters, Copper Development Association Publication no. 115, London, CDA, 1996.
33. B.C. Syrett, *Corrosion*, 1976, **32** (6), 242–252.
34. A.H. Tuthill, *Mater. Perform*, 1987, **26** (9), 12–22.
35. M. Bjordal, E. Bardal, T. Rogne, T.G. Eggen, *Wear*, 1995, **186–187** (2), 508–514.
36. E. Bardal, T.G. Eggen, T. Rogne, T. Solem, *International Thermal Spray Conference*, May 1995, Kobe, Japan.
37. *ASM Metals Handbook*, Materials Park, OH, ASM International, 1990, Vol. 13 – Corrosion, 10th edn, No. 13.
38. J.A. Wharton, R.C. Barik, G. Kear, R.J.K. Wood, K.R. Stokes, F.C. Walsh, *Corrosion Science*, 2005, **47** (12), 3336–3367.
39. T. Kawazoe, A. Ura, American Society for Testing and Materials, Special Technical Publication 1404, West Conshohocken, PA, ASTM, 2001, 296–305.
40. T. Hodgkiess, S. Shrestha, J.M. Perry, D. Mantzavinos, G. Vassiliou and A. Faber, *J. Corr. Sci. Eng*., 2003, **6**, C039.
41. C.T. Kwok, F.T. Cheng, H.C., *Materials Science And Engineering A – Structural Materials Properties Microstructure And Processing*, 2000, **290** (1–2), 145–154.
42. R.J.K. Wood, S.A. Fry, *J. Fluids Eng*., 1989, **111**, 271–277.
43. R.J.K. Wood, S.A. Fry, *J. Fluids Eng*., 1990, **112**, 218–224.
44. R.J.K. Wood, S.P. Hutton, D.J. Schiffrin, *Corrosion Science*, 1990, **30** (12), 1177–1201.
45. R.J.K. Wood, *Proc. Inst. Mech. Eng*., 1990, Part C, **204**, 63–65.
46. R.J.K. Wood, S.P. Hutton, *Wear*, 1990, **140**(2), 387–394.
47. T.D. Burleigh, D.H. Waldeck, *Corrosion*, 1999, **55** (8), 800–804.
48. A. Yabuki, K. Sugita, M. Matsumura, M. Hirashima, M. Tsunaga, *Wear*, 2000, **240** (1–2), 52–58.
49. H. Hocke, H.N. Wilkinson, *Tribol. Int*., 1978, **11**, 289–294.
50. H. Hojo, K. Tsuda, T. Yabu, *Wear*, 1986, **112** (1), 17–28.
51. J. Larsen-Basse, A. Tadjvar, *Wear*, 1988, **122** (2), 135–149.
52. M.M. Stack and N. Pungwiwat, *Mater. Sci. Technol*., 1999, **15**, 337–344.
53. R.J.K. Wood, PhD Thesis, Department of Mechanical Engineering, University of Southampton, 1987.
54. R.J.K. Wood, Y. Puget, K.R. Trethewey, K. Stokes, *Wear*, 1998, **219** (1), 46–59.
55. M.M. Stack, S. Zhou, R.C. Newman, *Wear*, 1995, **186–187** (Part 2), 523–532.
56. Y. Naerheim, M.W. Kendig, *Wear*, 1985, **104** (2), 139–150.
57. M. Stemp, S. Mischler, D. Landolt, *Wear*, 2003, **255** (1–6), 466–475.
58. D.C. Silverman, A review, *Corrosion*, 2004, **60** (11), 1003–1023.
59. ASTM G119-93(1998): Standard Guide for Determining Synergism Between Wear and Corrosion, West Conshohocken, PA, American Society for Testing and Materials.
60. H.G. Zelders, *Metaux et Corrosion*, 1949, **65**, 65–76.
61. R.J.K. Wood, *IMECHE Conference Transactions*, 2004, **1**, 113–132.
62. H.W. Wang, M.M. Stack, *J. Mat. Sci*., 2000, **35**, 5263–5273.
63. R.J.K. Wood, *La Houille Blanche*, 1992, **7–8**, 605–610.
64. K.S. Tan, R.J.K. Wood, J.A. Wharton, K.R. Stokes, *Corrosion/2002*, Paper no. 02199, NACE International, Houston, TX, 2002.
65. BSI, BS 4360: 1990 *Specification for weldable structural steels*, London, British Standards Institute.
66. A.J. Moore, R.J.K. Wood, *Proc. Plastic Pipes VIII Conference*, Paper no. E114, Koningshof, September, 1992, 1–10.

67. K. Sasaki, G.T. Burstein, *Philosophical Magazine Letters*, 2000, **80** (7), 489–493.
68. K.S. Tan, J.A. Wharton, R.J.K. Wood, *Wear*, 2005, **258** (1–4) 629–640.
69. R. Oltra, B. Chapey, L. Renuad, *Wear*, 1995, **186–187** (Part 2), 533–541.
70. A.J. Speyer, PhD Thesis, School of Engineering Sciences, University of Southampton, 2002.
71. A.F. Forder, PhD Thesis, University of Southampton, School of Engineering Sciences, 2001.
72. R.J.K. Wood, J.A. Wharton, Slurry handling and Pipeline Transport – Hydrotransport 15, Vol. 1, Cranfield, BHR Group, 2002, 173–186.

Part II

Copper alloys

3

Copper and copper–nickel alloys – an overview

ANTON KLASSERT and LADJI TIKANA,
Deutsches Kupferinstitut e.V., Germany

3.1 Introduction

With advancing industrialisation, the demand for and the number of copper alloys has risen continuously. Today, copper alloys have found an important position among metallic materials due to their large variety of metallurgical, physical and chemical properties. A modern industrial society uses copper in many areas (electrotechnology, building and construction, mechanical engineering, automotive, chemistry, offshore applications, marine engineering, medical purposes and many others). The overall demand for copper in Europe is approximately 4.3 million tonnes – approximate usage distribution is: 50 % electrical and telecommunications applications, 25 % building and construction, 11 % mechanical, 7 % automotive and 7 % others (Fig. 3.1).

Copper is the first metal ever used by mankind. Its name appears to be derived from the island Cyprus which in antiquity supplied copper to Greece, Rome and the other Mediterranean countries. The Romans called it 'ore from Cyprus' (*aes cyprium*), later *cuprum*. Copper is also occasionally deposited in metallic form and could be processed even in the late stone age simply by hammering [2]. A copper pipe with a length of 400 m provided water to the

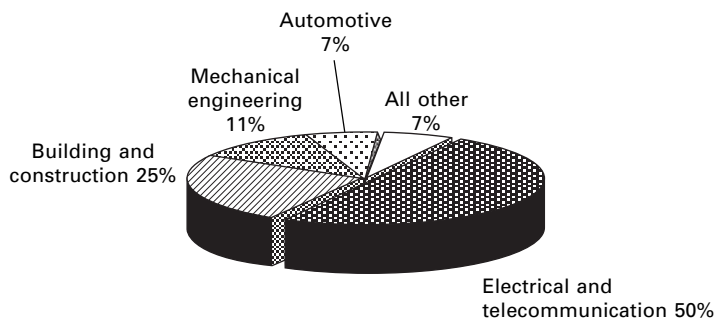

3.1 Distribution of copper usage in Europe [1].

Temple of Death in Sahure as early as 2500 BC (Fig. 3.2 [2]). In Europe, copper appeared in the late stone age, and mixing (alloying) of different metals allowed bronze to be made. It was probably also around 2500 BC that copper alloyed with tin was cast for the first time (Fig. 3.3 [2]). Early in the

3.2 Water pipe made from copper sheet in a stone groove and covered by gypsum. Ancient temple of Sahure, 2500 BC. Museums of Berlin, Germany [2].

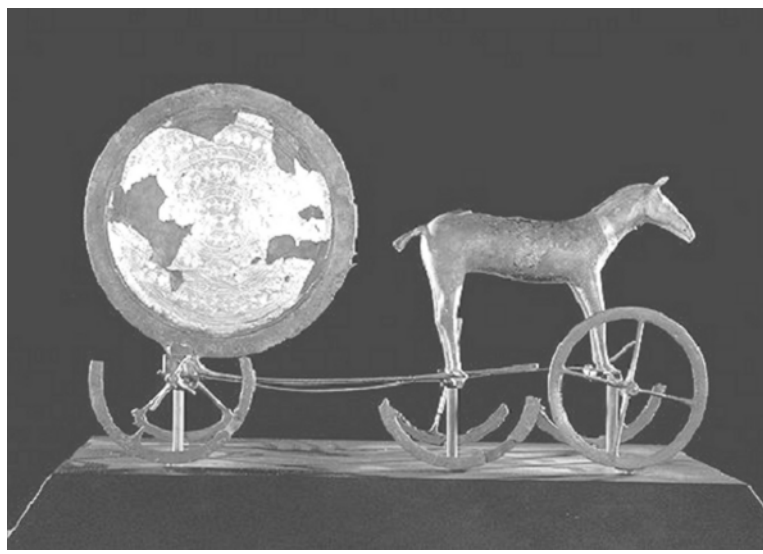

3.3 Sun Carriage of Trundholm. Nordic Bronze Era, 1400–1300 BC [2].

history of mankind, copper alloys with a tin content between 20 and 50 % were used for the production of mirrors because of their high reflectivity.

Copper, with an annual usage of more than 15 million tons, is the third most important metallic material. Only steel and aluminum are used in higher quantities.

3.2 Copper and copper alloys

The potential application of copper and copper alloys is strongly influenced by the alloying elements. Standardised materials are denominated by an abbreviation or by a materials number. According to European Standards (EN), materials are classified as products and their composition is described in product standards. Figure 3.4 represents a 'copper tree' showing the ramifications resulting from the combination of the main alloying elements. For better visibility the huge number of copper materials is subdivided into groups (Table 3.1).

3.3 Copper alloys in marine applications

Quite a number of copper alloys have found their place in marine and offshore applications, and they show a very good performance. Such materials are subject to stringent rules from classifying agencies such as the American Bureau of Shipping, Germanischer Lloyd, Bureau Veritas and others [4].

3.3.1 Wrought alloys

Tubes and parts of copper and wrought copper alloys which are to be used in pipes under pressure, condensers and heat exchangers (Table 3.2) are commonly produced seamless, i.e. by hot rolling and thereafter by rolling and cold drawing. For welded tubes and parts, special warranties are requested from the fabricators. Cold drawn tubes and parts are annealed for recrystallisation. As an exception to this rule, copper tubes which will be delivered as 'half-hard' or 'hard' may be cold drawn after annealing.

3.3.2 Cast alloys

For the production of fittings and pump bodies, friction bearings, bushings and similar parts, the casting alloys enumerated in Table 3.3 are used. The casting process (sandcasting, permanent mould, centrifugal or continuous casting) should be selected according to the geometry of the part. The castings can be delivered as cast or annealed, and this is a decision for the foundry as long as no details have been specified in the purchase order. All cast parts must be clean, free of cavities, pores, fissures and inclusions.

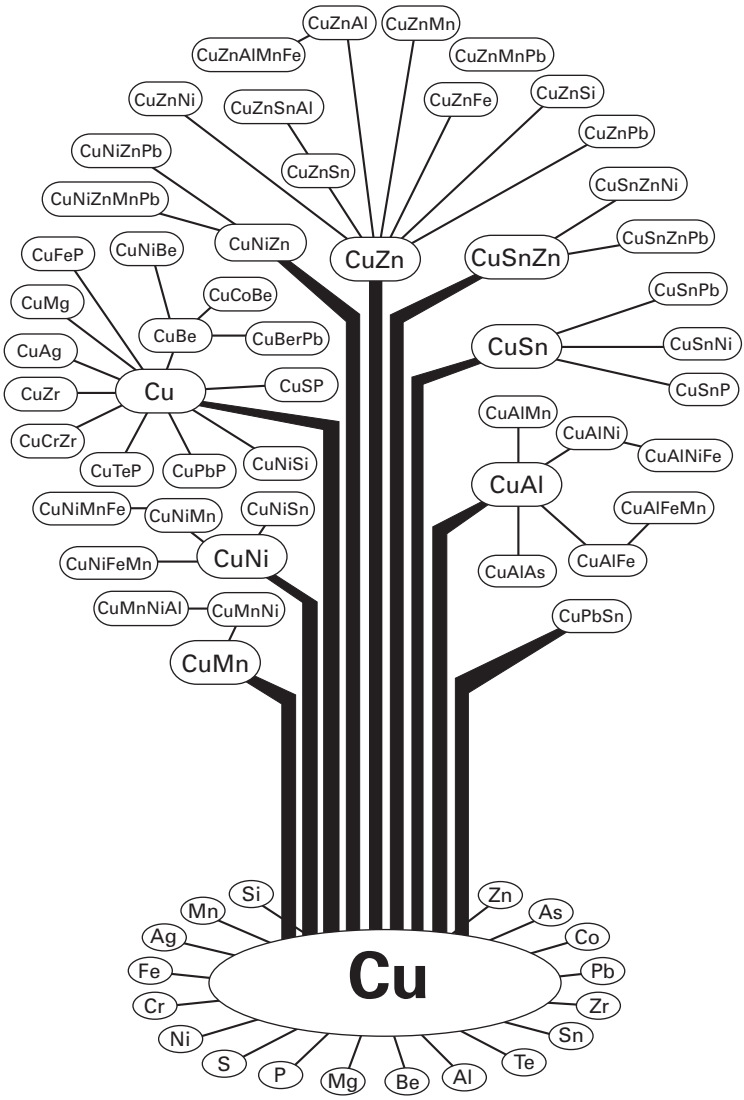

3.4 Copper tree [2].

Standard copper alloys widely used for propellers and parts thereof are subdivided according to the guidelines of 'Germanischer Lloyd' [7] into the categories CU1, CU2, CU3 and CU4, depending on their chemical composition (Table 3.4). Important characteristics for use of CU1 and CU2, such as toughness and corrosion resistance, are strongly influenced by the share of β-phase. To guarantee sufficient deformability behaviour and resistance to fatigue corrosion, the microstructure must have a share of α-phase of at least

Table 3.1 Copper and copper alloys according to DIN EN 1412 [3]

Material group	Positions 3, 4 and 5 (figure in that range)	Position 6 (letter for designation of the material group)
Copper	000–999	A or B
Low alloyed coppers (alloy element less than 5 %)	000–999	C or D
Miscellaneous copper alloys (alloy element min. 5 %)	000–999	E or F
Copper–aluminium alloys	000–999	G
Copper–nickel alloys	000–999	H
Copper–nickel–zinc alloys	000–999	J
Copper–tin alloys	000–999	K
Copper–zinc alloys, binary	000–999	L or M
Copper–zinc–lead alloys	000–999	N or P
Copper–zinc alloys, complex	000–999	R or S
Standardised alloys in the range 000–799. Non-standardised alloys in the range 800–999.		

Table 3.2 Copper alloys for condensers and heat exchangers in marine applications according to DIN EN 12451 [5]

Material designation	Material number EN	Chemical composition [Gew.-%] DIN	
Cu-DHP	CW024A	2.0090	Cu min. 99.9, P 0.015–0.04
CuAl5As	CW300G	2.0918	Al 4.0–6.0, As 0.1–0.4, Rem. Cu
CuNi10Fe1Mn	CW352H	2.0872	Ni 9.0–11.0, Fe 1.0–2.0, Mn 0.5–1.0, Rem. Cu
CuNi30Fe2Mn2	CW353H	2.0883	Ni 29.0–32.0, Fe 1.5–2.5, Mn 1.5–2.5, Rem. Cu
CuNi30Mn1Fe	CW354H	2.0882	Ni 30.0–32.0, Mn 0.5–1.5, Fe 0.4–1.0, Rem. Cu
CuZn20Al2As	CW702R	2.0460	Cu 76–79, Al 1.8–2.3, As 0.02–0.06, Rem. Zn
CuZn28Sn1As	CW706R	2.0470	Cu 70–72.5, Sn 0.9–1.3, As 0.02–0.06, Rem. Zn
CuZn30As	CW707R	–	Cu 69–71, As 0.02–0.06, Rem. Zn

Table 3.3 Standard cast copper alloys for use in marine applications [4, 6]

Material designation	Material number EN	Application DIN	
CuSn10-C	CC480K	2.1050.01	Fittings and pump bodies
CuSn7Zn4Pb7-C	CC493K	2.1090.01	Bearings, bearing bushings
CuSn5Zn5Pb5-C	CC491K	2.1096.01	Bearing bushings, valves, fittings
CuNi10Fe1Mn1-C	CC380H	2.0815.01	Fittings and pump bodies
CuNi30Fe1Mn1NbSi-C	CC383H	2.0835.01	Bearings, fittings and pump bodies

Table 3.4 Standard copper alloys for propellers [7]

Groups	Chemical composition	Typical materials		
		Designation	Standard number	
			EN	DIN
CU1	Rem. Cu, Al 0.5–3.0, Mn 0.0–4.0, Zn 35–40, Fe 0.5–2.5, Ni max 1, Sn 0.1–1.5, Pb max 0.5	CuZn32Al 2Mn2Fe1-C	CC763S	2.0592
CU2	Rem. Cu, Al 0.5–2.0, Mn 1.0–4.0, Zn 33–38, Fe 0.5–2.5, Ni 2.5–8.0, Sn 0.1–1.5, Pb max 0.5	CuZn35 Mn2Al1Fe1-C	CC765S	–
CU3	Rem. Cu, Al 7.0–11.0, Mn 0.5–4.0, Zn max 1, Fe 2.0–6.0, Ni 3.0–6.0, Sn max 0.1, Pb max 0.03	CuAl10Ni5Fe5-C	CC333G	2.0976
CU4	Rem. Cu, Al 6.5–9.0, Mn 8.0–20.0, Zn max 6, Fe 2.0–5.0, Ni 1.5–3, Sn max 1, Pb max 0.05	CuMn11Al8 Fe3Ni3-C	CC212E	–

25 %. To monitor this parameter, the 'zinc-equivalent' is used which may not exceed a value of 45 %:

$$\text{zinc-equivalent } [\%] = (100 - 100 * \text{Cu } [\%])/(100 + A) \qquad [3.1]$$

where A is total of $1 * [\%]$ Sn, $5 * [\%]$ Al, $-0.5 * [\%]$ Mn, $-0.1 * [\%]$ Fe and $-2.3 * [\%]$ Ni. The negative (–)sign attached to the elements Mn, Fe and Ni shows that these elements diminish the formation of β-phase.

3.4 Copper–nickel alloys

3.4.1 Material

Copper and nickel are adjacent to one another in the periodic system of elements and are completely miscible in the liquid as well as in the solid state (Fig. 3.5). As with other copper alloys, copper–nickel alloys exist as wrought alloys, where semi-finished products are further transformed by rolling and annealing processes, and cast alloys, used to produce cast parts with different casting processes (Table 3.5). Common alloys contain between

Table 3.5 Copper–nickel alloys [7] (Cu–Ni–Zn not covered here)

Wrought alloys			Cast alloys		
Material designation	Material number		Material designation*	Material number	
	EN	DIN		EN	DIN
CuNi25	CW350H	2.0830	CuNi10Fe1Mn1-C	CC380H	2.0815
CuNi9Sn2	CW351H	2.0875	CuNi30Fe1Mn1-C	CC381H	–
CuNi10Fe1Mn	CW352H	2.0872	CuNi30Cr2FeMnSi-C	CC382H	–
CuNi30Fe2Mn2	CW353H	–	CuNi30Fe1Mn1NbSi-C	CC383H	2.0835
CuNi30Mn1Fe	CW354H	2.0882	–	–	–

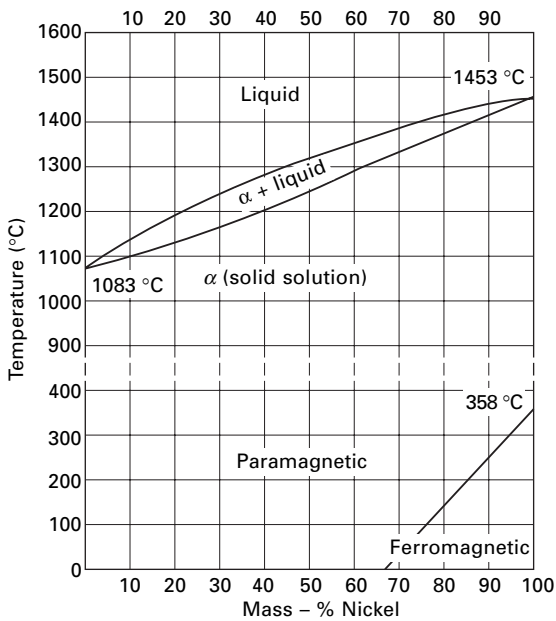

3.5 Equilibrium diagram CuNi.

8.5 and 45 % Ni and in many cases Mn, Fe and Sn to improve properties. Cast alloys may contain additional elements, mainly Nb and Si.

Influence of alloying elements

Nickel improves the tensile strength, 0.2 % proof strength, hot strength and corrosion resistance and diminishes the thermal and electrical conductivity.

Manganese is added to the melt for deoxidation. It improves the castability and increases the tensile strength and especially the softening temperature (Fig. 3.6).

Iron, dissolved in the matrix, increases the corrosion resistance of CuNi alloys. It promotes the formation of a uniform, strongly adhering corrosion protection layer and thereby increases corrosion resistance, especially in fast flowing seawater. The mechanical properties are somewhat increased with iron while the cold workability is slightly decreased (Fig. 3.7).

Tin increases the tensile strength, the high-temperature corrosion resistance and the wear resistance of CuNi alloys. CuNi alloys with 2 % Sn are characterised by an excellent stress relaxation and are therefore used as material for springs. In cast alloys it increases the castability and acts as a deoxidant.

In the copper–nickel system the solubility for **silicon** increases with increasing nickel content. Up to the limit of solubility, increasing the content of Si increases mechanical strength and ductility.

Niobium increases tensile strength and proof strength while elongation drops. It has a favourable influence on the weldability of cast alloys.

Lead is maintained below 0.02 % in those wrought alloys which are for hot working.

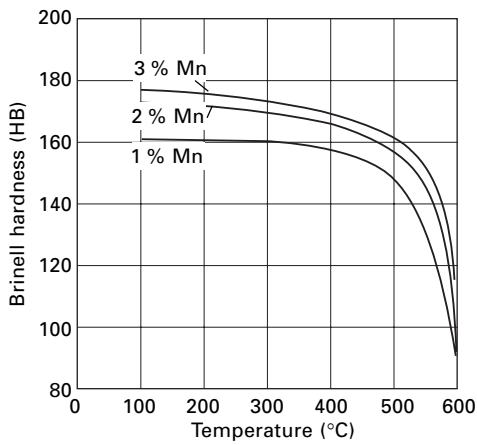

3.6 Effect of manganese on softening.

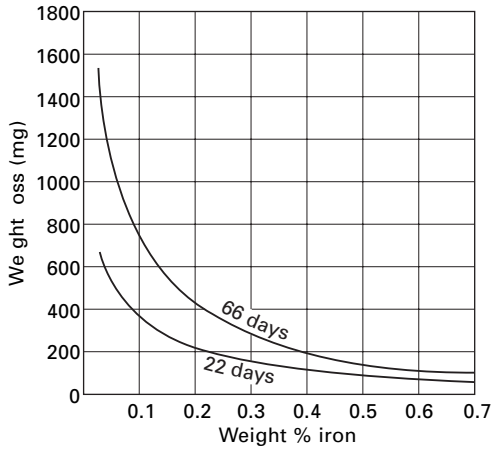

3.7 Effect of iron on the erosion resistance in seawater [8, 13].

The elements **zinc**, **titanium**, **phosphorus**, **chromium**, **aluminum** and **beryllium** allow the tailoring of further properties. Unwanted elements in CuNi alloys are As, S, Sb and Te which are embrittling.

3.4.2 Properties

Mechanical strength

At low and very low temperatures CuNi alloys show – similar to other copper materials – excellent tensile strength. These alloys exhibit no embrittlement at very low temperatures and are therefore very well suited for cryogenic engineering [8].

At elevated temperatures CuNi alloys show good tensile strength. Even low amounts of nickel increase the tensile strength at elevated temperature. The influence of nickel upon the softening of cold-rolled CuNi alloys at higher temperatures can also be observed. By adding iron, the mechanical properties are increased not only at room temperature, but also at higher temperatures.

The fatigue strength of CuNi alloys does not show a marked limit value of tension. With increasing number of load cycles a constant decline is observed, which becomes marginal at very high numbers of load cycles. The figures for very high numbers of load cycles (approx. 10^8) are given as fatigue strength values.

Corrosion properties

CuNi alloys are amongst the most corrosion-resistant materials. They resist humidity, non-oxidising acids, caustic and salt solutions, organic acids and

dry gases like oxygen, chlorine, hydrochloric and fluorochloric acid, sulphur dioxide and carbon dioxide. There is no risk of stress crack corrosion. The tendency towards selective corrosion is very low, and pitting corrosion is a rare exception.

The corrosion resistance of these alloys depends on the formation of a stable oxide layer on the surface caused by the added alloying element. Alloys with 10–30 % weight nickel have a good resistance, even against hot seawater and at high fluid velocities. They resist corrosion up to an average fluid velocity of 6 m/s. To avoid corrosive attack, a minimum fluid velocity of 0.6 m/s is required. These values are indicative figures [9].

Iron-containing wrought alloys CuNi10FeMn and CuNi30Mn1Fe may contain between 0.5 and 2 % weight of iron. This crucially improves the adhesion of the corrosion protection layer and thereby the resistance to erosion–corrosion, especially in seawater and other corrosive waters such as brackish and mining waters. If the iron content is in the optimal range CuNi alloys do not show any selective corrosion. Higher iron contents reduce the resistance to lining corrosion in stagnant seawater. CuNi30Mn1Fe is also corrosion-resistant against ammonia-containing condensates.

The resistance against decoloration of CuNi alloys is additionally enhanced through the presence of **tin**. The corrosion resistance, especially against rapidly flowing seawater, can be increased by adding **chromium**. The presence of aluminium has a favourable influence on the corrosion and scale formation resistance of wrought and cast CuNi alloys.

3.4.3 Processing

When preparing moulds for **casting** CuNi alloys, a shrinkage of approximately 2 % has to be considered. They can be processed in sand-, mould-, continuous and centrifugal casting. Sandcasting is done in dry sand of intermediate permeability.

Rolling is done in a semi-fabrication plant after preheating in a sulphur-free atmosphere. The possibility of warm rolling of CuNi alloys is not noticeably affected by the presence of iron or manganese. Warm rolling is carried out between 850 and 1100 °C. Cold rolling is easily done as well. A CuNi alloy with, e.g., 20 % by weight nickel can be cold shaped to a degree of 95 % without intermediate annealing.

Heat treatment of CuNi alloys is usually applied only for annealing and easing of products. The temperature range for recrystallisation annealing is 620–900 °C. Stress-relief treatment is done in a temperature range of 280–500 °C. Heat treatment is done excluding ambient air or in a slightly reductive atmosphere. A sulphur-containing atmosphere in the kiln is to be avoided. Before heat treatment the part must be degreased to avoid surface contamination with sulphur and/or carbon. Some CuNi alloys [e.g. chromium-

containing wrought alloy CuNi30Cr (non-standardised) or the cast alloy CuNi30Cr2FeMnSi-C] can be hardened with a heat treatment at 500 °C.

Machining of homogeneous CuNi alloys is difficult, especially in the non-hardened state, due to the high tenacity of these metals. Higher alloyed wrought and cast alloys are more easily machined.

Joining of CuNi alloys by **welding** and soldering does not in general present any difficulties. Well-known technologies such arc welding with coated electrodes, tungsten/inert gas welding and metal/inert gas welding are well suited for welding.

In principle, processes like plasma, powder, plasma-metal-inert gas or laser welding are applicable. The following welding fillers are in widespread use: CuNi10(Cu 7061) and CuNi30 (Cu 7158). Pre-heating is not necessary. The nickel content reduces the thermal conductivity of the alloy far enough to reach the heat accumulation needed for welding without difficulties. To prevent hot cracking in the heated area the admissible concentrations of trace elements are limited to: P and S 0.02 % each; Zn 0.5 %; Pb 0.02 %; and C 0.05 %, all by weight.

For a good weldability of cast CuNi alloys the correct relation between silicon and niobium content is important, and it should be according to the following equation:

$$\text{Nb}\ [\%] > (1.55 * \text{Si}\ [\%]) - 0.1 \qquad [3.2]$$

For welding different CuNi alloys with each other or with carbon steel it is advisable to use the welding agent EL-NiCu30Mn (ENi4060) (coated electrode). Resistance welding is possible without any difficulty with CuNi alloys. Other processes such as cold-pressing, ultrasonic, friction, electron beam, high frequency, diffusion or laser welding are also possible.

Joining by soldering can be achieved with tin–silver and tin–copper solder (e.g. S-Sn95Ag5 and S-Sn97Cu3.2.2) with fluxing agents such as 3.1.1, 3.2.1, 3.1.2 and 2.1.2. Remainders of the fluxing agents should be removed after soldering. The solders mentioned above have better strength and higher corrosion and temperature resistance than the lead-containing solders based on tin used previously.

For brazing, copper products such as Cu 303, Cu 304 and Cu 305 are well suited. To avoid the risk of cracking, the products used should be free of phosphorus. Fluxing agents like FH21 are suitable. For soldered connections exposed to corrosive media only solders with a high silver content should be used, e.g. for exposure to seawater AG 105, AG 203 and AG 103 [8, 10].

Mechanical joining of CuNi alloys is done with rivets or screws made from CuNi1Si.

3.4.4 Use in chemical, marine and offshore applications

The major areas of application of CuNi alloys containing iron are predetermined by their high corrosion and erosion resistance in aqueous media. More specifically this has led to the widespread use of the alloys CuNi10Fe1Mn and CuNi30Mn1Fe as very valuable materials in the building of ships, power plants and heat exchangers and as a tube and condenser material in desalination plants.

The CuNi cast alloys CuNi10Fe1Mn1-C and CuNi30Fe1Mn1-C are used as materials for pump bodies, fittings and valves in seawater cooling systems of ships, coastal power plants, desalination plants and in the chemical industry because of their excellent resistance against seawater and other chlorine solutions combined with good weldability and medium to high strength.

Sheet materials from CuNi10Fe1Mn are well suited for cladding the water–air zone of ships because of their good corrosion resistance combined with their antifouling effect on marine organisms, the growth of which they prevent, thus maintaining the propelling energy consumption of ships at its initial low level. In contrast with steel sheets, whose roughness increases with time, that of CuNi10Fe1Mn even decreases. Cladding the legs of offshore oil drilling rigs with CuNi10Fe1Mn to prevent corrosion and growth of marine organisms has also shown its beneficial effects [8, 11].

The chemical industry uses sheet, tube and cast products made of CuNi alloys in oil refineries, for fittings, valves, pump bodies and impeller wheels and piping for salt and other highly corrosive and aggressive solutions, for heat exchangers, mixers and agitators, pressure and other vessels, autoclaves, cooling devices and many other types of apparatus.

The food processing industry uses CuNi alloys for highly loaded multistage evaporators, in sugar refineries, feed water boilers, agitators, in piping and apparatus for food packaging, for fruit juices, fruit sieves, mixers and presses and a variety of other apparatus.

3.4.5 Limits of the material

Like any other materials, CuNi alloys also have their limitations in use and application. Their mechanical strength does not reach that of some competing materials. This is of little importance for systems with low to medium pressure and small tube diameters, but requires increased wall thickness in some of the high-pressure applications. For these applications an alloy with higher strength would represent a major advantage. As CuNi alloys do not form a protective layer in sulphidic media, alternating exposure to sulphide-contaminated and aerated seawater may cause corrosive damage. These alloys should therefore not be selected in such coastal installations, where a part of

the seawater is contaminated regularly and to a high degree with sulphides. Such situations have become increasingly rare since the mid-1990s, as measures for pollution control have gained more and more in efficiency. In the open sea, there are no serious problems of contamination. In these locations it is sufficient to ensure as a precautionary measure that during start-up and testing a sufficient protective layer is formed.

In the case of an excessive increase of flow speed or turbulence of seawater, a risk of erosive corrosion appears. This risk is often addressed, but it is of no real importance in practice, because the CuNi alloys may be used safely at any flow rate or velocity at which seawater can economically be pumped. It is only in some rare circumstances on oil and gas rigs that some additional cost may arise because pump speed is at a limit of accepted design criteria requiring an increase in pipe diameter.

According to the widely applied construction guideline BSMA 18 [12], flow velocities of 3.5 m/s shall not be exceeded in pipes of CuNi10Fe1Mn (and 4 m/s in CuMn30Mn1Fe) with more than 100 mm diameter. For smaller diameters, admissible flow velocities decrease continuously. This limitation does not apply for fire sprinkler installations, where water flows only in case of fire.

At temperatures in excess of 150 °C, denickeling may arise. This local corrosion attack is thermogalvanic in nature. In media rich in ammonia this phenomenon may also appear at room temperature. A remedy is to inoculate the liquid with iron ions to promote the formation and adhesion of the protective layer [13].

An overview and a first evaluation of the most important properties of CuNi alloys and of competing materials is given in Table 3.6.

3.5 Conclusions

Only a few metals if any have a success story similar to that of copper and its alloys. From the early days copper had a decisive influence on the evolution of mankind, and it has been the material of choice promoting the key growth industries of each era. In our time the different copper alloys find their application in nearly every industry, from automotive and telecommunication to power generation and distribution, marine and offshore industries and applications of medical technology.

Especially in marine and offshore technology, copper–aluminum and copper–nickel alloys are used as propeller, tubing and fitting material [14]. The excellent combination of corrosion resistance, erosion resistance and fouling growth inhibition combined with very high strength and decades of experience in many applications make the CuNi alloys a material indispensible in nearly every seawater application. Compared to competing iron and titanium alloys CuNi alloys offer many advantages [15].

Table 3.6 Properties and operating performance of marine alloys in comparison

Material	General corrosion	Scale/gap corrosion	Crevice corrosion	Effect sulphide	Effect chlorination	Marine fouling	Mech. strength	Fire resistance	Fabrication component
CuNi-90/10	+	+	o	o	+	+	o	+	+
CrNiMo-Austenite	+	o	+	o	o	–	+	+	o
CrMo-Ferrite	+	o	+	o	o	–	+	+	o
CrNiMo-Duplex	+	o	+	o	o	–	+	+	o
Titanium	+	+	+	+	+	–	o	+	o

Note: + good, o medium, – bad

3.6 References

1. Documentation on file at Deutsches Kupferinstitut e.V.
2. Kupfer, 2. Aufl., Düsseldorf, Deutsches Kupferinstitut, 1982.
3. DIN EN 1412:1995, Copper and copper alloys – European numbering system, Berlin, Deutsches Institut für Normung.
4. Uni-Duisburg FB IST: Liste der Klassifikationsgesellschaften und Organisationen. Available at: http://www.uni-duisburg.de/FB7/IST/links/Klassif.html
5. DIN EN 12451:1991 Copper and copper alloys – seamless, round tubes for heat exchangers, Berlin, Deutsches Institut für Normung.
6. CEN/TC 133 (CEN/TS 13388: 2004), Copper and copper alloys – compendium of compositions and products, Brussels, European Committee for Standardization.
7. Klassifikation und Bauvorschriften, II-Werkstoff und Schweisstechnik: Teil 1-Metallische Werkstoffe, Kapitel 1–5, Hamburg, Germanischer Lloyd, 1998.
8. Informationsdruck, Kupfer-Nickel-Legierungen [i14], Düsseldorf, Deutsches Kupferinstitut.
9. Informationsdruck, Loten von Kupfer und kupferlegierungen [i3], Düsseldorf, Deutsches Kupferinstitut.
10. K. Dies, *Kupfer und Kupferlegierungen in der Technik*, Berlin, Springer Verlag, 1967.
11. M. Jasner, M. Hecht, W. Beckmann, *The Behaviour of CuNi 90/10 vs 6Mo Superaustenitic and Superduplex Steels in Marine Environments*, Osnabrook, KME Publications, 2000.
12. BS MA 18: 1973, Salt Water Piping Systems in Ships, London, British Standards Institution.
13. C. A. Powell, H. T. Michels, *Corrosion/2000*, paper no. 627, NACE International, Houston, TX, 2000.
14. J. Castle, D. Apler, ESCA investigation of iron-rich protective films on aluminium brass condenser tubes, *Corr. Sci*., **16**, 1976.
15. A. Klassert, L. Tikana, Übersicht über Kupfer und seine Legierungen mit besonderm Schwerpunkt Kupfer-Nickel-Legierungen, Tagung, Korrosionschutz in der maritimen Technik, Hamburg, January 2004, GfKRR-Germanischer-Lloyd.

4

Experience with the use of copper alloys in seawater systems on the Norwegian Continental Shelf

ROY JOHNSEN, Norwegian University of Science and Technology, Norway

4.1 Introduction

The history of oil exploration on the Norwegian Continental Shelf (NCS) goes back to the 1970s. The first commercial fields put in operation were the Ekofisk and the Statfjord Fields, both of which were operated by American oil companies – Phillips Petroleum and Mobil. Due to the lack of people with experience in oil and gas production in Norway at that time, the operating companies brought people from the USA to design and manage the operation of the installations. They used their well-established onshore experience regarding both design and material selection.

On an offshore platform seawater is used for:

- cooling water;
- firewater;
- ballast water;
- injection water;
- fresh water generation.

Seawater is among the most corrosive environments in connection with oil and gas production. For seawater systems the original solution was carbon steel with or without internal concrete. Both the Ekofisk Field and the Statfjord Field used this solution. However, similar to the nuclear industry the preferred material selection for seawater systems changed according to Fig. 4.1.

Table 4.1 gives an example of the preferred seawater material for some main offshore installations on the NCS.

4.2 Copper alloys for seawater application

Copper–nickel (CuNi) alloys were developed specifically for seawater service in the 1950s. The main goal was to develop an alloy suited for tube heat exchangers and piping systems. Although originally developed for seawater corrosion resistance, it was soon recognised that the alloys also had good

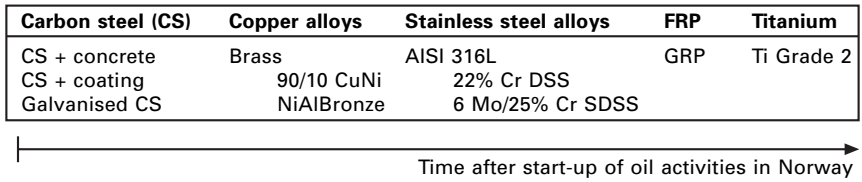

4.1 Change in material selection philosophy for seawater systems.

Table 4.1 Selected seawater piping materials on some offshore installations on the NCS

Field	Operator	Installed	Selected material
Statfjord A, B, C	Mobil	1976–1979	Carbon steel + cement lining Pumps made from NiAlBronze
Frigg Platforms	Elf	1976	Carbon steel + organic coating 90/10 CuNi in 'dry systems'
Ula	BP	1984	Copper alloys
Gullfaks A, B, C	Statoil	1984–1989	6Mo[2] stainless steel piping NiAlBronze pumps
Statfjord A, B, C[1]	Statoil	1986–1988	Ti Grade 2 + internal coating
Heidrun	Statoil	1995	6Mo + GRP[3] + Titan Grade 2
Grane	Norsk Hydro	2003	Titan Grade 2 in piping 25 % Cr SDSS[4] pumps

[1] Piping system replaced due to heavy corrosion in original solution
[2] Austenitic stainless steels with 6 % Mo
[3] Glass fiber reinforced plastic
[4] Super Duplex Stainless Steel

resistance to macrofouling. This property has been advantageous in avoiding or reducing the necessity for biocide dosing in heat exchangers and seawater piping systems.

The three most frequently used copper–nickel alloys for seawater applications within the oil and gas industry are:

- 90/10 CuNi (piping systems, tubes in heat exchangers);
- 70/30 CuNi (piping systems, tubes in heat exchangers);
- NiAlBronze (pumps, valves).

Their chemical compositions are given in Table 4.2. The main difference between these three alloys with regard to properties is in their resistance to flowing seawater.

Table 4.2 Typical chemical composition of CuNi alloys for seawater applications

Alloy	UNS no.	Chemical composition (mass %)				
		Cu	Ni	Al	Mn	Fe
90/10 CuNi	C70600	88	10	–	1.0	1.5
70/30 CuNi	C71500	68	30	–	1.0	1.0
NiAlBronze	C95800	79	5.2	10.3	0.4	5.2

4.3 Corrosion properties in seawater [2–6]

4.3.1 General corrosion

The seawater corrosion resistance offered by copper–nickel alloys results from the formation of a thin, adherent, protective surface film which forms naturally and quickly upon exposure to *clean* seawater. The film is complex and mainly composed of cuprous oxide, often containing nickel and iron oxide, cuprous hydroxychloride and cupric oxide. Initial exposure to clean seawater is crucial to the long-term performance of copper–nickel alloys. The initial film forms fairly quickly over the first couple of days but takes 2–3 months to fully mature. The time depends on the temperature; the higher the temperature, the faster the film is developed.

As long as a good surface film is formed, the corrosion rate continues to decrease. This is the reason why it is difficult to predict the corrosion rate of a copper–nickel alloy based on short-term exposure. Normally, general corrosion rates in unpolluted natural seawater in the order of 0.002–0.02 mm/y are anticipated.

4.3.2 Localised corrosion

Copper–nickel alloys have good resistance to pitting and crevice corrosion in seawater and are not susceptible to chloride or sulphide stress corrosion cracking or hydrogen embrittlement. Experience has shown that copper–nickel alloys can be used in chlorinated seawater with 1–2 ppm residual chlorine and temperatures up to 40 °C without suffering localised corrosion.

4.3.3 Galvanic corrosion

Figure 4.2 shows the galvanic series for some alloys in seawater [7]. As can be seen from the figure, 90/10 CuNi lies midway in the galvanic series, compatible with other copper alloys less noble than stainless steel alloys and titanium, but nobler than carbon steel, aluminium and zinc. This is important information in connection with bi-metallic couplings. To avoid galvanic

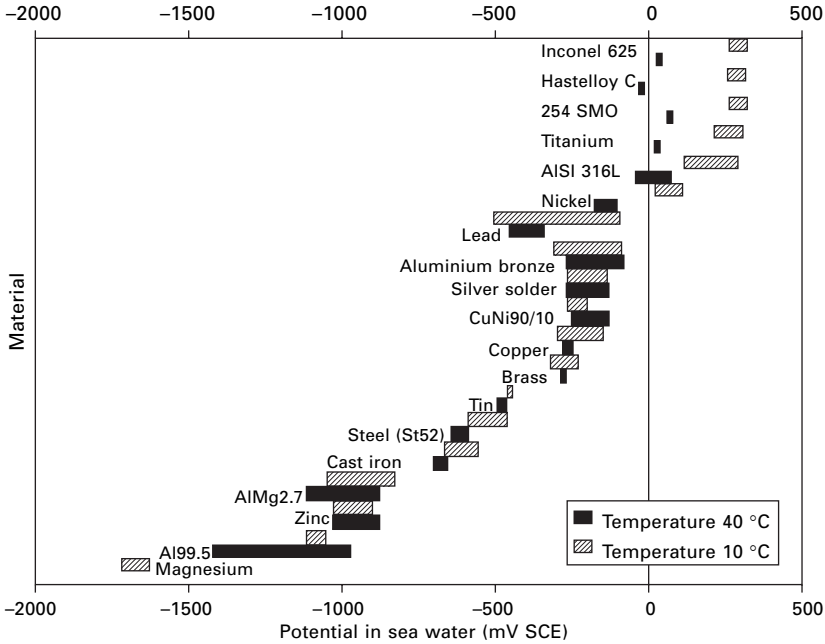

4.2 Galvanic series in natural seawater at 10 and 40 °C.

corrosion between copper–nickel and a second alloy in a piping system, the following precautions should be taken:

- install a *distance spool* between the dissimilar metals so that they will be separated from each other by at least 10 pipe diameters;
- the distance spool may either be of a solid electrically non-conducting material (e.g. GRP) or of a metal internally coated with an electrically non-conducting material (e.g. rubber);
- the coated metal in the distance spool should be the *most noble* of the dissimilar metals.

Figure 4.3 shows a calculation of galvanic corrosion on a 90/10 CuNi pipe connected to a pipe made from 6Mo stainless steel (UNS S31254) in a firewater system. Corrosion rates have been calculated for uniform attack and local attack in a 2 cm wide weld area (circumferential) on the 90/10 CuNi alloy. As can be seen from the figure, the corrosion rate in the 2 cm wide weld area is 0.5 mm/y with no insulation spool, assuming a pipe with 10 inches diameter. Installing a 10 m long insulation spool (40 × diameter) reduces the corrosion rate to approximately 0.2 mm/y. With uniform corrosion on the entire surface of 90/10 CuNi, the average corrosion rate would have been below 0.1 mm/y even without any insulation spool. However, experience has shown that the corrosion attack is more localised than general in nature on a welded 90/10 CuNi pipe.

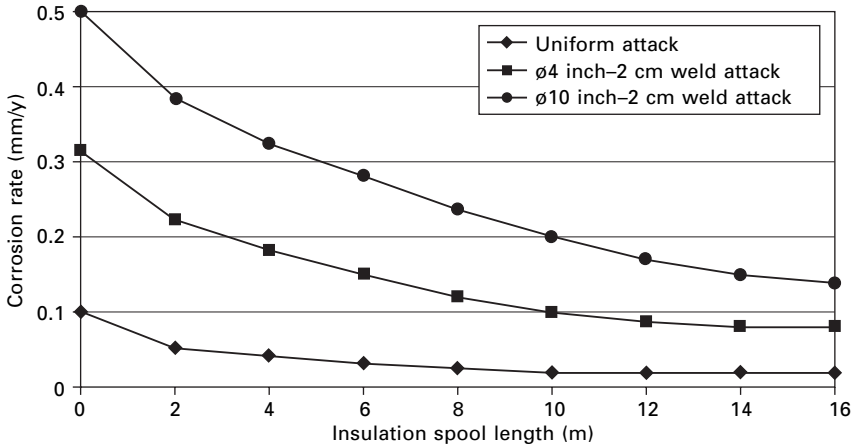

4.3 Maximum calculated corrosion rate as function of insulation spool length.

Galvanic contact with less noble alloys – e.g. when connected to sacrificial anodes – will negate the biofouling resistance of copper–nickel. This is due to the fact that the sacrificial anodes will prevent copper ions from being released.

4.3.4 Velocity restrictions

The resistance against corrosion of copper–nickel alloys is due to the protective surface film. Once the velocity for a given geometry exceeds a critical value, at which shear forces are sufficiently high to destroy the protective surface film, damage in the form of flow-induced–corrosion attack will occur. Critical velocity depends on the local geometry and the pipe dimension. The following average critical velocities are normally used in design:

- **90/10 CuNi:** 3 m/s
- **70/30 CuNi:** 3.5 m/s
- **NiAlBronze:** 20–25 m/s

These critical velocities are valid in an environment without any solids. If sand particles are present in the seawater to be pumped around, critical velocities will be reduced due to erosion by the solids. Actual critical value will depend on the sand concentration (ppm), the particle size (μm) and the local geometry of the component exposed to erosion.

Build-up of sediments on the bottom of piping systems can give initiation sites for under-deposit corrosion. To avoid settlement build-up, a minimum flow rate of 0.5 m/s is normally required for copper–nickel alloys.

4.3.5 Sulphide-polluted seawater

On exposure to polluted seawater, any sulphides present can interfere with the surface film and destroy the good corrosion protection properties of a film developed in clean seawater. Sulphides are present in polluted seawater either as industrial effluent or when the water conditions support the growth of sulphate-reducing bacteria. This can be the case in connection with the handling of ballast water. They can also occur in stagnant conditions as a result of decomposition of organic matter. The result of a copper–nickel alloy being exposed to sulphide-polluted seawater is very rapid corrosion of the alloy destroying the structural integrity of the component.

4.4 Experience from the Norwegian Continental Shelf [6]

Copper–nickel alloys have been used to some extent on the NCS. However, a change took place in their use from early 1990s, as described in Table 4.3.

This is in contrast to the use of copper alloys among operators in other regions, e.g. the UK and the Gulf of Mexico (GOM). There are several reasons for the change in philosophy on the NCS. However, one reason is the number of corrosion and/or erosion failures that were seen during operation. The operators frequently observed traditional failures such as the following:

- **Galvanic corrosion:** due to coupling to more noble alloys without insulation;
- **Flow-induced–corrosion:** local velocities above 3–4 m/s (e.g. outlet ball valve) and solids in the seawater;
- **Stagnant seawater:** under-deposit corrosion;
- **Polluted seawater:** sulphide-polluted seawater causing degradation of the corrosion-resistant oxide layer

Table 4.3 Summary of the use of CuNi alloys in seawater systems on the NCS

1970–1990	1990–today
• 90/10 CuNi and 70/30 CuNi used as piping material in complete seawater systems by several operators • 90/10 CuNi used in deluge systems (dry) • 90/10 CuNi used in tube heat exchangers • NiAlBronze used as valve and pump material	• 90/10 CuNi used in deluge system (dry) • ***Restricted*** use of NiAlBronze in pumps • ***No*** use of copper alloys in seawater piping systems

Through the introduction of alternative materials – see Table 4.1 – Life Cycle Cost (LCC) analysis showed that the use of copper alloys was not the preferred solution for seawater handling systems.

4.4.1 Summary

Table 4.4 presents a summary of information given by six oil companies operating on the NCS. These companies were asked to give feedback on their experience with the use of copper alloys and their strategy for future use of the alloys in seawater handling systems.

4.5 Discussion

As described above, the operators on the NCS have some experience with the use of CuNi alloys in seawater handling systems. However, the extent of their use is less than in the UK and the GOM. The main reason for the reluctance to use copper alloys is probably the lack of robustness that has been experienced in practice.

Experience has shown that CuNi alloys for seawater applications can survive without suffering corrosion assuming that the following precautions are taken:

- max. water velocity 3 m/s for 90/10 CuNi and 25 m/s for NiAlBronze;
- min. velocity 0.5 m/s in order to avoid stagnant conditions;
- avoid sulphide pollution of the seawater;
- avoid solid particles (e.g. sand) in the seawater;
- separate dissimilar metals by installing an insulation spool with necessary length between the two alloys;
- in a mixed metal system which comprises the biofouling resistance of copper–nickel due to galvanic action, treat the seawater with a biocide to prevent the development of a biofilm on the surface.

However, field experience has shown that some of these factors are very often neglected during installation and operation of an installation. The result is normally a leak in the piping system resulting in costly repair and sometimes shutdown of the installation.

The Norwegian oil companies have been a ‘pusher’ for introducing so-called *maintenance-free* materials. The result has been the introduction of high alloyed stainless steels like 6Mo (S31254/N08925) and 25 % Cr SDSS (S32750) and Titanium Grade 2 (R50400) in seawater systems to replace copper alloys. Experience has shown that the high alloyed stainless steels have a maximum operating temperature in the range 20–25 °C for use in chlorinated seawater. Titanium Grade 2 has a much higher critical temperature in seawater (> 70 °C). LCC analysis taking into account all costs related to

Table 4.4 Feedback from oil companies operating on the NCS regarding use of copper alloys in seawater handling systems

BP	ConocoPhillips

• 90/10 CuNi used on Ula and Gyda fields
• Commisioning period can give problems due to
  ○ 'left' stagnant water in the pipes
  ○ bacterial activity preventing build up of protective oxide layer
  ○ pitting corrosion in welds
• Problems with erosion and galvanic corrosion
• BP use NORSOK M-001 as basis for material selection
• BP see 'copper' alloys as an alternative assuming LCC[1] analysis favour this material
	• Use copper alloys in firewater system and water injection system
	• 90/10 CuNi used as tubing material in heat exchangers originally – later replaced with titanium tubing
	• Only minor problems with 'copper' alloys in piping system
	• ConocoPhillips include copper–nickel alloys as alternative materials; final selection based on LCC[1] analysis

ExxonMobil	**Norsk Hydro**

• Have used 'copper' in piping systems – problems have been observed
  ○ stagnant seawater
  ○ high temperature (> 50–60 °C)
  ○ high local velocities
  ○ galvanic couplings
• Originally installed 'copper' pipes/components replaced with more corrosion-resistant alloys
• ExxonMobil ***do not*** evaluate 'copper' as an alternative material for seawater systems
	• Restricted use of 'copper' alloys in seawater
	• Topside firewater stations originally made from 90/10 CuNi – replaced with a more corrosion-resistant alloy
	• HVAC[4] coolers originally delivered with 90/10 CuNi tubes – changed to titanium tubes shortly after start-up
	• One installation (Heimdal Field) has 90/10 CuNi in firewater system (incl. pumps) – *can live with the solution*
	• Norsk Hydro ***do not*** evaluate 'copper' as an alternative material for seawater systems

Table 4.4 Continued

Statoil	Total (former Elf)
• Extensive use of 'copper' on one installation – Veslefrikk – serious corrosion problems causing replacement of entire system with titanium • Firewater pumps on the Gullfaks A, B and C platforms originally delivered in NiAlBronze – serious corrosion/ erosion in critical components; replaced with pumps made from 25 % Cr SDSS[2] • Seawater piping on an onshore plant – Kårstø – originally delivered in 70/30 CuNi. Erosion problems due to local high velocities after valves. Piping replaced by GRP[3] • Statoil ***do not*** evaluate 'copper' as an alternative material for seawater systems	• Firewater system downstream deluge valve made from 90/10 CuNi on the complete Frigg field. Dry condition due to drain holes drilled in the pipes – acceptable solution • Firewater system on the Heimdal field (see also Norsk Hydro) made from 90/10 CuNi – problems associated with: ○ stagnant seawater ○ erosion close to the pumps due to a combination of solids and flow • Total include copper–nickel alloys as alternative materials; final selection based on LCC[1] analysis

[1] Life Cycle Cost
[2] Super Duplex Stainless Steel
[3] Glass fiber reinforced plastic
[4] HVAC = heating, ventilation and air conditioning

the lifetime of an installation has often shown that Titanium Grade 2 is a cost-effective solution as piping material for seawater applications. Pumps are normally made from 25 % Cr SDSS while valves can be made from rubber lined carbon steel or 25 % Cr SDSS [2].

NORSOK M-001 'Material Selection' is the standard that most of the oil companies operating on the NCS currently specify when selecting materials for oil and gas production systems. This standard mentions 90/10 CuNi and NiAlBronze as alternative seawater handling materials for:

- piping;
- piping components;
- valves.

NiAlBronze is *not* mentioned as an alternative material for seawater pumps.

According to the comments given by the operating companies as described in Table 4.4, some of the companies still see copper alloys as an alternative material for seawater systems. The only way for the supplier industry to make copper alloys the preferred solution is to make them economically attractive (based on LCC analysis) and to strengthen their image as a robust material selection.

As a final remark it is fair to say that oil companies operating outside Norway use copper–nickel alloys for seawater handling systems with acceptable results [8]. Most of the newly built floating production, storage and offloading installations (FPSOs) are constructed with 90/10 CuNi for the dry and wet firefighting systems.

4.6 Conclusions

The following conclusions can be drawn for operators on the NCS.

- CuNi alloys have been used for seawater handling systems by the oil companies.
- Field experience has shown serious corrosion and/or flow-induced corrosion problems; often due to operation outside of acceptable parameter windows, including galvanic couplings.
- Robust material selection and material selection based on LCC analysis is the basis for the oil companies.
- Preferred materials for seawater handling systems are Titanium Grade 2, high alloyed stainless steels (25 % Cr SDSS and 6Mo) and GRP.
- CuNi alloys will have a limited market as piping material in seawater systems on the NCS in the future.

4.7 References

1. L. Lunde, R. Johnsen, Seawater-resistant alloys – transfer of experience from the nuclear industry to offshore (in Norwegian), In. Nytt nr 18–20, 1986.
2. NORSOK M-001 'Material Selection', available at: www.standard.no
3. A. Tuthill, *Guidelines for the Use of Copper Alloys in Seawater*, NiDi Publication 12003, 1988.
4. M. Jasner, M. Hect, W. Beckman, *Heat Exchanger and Piping Systems from Copper Alloy – Commissioning, Operating and Shutdown*, KME Publication 1098 005 0104 (1998).
5. C.A. Powell, H.T. Michels, *Corrosion 2000*, paper no. 00627, NACE International, Houston, TX, 2000.
6. R. Johnsen, 'Corrosion problems in the oil industry', *Proc. 11th Scandinavian Corrosion Congress*, Stavanger, Norway, June 1989.
7. S. Valen, E. Bardal, T. Rogne, J.M. Drugli, 'New galvanic series based upon long duration testing in flowing seawater', *Proc. 11th Scandinavian Corrosion Congress*, Stavanger, Norway, June, 1989.
8. W. Schleich, EUROCORR 2004, Paper no. 12-O-124, EFC, Nice, France, September, 2004.

5

CuNi 90/10: How to avoid typical failures of seawater tubing systems and marine biofouling on structures

WILHELM SCHLEICH, K.M. Europa Metal AG Germany; CAROL POWELL, Consultant to Copper Development Association, UK

5.1 Introduction

Since the 1950s, many thousand tonnes of the copper–nickel alloy UNS C70600 (CuNi 90/10) have been installed on different marine engineering structures, mainly as piping for seawater handling and heat exchangers in the shipbuilding, offshore, power and desalination industries. The alloy has been adopted by various international standards (Table 5.1) and, with its good physical and mechanical properties, it is easily fabricated.

In clean oxygenated seawater, the alloy has excellent resistance to uniform and localised corrosion. The maximum allowable flow rate is sufficiently high in the majority of applications to allow its economical use as a piping material. Copper–nickel also has a high resistance to macrofouling due to

Table 5.1 Comparison of chemical composition between various specifications for cupronickel 90/10 used as tubing material. The values represent % wt. Single values represent the maximum content

Standard	DIN/EN	ASTM	ISO	EEMUA [1]
Designation	CuNi10Fe1Mn		CuNi10 Fe1Mn	
Ref. No.	2.0872/CW352H	UNS C70600		UNS 7060X
Copper	Rem.	Rem.	Rem.	Rem.
Nickel	9.0–11.0	9.0–11.0	9.0–11.0	10.0–11.0
Iron	1.0–2.0	1.0–1.8	1.0–2.0	1.5–2.00
Manganese	0.5–1.0	1.0	0.5–1.0	0.5–1.0
Tin	0.03	–	0.03	–
Carbon	0.05	0.05	0.05	0.05
Lead	0.02	0.02	0.02	0.01
Phosphorus	0.02	0.2	0.02	0.02
Sulphur	0.05	0.02	0.02	0.02
Zinc	0.05	0.5	0.5	0.2
Cobalt	0.1	–	0.05	–
Total other impurities	0.2	–	0.1	0.3

the release of copper ions and the structure of oxide layers that are established during natural corrosion processes. This is not only beneficial for sea water systems but, when combined with its corrosion resistance, is also useful for protection of marine structures and boat hulls.

However, occasional instances of failure in copper–nickel systems have been reported. These tend to be due to:

- enhanced corrosion rates in seawater polluted with sulphide;
- erosion–corrosion under critical flow conditions;
- galvanic corrosion.

Based on a literature review and the experience of KM Europa Metal AG and the Copper Development Association, this chapter describes the relevant corrosion mechanisms and provides useful service recommendations to avoid problems in service, particularly for piping systems.

The biofouling behaviour of copper–nickel is also reviewed. This includes recent eight year sheathing trials carried out on behalf of the Nickel Institute by Portsmouth University, examining three different levels of surface area exposure and reported service experience of boat hulls in New Zealand.

5.2 Effect of alloying elements

Copper and nickel have similar atomic radii and lattice parameters and so the phase diagram is relatively simple. At all temperatures, copper–nickel alloys are represented by a single-phase face-centred cubic structure. The absence of phase transformation during thermal cycles reduces the effect of welding on mechanical characteristics and the corrosion resistance of the material. This crystallographic structure reveals very good ductility and impact strength even at cryogenic temperatures. The slow diffusion rate of nickel in copper leads to concentration gradients in the melt and consequently increases the tendency for segregation in the cast structure at normal cooling rates. Hot forging or cold working followed by a recrystallisation anneal homogenises the structure allowing more uniform development of protective oxide layers.

The influence of iron on the properties of CuNi 90/10 has been extensively studied [2–5]. Bailey [2] revealed the effect of iron additions in a series of copper–nickel alloys on impingement corrosion and corrosion under stagnant conditions in natural seawater. It was found that both iron content and microstructure of the alloy play an important role, with the presence of visible iron precipitates causing a deterioration in performance. Data collected from different literature sources [6] for CuNi 90/10 quenched from its solution temperature reveal the optimum iron content to be between 1.5 and 2 % wt.

North and Pryor [7] attempted to understand the role of iron in improving the properties of the passive film on copper–nickel alloys in terms of erosion–corrosion and impingement attack. Iron and nickel atoms incorporated into

the Cu_2O oxide film result in a reduction in the number of positive holes there due to greater uptake of higher charged cations. This provides a decrease in the number of cavities and, thus, a reduction in ionic conductivity. Manganese increases mechanical strength and recrystallisation temperatures [8]. However, the beneficial effect on impingement resistance was found to be less than that of iron [2].

It is emphasised that, in order to ensure reliable service of a copper–nickel system, the components must comply with international standards. Figure 5.1 illustrates one of many weld necks installed on an offshore unit operating off the coast of South America which suffered erosion–corrosion. The system was operated at ambient temperature and at a flow rate below 3.5 m/s. The cross-section of the weld neck shows a cast structure that is not allowed by international standards [1]. Chemical analysis of the weld neck revealed the presence of 0.952 % wt. Fe, 0.012 % wt. Mn and 0.087 % wt. S.

5.3 General corrosion mechanism and establishment of oxide layers

The corrosion behaviour of copper–nickel depends on the presence of oxygen and other oxidisers because it is cathodic to the hydrogen electrode. During the primary anodic reaction, a cuprous oxide film is produced that is predominately responsible for the corrosion protection. The products of corrosion reactions can react with compounds in seawater to form, for example, $CuCl_23Cu \cdot (OH)_2$ or $Cu_2(OH)_3Cl$ and, in so doing, build a multi-layered structure [9].

The corrosion rate quickly decreases over a few days, with one study indicating that the associated discharge of copper ions was reduced ten-fold during 10 min and 100-fold in the first hour [10]. However, establishment of a fully mature film takes from two [9] to three [10] months at temperatures of 15–17 °C. At 27 °C, a common inlet temperature for the Middle East, the establishment of the protective film within a few hours was reported [11]. The long-term general corrosion rates of CuNi 90/10 have been found to continuously decrease with time of exposure, stabilising at below 2 µm/y [12]. The following recommendations for hydrotesting and commissioning should be followed to ensure the appropriate establishment of the oxide layers.

- The system should be cleaned of dirt, lubricants and debris. Introduction of solid matter should be avoided by installation of strainers.
- Clean seawater or fresh water should be used for hydrostatic testing. If polluted water has been used, it should be disposed of and the pipework should be thoroughly rinsed with clean seawater or fresh water. If subsequent stagnant conditions are expected, blow-drying the system is advisable.

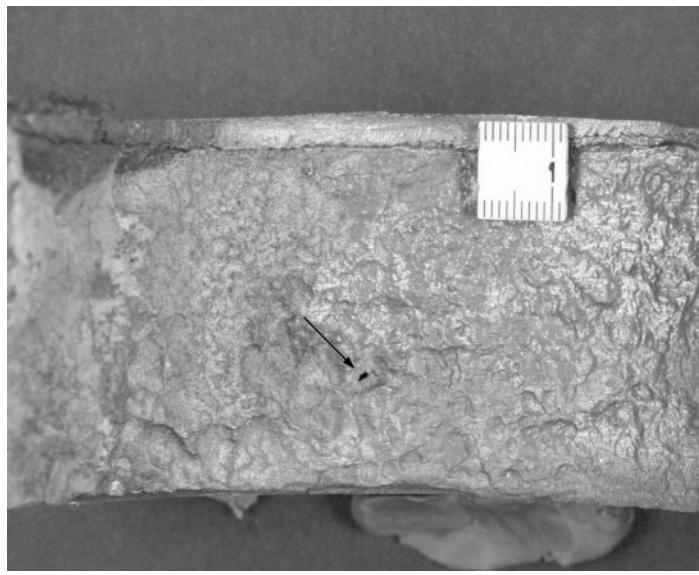

(a)

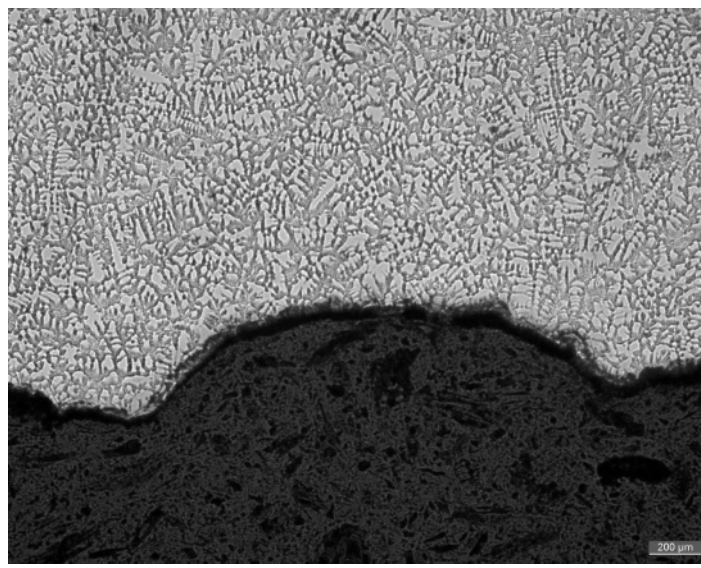

(b)

5.1 (a) Erosion–corrosion damage of the inner surface of a weld neck (10 mm scale). The arrow indicates a perforation. (b) Cross-section of the weld neck demonstrates a cast structure (200 µm scale).

- During commissioning of a new or retubed system, continuous exposure to clean seawater for up to three months, depending on water temperature, is needed to establish a mature protective film.
- A system with continuous pumping activity, such as a cooling system, can be operated under normal operating conditions. In seawater and water containing high levels of suspended matter, the minimum flow rate should not be below 0.5–1 m/s in order to prevent the formation of deposits.
- The commissioning of a system with intermittent flow, such as a firefighting system, should be conducted in seawater free from suspended matter, e.g. in water from the open sea. However, the seawater has to be replaced by oxygenated seawater within 4–5 days to avoid putrefaction [13].

5.4 Localised corrosion

In clean natural seawater, CuNi 90/10 has a high resistance to localised attack, and this is maintained at higher temperatures. The alloy does not have the same susceptibility to chlorides in terms of response to pitting and crevice corrosion that stainless steels have. Localised pitting can occur in the presence of sulphides, and this is described in Section 5.5. Sulphides are present in polluted seawater and can also occur under stagnant conditions due to decomposition of organic matter. Dosing the cooling water with ferrous ions is an advantage, although prevention normally requires avoidance of slow flow or stagnant areas. Minimum flow rates of more than 0.5–1 m/s are usually preferred to avoid sediment build-up. Crevice effects are very rarely reported and are of metal ion concentration cell type where any corrosion is shallow and occurs outside the crevice.

CuNi 90/10 is not susceptible to chloride or sulphide stress corrosion cracking or hydrogen embrittlement and, unlike brasses, has not been found to suffer cracking due to ammonia in seawater service [6]. De-alloying is not a common occurrence in CuNi 90/10. Denickelification has been identified as occurring under heat transfer at near ambient temperature seawater if ammonia is present and the flow rate is low or stagnant [14]. Chlorination or ferrous sulphate dosing and avoidance of low flow conditions help prevent this type of corrosion.

5.5 Effect of sulphides

Most accelerated corrosion problems and premature failures have been associated with sulphides due to copper–nickel tubing operating in polluted seawater or to the activity of sulphate-reducing bacteria (SRB) originating from biochemical reactions arising from putrefaction in stagnant conditions or under deposits. The thermodynamics and kinetics of the hydrogen sulphide system in natural waters are described elsewhere in the literature [15]. It was

demonstrated [16] that, in seawater containing no sulphide, the free corrosion potential of CuNi 90/10 lies on the noble side of hydrogen evolution. In the presence of sulphide, however, the corrosion potentials are shifted to negative values. Therefore, hydrogen evolution becomes possible as a part of the cathodic reaction. Sulphur can be reduced to sulphide at the cathodic site. HS^- reacts with Cu^+ and produces a non-protective black cuprous sulphide which is poorly adherent and results in enhanced probability of erosion attack.

Eiselstein *et al*. [17] investigated the behaviour of CuNi 90/10 tubing during alternating exposure to de-aerated sulphide polluted, aerated unpolluted, aerated polluted and aerated unpolluted seawater at 3 m/s while monitoring the corrosion rate as a function of exposure history (Fig. 5.2). The level of applied sulphide concentration was high. During the exposure of samples to deaerated sulphide-polluted water, the corrosion rate of copper–nickel was comparably lower than that during the exposure to aerated water. Moreover, it was found that the samples pre-exposed to deaerated sulphide-polluted water corroded more rapidly than fresh tube (initial difference more than 1.4 times) after exposure to aerated water. After exposure of the samples to aerated polluted water, significant enhancement of localised corrosion was detected. In addition, it was demonstrated that samples pre-exposed to aerated water corroded much more slowly even than fresh material in aerated polluted water. This indicated that corrosion films formed in sulphide-free environments offered some protection against accelerated attack. Finally, samples pre-exposed to aerated polluted and then exposed to aerated unpolluted water were repassivated in less than five days.

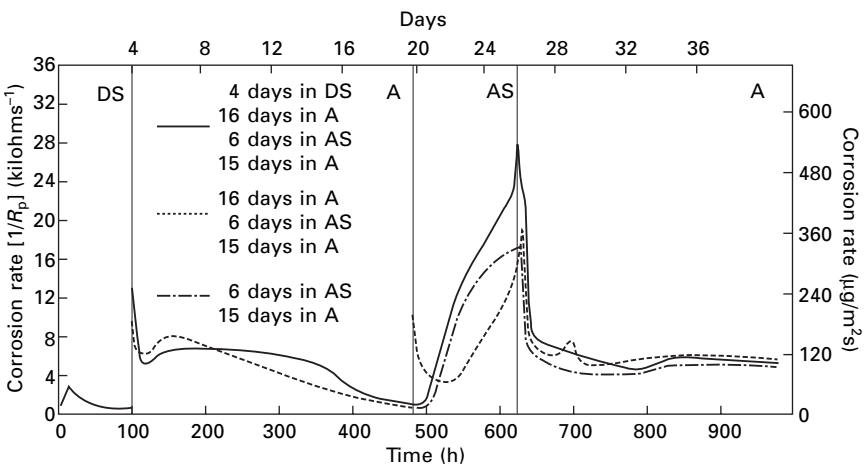

5.2 Corrosion rates of CuNi 90/10 in flowing seawater showing the effect of exposure history and seawater chemistry: DS – deaerated and sulphide-polluted (0.05–0.1 g/m^3 O_2, 0.2–1.3 mg/l HS^-); A – aerated (6.6 g/m^3 O_2); AS – aerated and sulphide-polluted (0.1–0.3 g/m^3 O_2, 0.4–1.6 mg/l HS^-).

From general experience, CuNi 90/10 installed on offshore systems or seagoing vessels does not experience corrosion problems due to the presence of sulphides. However, care should be taken if there is a risk of prolonged exposure to sulphide-polluted water as could be the case in some harbours and brackish water. The following recommendations will be helpful to ensure corrosion-free service of CuNi 90/10 systems in these critical circumstances:

- fill the system with clean seawater prior to entering, while within and when leaving the harbour;
- replace the water in systems with stagnating conditions every 4–5 days with oxygenated clean seawater;
- avoid prolonged exposure of the alloy in waters containing hydrogen sulphide when not using any precautionary measures such as seawater treatment with ferrous ions;
- during construction of the seawater system, treatment of the pipework with ferrous ions or sodium dimethyldithiocarbamate can be applied to prevent excessive corrosion [18].

Copper–nickel performs well as a material for firefighting systems with predominantly quiet conditions. However, if the region under any deposits becomes anaerobic, contributing to the establishment of SRB, the situation could become critical. To improve operating conditions in the seawater system, it is advisable to apply screens and strainers between the water box and pumps to remove travelling debris from intake waters. It is advantageous to apply a pair of strainers so that one can be in operation while the other is being backwashed. When specifying fine filtration, a designer should consider the diameter of the tubes and orifice in heat exchanger equipment. Another possibility is to apply side stream filtration or centrifugal separators, which distinguish themselves by a low pressured drop and are capable of removing sand and other small solids [19]. The description of the analytical methods for the measurement of the sulphide concentration is outside the scope of this chapter, but they have been described in the literature, e.g. Ref. [20].

5.6 Effect of ferrous ion containing solutions

The presence of Fe^{2+}, which originates from additions of ferrous sulphate ($FeSO_4$) or installation of stimulated iron anodes, can reduce the extent of sulphide-induced corrosion when exposure to polluted conditions is anticipated. It is worth remembering, however, that many systems operate successfully without ferrous dosing and, due to ecological policies, the water quality in many previously polluted areas has been improved significantly allowing prolonged stays without any precautions.

It was indicated [21] that the protection mechanism by ferrous ions is due to establishment of a protective film consisting primarily of lepidocrocite

(γ-FeO·OH). Two possibilities for film formation were suggested: lepidocrocite was electrophoretically deposited on the surface from γ-FeO·OH colloid formed in the solution or, through an intermediate step, ferrous ions were transported to cathodic sites and ultimately oxidised to γ-FeO·OH. The substance acted as a cathodic inhibitor increasing the cathodic polarisation.

However, it has been recognised that extensive application of ferrous ions can result in formation of a bulky scale on the tube surface leading to deterioration of the heat exchanger performance. Therefore, the control of treatment efficiency and periodical mechanical cleaning of the heat exchanger might be required. Sato [22] recommended a gradual decrease in dosing levels after the initial film formation.

Effertz and Fichte [23] investigated the effect of temperature, retention time and pH on colloid concentration as well as treatment efficiency. Between 5 and 25 °C, it was demonstrated that a 10 °C rise in temperature doubled the yield of colloid. For up to 5 ppm $FeSO_4$, the colloid concentration increases with concentration of Fe^{2+} ions. In addition, the yield of colloid increased linearly up to 50 % maximum possible concentration and approached asymptotically the maximum level approximately after 1000 s, whereas the formation was finished between 400 and 1000 s. Provided that the colloid concentration is constant, the deposition rate [μg Fe/cm^2 ∗ day] was independent of seawater pH, retention time and Fe^{2+} concentration. The Fe^{2+} concentration in the stock solution should be between 5 and 50 g/l with pH between 2 and 3 to provide the maximum colloid yield. The presence of suspended matter might diminish the efficiency of the treatment. Since the lepidocrocite layer took up a significant amount of water, the drying out of the tube surface can result in sloughing off the protecting films. Assessment of the film quality by application of polarisation resistance measurements was suggested.

In contrast to ferrous sulphate treatment, it has been reported that ferrous ions released from a stimulated iron electrode were oxidised within 3 min. Thus, the recommendation was to situate the anode so that ions reach the points to be protected within 2 min after generation [24]. In the same report it was shown that corrosion already actively proceeding (five days of pre-exposure to 0.2 mg/l sulphide followed by continuous 0.01 mg/l sulphide) was significantly reduced and adverse effects of additional low-level sulphide exposure were nullified by ferrous ion treatment in the range between 0.05 and 0.2 mg/l Fe^{2+}.

Simultaneous treatment with ferrous ions and chlorine is not recommended as it will lead to flocking of the ferrous sulphate making it ineffective. It is recommended to discontinue the treatment with ferrous ions 1 h before chlorination.

The concentration and type of dosage capable of preventing sulphide-induced corrosion are given in Table 5.2. During normal service on offshore units or seagoing vessels, additional ferrous sulphate dosing is seldom required.

Table 5.2 Ferrous ion treatments capable of preventing sulphide-induced corrosion

Type of treatment	Dosage regime	Fe^{2+} concentration (ppm)	S^{2-} concentration (ppm)	Remarks	Ref.
Stimulated anode	Continuous	0.01–0.2	0.01–0.1	No appreciable effect of 0.01 S^{2-} on general corrosion but increased localised attack. The corrosion was significantly reduced by ferrous ion treatment but not completely eliminated; the pitting was eliminated after 90 days	24
Ferrous sulphate	Continuous	5	0.1	Build up of sludge	25
Ferrous sulphate	2 h/day	1	0.01	20–40 days were necessary for inhibitor to achieve the full effectiveness	25
Ferrous sulphate	Continuous	0.1	0.05	90 days of exposure were necessary for full counteraction of inhibitor	26
Ferrous sulphate	Continuous	2–3	See remark	The treatment is recommended during commisioning period to accelerate the formation of protective film	27
Ferrous sulphate	1 h/day	5	See remark	The treatment is recommended during commisioning period to accelerate the formation of protective film	27

However, if exposure to known polluted water is going to occur (e.g. when entering port), a reasonable additional precaution might be to apply dosing prior to entering, while in and after leaving port. In addition it has been reported that application of ferrous sulphate treatment is beneficial in combating the erosion of condenser tubing [28].

5.7 Erosion–corrosion

It has been generally recognised for copper alloys that increasing flow velocities have no significant effect on the corrosion rate until a critical velocity – so called breakaway velocity – is reached. The maximum flow rates in CuNi 90/10 systems are dependent on diameter and are limited to 3.5 m/s for systems with continuous flow [29].

The mechanism of erosion–corrosion is affected by hydrodynamic characteristics of the flow depending on the thickness of both the velocity boundary layer and the diffusion boundary layer at similar average flow velocities. As a result, the increasing boundary layer causes a decreased concentration gradient and thus reduces the mass transport. Consequently, if the passive film breaks down and metal removal corresponds to the shear stress in the surface, or if the corrosion process is determined by the mass transport from or to the surface, it can be expected that an increasing pipe diameter results in lowering erosion–corrosion rates and an increased breakdown velocity [30].

Efird [31] estimated that the critical velocity was 4.4 m/s for a tube 0.03 m in diameter and 6 m/s for a tube 3 m in diameter at 27 °C. The calculated critical shear stress was 43.1 N/m^2 for CuNi 90/10 in seawater, indicating that the conditions under which the passive film is formed must be considered.

Sand is typically present in estuarine or brackish waters and may be detrimental to the performance of the alloy. The severity of this is difficult to quantify because it is affected by many factors such as sand content, size of sand particles, flow profile, magnitude of impingement and water chemistry. A survey on sand loading in seawaters used as coolant in power plants revealed that in most cases the sand content is less than 1000 ppm with particle size in the range of less than 50 ~250 μm. At 10 Pa shear stress, it was shown using a rotating drum test that 1000 ppm sand particles up to 30 μm do not impose any appreciable effect. Larger diameters tend to be increasingly abrasive. At flow rates of 2 m/s, the effect of 20 ppm sand particles with a size less than 100 μm caused a negligible corrosion increase whereas higher sand content caused enhanced corrosion. It has to be noted that these data were collected for aluminium brass condenser tubing [28] and the critical sand content for copper–nickel may be higher.

Severe conditions might be expected if the pipe opening has a foreign

body lodged in it causing throttling of the flow and leading to an abnormal local increase of flow velocity [28]. Therefore, entrance of debris has to be prevented by installation of strainers. Also growth of macrofouling accumulations must be prevented by appropriate biocide treatment.

Further, Campbell and Carter [32] evaluated the effect of controlled bubble size (1.0 and 2.3 mm) on erosion–corrosion resistance and compared these results with bubble-free water using a jet impingement apparatus. The deleterious effect decreases with smaller bubble size.

It appears reasonable to suppose that an occasional reduction in velocity may contribute to repassivation and thickening of the surface film [30]. Knutsson *et al*. [33] presented results of an examination of flow regimes over 12 months using a copper alloy. From 1 to 25 % flow duration, no attack was observed at 11.9 m/s. Continuous flow produced results of < 15 µm/y at 6.1 m/s and 76 µm/y at 11.9 m/s. Therefore, for emergency or testing situations, as in firefighting systems which do not experience frequent pumping activity, the high flow velocities normally applied in such situations (e.g 7 m/s) are acceptable for Cu/Ni 90/10. During two years of testing with sand-loaded (100–2000 mg/l) natural seawater by means of a once-through loop operated intermittently, no appreciable corrosion attack was detected at velocities up to 5 m/s [34].

The effects of erosion are preventable by good design, which is also necessary to improve the efficiency of the piping system. The general guidelines for reduction of friction loss depend on the flow velocity, pressure drop in the system due to the geometry of bends and valves, the required pumping power and the probability of erosion–corrosion:

- avoid sudden changes of direction;
- bend radii $r \geq 1.5d$ or angled branches are preferable; for smaller bending radii use prefabricated fittings;
- avoid excessive weld root penetration into the pipe cavity (Table 5.3);
- control the flow with the least number of valves;
- cut the gasket flush with the inner surface of the pipe;
- avoid the positioning of valves, pumps, orifice plates and bends in close proximity;
- provide a straight downstream distance (min. $5 \times$ I.D.) from valves, pumps and orifice plates to bends;
- consider the water demand within the entire range of operational conditions.

5.8 Effect of chlorination

Chlorination of seawater is the most common method used to control biofouling, and it has been reported that continuous chlorination to a residual-free chlorine level of 0.25 ppm can be 100 % effective against fouling [35]. There is only limited information on the effect of chlorination on the corrosion behaviour

Table 5.3 The maximum depth of excessive weld root penetration including the mismatch of the pipe depending on pipe diameter according to DIN 85004-2:1996-06, Piping Systems of Copper–Nickel Alloys – Part 2: Basic Principles for Design, Fabrication, Inspection and Testing

Nominal pipe diameter (mm)	The max. excessive penetration of the weld root (mm)
< 40	1.5
50–150	2
175–250	2.5
> 300	3

of copper–nickel. It has been reported that, in the presence of 0.25 ppm free chlorine, the corrosion of CuNi 90/10 increased during 30 days of exposure, but the effect of the chlorine weakened subsequently [36]. Kirk and Tuthill [37] stated that, according to general experience, no negative effect of chlorine concentrations 0.2–0.5 ppm was indicated on the corrosion behaviour of copper–nickel alloy during many years in coastal power and process industries. In spite of the biofouling resistance of copper–nickel, the chlorine treatment extended the intervals between mechanical cleanings to restore the performance of heat exchangers from two months without chlorination to up to one year under chlorinated conditions in coastal plants.

Francis [38, 39] published the results of tests related to the effect of chlorine additions in the range between 0.3 and 4.0 ppm on corrosion and jet impingement tests (jet velocity 9 m/s for two months) of CuNi 90/10 exposed to natural seawater. The products formed on CuNi 90/10 during chlorination led to appreciable anodic and cathodic polarisation and, thus, somehow to an improvement in corrosion resistance. Nevertheless, these products impaired the mechanical resistance of the copper–nickel surface leading to an increase in impingement susceptibility. For continuous and intermittent chlorine additions, the residual concentrations of 0.3 and 0.5 ppm, respectively, were recommended. Finally, the author pointed out that his results require more research in this area.

Another study [40] proposed a possible mechanism for the effect of free chlorine on corrosion performance of CuNi 90/10 in highly polluted brackish water containing appreciable amounts of planktonic and sessile SRB. It was assumed that the corrosion process in the presence of chlorine was controlled by transformation of a Cu_2O layer into secondary compounds such $Cu_2(OH)_3Cl$ due to the high oxidising power of the medium. These secondary products were not strongly adherent to the surface and were easily removed, allowing further Cu_2O formation. Unfortunately, no mass loss or depth of corrosion attack were presented in this paper.

Clearly, more research is needed on the effect of chlorination on the

corrosion behaviour of copper–nickel in clean and polluted seawater, or on the alteration of the critical shear stress. However, it can be concluded that chlorination of seawater to levels higher than those which are sufficient to control the biofouling activity should be avoided.

5.9 Galvanic corrosion

The avoidance of galvanic corrosion is a principal design consideration. Stainless steels undergo significant potential variations depending on chlorine and oxygen content and temperature, as well as presence of a biofilm, e.g. from +600 mV SCE in seawater containing 0.5–1.0 ppm free chlorine to less than –400 mV SCE in deaerated seawater. In contrast, CuNi 90/10 reveals only small changes. It has been reported that the corrosion potential of this alloy remains in the range between –50 and –300 mV SCE in natural aerated seawater at 10 and 40 °C, in seawater flowing at 3–15 m/s at the same temperatures and in seawater containing 0.5 ppm Cl_2 at 15 °C.

Bardal *et al*. [41] studied coupling of CuNi 90/10 with high-alloy stainless steel in natural and chlorinated seawater. During connection of the metals in chlorinated water, no significant effect of galvanic corrosion was found. The difference was attributed to the establishment of biofilm on high-alloy stainless steel in natural seawater providing a much higher cathodic efficiency. However, precautionary measures should be taken if the chlorination might be turned off.

For prevention of galvanic corrosion, it is recommended to use compatible materials wherever possible; CuNi 90/10 is generally compatible with other copper alloys in seawater as long as surface area ratios are not extreme. However, in multi-material systems, the combination of different metals is often unavoidable and so the electrical contact of CuNi 90/10 with aluminium, nickel and titanium alloys, carbon and stainless steels should be avoided by application of commonly used protection measures.

5.10 Biofouling

The high resistance of copper–nickel to macrofouling is well recognised and widely used [42]. This property is attributed to a continuous release of copper ions that cannot be tolerated by many organisms and decelerates considerably the establishment of the primary bacterial film. Also the biofouling resistance is attributed to the mechanical properties of the top oxide layer formed during secondary corrosion reactions; the top layers can be fouled, but they slough away easily leaving a clean surface.

Nevertheless, bacteria of certain genus, which are protected by a polysaccharide lining from the copper ions and build up a slime layer, can remain intact even within the layer of secondary corrosion products [43]. In contrast to stainless steels, however, the slime layer on copper–nickel surfaces

5.3 Cathodically protected steel, CuNi90/10 partially sheathed steel and CuNi 90/10 panels and a freely exposed copper nickel panel prior to immersion from a raft, UK.

5.4 After one year exposure, the freely exposed sample has no macrofouling.

exposed to natural seawater does not change the free corrosion potential of the alloy [44, 45].

To achieve the optimum resistance, the alloy should be freely exposed to seawater and not be cathodically protected or connected galvanically to less noble materials. This is illustrated in Figs 5.3 and 5.4 [46]. Figure 5.3 shows a rack of panels before immersion from a raft. From left to right the first three panels are steel, steel partially sheathed by welding with copper–nickel sheet and copper–nickel. All have aluminium anodes attached. The fourth panel is copper–nickel freely exposed without an anode. Figure 5.4 shows the panels after 12 months exposure. The copper–nickel panels with anodes have fouled to a similar extent as the steel whereas the freely exposed panel has a slime layer but no macrofouling. This explains why, in some mixed metal systems and when ferrous ions are dosed into piping systems using anodes connected directly to the pipe, there is a reduction in biofouling resistance. General experience of copper–nickel not in contact with less noble alloys or insulated from them has indicated that, in open seas, microfouling (slime layers) does not build up sufficiently to support macrofouling. When exposed to quiet conditions for long periods, some macrofouling will occur eventually but, as it is loosely attached it will slough away at intervals or can be easily removed by finger pressure or a light scraping action [47–50].

5.10.1 New Zealand ferry trials

An evaluation programme on the performance of adhesively backed CuNi 90/10 foil sheathing gives practical insight into biofouling properties of the alloy. The evaluation commenced in August 1993 [49] with two commercial passenger ferries, the MV Koru and the MV Osprey, both of which were in service around Auckland Harbour, New Zealand. MV Koru was a slow ferry (10 knots), constructed of fibreglass reinforced polymer (FRP), which was retrofitted with copper–nickel sheathing in 1993. The other vessel, a fast catamaran ferry (22 knots) with a FRP hull, was sheathed during construction in 1994. The older monohull vessel, MV Koru, was kept in reserve most of the time, whereas the catamaran, MV Osprey, had been in service for about 40 000 nautical miles since construction by the time the work was reported in 1999.

The corrosion resistance of the copper–nickel appeared good. Slime (microfouling) formed on the copper–nickel, but macrofouling was restricted. If colonisation did eventually occur, it was readily removed, such that a light water blast would quickly remove any growth. The turnaround time for cleaning the MV Koru on the slip by this method was about 1.5 hours whereas removal of fouling from the equivalent painted vessels in the fleet could take up to one day.

Flow velocity and sunlight appeared to influence biofouling behaviour. More algae formed on the copper–nickel foil just below the water line on both vessels, and it was more prevalent on the side of the MV Koru hull facing the sun during out-of-service time. Typically, the stern and water line tended to show earlier signs of fouling than other hull areas. Areas between the hulls of the MV Osprey which experienced higher velocities remained almost entirely free.

5.10.2 Langstone Harbour sheathing product trials

A seven and eight year raft exposure trial study in Langstone Harbour, UK, evaluating the corrosion and biofouling behaviour of the adhesive backed foil and three other copper–nickel sheathing products has also recently been completed [51]. The samples were exposed from a raft for up to eight years and are listed in Table 5.4, the final samples being removed in November 2002. There were three different levels of copper–nickel surface area coverage: 30 %, 60 % and 100 %. Of the 100 % coverage, the foil samples had a bright surface whereas the hot rolled sheet had a dull surface finish. The samples were inspected at regular intervals over the exposure period, particularly prior to and after the spring and autumn fouling seasons. No cleaning regime was applied to the panels although small, localised areas were occasionally wiped manually to assess adherence of fouling. Photographic records of the appearances of these alloys as a function of time were obtained, the nature and development of the associated fouling community monitored and laboratory testing of removed samples carried out at exposure periods of 1, 3–5 and 6–8 years. The progression of the fouling over the years of exposure is shown in Figs 5.5–5.8.

The trials confirmed documented experience that microfouling will eventually colonise on CuNi 90/10 but macrofouling is restricted. Most of the macrofouling identified had colonised on the rubber substrates or adhesive exposed at overlaps. Where microfouling and macrofouling had colonised on the copper–nickel, it could normally easily be removed with a wipe when exposed and wet but with slightly more effort when taken from the raft and dried out.

Surface area coverage of copper–nickel had some effect on biofouling, but this did not seem to be a linear relationship. The embedded granule product, having the least copper–nickel surface area cover, might have been predicted to show higher fouling levels than the other products. In reality it showed very good resistance for the majority of the exposure. The hot rolled sheet provided the best biofouling resistance which might be taken to be associated with the 100 % copper–nickel surface area, but it also had a thicker oxide surface film, and the composition of this could also have played a part. The copper–nickel on the flat surfaces of foil had thinned by a decreasing

Table 5.4 Product and panel and details

	Embedded granules	Expanded mesh	3 mm hot rolled sheet	Adhesive backed foil
Description	90/10 CuNi rods (1 mm dia, 1 mm length) embedded by hot bonding into a 3 mm thick poly-chloropropene rubber sheet	90/10 CuNi expanded mesh, bonded to an elastomeric rubber base (EPDM)	As-manufactured and retaining surface oxide film	90/10 CuNi foil sheets, with adhesive backing, hot pressed onto suitably prepared steel, aluminium and FRP surfaces
Sample details	18.4 × 24.0 cm. Mounted on FRP backing, 6 samples	~ 9 × 19.0 cm curved samples 0.1 cm thick mesh, with slits 0.3 × 1 cm, 6 samples	19.8 × 19.2 × 0.3 cm, 1 sample	Alloy and backing plate: 61.0 × 31.0 cm, 3 panels each with Al, steel and FRP backing plates
Area coverage of copper–nickel	30 %	60 %	100 %	100 %

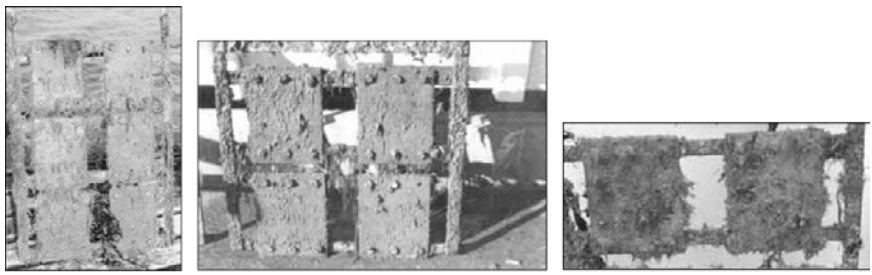

5.5 Embedded granule panels after exposure of (a) 1 year, (b) 5 years and (c) 8 years.

5.6 Expanded mesh panels after exposure of (a) 2.5 years and (b) 7 years.

rate which was measured as averaging 5.5 μm per annum over a seven year exposure period and appeared consistent with US trials [12] which decreased over similar time, stabilising at less than 2 μm per annum.

5.11 Conclusions

The literature has been reviewed and shows CuNi 90/10 to have a unique combination of good resistance to both corrosion and biofouling in marine environments. The main reasons for premature failure of seawater piping systems are associated with incorrect chemical composition and production techniques for copper–nickel components, inappropriate conditions during commissioning and operation of the system, presence of deposits and hydrogen sulphide, excessively high flow rates and poor design layout of the system. Practical recommendations have been presented to avoid future failures.

Recent results from eight year exposure trials on sheathing products at Langstone Harbour, UK, confirm that colonisation of fouling species is

(a)

(b)

5.7 Hot rolled sheet after exposure of (a) 13 months and (b) 7 years.

restricted on CuNi 90/10 which remained largely free of macrofouling. Where present it could be wiped away fairly readily.

5.12 Acknowledgement

The authors thank the Nickel Institute for permission to include the Langstone Harbour trials.

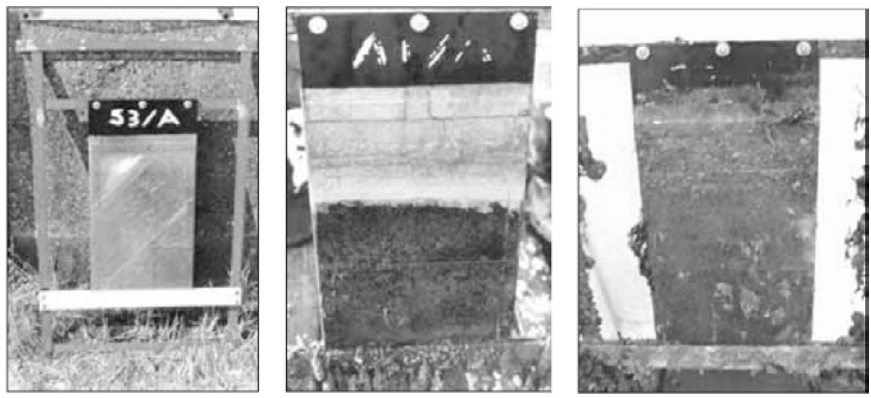

(a) (b) (c)

5.8 Adhesive backed foil panels (a) as immersed and after exposure of (b) 18 months and (c) 7 years.

5.13 References

1. EEMUA Publication Nos 144, 145, 146–7: *90/10 Copper Nickel Alloy Piping for Offshore Applications*, London, Engineering Equipment and Material Users Association, 1987.
2. G.L. Bailey, *J. Inst. Met*. **79** (1951) 243–292.
3. L.J.P. Drolenga, F.P. Ijsseling, B.H. Kolster, *Werkstoffe und Korrsion*, **34** (1984) 167–172.
4. INCRA, contractor report, PRJ 382, New York, International Copper Association, April 1986, 7.
5. J.P. Frick, L.H. Scharfstein, T.M. Parrill, G. Haaland, *J. of Metals*, **3** (1985) 28–30.
6. M.S. Parvizi, A. Aladjem, J.E. Castle, *International Materials Reviews*, **33** (4) (1988) 164–199.
7. R.F. North, M.J. Pryor, *Corr. Sci*., **10** (1970) 297.
8. F.W. Nothing, *Kupfer-Nickel-Legierungen*, Düsseldorf, Nickel-Inforamtionsbüro GmbH, 1964.
9. F.J. Kievits, F.P. Ijsseling, *Werkstoffe und Korrosion*, **23** (12) (1972) 1084–1096.
10. A. Tuthill, *Guidelines for the Use of Copper Alloys in Seawater*, NiDI Publication 12003, 1988.
11. A. Tuthill, B. Todd, J. Oldfield, Experience with Copper Nickel Alloy Tubing, Water Boxes and Piping in MSM Desalination Plants, *IDA World Congress on Desalination and Water Reuse*, paper no 73, Vol. III, 251, Madrid, October, 1977.
12. K.D. Efird, *Mater. Perform*., November 1975, 37.
13. K.D. Efird, T.S. Lee, *Corrosion*, **35** (2) 1979, 79–83.
14. R. Francis, *B. Corr. J*., **22** (3), (1987) 199–201.
15. F.J. Millero, *Marine Chem*., **18** (1986) 121–147.
16. B.C. Syrett, D.D. MacDonald, S.S. Wing, *Corrosion*, **35** (9) (1979) 409–422.
17. L.E. Eiselstein, B.C. Syrett, S.S. Wing, R.D. Caligiuri, *Corros. Sci*., **23** (3) (1983) 223–239.
18. Naval Engineering Standard (NES) 781 3rd Issue, UK, MOD, May 1979.

19. S.D. Strauss, P.R. Puckorius, 'Cooling-water treatment and control of scaling, fouling, and corrosion,' *Power*, June 1988, 46–49.
20. *Standard Methods for the Examination of Water and Wastewaters*, 20th edn, pp. 4–162 to 4–173, jointly published by American Public Health Association, American Water Works Association, Water Environment Association, 1998.
21. R. North, M.J. Pryor, *Corr. Sci*., **8** (3), (1968) 149–157.
22. S. Sato, *Rev. Coatings Corr*., (1973) 139.
23. P.H. Effertz and W. Fichte, *Der Maschinenschaden*, **49** (1976) 163.
24. H.P. Hack, J.P. Gudas, *Mater. Perform*., April 1980, 49.
25. H.P. Hack, J.P. Gudas, *Corrosion/78*, paper no. 23, NACE International, Houston, TX, 1978.
26. H.P. Hack, T.S. Lee, The Effect of Ferrous Sulfate on Sulfide-Induced Corrosion of Copper-Base Condenser Alloys in Aerated Seawater, Report No. DTNSRDC/SME-81-91, David W. Taylor, Naval Ship Research and Development Center, Maryland, January 1982.
27. C.A Powell, H.T. Michels, *Corrosion/2000*, paper no. 627, NACE International, Houston TX, 2000.
28. S. Sato, K. Nagata, Factors affecting corrosion and fouling of condenser tubes of copper alloys and titanium, *Sumitomo Light Metal Technical Reports*, **19** (3–4) (1978), 83–94.
29. BSI, BS MA 18: 1973 Salt water piping systems in ships, London, British Standards Institution.
30. B.C. Syrett, *Corrosion*, **32** (6) (1976) 242–252.
31. K.D. Efird, *Corrosion*, **33** (1) (1977) 3–8.
32. H.S. Campbell, V.E. Carter, *J. Inst. Metals*, **90** (1961–62) 362.
33. L. Knutsson, E. Mattsson, B.E. Ramberg, *B. Corr. J*., **7** (1972) 208.
34. M. Jasner, K. Steinkamp, *Stainless Steel World*, **14** (June) (2002), 38–43.
35. D.B. Anderson, B.R Richards, *Trans. ASME, J. Eng. Power*, July (1966), 203–208.
36. R.O. Lewis, *Mater. Perfom*, **22** (8), (1981), 31.
37. W.W. Kirk, A.H. Tuthill, Copper-Nickel Condenser and Heat Exchanger Systems, Paper from a Seminar, The Application of Copper-Nickel Alloys in Marine Systems, presented jointly by ICA, CDA and Nickel Development Institute in Cooperation with Japan Copper Development Association, Korean Institute of Metals, Tokyo, Osaka and Nagasaki, Japan, Pusan and Kirje Island, Republic of South Korea, November, 1991.
38. R. Francis, *Mater. Perfor*., **21** (8) (1982) 44.
39. R. Francis, *Corrosion*, **26** (3) (1985) 205.
40. M. De Romero *et al*., *Corrosion*, **56** (8), 2000, 867–876.
41. E. Bardal, R. Johnsen, P.O. Gartland, *Corrosion* **40** (1984) 12.
42. W. Schleich, K. Steinkamp, Stainless Steel World 2003, paper no P03 79, Maastricht, November, 2003.
43. G.W. Blunn, E.B.G. Jones, 'The Immobilisation of Copper by Marine Fouling Microorganisms', INCRA Project No. 332A, New York, International Copper Association, 1984.
44. F. Mansfeld, B. Little, *Electrochemica Acta*. **37** (12), 1992, 2291.
45. R. Francis, 'Galvanic Corrosion: Practical Guide for Engineers', NACE International, Houston, TX, 2001, 8–13.
46. C. Powell, CDA Inc., Seminar Technical Report 7044-1919, The Application of

Copper Nickel Alloys in Marine Systems. Copper Nickel Alloys; Resistance to Corrosion and Biofouling, New York, Copper Development Association, 1992.
47. K.D. Efird, *Mater. Perform.*, **15** (4), 16–25, 1976.
48. J. Manzolillo, E. Thiele, A. Tuthill, CA 706 Copper-Nickel Alloy Hulls: The Copper Mariner's Experience and Economics, paper no. 13, pp 22, *Trans Society of Naval Architects and Marine Engineers*, New York, November 11–13, 1976.
49. L. Boulton, W. Hudson, C. Powell, in *10th International Congress on Marine Corrosion and Fouling*, J.A. Lewis (ed.), University of Melbourne, February 1999: Additional Papers, DSTO General Document DSTO-GD-0287, Defence Science & Technology Organisation, Australia, 2001, 73–87.
50. C.A. Powell, Preventing Biofouling with Copper-Nickel, CDA UK publication 157, Hemel Hempstead, Copper Development Association UK, 2002.
51. S.A. Campbell, R.L. Fletcher, C.J. West, Final Report on the Exposure Trial Studies of Copper-nickel Coatings Avonclad, Arncote and Mariner 706, Portsmouth University Report No 7 for the Nickel Development Institute, December, 2002.

6

70/30 copper–nickel seawater piping systems – use of descaling agents and their effects on corrosion properties

HERVÉ LE GUYADER and ANNE-MARIE GROLLEAU, DCN Cherbourg, France; EDWARD LEMIEUX and KEITH LUCAS, Naval Research Laboratory, USA; THERESA WOLEJSZA, Geo Centers, USA

6.1 Introduction

Use of copper–nickel alloys in seawater-cooled heat exchangers is common due to the inherent properties of these alloys, namely, a relatively low corrosion rate, antifouling properties and erosion–corrosion resistance relative to other alloys. The corrosion behavior of these alloys is strongly dependent on the formation of a 'protective film' on the underlying metal. In addition, alloying of copper with nickel increases the tendency towards passivity as compared to pure copper and has beneficial effects on erosion–corrosion resistance. Erosion–corrosion is also improved by addition of iron and manganese. The ability to form a protective film in seawater is influenced by various parameters among which are:

- alloy-related properties (microstructure, chemical composition);
- seawater properties (oxygen and contaminant content);
- physical conditions (design, temperature, flow velocity).

The main causes of failure of copper–nickel alloy components in seawater are usually attributed to either erosion–corrosion at extreme velocities or pitting phenomena. It is well-established that these failures are generally due to detrimental seawater conditions, such as the presence of sulphides [1–5], or poor designs resulting in extreme flow velocities [6]. Periodic cleaning is necessary on seawater cooling systems, due to the gradual formation of scaling and macrofouling during operation. Several chemicals and procedures can be used to remove these deposits and growths [7], the most common products being hydrochloric, citric or sulfamic acids. Hydrolancing and mechanical cleaning are currently in use by the fleet, but these have major drawbacks in terms of costs and labor hours. In addition, most of these methods raise some safety and environmental issues.

Currently, three commercial descaling solvents, two hydrochloric acid-based and one phosphoric acid-based, have been identified that claim to be safe, environmentally friendly, inexpensive and exhibit no detrimental effects

on the materials. However, demonstrations with one of them have noted an appreciable metal loss during cleaning of equipments on board Navy ships.

As a result of these demonstrations, the Naval Research Laboratory in Key West, FL (NRLKW) was tasked to provide support to determine the actual mechanism of these descaling solvents. The objectives of the work reported in this chapter were to:

- identify the effect of cleaning on the corrosion behavior of 70/30 CuNi;
- identify and determine the effect of such cleanings on the existing protective oxide film;
- evaluate the subsequent repassivation of 70/30 CuNi in seawater after cleaning with descalant.

6.1.1 Scale and descaling chemistry

Although mechanisms are still not completely understood, the oxide film on copper–nickel alloys is known to be made of an outer porous layer of cupric hydroxy chloride ($Cu_2(OH)_3Cl$) overlaying a compact inner layer of Cu_2O [8–11]. The cuprous oxide is reported to be responsible for the good corrosion resistance of copper–nickel alloys. The reactions at the metal interface, which naturally occur in seawater without the application of cathodic protection, can be defined by the following equations:

$$2\ Cu + H_2O \rightarrow Cu_2O + 2\ H^+ + 2e^- \quad [6.1]$$

$$Cu_2O + H_2O \rightarrow 2\ CuO + 2\ H^+ + 2e^- \quad [6.2]$$

$$Cu_2O + 3H_2O \rightarrow 2\ Cu(OH)_2 + 2H^+ + 2e^- \quad [6.3]$$

$$Cu_2O + {}^1/_2\ O_2 + Cl^- + 2H_2O \rightarrow Cu_2(OH)_3Cl + OH^- \quad [6.4]$$

$$Ni + H_2O \rightarrow NiO + 2\ H^+ + 2e^- \quad [6.5]$$

In operational conditions, calcium carbonate scale is formed gradually due to the combined effects of water composition, temperature and cathodic protection. This calcareous deposition or 'scaling' process can be summarized by the following reaction:

$$M^{2+} + HCO_3^- + OH^- \rightarrow MCO_3 + H_2O \quad [6.6]$$

where M represents Ca or Mg, both of which are abundant in natural seawater. During acid cleaning with hydrochloric acid, the reactions occurring are assumed to be:

$$Cu_2O + \tfrac{1}{2}O_2 + 4\ HCl \rightarrow 2\ CuCl_2 + 2H_2O \quad [6.7]$$

$$MOH\ (\text{hydroxides}) + HCl \rightarrow MCl\ (\text{water soluble}) + H_2O \quad [6.8]$$

$$MCO_3\ (\text{carbonates}) + HCl \rightarrow MCl + CO_2 + H_2O \quad [6.9]$$

6.2 Experimental procedure

6.2.1 Materials

Two types of specimens were used in the course of this study. The first series of specimens was composed of 'flag specimens' as shown in Fig. 6.1. They were provided by Metal Samples Inc. and had the chemical composition shown in Table 6.1. Before immersion, all the specimens were wet polished in sequence with 120–240 and 600 grit SiC paper. Electrical wires were soldered on each specimen and shrinkable tubing was used to protect the electrical connection.

A second set of specimens was taken from two heat exchangers (HE) that had been removed from service and shipped to NRLKW after operation. Both were U-bend type heat exchangers. Removal of individual tubes was conducted such that the outer shell was first removed to expose the tube

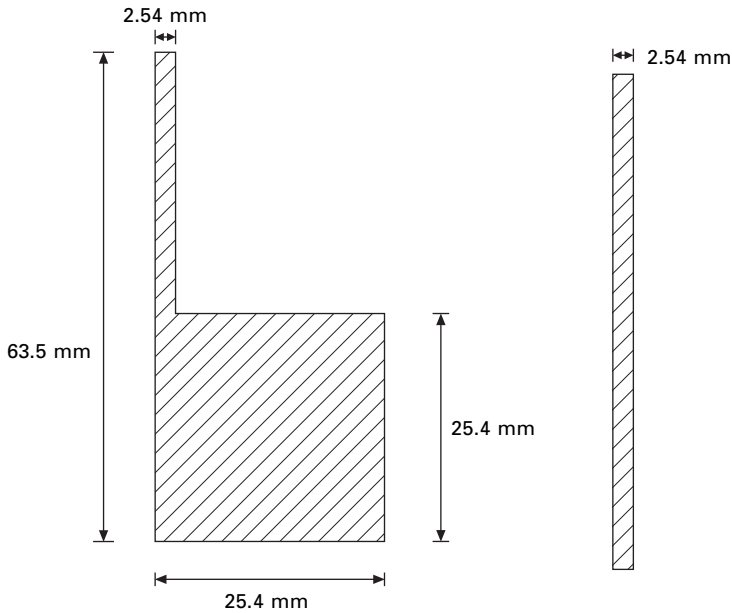

6.1 Flag specimen.

Table 6.1 Chemical composition of flag specimens in percent by weight

	Cu	Ni	Fe	Mn	Zn	C	S
Flag specimens	68.8	29.8	0.665	0.55	0.05	0.015	–
ASTM B111 [12]	Bal	29.0–33.0	0.4–1.0	1.0 max	1.0 max	0.05 max	0.0035

bundles. Two tubes that had apparently experienced different operating conditions were selected, one from each heat exchanger. Tube #1 was taken from an area of HE #1 where corrosion products were clearly visible on the tube sheet as identified in Fig. 6.2. It was then expected that the tube interior

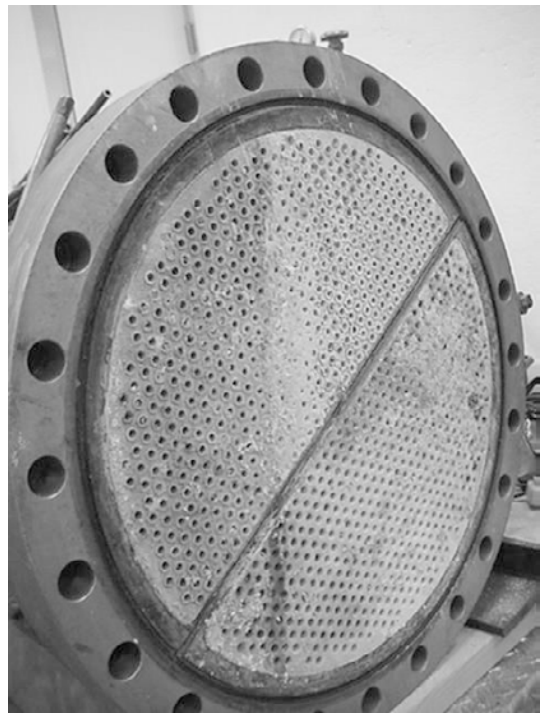

(a)

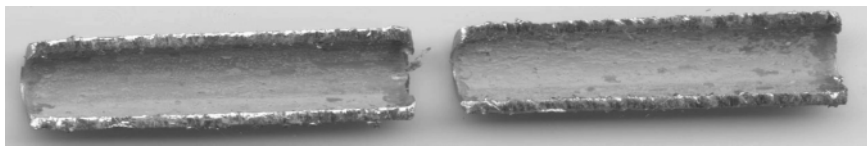

(b)

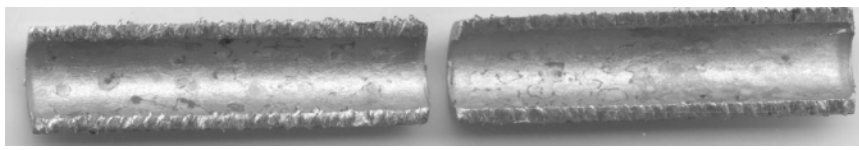

(c)

6.2 Heat exchanger #1 (HE #1) (a), tubes before cleaning (b) and tubes after cleaning according to ASTM G1 [12] (c).

would be covered by corrosion products as well. Corrosion was confirmed by longitudinally sectioning tube #1 as can be seen in Figs 6.2a and b. Both sections revealed localized corrosion-type patterns and patina. The tube sheet of the HE #2 displayed mainly scale (calcareous deposit) with a few embedded shells (Fig. 6.3). A longitudinal section of tube #2 confirmed that scale was present inside the tube. The chemical compositions of the two tubes was determined with a portable X-Ray analysis system and are given in Table 6.2. 20 mm pieces were then cut with a tubing cutter. Electrical wires were soldered on each specimen and the connection masked with a five-minute

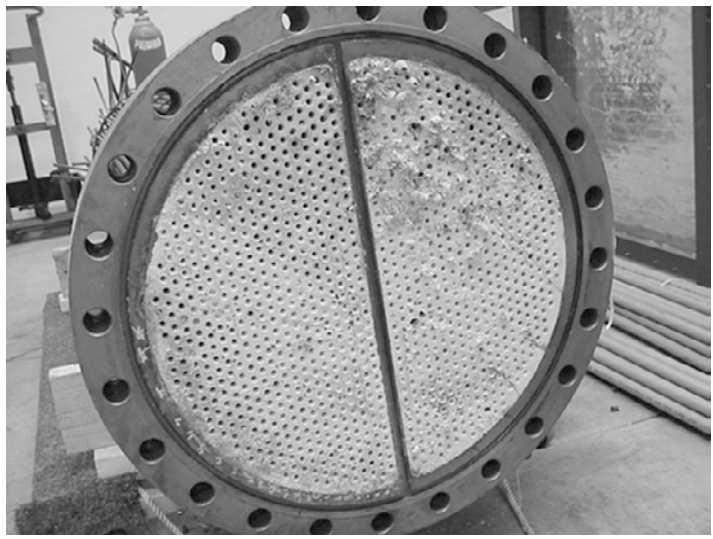

(a)

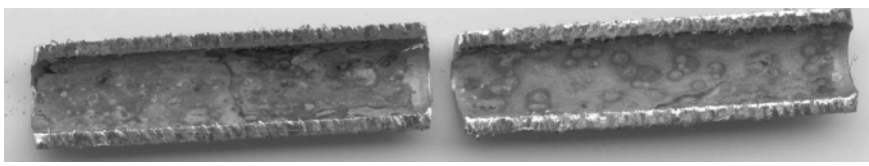

(b)

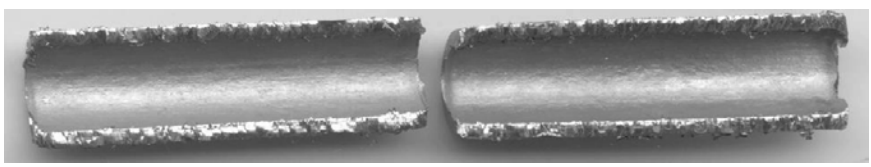

(c)

6.3 Heat exchanger #2 (HE #2) (a), tubes before cleaning (b) and tubes after cleaning according to ASTM G1 [12] (c).

Table 6.2 Chemical composition of HE tubular specimens in percent by weight

	Cu %	Ni %	Fe %	Mn %
Tube #1	69.7	29.3	0.67	0.37
Tube #2	70.7	27.8	0.7	0.58

epoxy resin or a silicone rubber adhesive sealant. The specimens were then coated with a MIL-P-24441 epoxy-polyamide paint. Care was taken to completely protect the edges of the specimens, as any freshly cut bare area would not be representative of service conditions and would greatly influence the electrochemical measurements. So that a fair comparison of the scaled/corroded tubes to the substrate material could be made, some of the specimens were cleaned according to ASTM G1 [13] and were used as control specimens.

6.2.2 Specimen conditioning

The flag specimens were immersed for about 25 days in flowing natural seawater (NSW) in a set of six-liter tanks. Conditioning was performed at ambient temperature seawater in Key West, FL, that is, ranging from 23 to 30 °C.

While most of the specimens were left under open circuit potential during conditioning, two sets of specimens were placed under potentiostatic conditions using a Gamry potentiostat (Fig. 6.4) with the aim of reproducing the wide range of conditions possibly encountered by the materials. The first set was held at –1.0 V vs Ag/AgCl in order to investigate the effect of cathodic protection. The potentials applied to the second set were typically –0.050 V for three days followed by –0.150 V vs Ag/AgCl reference electrode for one day with the intent of promoting corrosion on the specimens that would be

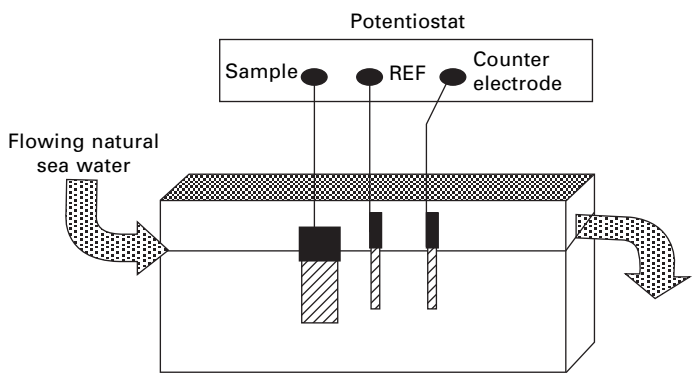

6.4 Experimental setup for potentiostatic conditioning.

later cleaned with the descaling solutions. Additionally, some specimens were galvanically coupled to a nickel-base alloy with a cathode/anode ratio of 35/1.

The tubular specimens taken from the heat exchangers were mounted in a mini-loop as described in Fig. 6.5a and shown in Fig. 6.5b. The velocity was in the range 0.15–0.60 l/min. The temperatures of the seawater and the scale solvent were around 29 and 23 °C, respectively. Seawater was allowed to circulate for four days before cleaning the loop with the scale solvent.

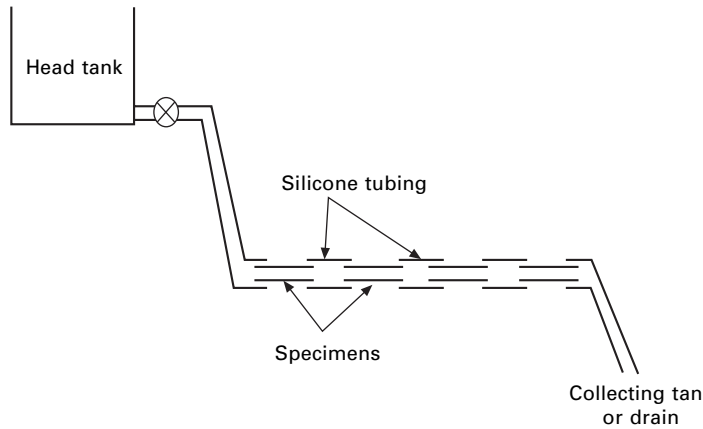

(a)

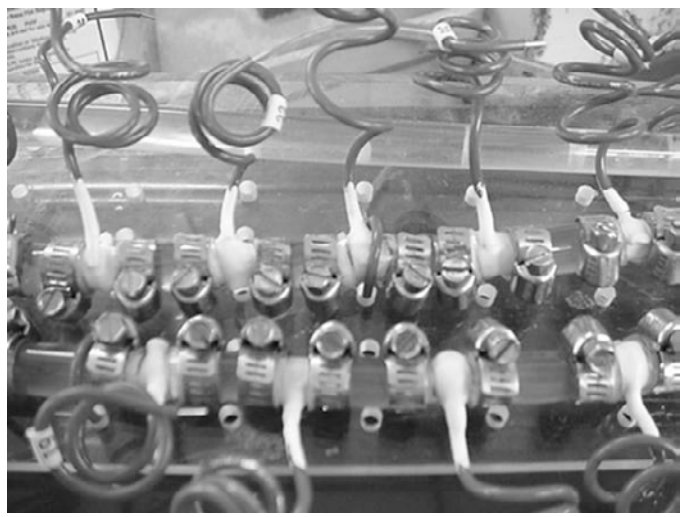

(b)

6.5 (a) Schematic principle of the mini-loop; (b) mini-loop for corrosion testing on HE tubes.

6.2.3 Cleaning procedure

The cleaning procedure for all specimen types was modeled after the procedure given by the US Navy and performed according to the following steps:

- draining of tank or loop;
- rinsing with fresh water;
- addition of descaling solvent at various volume dilutions with fresh water;
- circulation allowed for 5 min every 25 min;
- draining of tank or loop;
- rinsing with fresh water;
- refill with seawater.

The duration of the cleaning varied from 2 to 6 h depending on the aim of each test. A peristaltic pump was used to circulate the descalent in the tanks at a flow rate of 1.6 l/min.

6.2.4 Cleaning solutions

The water scale solutions tested were two hydrochloric acid-based solvents (solvent A and B) and one phosphoric acid-based solvent (solvent C). As the primary purpose was to understand the mechanism of descaling solvents, most of the tests were carried out with solvent A. Comparative tests were later performed on solvents B and C. It must be noted that this work should not be considered as an exhaustive comparison between solvents A, B and C. Unless otherwise stated the descaling products were diluted 50 % by volume with fresh water.

6.2.5 Corrosion testing

Polarization curves

The formation of the protective layer in NSW and the effects of solvent cleaning were investigated by running polarization curves on the CuNi specimens after several periods of exposure. Tests were first performed on control specimens after exposure in quiescent natural seawater for a period of up to 80 days.

To assess the effect of cleaning duration, specimens were gradually removed from the cleaning solution, rinsed in fresh water and placed in NSW for at least 30 min prior to starting a polarization sweep. Similarly, to evaluate the effect of cleaning on repassivation, some specimens were maintained in quiescent seawater for various durations after cleaning. The curves were generated at a scan rate of 0.167 mV/s from the corrosion potential, E_{corr}, to 0.2 V vs Ag/AgCl using a EGG 273 potentiostat controlled by the CorrWare® software (Scribner Associates, Inc., Southern Pines, NC).

Polarization resistance measurements

Linear polarization data were obtained on the tubular specimens by imposing a small amplitude potential of 15 mV around the open circuit potential, E_{oc}. The sweep rate used was 0.05 mV/s. The polarization resistance R_p was taken as the slope of the IV curve near the origin, and calculations of R_p were carried out using the Gamry DCIOS^{TM} Corrosion Techniques Software (Gamry Instruments, Warminster, PA). The corrosion currents were calculated according to the Stern-Geary equation:

$$I_{corr} = \beta_a * \beta_c / 2.303 R_p (\beta_a + \beta_c)$$

where β_a and β_c are the Tafel coefficients for the partial anodic and cathodic reactions, respectively. No direct evaluation of these coefficients has been done and calculations were made with 0.12 V for both β_a and β_c. Faraday's Law was applied to determine the corrosion rate in μm/year.

One of the advantages of using R_p measurements is that it is a non-destructive method as compared to polarization curves. The effect of descaling solutions can therefore be assessed on the same specimen throughout the whole cleaning cycle.

Weight loss measurements

Specimens were weighed before immersion and after cleaning with descaling solvents. Comparisons were made in each case with control specimens. Weight loss measurements were used to estimate the corrosion rates in microns/year (μm/y).

6.3 Results and discussion

6.3.1 Protective film formation

The polarization curves conducted on 70/30 CuNi specimens after various durations of immersion in flowing NSW under free potential are shown in Fig. 6.6. After one hour of immersion in NSW current densities are high, which reflects the behavior of a specimen still actively corroding. Subsequent polarization curves after 24 h, three weeks and 80 days of immersion in NSW show a gradual decrease in current density with time or oxide growth with prolonged immersion.

6.3.2 Effect of descaling solutions on protective film

In order to determine the effects of the descaling solution on the oxide film, cleanings were performed on specimens following immersion in NSW for three weeks. The polarization curves for these are presented in Fig. 6.7.

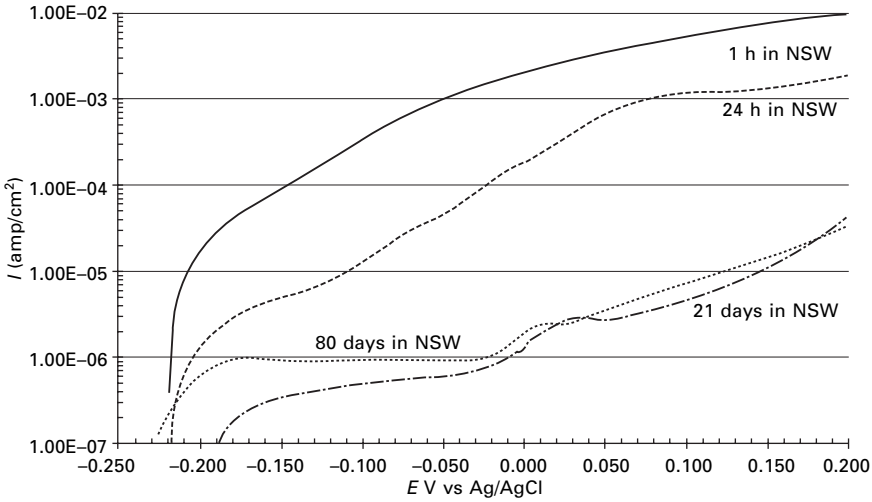

6.6 Anodic polarization curves of 70/30 CuNi immersed in NSW for various periods from 1 h to 80 days.

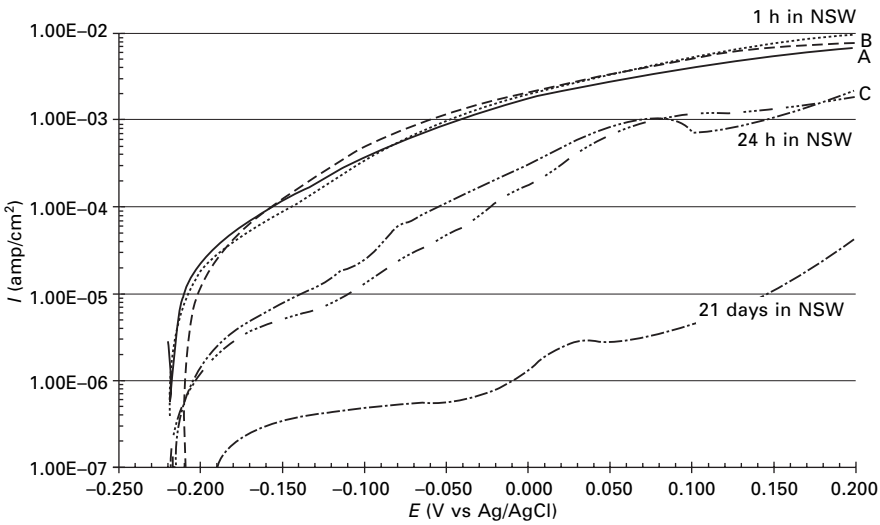

6.7 Anodic polarization curves of 70/30 CuNi after three weeks pre-exposure in NSW and cleaning with solvent A. Polarization curves without cleaning are given for comparison: (A) 5 min cleaning, 1 h re-immersion; (B) 6 h cleaning, 1 h re-immersion; (C) 6 h cleaning, 18 h re-immersion.

These results indicate that the film grown from a three-week exposure to NSW is completely removed for all cleaning durations greater than 5 min and for specimens exposed under free potential, that is, without any significant calcareous deposit. After 5 min in the 50 % descaling solution A and for all subsequent times (for clarity the intermediate cleaning durations are not shown here, but similar results were obtained after 30 mins, 2 and 4 h), the polarization curve exhibited no threshold and the corrosion rate remained comparable to those obtained on 70/30 CuNi specimens after 1 h of immersion in NSW with no cleaning. Similar results were obtained after a 6 h cleaning with solvents B and C as presented in Fig. 6.8.

Additional polarization curves performed on specimens cathodically protected at –1 V vs Ag/AgCl for three weeks and then cleaned with solvent A (Fig. 6.9) indicated that the scale deposited on the specimens was removed and that the behavior of the cleaned specimens was the same as what had been observed on newly immersed samples.

Clearly, a central issue was to determine the ability of 70/30 CuNi to regrow a protective film and to compare any film growth and post-cleaning to those formed on these substrates prior to any descalent cleanings. The results presented in Figs 6.7 (curve C) revealed that 18 h subsequent to a cleaning with solvent A and re-immersion in NSW, a sharp decrease in the corrosion rate occurs similar to that exhibited by a passivated 70/30 CuNi specimen. Given that the cleaned surface behaves similar to a newly immersed 70/30 CuNi surface, the reformation of the protective oxide film of its original

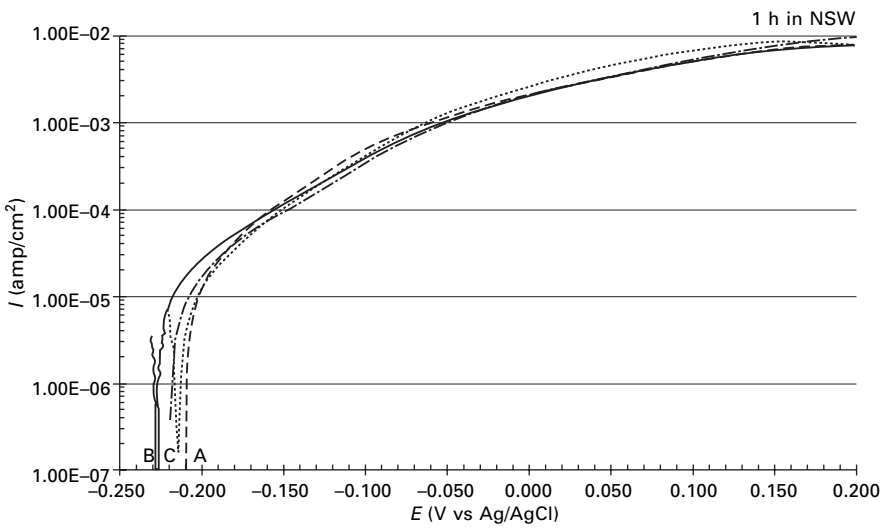

6.8 Anodic polarization curves of 70/30 CuNi after three weeks pre-exposure in NSW, 6 h cleaning, 1 h re-immersion in NSW: (A) solvent A; (B) solvent B; (C) solvent C.

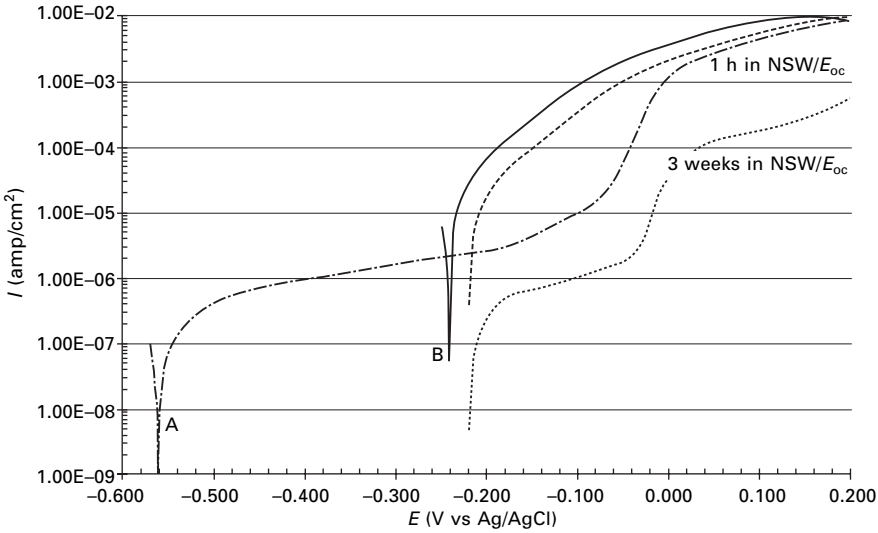

6.9 Anodic polarization curves of 70/30 CuNi after three weeks pre-exposure in NSW at –1 V vs Ag/AgCl; (A) three weeks pre-exposure in NSW at –1 V vs Ag/AgCl; (B) pre-exposure as in (A), 6 h cleaning in solvent A, 1 h re-immersion in NSW.

integrity/protectiveness over the period of three weeks was presumed to occur and was subsequently confirmed as shown by the polarization curve (F) in Fig. 6.10. Specimens cleaned with solvent C exhibited a different behavior as shown in Fig. 6.10 (curves A, B, C, D). Corrosion rates after 21 days of re-exposure in NSW were indeed still high and no threshold was observed on the polarization curves. There is clearly a discrepancy between solvent A and solvent C regarding reformation of the protective film. After cleaning with solvent C (Fig. 6.10 – curve E), 29 days of re-exposure were necessary to obtain a significant threshold (current density around 10^{-6} A/cm^2 from the corrosion potential to –0.050 V vs Ag/AgCl).

6.3.3 Corrosion rate during cleanings

Table 6.3 contains the results of corrosion rate measurements for passivated 70/30 CuNi, that is for specimens immersed in NSW under free potential (around –220 mV after three weeks in NSW) and exhibiting no corroded areas. The corrosion rates of 70/30 CuNi control specimens in quiescent natural seawater were in the range 5–15 µm/y for a 25 days period, which is in good agreement with the literature [11].

The cumulative corrosion rate (NSW pre-exposure + cleaning) of 70/30 CuNi with descaling solution A was determined to be in the range 12–15 µm/y for durations up to 6 h, which is the same as the results given above for

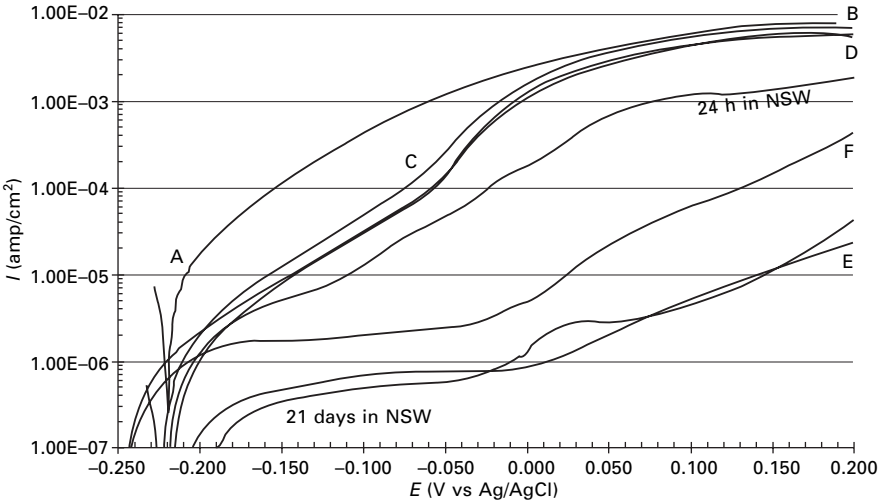

6.10 Anodic polarization curves of 70/30 CuNi after cleaning with solvents: (A) cleaning with solvent C, 24 h re-immersion; (B) cleaning with solvent C, 14 days re-immersion; (C) cleaning with solvent C, 15 days re-immersion; (D) cleaning with solvent C, 21 days re-immersion; (E) cleaning with solvent C, 29 days reimmersion; (F) cleaning with solvent A, 21 days re-immersion. Polarization curves without cleaning are given for comparison after 24 h and 21 days of immersion.

prolonged (25 days) exposure in NSW. Cleaning with solution C led to similar results. Corrosion rates were significantly higher on specimens cleaned with descalent B. As expected, cathodically protected specimens exhibited low corrosion rates. No major difference in weight loss was observed after cleaning with solvent A.

Weight loss measurements during cleanings were also assessed on specimens that had been conditioned under potentiostatic conditions, that is specimens actively corroding in NSW before cleaning. Results presented in Fig. 6.11 showed that cleaning such specimens with descaling solutions had an aggravating effect on 70/30 CuNi. Significant weight losses were noted during the cleaning, reaching values as high as 1 g after 2 h in a 50 % solvent A solution for a 17.5 cm^2 specimen. Results showed that weight losses are a function of the descaling solution dilution, as could be expected. The use of a 25 % solvent A solution led to a weight loss of around 0.6 g after 2.5 h.

These latter observations raise the question of the effect of descaling solution on specimens affected by localized corrosion before cleaning and on specimens possibly suffering from galvanic coupling phenomena. Results of weight loss measurements performed on specimens galvanically coupled to a nickel-based alloy are presented in Table 6.4. When coupled to a nickel-

Table 6.3 Weight loss measurements on 70/30 CuNi

#	Pre-exposure in natural seawater (days)	Descaling agent	Cleaning duration (h)	Initial weight (g)	Final weight (g)	Weight loss (g)	Cumulative corrosion rate (NSW + cleaning) (μm/y)	Weight loss during cleaning (mg)	Corrosion rate during cleaning (μm/y)
F3	26	none	0	36.37077	36.35445	–0.01632	15		
F7	26	A	1 h	35.92221	35.90824	–0.01397	13	2	0
F9	26	A	2 h	36.42045	36.40360	–0.01685	15	–1	280
F10	26	A	2 h	33.73790	33.72296	–0.01494	13	1	0
F13	26	A	6 h	33.99895	33.98521	–0.01374	12	3	0
F14	26	A	6 h	34.81692	34.80273	–0.01419	13	2	0
F22	27	none	0	38.63338	38.62235	–0.01103	10		
F23	27	B	6 h	38.64675	38.51839	–0.12836	111	–117	10918
F24	27	B	6 h	38.66320	38.52933	–0.13387	116	–123	11478
G1	25	none	0	42.11250	42.10690	–0.00560	5		
G2	none	C	6 h	43.49100	43.48790	–0.00310		–3	315
G3	25	C	6 h	41.83210	41.82190	–0.01020	10	–5	467
G4	25	C	6 h	41.57670	41.56730	–0.00940	9	–4	373

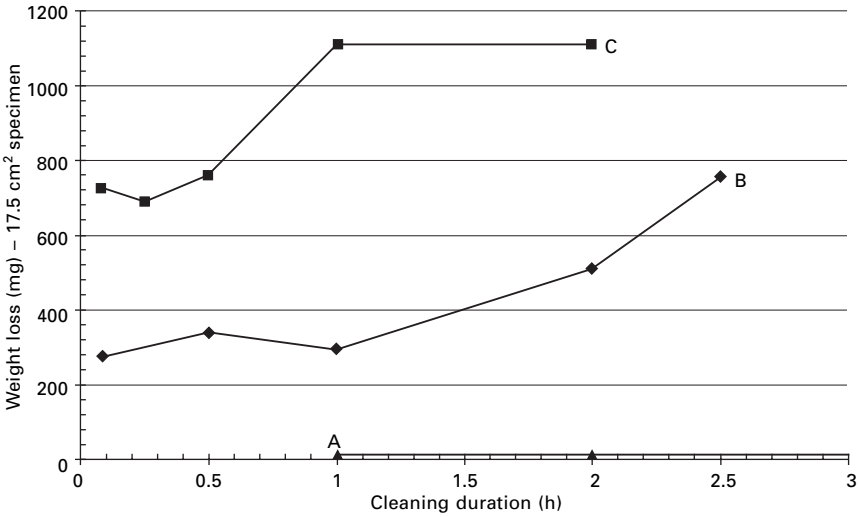

6.11 Weight loss measurements on 70/30 CuNi specimens during cleaning with solvent A: (A) specimens after three weeks pre-exposure in NSW (no conditioning), cleaning with a 50 % solution; (B) specimens conditioned at –50 mV then –150 mV, cleaning with a 25 % solution; (C) specimens conditioned at –50 mV then –150 mV, cleaning with a 50 % solution.

based alloy for 25 days and subsequently cleaned with solvent A, specimens displayed significantly higher weight losses than the control specimen, as may have been anticipated from the potentiostatic results discussed above. On further examination, such effects can be considered as not being critical considering the durations and the frequency of the cleaning usually involved (a weight loss of 1 g per cleaning would lead to a 60 µm thickness loss). However, care should be taken when prolonged or frequent cleanings are used. Moreover, the effect of such cleanings on complex geometries has not been taken into account and should be considered, especially when crevice corrosion phenomena are encountered.

6.3.4 Overall results

Based on the results obtained on laboratory-conditioned specimens, copper contents found during actual cleaning in effluents solutions can be explained by (i) the removal of the protective film and (ii) a detrimental action of the descalent on the substrate of heat exchangers. Under completely satisfactory operating conditions, namely building of the oxide film in aerated seawater, results have shown that 50 % descalent solutions had no lasting effects during cleaning. The major drawback linked with the use of descalent is that after cleaning, piping should be considered as newly immersed and without

Table 6.4 Weight loss measurements on 70/30 CuNi when galvanically coupled with a nickel-based alloy (cathode/anode ratio: 35/1)

#	Pre-exposure in natural seawater (days)	Descaling agent	Cleaning duration (h)	Initial weight (g)	Final weight (g)	Weight loss (g)	Cumulative corrosion rate (NSW + cleaning) (µm/y)	Weight loss during cleaning (mg)	Corrosion rate during cleaning (µm/y)
28	25	none	0	34.25535	34.20719	–0.04816	55		
27	25	A	6 h	30.59803	30.52820	–0.06983	83	–22	2603
29	25	A	6 h	31.36315	31.29050	–0.07265	85	–24	2820

a protective oxide film. Consequently, immediately after cleaning, normal operating conditions should be carefully followed in order to rebuild a sufficiently protective oxide film or scale.

6.3.5 Cleaning of actual heat exchanger specimens

Figure 6.12 shows the anodic polarization curves of specimens taken from HE #1 and HE #2 left in their original condition as well as a control specimen re-immersed for four days in NSW. These curves confirm the results of the visual examination. Presence of corroded areas on HE #1 has been evidenced by higher current densities with no passive-type threshold as well as a shift in potential as compared to HE #2 and the control specimen. Current densities on HE #2 are low (curve B) owing to the presence of a significant scale deposit. When cleaned for 6 h with solvent A, all the specimens displayed a similar response no matter what their previous condition was (D, E, F), and polarization curves obtained after cleaning are in good agreement with the results obtained on laboratory-conditioned specimens.

In order to demonstrate the real effect of the descaling solution on each HE, representing different operational conditions, individual comparisons are made for each HE in Figs 6.13 and 6.14. Polarization curves were carried out on specimens left in the mini-loop for 16 days after cleaning. On HE #1, a shift in potential toward –0.22 V vs Ag/AgCl was observed as well as a decrease in the anodic current. On HE #2, anodic currents are higher after 16 days than the original level before cleaning. However, it should be emphasized

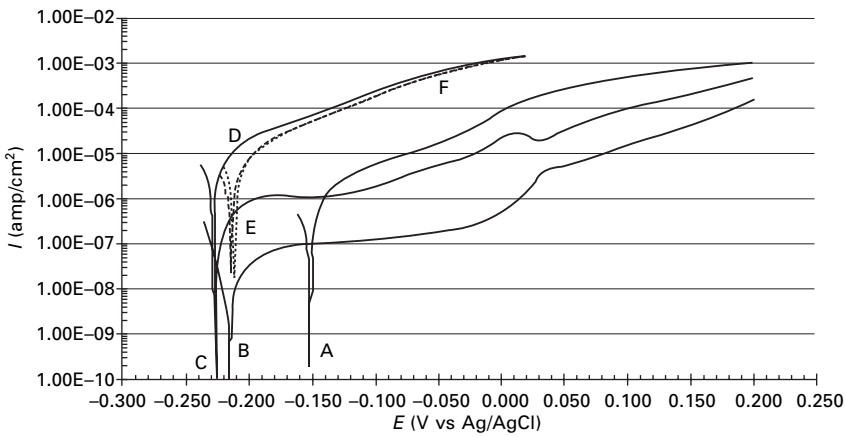

6.12 Anodic polarization curves of tubular HE specimens; (A) HE#1 after four days re-immersion; (B) HE#2 after four days re-immersion; (C) control specimens after four days re-immersion; (D) HE#1 after a 6 h cleaning with solvent A; (E) HE#2 after a 6 h cleaning with solvent A; (F) control after a 6 h cleaning with solvent A.

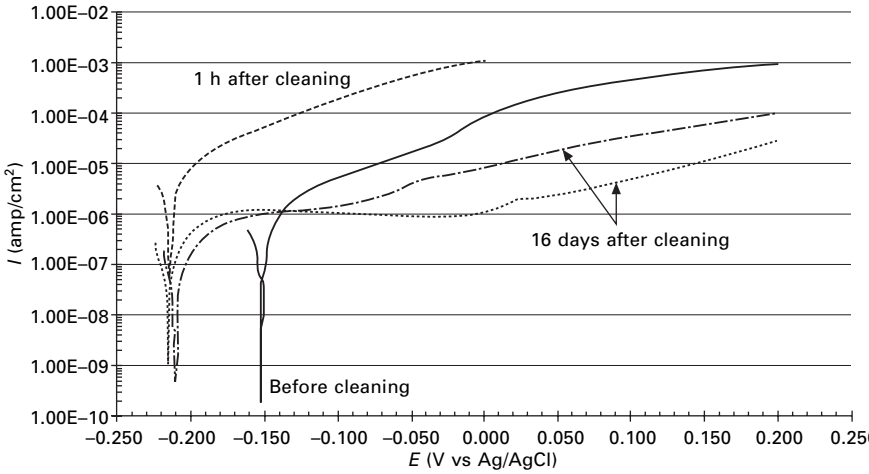

6.13 Anodic polarization curves of tubular specimens taken from HE#1 (HE with corroded areas).

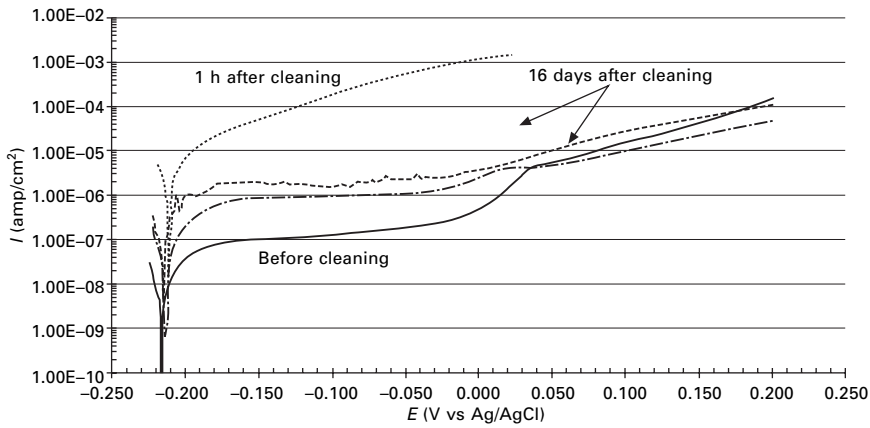

6.14 Anodic polarization curves of tubular specimens taken from HE#2 (scale).

at this point that HE specimens mounted in the mini-loop were not cathodically protected. For that reason no deposition of protective calcareous deposit was possible.

As shown in Fig. 6.15, all the cleaned specimens displayed a similar behavior after a 16 days period of exposure in NSW, whether or not they suffered from corrosion before cleaning. Cleaning with descaling solutions could then be considered as a way of restoring pipings by eliminating localized corrosion areas. Comparisons with control non-cleaned specimens after 16 days in NSW indicate that there is no apparent detrimental effect on the repassivation of 70/30 CuNi in NSW when cleaned with solvent A.

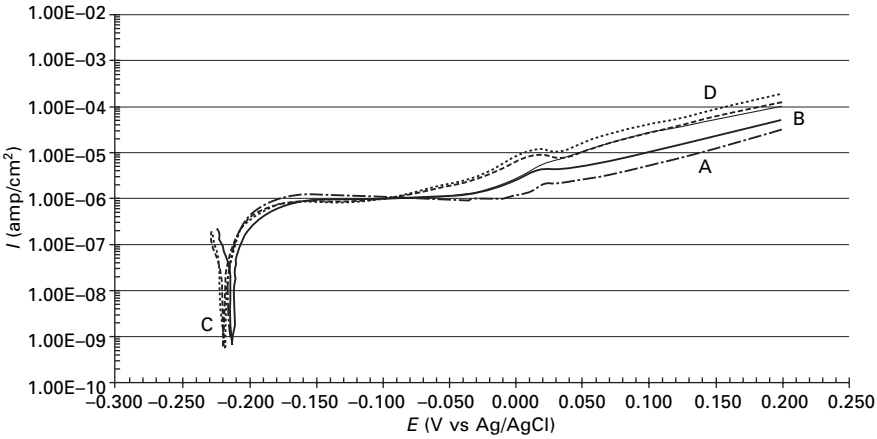

6.15 Anodic polarization curves of tubular HE specimens: (A) HE#1 after 6 h solvent A cleaning, re-immersion in NSW for 16 days; (B) HE#2 after 6 h solvent A cleaning, re-immersion in NSW for 16 days; (C) control specimens after 6 h solvent A cleaning, re-immersion in NSW for 16 days; (D) control specimens after 16 days.

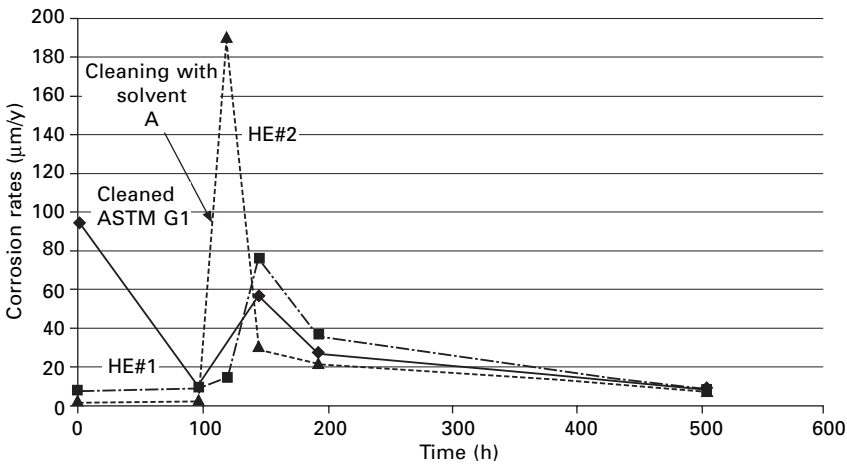

6.16 Estimated corrosion rates based on R_p measurements throughout the cleaning procedure on HE#1, HE#2 and a control specimen.

Data obtained with linear polarization measurements are in complete agreement with the results presented above (Fig. 6.16). Corrosion rates calculated with R_p results before cleaning were higher on the specimens taken from HE #1 than on specimens taken from HE #2. After 16 days in NSW, equal corrosion rates were found for non-cleaned control specimens

and solvent-cleaned specimens. Again, after cleaning similar results were obtained on HE #1 and HE #2.

6.4 Conclusions

The tests carried out on both laboratory-conditioned specimens and specimens taken from actual heat exchangers have shown that:

- Assuming a naturally formed oxide film is in place on seawater heat exchangers, cleaning with 50 % descaling solution (solution A and B) over a 6 h period, results in no higher a corrosion rate afterwards than would otherwise exist in NSW upon initial immersion (in the range 5–15 μm/year).
- The protective oxide film was removed during the cleaning procedure. In all samples tested, the oxide was removed in the first 5 min of cleaning.
- After cleaning, when seawater was allowed to recirculate in tubing, copper–nickel behaves similarly to a newly immersed substrate. Repassivation of 70/30 CuNi should occur in flowing NSW for a minimum of three weeks.
- Cleaning with 50 % solvent did not preclude the repassivation process of 70/30 CuNi and consequent low corrosion rates due to oxide film formation.
- Corrosion of the 70/30 CuNi substrate can be observed during cleaning on corroded areas or in the absence of a protective film and when galvanic coupling phenomena are encountered. However, considering the durations and frequency of cleanings involved, these results are not considered critical. Cleaning durations should be kept as short as possible.
- Use of descaling agents could be beneficial on systems displaying corrosion before cleaning and help restore materials to their original conditions. Such cleanings should be followed by a minimum of three weeks of operation under flowing NSW.
- Presence of sulphide-polluted zones before cleaning has not been taken into account in the course of this work. The question remains as to whether or not commercial descaling solutions would help in completely removing sulphide-induced corroded areas and restoring the normal protectiveness of CuNi in NSW.

6.5 Acknowledgements

The authors gratefully acknowledge the efforts of Jean Pierre Pautasso of DGA, Direction des Systemes d'Armes, for initiating the French/US Scientist exchange (DEA 5645), which significantly enhanced this research effort.

6.6 References

1. D.D. MacDonald, B.C. Syrett, S.S. Wing, 'A Study to Determine the Mechanisms of Corrosion of Copper–Nickel Alloys in Sulphide-Polluted Seawater', Annual report 2nd Feb. 1944–1st Feb. 1978, SRI project No. PYU 6077 under ONR Contract No. N00014-77-C-0046, Menlo Park, CA, SRI International.
2. B.C. Syrett, S.S. Wing, *Corrosion*, 1980, **35** (2),
3. L.E. Eiselstein, B.C. Syrett, *Corr. Sci.*, 1983, **23** (3), 223–239.
4. J.N. Al-Haji, M.R. Reda, *Corr. Science*, 1993, **34** (1), 163–177.
5. A.M. Beccaria, *Corr. Sci.*, 1991, **32** (11), 1263–1275.
6. 'Velocity Design Criteria for 90.10 CuNi Seawater Piping', Technical Instruction 520-714, 30 November 1987, prepared by Westinghouse Electric Corporation under NAVSEA contract N00024-86-C-4030.
7. B. Buecker, *Mater. Perform.*, January 2001, 52–55.
8. L.D. Hulett *et al*, *J. Electron. Spect. Related Phenomena*, 1973, 169–178.
9. K.D. Efird, *Corrosion*, 1975, **31** (3), 77–83.
10. J. Mathiyarasu, N. Palaniswany, V.D. Muralidharan, *Corrosion Reviews*, 2000, **18** (1), 65–103.
11. T. Rostan, *Soudage et Techniques Connexes*, 1990, **44** (11–12), 9–28.
12. ASTM B111/M-04: Standard Specification for Copper and Copper-Alloy Seamless Condenser Tubes and Ferrule Stock, West Conshohocken, PA, American Society for Testing and Materials.
13. ASTM G1-03: Standard Practice for Preparing, Cleaning, and Evaluating Corrosion Test Specimens, West Conshohocken, PA, American Society for Testing and Materials.

Part III

Aluminium bronzes

7

Long-term and accelerated corrosion testing methods for cast nickel–aluminium bronzes in seawater

R. S. OAKLEY, J. C. GALSWORTHY and G. S. FOX, QinetiQ Ltd, UK; K. R. STOKES, Defence Science and Technology Laboratory, UK

7.1 Introduction

Copper-based alloys are widely used in marine engineering and on board ships for pipework systems that carry seawater supplies, typically for cooling purposes. These materials offer a good combination of strength, toughness, antifouling properties and corrosion resistance at reasonable cost for many applications [1,2]. For higher strength and corrosion resistance, aluminium bronzes are commonly selected. Cast nickel–aluminium bronze (NAB) finds wide application in naval vessels, being of a Cu-10 % Al-5 % Ni-5 % Fe formulation, with a general corrosion rate of 0.06 mm/year [3] and high resistance to cavitation and impingement erosion damage.

NAB is a complex alloy with several intermetallic phases. The generally agreed phases present in the cast materials are:

- α: copper-rich solid solution;
- β: retained high-temperature phase, which can be converted to α and κ phases by post-casting heat treatment: 675 °C for 6 h;
- κ_I: a rosette, iron-rich form (based on Fe or Fe_3Al), which is rarely found in NAB castings with the correct thermal history and iron content;
- κ_{II}: a spherodised precipitate formed at the grain boundary (based on NiAl–FeAl);
- κ_{III}: commonly referred to as lamellar κ (composition varying from NiAl to FeAl);
- κ_{IV}: a fine, needle-like, iron-rich phase (again based on Fe_3Al) formed within the α grains, becoming more densely distributed after heat treatment.

Figure 7.1 presents the phases normally found in heat-treated NAB castings to naval standards, where no κ_I is found and any retained β phase has been removed by the heat treatment.

Problems have been encountered with degradation of the alloy through the action of selective phase corrosion [4], where preferential corrosion of the κ_{III} lamellar intermetallic phase results in the loss of mechanical strength

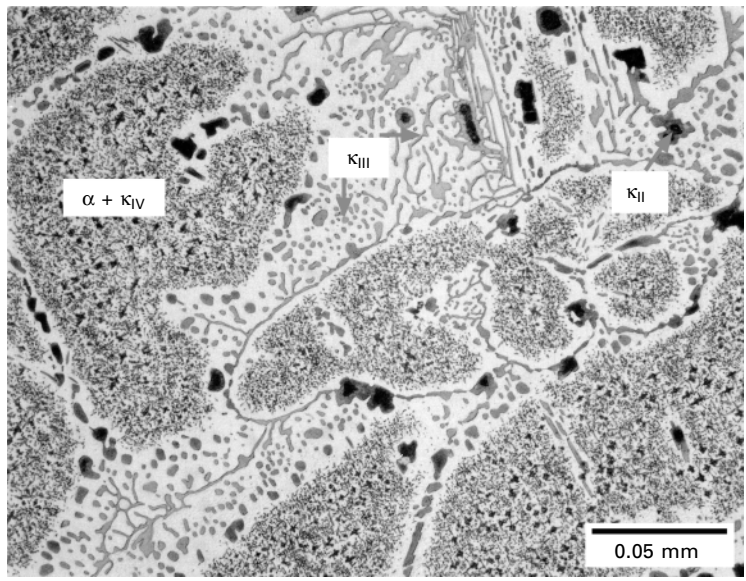

7.1 Phases typically present in microstructure of cast and heat-treated NAB.

from areas of the alloy so affected. Previous studies have used long-term seawater immersion to investigate the effectiveness of post-casting heat treatments on the selective phase and general corrosion of NAB [5,6] which, although realistic, are restricted in the temperature and seawater chemistry obtainable at a single test site and do not provide rapid results to evaluate specific changes in alloy metallurgy or the corrosivity of the environment. Faster evaluation of the seawater corrosion behaviour of NAB is required and therefore electrochemical evaluation methods previously successfully applied to studies of stainless steel corrosion were considered for application to NAB.

7.2 Experimental procedures

Long-term corrosion testing was carried out by immersing 75 × 100 × 6 mm NAB plates (of wt% composition Cu-10.6Al-5.25Ni-4.3Fe-1.2Mn) fitted with 50 mm diameter flat continuous plateau Perspex crevice formers. These were placed in tanks of circulated, filtered seawater extracted from Portland Harbour, Dorset, UK (an unpolluted, full-salinity coastal seawater), with the water replenished at regular intervals. These tanks were controlled at temperatures of 20 or 40 °C for periods of up to 12 months, with samples removed for mass loss and depth of corrosion measurements periodically. A separate immersion test of 24 months was carried out in a covered plastic

trough with a filtered flowing seawater supply from Portland Harbour (see Fig. 7.2 for temperature and salinity of this seawater), which was passed once through the system at a velocity of approximately 0.1 m/s.

These immersion samples were evaluated for mass loss after cleaning with 50 % hydrochloric acid as described in ASTM G1 [7] and by measurement of the depth of any surface pitting or crevice corrosion using a Talysurf surface profilometer (Taylor Hobson Ltd, Leicester, UK) modified for a maximum deflection range of several millimetres. Metallographic sections were prepared from selected samples to establish any presence of selective phase corrosion.

To provide short-term data to compare with the long-term immersion trials, polarisation measurements of NAB were made according to ASTM G5 [8], using a potential scan rate of 10 mV/min applied to 44 mm diameter samples freshly ground with 600 grit SiC paper, and acetone degreased. Scans were carried out using an ACM GalvoGill 12 (ACM Instruments, Grange-over-Sands, UK) in the anodic direction until a limiting anodic current density of 500 μA/cm^2 was achieved. The polarisation scans were carried out at 10, 20, 35 and 45 °C in Portland Harbour seawater, and Tafel extrapolation of the anodic curve was used to estimate values of corrosion current i_{corr}. These values were converted to physical rates of corrosion using Faraday's Law and an equivalent weight for NAB of 37.81 g, based on the univalent dissolution of copper in seawater and the alloy equivalent weight calculation method set out in ASTM G102 [9].

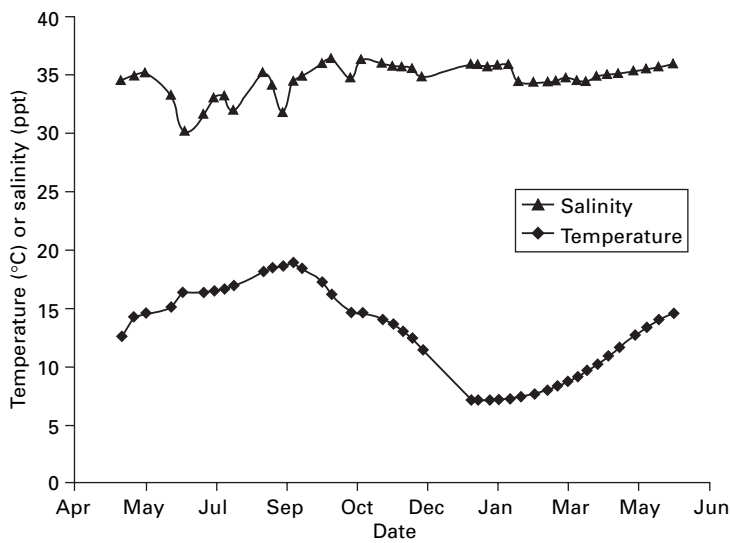

7.2 Temperature and salinity variations of Portland Harbour seawater in once-through system over typical year.

An estimation of the potentiostatic critical corrosion temperature of cast NAB was measured using a modification of a thermocyclic method previously used to study the behaviour of super-austenitic stainless steels [10]. The tests employed 25 × 40 × 6 mm samples, with an electrical contact made to the sample via a waterproofed screw connection to a plastic sleeved brass rod, minimising possible crevice corrosion sites. These were immersed in aerated seawater at 10 °C without an applied potential for 30 min, so that a stable open circuit potential could develop. After this potential stabilised, a test potential of –150 mV was applied, replicating the maximum potential likely to be attained by NAB in seawater. At least 30 min was required for the corrosion current to reach a stable value. The temperature was then increased at 20 °C/h and the corrosion current monitored. A sharp increase in the corrosion current would indicate the critical temperature for aggressive local corrosion in stainless steels, although the response of the copper alloy was initially unknown.

7.3 Results and discussion

7.3.1 Seawater immersion testing

The mass loss and depth of corrosion results for cast NAB in recirculating tanks of Portland Harbour seawater (Table 7.1) show moderate levels of general corrosion at 20 °C. Significant crevice corrosion occurred on some samples, up to 360 µm deep after 12 months, but was absent in other samples immersed for similar periods. This crevice corrosion occurred outside the perimeter of the Perspex crevice former, in agreement with the metal ion concentration model for crevice corrosion of copper alloys. An increase in seawater temperature to 40 °C led to the formation of a soft, pale, calcareous deposit on the metal surface, with a significant reduction in the corrosion rate and the elimination of localised pitting or crevice corrosion. Small areas of selective phase corrosion of up to 310 µm in depth were identified after 12 months at 20 °C, but none at 40 °C.

In contrast, immersion in once-through ambient flowing seawater produced samples with adherent green/brown corrosion deposits and much greater general and local corrosion than in recirculated seawater at similar temperature. Corrosion of the NAB accelerated significantly after three months of immersion and then stabilised after 12 months, associated with the building up of a layer of corrosion products and marine sediments. Crevice corrosion up to 580 µm in depth was observed around the Perspex crevice former, and also under areas of thick corrosion deposits. Areas of selective phase corrosion of between 350 and 500 µm deep were found under such creviced areas on several of the samples after extended periods (≥ 12 months) of immersion. This may indicate that the formation of thick surface deposits on the NAB samples is a prerequisite

Table 7.1 Corrosion mass loss and corrosion depth results for NAB during immersion in re-circulated and once-through seawater at different temperatures

Immersion conditions	Time (months)	Corrosion mass loss (mg/cm^2)	Uniform depth of corrosion (μm)	Max. depth of crevice corrosion (μm)
Recirculated (20 °C)	3	0.91, 1.15	1.2, 1.5	0, 0
	6	1.48, 1.54	1.9, 2.0	40, 0
	12	3.76, 7.26	4.9, 9.6	360, 0
Recirculated (40 °C)	3	0.3	0.4	0
	6	0.68	0.9	0
	12	0.62	0.8	0
Once-through (7–19 °C)	3	4.51, 4.85	5.9, 6.4	20, 40
	12	27.75, 36.72	37, 48	540, 580
	24	31.98, 38.16	42, 50	500, 480

for selective phase corrosion, and that this attack continues after general mass loss has been stifled by the accumulation of corrosion products.

7.3.2 Accelerated electrochemical tests

Polarisation scans of cast NAB in Portland Harbour seawater at differing temperature (10–45 °C, Fig. 7.3) showed that the corrosion potential (E_{corr}) values become more anodic with increasing temperature. The presence of an anodic peak at temperatures above 20 °C was indicative of a passivation mechanism which was absent at lower temperatures. Estimation of the corrosion current i_{corr} by Tafel extrapolation of the anodic curves (Table 7.2) produced general corrosion rates similar to those determined in long-term once-through seawater testing (up to 48 μm/y), but did not replicate the increase in NAB passivation observed from the polarisation curves or the low corrosion mass loss recorded when immersed in seawater at 40 °C.

The thermocyclic test method used to establish critical corrosion temperature produced a very high initial corrosion current density (500 μA/cm^2) from a freshly ground NAB sample, which reduced as the temperature of the seawater was increased with time (Fig. 7.4). When the temperature curve was reversed, much lower final current densities were observed, suggesting that significant passivation of the NAB surface had occurred at the elevated temperatures, as previously suggested by the polarisation scans.

When the thermocyclic test was repeated on a sample which had been previously tested at up to 70 °C, the passive film formed resulted in a much lower initial corrosion current density (< 0.1 μA/cm^2). Further increase and decrease of the test temperature resulted in a near linear and reversible increase and decrease in the corrosion current (Fig. 7.5), suggesting that the

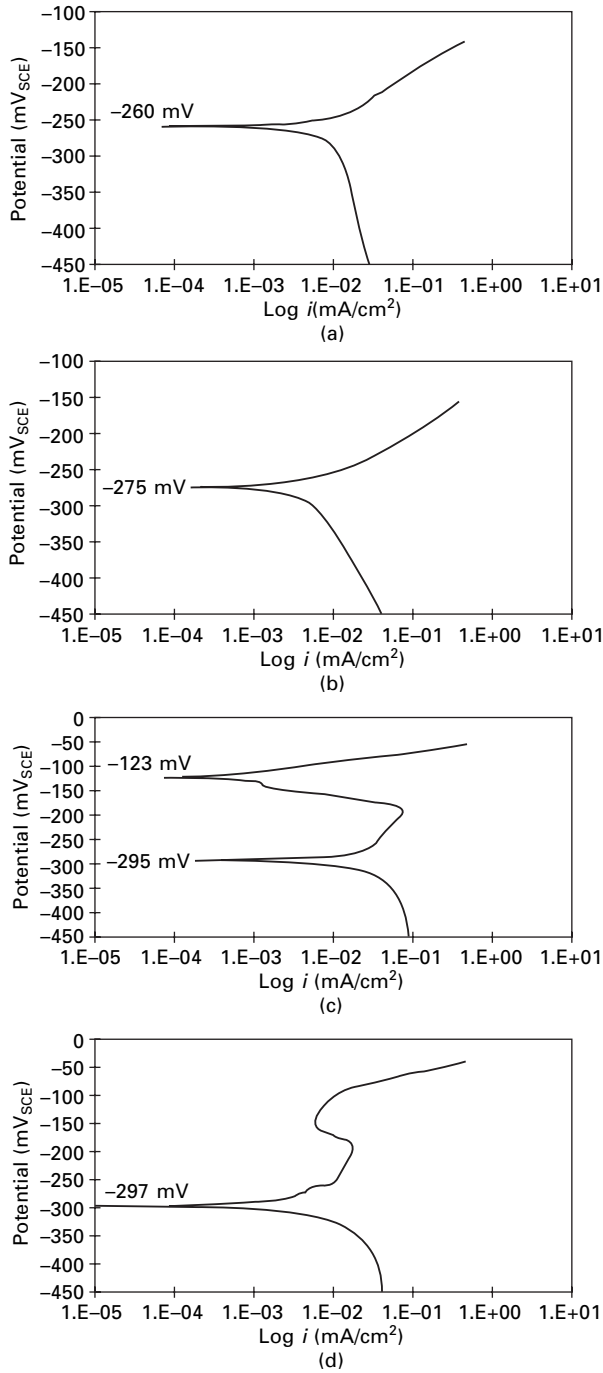

7.3 Polarisation curves for NAB at (a) 10 °C, (b) 20 °C, (c) 35 °C and (d) 45 °C.

Table 7.2 Quantitative electrochemical data from polarisation of NAB in seawater at increasing temperature

Temperature (°C)	E_{corr} (mV_{SCE})	i_{corr} ($\mu A/cm^2$)	Corrosion rate (μm/y)
10	–260	3	48.8
20	–275	5	81.3
35	–295	4	65.0
45	–297	3	48.8

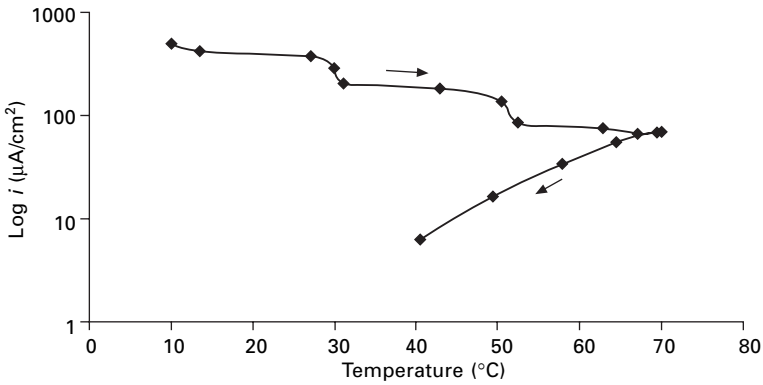

7.4 Thermocyclic curve at –150 mV for freshly ground NAB sample. Arrows indicate direction of temperature cycle.

passive film on the copper alloy had achieved some degree of stability. As the measured corrosion current did not decrease with increasing temperature, as seen with the freshly prepared NAB surface, it may be inferred that there was little further growth of the surface film after the initial period in hot seawater.

While the protective properties of the NAB passive film were reduced at elevated seawater temperatures (indicated by the increasing corrosion current), no sharp increase in corrosion activity associated with irreversible failure of the film occurred. In comparison, the localised failure of the passive film of stainless steels in chloride-containing solutions at elevated temperature had previously been found to result in the formation of small anodic pitting areas that caused a rapid increase in corrosion current and so provided an identifiable critical corrosion temperature. A critical temperature threshold was not found for NAB, implying that different mechanisms are active in the corrosion process. The protective properties of films formed on NAB in warm chloride-containing solutions have previously been noted [11] and the film identified as an aluminium-rich layer within the Cu_2O corrosion product film typically produced by copper alloys in seawater.

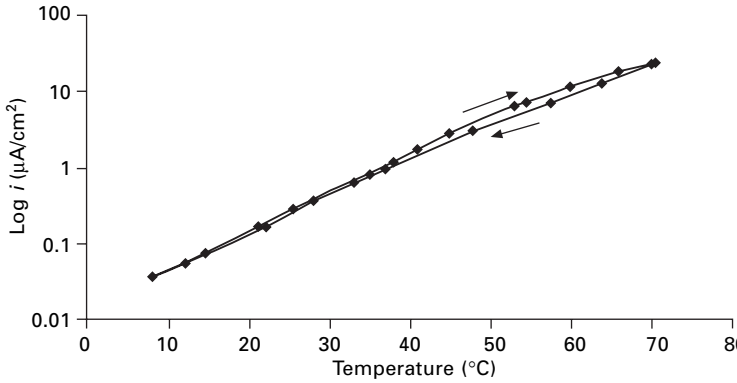

7.5 Thermocyclic curve at –150 mV for pre-exposed NAB sample. Arrows indicate direction of temperature cycle.

7.4 Conclusions

- The formation of adherent corrosion and marine sediment deposits in the once-through flowing seawater immersion trial increased the severity of pitting, and crevice and selective phase corrosion compared with immersion in a recirculated seawater tank at 20 °C. Determination of the corrosion rate of NAB in realistic seawater applications must reflect this importance of surface films and deposits.
- Polarisation scans at increasing seawater temperatures identified anodic peak features at 35 and 45 °C that may be associated with passivity of the NAB surface at these temperatures. This hypothesis agreed with the observed reduction in NAB corrosion attack when immersed in seawater at 40 °C compared to 20 °C.
- Tafel extrapolation of the anodic polarisation scans produced quantitative estimates of corrosion rate that were similar to those observed for low-temperature flowing seawater immersion but did not replicate the increased passivation of NAB observed at higher seawater temperatures.
- Thermocyclic testing of NAB was complicated by the passivating effects of increasing seawater temperature. Accelerated corrosion test methods devised for stainless steels require modification before application to copper alloys, due to the differences in anodic behaviour, especially at elevated seawater temperatures.
- Possible opportunities for improved accelerated tests may combine electrochemical methods with specific chemical test solutions that replicate the composition of the surface deposits formed on copper alloys in long-term seawater immersion service.

7.5 Acknowledgements

The authors wish to thank the UK Defence Procurement Agency Sea Technology Group for their financial support of this work.

7.6 References

1. A. Tuthill, *Mater. Perform.*, **26** (9) (1987) 12–22.
2. P. Gilbert, *Mater. Perform.*, **21** (2) (1982) 47–53.
3. 'Aluminium Bronze Alloys Corrosion Resistance Guide'. Potters Bar, UK, Copper Development Association, (1981).
4. C. Zanis, R. Ferrara, *Trans American Foundrymans Society*, **53** (1974) 71–78.
5. E. Culpan, G. Rose, *Br. Corr. J.*, **14** (3) (1979) 160–166.
6. J. Rowlands, Studies on the preferential phase corrosion of cast nickel aluminium bronze in seawater, Proc 8th International Congress on Metallic Corrosion, Mainz, September, 1981, 1346–1351.
7. ASTM G1-03: Standard Practice for Preparing, Cleaning, and Evaluating Corrosion Test Specimens, West Conshohocken, PA, American Society for Testing and Materials.
8. ASTM G5-94 (2004): Standard Reference Test Method for Making Potentiostatic and Potentiodynamic Anodic Polarization Measurements, West Conshohocken, PA, American Society for Testing and Materials.
9. ASTM G102-89(2004)e1: Standard Practice for Calculation of Corrosion Rates and Related Information from Electrochemical Measurements, West Conshohocken, PA, American Society for Testing and Materials.
10. U. Steinsmo, T. Rogne, J. Drugli, *Corrosion,* **53** (12) (1997) 955–964.
11. A. Schüssler, H. Exner, *Corr. Sci.* **34** (11) (1993) 1793–1802.

8

Galvanic corrosion of nickel–aluminium bronze coupled to titanium or Cu-15Ni alloy in brackish seawater

R. C. BARIK, J. A. WHARTON and R. J. K. WOOD,
University of Southampton, UK; K. R. STOKES,
Defence Science and Technology Laboratory, UK

8.1 Introduction

This investigation aims to study the corrosion performance of both coupled and uncoupled nickel–aluminium bronze (NAB) in seawater over a three-year period, an area where few data exist, especially with regard to the influence of surface deposits and biofouling. In-service combinations of NAB endplates (tubesheets) and titanium tubes within heat exchangers have produced significant accelerated corrosion of the NAB. Studies have shown that the effective cathode area is an important consideration, with severe corrosion occurring in situations when the cathode to anode ratio has approached 1000:1 [1]. However, negligible acceleration corrosion rates have been reported where the effective cathode area is not greatly in excess of that of the NAB anode area [2]. Similarly, copper–nickel alloys are widely used for seawater piping where they are often directly coupled to NAB, although the alloy used in this work is more representative of bolting material. Analysis of the immersion site showed that the seawater was brackish in nature and not necessarily representative of open seawater. Under operational conditions it is also unlikely that 1:1 area ratios would be found or that the alloys would be exposed to direct sunlight.

8.2 Background

The corrosion resistance of copper-based alloys in seawater is determined by the nature of the protective oxide film [3]. Initially, cuprous oxide (Cu_2O) is the most stable oxide formed in seawater on immersion [4,5]; however, as the oxide film thickens a transformation occurs of Cu_2O to cupric oxide (CuO) [5,6]. After prolonged seawater exposure a green corrosion product, cupric hydroxychloride [atacamite, $Cu_2(OH)_3Cl$)], is also formed [1,6]. For copper–nickel alloys, the protective nature of the film increases with time and is improved by the presence of nickel and iron within the film. Similarly, the protective oxide films on NAB are considered to reduce the corrosion

rate by a factor of 20–30 [7]. The oxide layer is aluminium-rich adjacent to the base metal and richer in copper in the outer regions. There are also oxides of nickel and iron, together with trace amounts of copper salts and copper hydroxychlorides, e.g., $Cu_2(OH)_3Cl$ and Cu(OH)Cl, which form after longer exposure times to seawater. Passivation has been attributed to a decrease in ionic transport across the aluminium-oxide-rich inner layer, in addition to the rate of oxygen reduction decreasing during the development of the protective film surface [7,8].

Galvanic corrosion is one of the most common and damaging forms of corrosion. It occurs when two dissimilar metals or alloys are in electrical contact in an electrolyte, resulting in accelerated corrosion of the more electrochemically active of the two metals. It is the generally accepted view that there is little acceleration of corrosion when two copper-based alloys are galvanic coupled [2]. Likewise, titanium is often coupled with copper-based alloys despite being much more electropositive, a combination which can work because titanium is not a very efficient cathode for reducing oxygen [9].

Galvanic corrosion becomes a more complex process in seawater that supports the growth of biofilms [10], i.e. the colonisation and the subsequent development of microorganism clusters, together with the extracellular polymeric substances (EPS) [11]. An entire dynamic system is formed at the biofouled/solution interface that is governed by different transport processes taking place through the biofilm [12]. Copper-based alloys are more resistant to the attachment of biofouling organisms than most other metals due to the toxicity of copper-ion release within the protective oxide film although, when coupled to more active metals, the release is greatly reduced, hence biofouling becomes similar to that observed with other metals. Ennoblement of passive metals as a result of biofilms is also well-documented and occurs at all salinities on a range of metals and alloys including stainless steels and titanium. A biofilm on a titanium surface is considered to catalyse the cathodic reduction of oxygen, thereby increasing the cathodic efficiency and thus accelerating the corrosion rate of the anode component [9,13].

There are numerous reports describing a shift in the corrosion potential of different metals in the positive direction when exposed to natural waters [e.g. 14,15]. This ennoblement has been related to the growth of aerobic microbial biofilms, although the mechanism governing the process is still subject to much debate. The electrochemical explanation to the ennoblement process is based on the increase of the oxygen reduction rate induced by the presence of bacteria [14]. A modification of the oxygen reduction kinetics by bacteria of genus *Pseudomonas* has been proposed where the bacterial metabolites act as electrocatalysts [16]. It has been suggested that enzymes (for example catalase) entrapped in the EPS could be responsible for the increase in cathodic currents [17]. Catalase is an integral component of bacterial cells' response

to oxidative stress and is believed to limit the accumulation of reactive oxygen species [18]. The mechanism requires the electrochemical production of hydrogen peroxide during the oxygen reduction process, and it involves electron recycling during the enzymatic decomposition of the peroxide to water and oxygen by catalase.

The oxygen generated by the enzyme can be electrochemically reduced, as well as reaching the surface by diffusion, resulting in higher cathodic currents. It has been established that oxides forming the protective films on copper and copper-based alloys play a key role in both the hydrogen peroxide and oxygen reduction reactions [19,20]. Hydrogen peroxide reduction proceeds through the chemical oxidation of Cu_2O, to yield CuO. Cupric oxide is then electrochemically reduced to regenerate Cu_2O [19]. Cu_2O acts as a redox mediator allowing fast electroreduction of H_2O_2. However, on a CuO surface the reduction of peroxide is inhibited and H_2O_2 may accumulate at the interface to finally desorb to the solution. The catalytic reduction of oxygen and hydrogen peroxide on copper–nickel alloys appears to emulate that which occurs on copper [21]. This has been verified in a comparison of oxygen reduction on 90–10 copper–nickel, copper and nickel–aluminium bronze in artificial and filtered seawater [22]. It was found that surface corrosion products in each case influenced the reaction rate where cuprous and cupric species acted to catalyse and slow the kinetics of oxygen reduction, respectively. Similarly, differences in the reduction kinetics of oxygen and hydrogen peroxide on 70–30 and 90–10 copper–nickels have been attributed to the nickel content within the protective oxide film [20], since H_2O_2 reduction is inhibited on nickel oxide.

8.3 Experimental procedures

The chemical compositions of cast NAB (NES 747 Part 2 [23]), Cu–15Ni alloy and commercially pure titanium specimens used for the immersion tests are shown in Table 8.1. The specimens were wet polished to a final finish with 600-grade SiC paper, degreased in acetone, rinsed in distilled

Table 8.1 Chemical composition of copper-based alloys and titanium

	Composition (wt.%) – balance copper									
Alloy	Al	Fe	Ni	Mn	Zn	Pb	Sn	Si	Cr	Mg
NAB[1]	9.32	5.00	5.38	1.10	0.01	0.01	0.01	0.05	0.01	0.01
Cu–15Ni	1.61	0.94	15.4	4.36	0.01	0.005	0.005	0.04	0.38	0.01
Titanium	Commercially pure (99%)									

[1]British Naval Specification (NES 747 Part 2 [23]) – castings annealed at 675 °C for 2–6 h and cooled in air – for superior corrosion resistance.

water and then air dried and weighed using a precision balance with a range of 205 g and accuracy of ± 0.02 mg. After testing, any loose corrosion products were mechanically removed. Then the specimens were chemically cleaned in a mixture of 10 % HNO_3, 2 % tartaric acid and 3 % HCl solution [24], rinsed with water, dried and finally reweighed.

The galvanic couples had dimensions of 5.0 ×4.0 ×0.7 cm for NAB/Ti and 5.0 ×4.0 ×0.4 cm for NAB/Cu–15Ni. The cathode to anode area ratio was 1:1. Single metal samples had dimensions of 5.0 ×5.0 ×0.4 cm. The NAB/Ti or NAB/Cu–15Ni couples were connected via electrical leads, with a separation of 50 mm to avoid direct contact. The galvanic (×2 replicates) and uncoupled (×3 replicates) specimens were mounted in a planar orientation on a non-metallic board (see Fig. 8.1). The experimental procedures for measuring the galvanic current and couple potentials have been detailed elsewhere [25]. The galvanic currents were measured using a GalvoGill zero resistance ammeter (ZRA) (ACM Instruments, Grange-over-Sands, UK). The ZRA measured the couple potential with respect to a Ag/AgCl reference electrode; all potentials are given with respect to Ag/AgCl. Measurements were taken weekly. The decoupled potential measurements were made using a multimeter (± 1 mV) by decoupling the galvanic couple for 30 min and

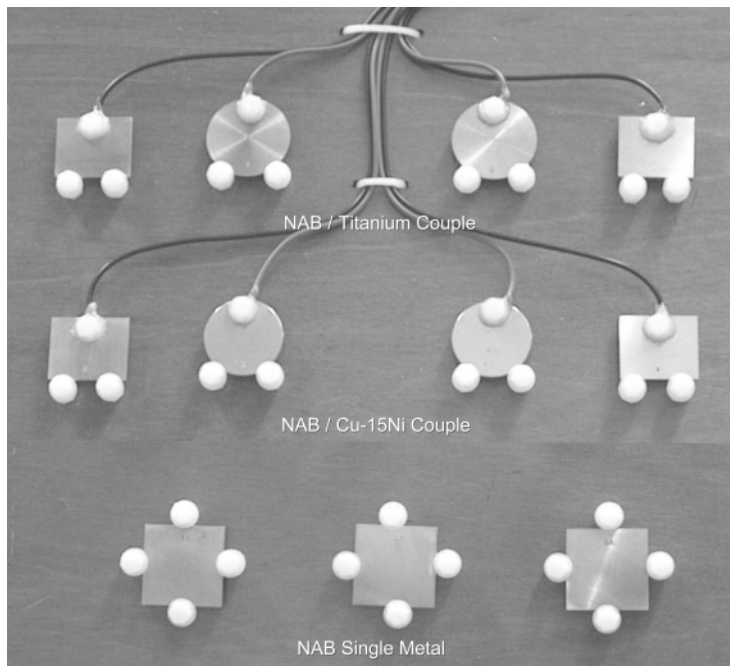

8.1 Coupled (1:1 area ratio) and single specimen layout for the NOCS immersion trial.

then measuring the single metal potentials. Three boards were immersed in brackish seawater (below the splash zone) from a pontoon located at the National Oceanographic Centre, Southampton (NOCS) on 10th January 2003. Board 1 was retrieved after six months (June 2003), board 2 after 12 months (January 2004) and board 3 after 36 months (January 2006). The salinity of the seawater at the NOCS was ~ 31 % (g kg^{-1}) reflecting its brackish nature and the pH was 7.9, which is within the range normally cited for seawater (i.e. pH 7.7–8.3 for surface waters). The seawater temperature followed seasonal trends. The dissolved oxygen (DO) was measured using a H19145 DO probe (Hanna Instruments, Leighton Buzzard, UK) and ranged between 6 and 10 ppm, being dependent on seawater temperature and salinity.

8.4 Results and discussion

8.4.1 Visual inspection

After 12 months immersion the uncoupled NAB surfaces were uniformly covered in an adherent green–brown corrosion product (Fig. 8.2a) with some evidence of pitting at the specimen centres. The NAB/Cu–15Ni couples showed corrosion occurring on both components, with the NAB surfaces covered with a thick corrosion product (Fig. 8.2b) whilst the Cu–15Ni were covered with a more uniform corrosion film plus significant areas of biofouling (Fig. 8.2c). When coupled to titanium, the NAB surfaces were covered in thick and loosely adherent corrosion products (Fig. 8.2d). The titanium surfaces were entirely covered with a biofilm of varying thickness; in particular one surface on board 2 had a visibly thicker biofilm. Macrofouling was clearly evident on the titanium with the attachment of barnacles and various forms of seaweed (Fig. 8.2e). Finally, close visual inspection of all the copper-based alloys revealed the presence of patchy biofilms/slimes covering all surfaces, most notably for the Cu–15Ni.

NAB/Cu–15Ni couple

The couple and decoupled (single metal) potential measurements over the 18-month immersion period can be seen in Fig. 8.3. When initially immersed the NAB/Cu–15Ni couple potential is approximately –230 mV, which is close to the generally acknowledged corrosion potential of both NAB and Cu–15Ni in seawater and has been reported to indicate the formation of a Cu_2O film [5,6,25]. There is a sharp noble shift in the couple potential after one month to between –60 and –100 mV, which is normally attributed to the oxidation of Cu_2O to CuO as the oxide film matures [5,6]. The galvanic current density for the same period shows a low net current (0.1–0.5 μA cm^{-2}) consistent for two similar alloys coupled galvanically (Fig. 8.4). In quiet,

(a)

(b)

(c)

(d)

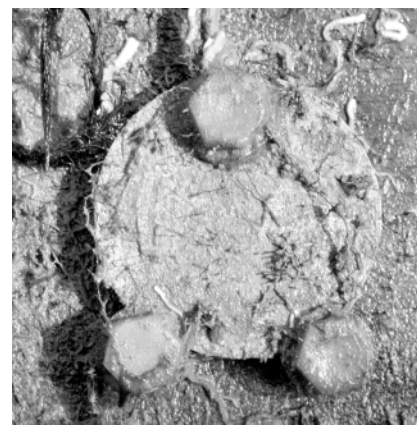

(e)

8.2 Surface conditions after 12-months immersion (board 2); (a) uncoupled NAB; (b) NAB and (c) Cu–15Ni from the NAB/Cu–15Ni couple; (d) NAB and (e) titanium from the NAB/Ti couple.

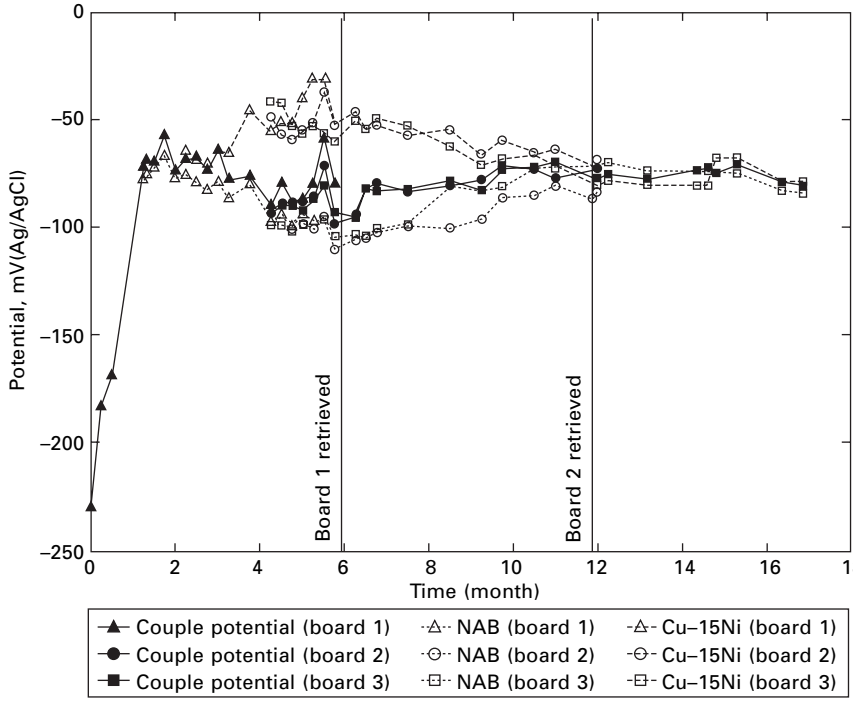

8.3 Coupled and decoupled potential measurements for the NAB/Cu–15Ni couple immersed in brackish seawater.

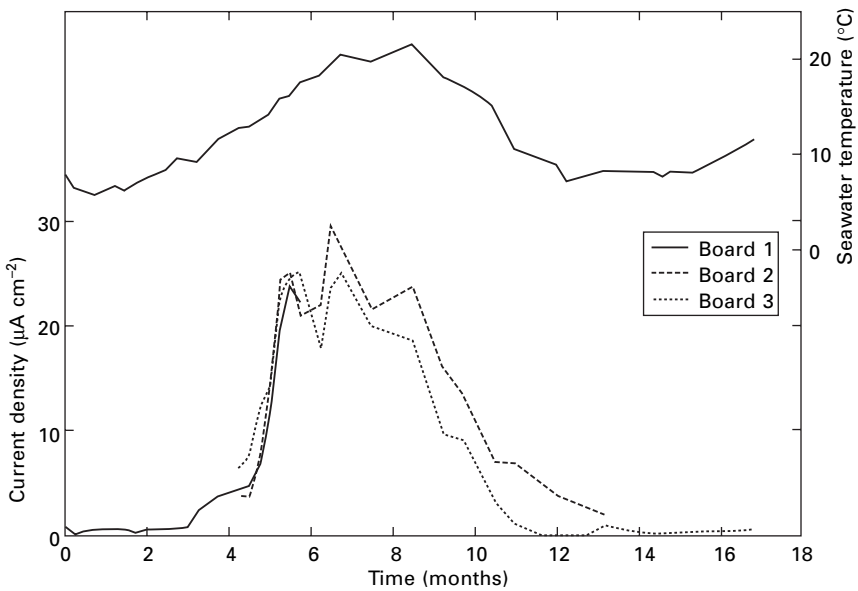

8.4 Measured seawater temperature and galvanic current densities for the NAB/Cu–15Ni couple immersed in brackish seawater.

tidal or flowing seawater, provided the flow velocity does not exceed a certain limit, the protective film corrosion resistance continues to improve until it achieves a long-term steady state of 0.6–2.0 μA cm^{-2} (0.015–0.05 mm y^{-1}) [1,2]. During this time both couple components are undergoing film formation and growth, with anodic and cathodic sites constantly shifting over the surfaces (internal current flow within couple surfaces).

After the development of mature protective oxide films, at around three months, it is evident that the couple components become increasingly polarised. The Cu–15Ni is depolarised by 40–50 mV in the noble direction while the NAB depolarises in the active direction by 20 mV. Overall, this suggests that the Cu–15Ni is cathodic to the NAB. Increased corrosion resistance and the cathodic nature of the copper–nickel alloys has been attributed to enrichment in iron and nickel within the protective oxide film, which influence the polarisation of the cathodic reaction (oxygen reduction). In contrast, the aluminium within the protective oxide film for NAB has been reported to act as a barrier for ionic transport and thus the copper oxide/hydroxide/hydroxychloride outer layer is not significantly enriched with iron and nickel [7]. With the Cu–15Ni becoming the cathodic component, additional effects such as biofouling could further contribute to the polarisation behaviour, since the toxic effect of leaching copper ions is reduced. At the same time as the couple depolarises, the galvanic current density increases significantly with a maximum of ~ 30 μA cm^{-2} at six months. This coincides with the seasonal increase in seawater temperature and the associated biofouling activity. For copper-based alloys, it has been previously reported that after exposure to natural seawater for several months, a multilayer structure of microorganisms and EPS were found entrapped between layers of different copper corrosion products [26]. The biofouling colonisation of copper–nickel alloys in seawater is attributed to variations in iron content. Alloys with low iron contents were rapidly corroded and scarcely colonised [27]. Once a biofilm is established, modification of the oxygen reduction kinetics can occur simply by the presence of the bacteria and bacterial metabolites/enzymes, which act as electrocatalysts [16,20]. This bacterial influence may be responsible for the increased galvanic currents observed during this period. At the end of the summer (after 10 months exposure) the biofouling activity diminishes and the depolarisation of the couple components is seen to reduce with a corresponding decrease in the galvanic current density.

Even when the biofouling season comes to an end, the presence of a patchy biofilm on the Cu–15Ni can create chemical conditions vastly different from those of the ambient environment [28]. The biofilm can act as a diffusion barrier as well as a source or sink for chemical species that are important to corrosion processes. Factors such as pH, dissolved oxygen and peroxides can vary greatly at the metal/biofilm interface. In the presence of a biofilm the subsequent corrosion behaviour will vary according to the extent of the

interactions between corrosion products layers and the various components in the biofilm. Patchy biofilms on copper–nickel samples have been reported to produce complex corrosion behaviours resulting in physical heterogeneities on the metal surface, thus leading to the formation of differential aeration cells [29]. Another aspect related to biofilm–corrosion product interactions is spalling or sloughing of corrosion products associated with EPS in the biofilms, and this has been observed for copper-based alloys exposed to seawater [30].

NAB/Ti couple

The couple potential of the NAB/Ti couple on immersion was approximately –230 mV (Fig. 8.5), clearly indicating only weak/negligible polarisation of the NAB by the titanium, i.e. the titanium is readily polarised. During the first month, there was a net rise in galvanic current density (Fig. 8.6), possibly related to the Cu_2O to CuO transformation when the NAB oxide film thickens, as indicated by the rapid change of couple potential to –50 mV. The decoupled potential for the Ti was in the order of 75–90 mV more noble than the couple

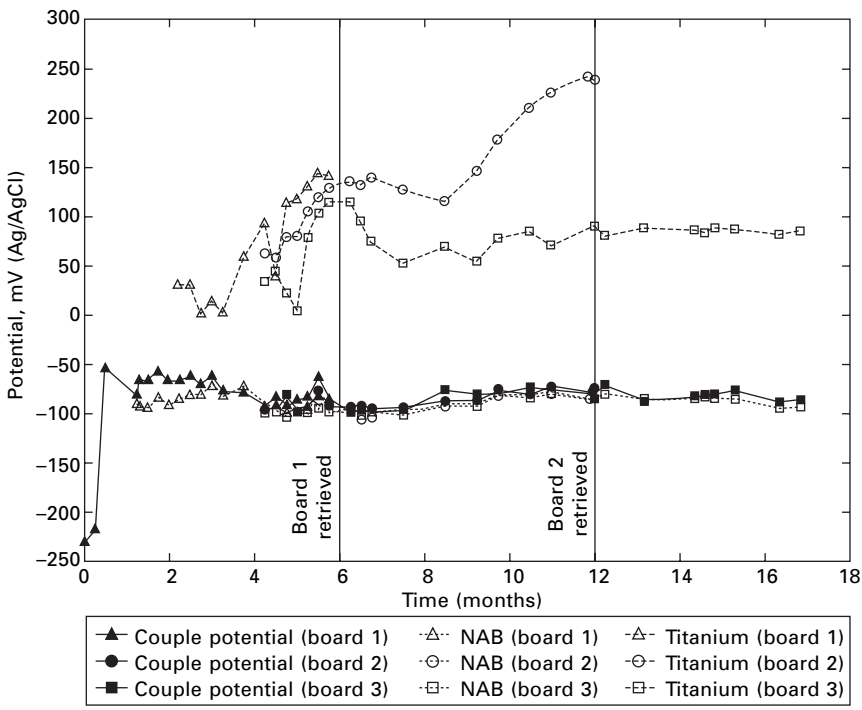

8.5 Coupled and decoupled potential measurements for the NAB/Ti couple immersed in brackish seawater.

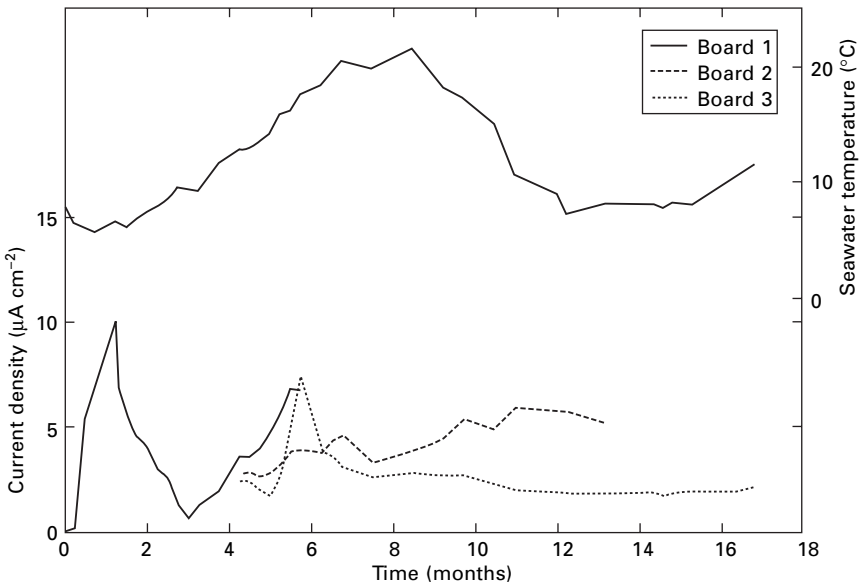

8.6 Measured seawater temperature and galvanic current densities for the NAB/Ti immersed in brackish seawater.

potential, with a slight 20–30 mV depolarisation in the active direction for the NAB. It has been reported that titanium undergoes slow ennoblement in both fresh and brackish water [31] and, since titanium does not display any toxicity toward marine organisms, biofouling can occur rapidly on immersed surfaces. In the third month of exposure, at the start of the fouling season, ennoblement of the Ti occurs with the decoupled potentials increasing to approximately 150–180 mV. However, the NAB decoupled potentials remain close to the couple potentials with little depolarisation occurring. The influence of the biofouling season appears to be less dramatic for the NAB/Ti couples compared with the NAB/Cu–15Ni. The galvanic current densities at six months are significantly lower than the NAB/Cu–15Ni couple at 7 μA cm^{-2}, possibly due to the poor catalytic activity of the oxide layer for oxygen reduction even in the presence of a biofilm. The difference in the galvanic current densities for boards 2 and 3 may be related to the relative biofilm thickness on the titanium. As discussed in the previous section, the only significant difference between the NAB/Ti couples was a thicker biofilm on one of the Ti surfaces on board 2.

Gravimetric measurements

Gravimetric analysis of the uncoupled NAB specimens immersed for six months indicated a corrosion rate of 0.014 mm y^{-1}, very similar to the 0.015

Table 8.2 Gravimetric analysis and corrosion rates

	NAB	NAB/Ti		NAB/Cu–15Ni	
		NAB	Ti	NAB	Cu-15Ni
6 months					
Average mass loss (g)	0.31	1.00	–	1.21	0.23
Corrosion rate (mm y^{-1})	0.014	0.05	–	0.07	0.01
12-months					
Average mass loss (g)	1.20	3.59	–	4.21	1.91
Corrosion rate (mm y^{-1})	0.027	0.09	–	0.11	0.05

mm y^{-1} value reported for NAB in natural seawater [1] (see Table 8.2). The NAB, when galvanically coupled to either titanium or Cu–15Ni, had a higher corrosion rate of 0.05 and 0.07 mm y^{-1}, respectively. The predominately cathodic Cu–15Ni also had a corrosion rate of 0.01 mm y^{-1}, consistent with the initial formation of a protective oxide film. Assessment after 12 months exposure shows increased corrosion rates for NAB by a factor of 1.5–1.9 when compared to the six months data. In contrast, the corrosion rate of the Cu–15Ni over the same period was five times greater, possibly due to the presence of a patchy biofilm as discussed previously.

The measured galvanic corrosion rates appear to be contrary to the view that when NAB is coupled to other copper-based alloys no acceleration of corrosion occurs [2]. In this study, the poor galvanic compatibility can be attributed to a surface modification of the cathode component. For Cu–15Ni, the nature of the oxide film after prolonged immersion affected its relative corrosion resistance compared to NAB and ultimately polarises the couple making NAB the anode component. A biofilm can occur more readily when the Cu–15Ni is predominately the cathodic component, thus increasing the cathodic efficiency, resulting in higher corrosion rates. For the NAB/Ti couple, the degree of corrosion acceleration is reported to be slight for a cathode to anode ratio of 1:1 [2]. The formation of a biofilm on titanium and the slow ennoblement will, however, ultimately influence its cathodic efficiency [9]. The relative thickness of the biofilm also appears to have an effect with thicker films resulting in higher galvanic currents.

In addition to the gravimetric method, the NAB mass loss can be assessed using Faraday's laws of electrolysis, equation [8.1], where Q is the charge, F is Faraday's constant (96485 C mol^{-1}), z is the number of electrons involved in the reaction and Δw is the mass loss. For the given NAB composition, the calculated equivalent oxidation state of the cations produced by dissolution is 2.09 and the equivalent molar mass (M_m) is 59.5 g mol^{-1}.

$$Q = zF\frac{\Delta w}{M_m} \qquad [8.1]$$

Table 8.3 Faradaic assessment of NAB mass loss from Figures 8.4 and 8.6

	NAB Faradaic analysis	
	Ti couple	Cu–15Ni couple
6–months		
Total charge (C)	3067	3122
Mass loss (g)	0.90	0.92
12–months		
Total charge (C)	7351	16668
Mass loss (g)	2.2	4.9

By integration of the board 1 current–time curve the total estimated charge for the NAB/Ti couple at six months was 3067 coulombs (see Table 8.3). Using equation [8.1], a mass loss of 0.90 g was calculated which is in good agreement with the gravimetric result of 1.00 g. For the 12 months data (boards 1 and 2), the Faradaic mass loss under-estimates the true mass loss, probably due to local current flows resulting from the patchy biofilm that developed on the NAB surface by this time. Evaluation of the Faradaic mass loss for the NAB/Cu–15Ni couple during the first six months is more complicated as both surfaces form a protective film. Localised anodic and cathodic sites will develop on both surfaces and current will flow between these sites. Only after the development of mature protective layers were significant galvanic currents measured. This could partly explain the under-estimate in the NAB mass loss of 0.92 g for the NAB/Cu–15Ni couple. The over-estimation for the 12-month data could result from a number of factors including; (i) incomplete removal of corrosion products; (ii) redeposited copper during chemical cleaning; (iii) biofouling affecting the dissolution kinetics; or (iv) a combination of (i) to (iii).

In summary, it is worth noting that it has been reported previously that short-term (less than a year) corrosion performance data for copper-based alloys in seawater tend to under-estimate actual in-service performance [1] and thus can be misleading if used to estimate service life.

8.5 Conclusions

- Accelerated corrosion rates were measured for both the NAB/Ti and NAB/Cu–15Ni couples compared to uncoupled NAB, particularly during the biofouling season.
- After three months, both the titanium and Cu–15Ni couple components depolarised in the noble direction. This behaviour coincided with the seasonal increase in seawater temperature and increased likelihood of biofilm formation and activity.

- The mechanism of the noble depolarisation in the presence of a biofilm probably involves a change in the kinetics of the oxygen reduction reaction.
- For the Cu–15Ni couple, significant increases in the cathodic current have previously been linked to copper species within the protective oxide film acting to catalyse the reduction reactions. Furthermore, the role of bacterial metabolites/enzymes in the biofilm will also modify reduction kinetics and could be responsible for the increase in galvanic currents.
- The NAB/Ti couple is less affected by the seasonal biofouling activity. This is probably due to the relatively poor catalytic activity of the oxide layer for oxygen reduction even in the presence of a biofilm.

8.6 Acknowledgements

The authors would like to acknowledge the financial support of Dstl (Defence Science and Technology Laboratory) and Dr Clive Tuck from Meighs Ltd for supplying the copper-based alloys. Contents include material subject to © Crown Copyright 2005 Dstl.

8.7 References

1. A.H. Tuthill, *Mater. Perform.*, 1987, **26**, 12–22.
2. H.J. Meigh, *Cast and Wrought Aluminium Bronzes – Properties, Processes and Structure*, 1st edn., London, IOM Publications, 2000.
3. R.F. North, M.J. Pryor, *Corros. Sci.*, 1970, **10**, 297–311.
4. R.N. Singh, N. Verna, W.R. Singh, *Corrosion*, 1989, **45**, 222–229.
5. S.A. Campbell, G.J.W. Radford, C.D.S. Tuck, B.D. Barker, *Corros. Sci.*, 2002, **58**, 57–71.
6. G. Bianchi, P. Longhi, *Corros. Sci.*, 1973, **13**, 853–864.
7. A. Schüssler, H.E. Exner, *Corros. Sci.*, 1993, **34**, 1793–1802.
8. B.G. Ateya, E.A. Ashour, S.M. Sayed, *Corrosion*, 1994, **50**, 20–25.
9. R. Francis, *Galvanic Corrosion – A Practical Guide for Engineers*, Houston, TX, NACE International, 2001.
10. S.C. Dexter, J.P. LaFontaine, *Corrosion*, 1998, **54**, 851–861.
11. W.G. Characklis, K.C. Marshall, *Bio-films*, New York, Wiley, 1990.
12. G.G. Geesey, *Am. Soc. Microbiol. News*, 1982, **48**, 9.
13. M.C.M. Bruijs, L.P. Venhuis, H.A. Jenner, G.J. Licina, D. Daniels, *PowerPlant Chem.*, 2001, **3**, 400–405.
14. V. Scotto, R. Dicinto, G. Marcenaro, *Corros. Sci.*, 1985, **25**, 185–194.
15. S.C. Dexter, G.Y. Gao, *Corrosion*, 1988, **44**, 717–723.
16. D.J. Schiffrin, S.R. de Sánchez, *Corrosion*, 1985, **41**, 31–38.
17. J.P. Busalmen, M. Vázquez, S.R., de Sánchez, *Electrochim. Acta*, 2002, **47**, 1857–1865.
18. H. Schellhorn, *FEMS Microbiol. Lett.*, 1994, **131**, 113.
19. M.V. Vazquez, S.R. de Sánchez, E.J. Calvo, D.J. Schiffrin, *J. Electroanal. Chem.*, 1994, **374**, 179–187.
20. S. Ceré, M.V. Vazquez, S.R. de Sánchez, D.J. Schiffrin, *J. Electroanal. Chem.*, 1999, **470**, 31–38.

21. F. King, M.J. Quinn, C.D. Litke, *J. Electroanal. Chem*., 1995, **385**, 45–55.
22. G. Kear, Electrochemical Corrosion of Marine Alloys under Flowing Conditions, PhD Thesis, University of Portsmouth, UK, 2001.
23. Naval Engineering Standard NES 747, Nickel–Aluminium–Bronze Castings and Ingots, Part 2 Sand castings and ingots, London, Ministry of Defence.
24. I.D. MacLeod, *Corros. Australas*., 1985, **10**, 10–13.
25. R.C. Barik, J.A. Wharton, R.J.K. Wood, K.R. Stokes, *Corrosion/2004*, paper no. 04301, NACE International, Houston, TX, 2004.
26. G. Blunn, in *Biodeterioration 6*, S. Barry, D.R. Houghton, G.C. Llewellyn, C.E. O'Rear (eds), London, CAB International, 1986, 567.
27. A.H.L. Chamberlain, B.J. Garner, *Biofouling*, 1988, **1**, 79–96.
28. S.C. Dexter, *Biofouling*, 1993, **7**, 97–127.
29. H.A. Videla, W.G. Characklis, *Int. Biodeter. Biodegr.*, 1992, **29**, 195–212.
30. H.A. Videla, M.F.L. de Mele, G.J. Brankevich, *Corrosion/89*, paper no. 291, NACE International, Houston, TX, 1989.
31. S.C. Dexter, H.J. Zhang, Proc. *11th International Corrosion Congress*, Florence, Italy, April, 1990, **4**, 333.

Part IV

Aluminium alloys

9

Corrosion and protection of aluminum alloys in seawater

KEMAL NI ANCIOĞLU, Norwegian University of Science and Technology, Norway

9.1 Introduction

Use of aluminum alloys in seawater is of continuous interest because of the need for light-weight structural materials. As long as galvanic contact with more noble metals is avoided, most structural alloys, such as those in the AA1000 (commercially pure), 3000 (AlMn), 5000 (AlMg) and 6000 (AlMgSi) series, are resistant to corrosion in seawater, especially the so-called seawater-resistant alloys in the 5000 series [1]. The high-strength alloys in the 2000 (AlCu) and 7000 (AlZnMg) are normally not recommended for use in seawater.

In support of the foregoing, aluminum boats constructed from 5000-series alloys were already in use in 1930s with recorded lifetimes exceeding 40 years. Since then, areas of application have increased significantly. The largest use still involves marine vehicles of all types. Other applications include outboard motors, propellers, masts, ladders, floating bridges, desalting equipment, buoys, etc.

Under stagnant and low flow-rate conditions, uniform corrosion rate lies below 1 μm/y. Crevice corrosion is normally not a problem for aluminum alloys. However, it is observed in joints, and it is basically a design problem like galvanic corrosion. Alloys in the 5000-series become susceptible to intergranular corrosion if the Mg content exceeds 4.5 %. The 6000-series may also become susceptible to intergranular corrosion if the Si/Mg ratio exceeds the stoichiometric ratio for the intermetallic compound Mg_2Si, especially if Cu is also present, even if in small amounts. Thus, proper design and material selection can prevent these corrosion forms. Pitting, flow-dependent corrosion and erosion–corrosion are the basic corrosion problems for aluminum alloys in seawater. The purpose of this chapter is, therefore, to review the danger and mechanisms of these corrosion types and possible protection methods, especially cathodic protection.

9.2 Fundamental aspects of corrosion

Starting with the thermodynamic aspects, the Pourbaix diagram for aluminum, published recently for the type of oxide (bayerite) which is realistic for seawater [2], is shown in Fig. 9.1. It may look unfavorable for applications of the metal in seawater at pH 8.2. Therefore, the passivity of the metal in slightly alkaline environments like seawater is ensured by use of alloying elements such as Mg and Mn, which have small but adequate solid-solution solubility in aluminum. The point is demonstrated for the practical Pourbaix diagram of Gimenez *et al*. [3] for seawater-resistant alloy 5086 (nominal composition in wt% 0.1 Si, 0.3 Fe, 0.4 Mn, 4.3 Mg, 0.1 Cr) reproduced in Fig. 9.2. The diagram is based on experimental corrosion data obtained in chloride solutions rather than thermodynamic calculations. It is probably due to the presence of the passivating alloying elements Mn and especially Mg, whose oxide becomes increasingly passive with increasing pH, that the range of passivity of the oxide forming on the alloy becomes significantly larger than that obtained by thermodynamic calculation. These solid-solution alloying elements become enriched in the oxide in exposure to seawater as a result of selective dissolution of the more active aluminum component and, thereby, render the oxide more passive against seawater.

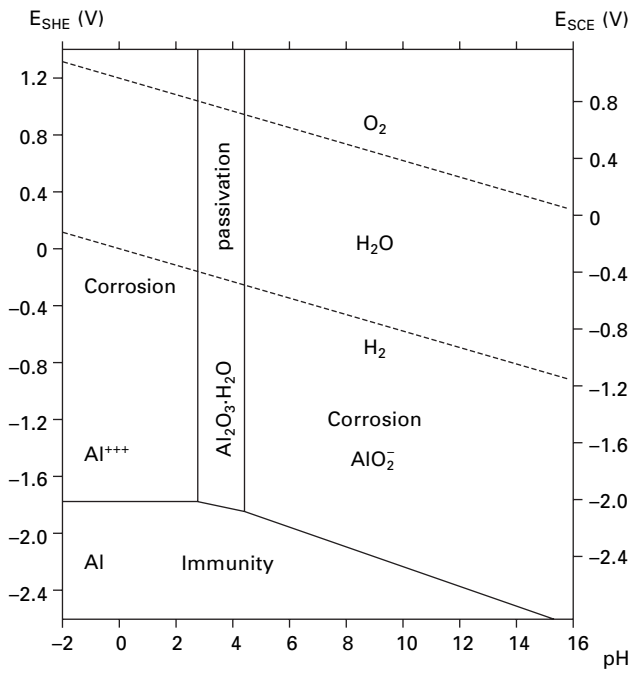

9.1 Pourbaix diagram for aluminum [2].

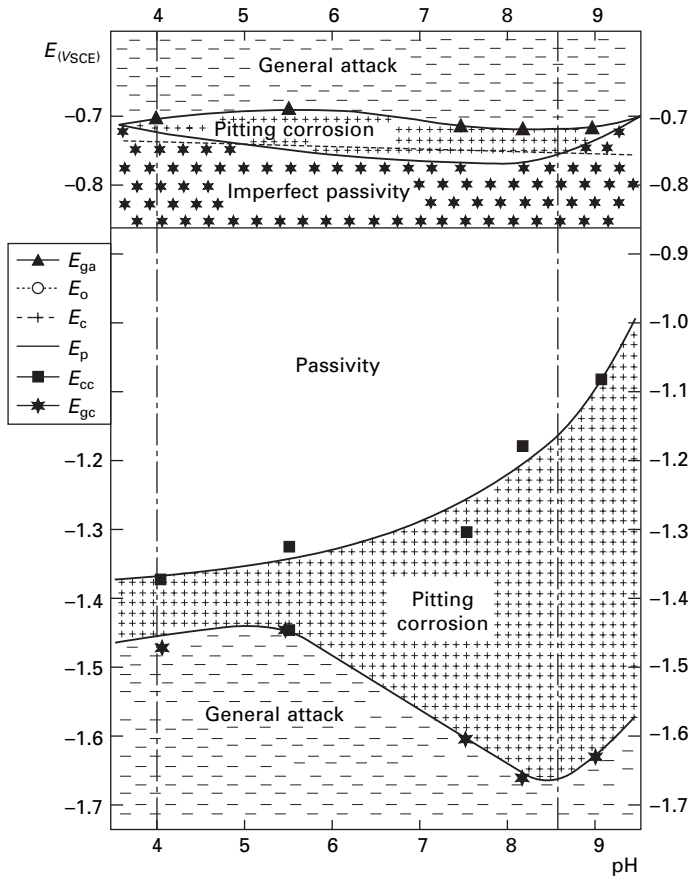

9.2 Experimental potential–pH diagram for alloy 5086 in chloride solution [3].

It is not always realized that, in contrast to steel, the localized corrosion of aluminum is primarily determined by the properties, size, and distribution of intermetallic compounds and secondarily by the properties of the solid-solution matrix alloy discussed above, unless copper is present. Pit initiation on multiphase commercial alloys occurs invariably at weak spots on the oxide around the intermetallic particles [4,5]. The weakness results firstly from the presence of a flaw in the oxide at the particle–matrix interface. Secondly, since the stable oxides on these solid-solution matrix aluminum alloys are largely insulators against electronic conduction, the reduction reaction required for the corrosion process can occur only on the type of intermetallic particles which are electrochemically nobler than the matrix.

The events which occur during stable localized attack, e.g. pitting, are summarized in Fig. 9.3, illustrating the development of localized environments

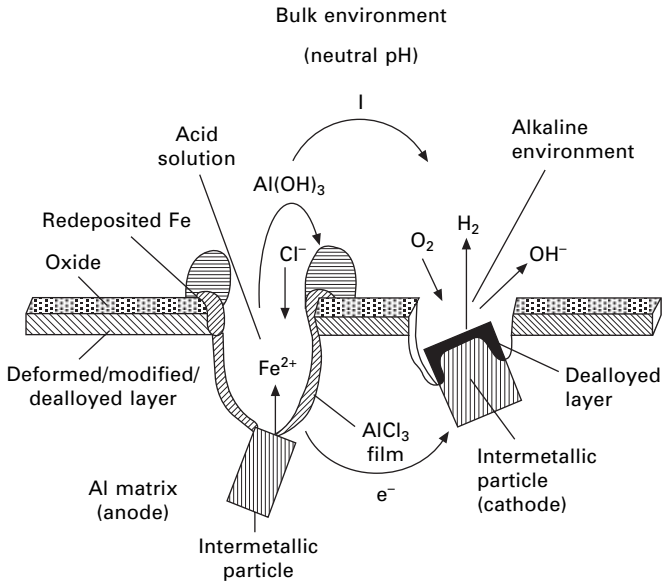

9.3 Schematic illustration of localised corrosion on aluminum alloys.

in the pit (acid) and adjacent to the cathodic site (alkaline), resulting from metal hydrolysis and reduction processes, respectively. High pH developing adjacent to the cathodic site causes etching of aluminum matrix around the particle as a result of destabilization of the amphoteric aluminum oxide. At the same time, this local alkalinization alters the chemistry and structure of the intermetallics on aluminum. The particles with more noble components become essentially enriched at the surface as a result of the selective dissolution of the aluminum component. It has also been shown for aluminum that the Fe^{2+} produced in the pit by the corrosion of iron-rich intermetallics redeposits in or at the immediate vicinity of the pit, thereby increasing the cathodic area fueling the corrosion process [6]. Selective dissolution of the aluminum from the matrix alloy and the resulting enrichment of a more active, passive or noble component may also have a beneficial or deleterious effect on the corrosion process. For example, while enrichment of the surface with magnesium may be beneficial against pitting of aluminum in the manner discussed above, enrichment of copper is known to have the opposite effect.

Nearly all aluminum alloys exposed to an aqueous solution, whether chloride is present or not, are likely to exhibit micropitting in the form of crevicing around the intermetallic particles as a result of the microgalvanic coupling between the noble, Fe-containing intermetallic particles and the surrounding more active solid-solution aluminum matrix, as described above and shown in Fig. 9.4 [7]. This gives only superficial attack, so-called cathodic etch pits, with pit size commensurate with the size of the intermetallic particles. This

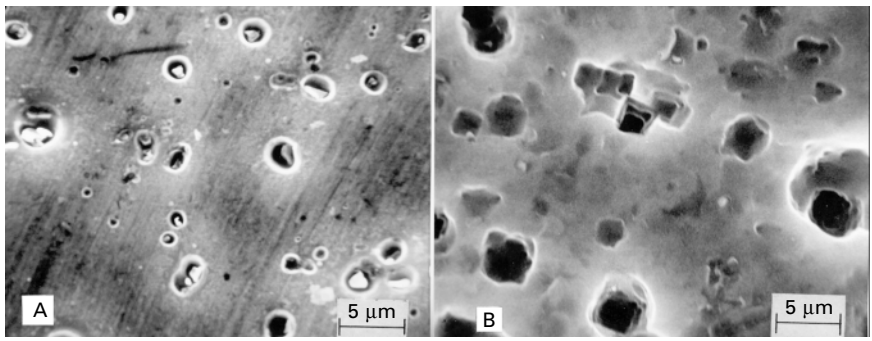

9.4 Initiation of micropits around Al_3Fe phases (A) and the passivated pits after the intermetallics are undermined (B) and removed from the surface of commercially pure alloy 1050 in chloride solution [7].

type of pitting corresponds to the pitting region depicted in Fig. 9.2 under the passive zone. Pits passivate after the intermetallic particles, visible in Fig. 9.4A, are undermined and removed from the surface as shown in Fig. 9.4B. The type of pit sketched in Fig. 9.3 with the acidified anolyte, which can propagate autocatalytically and cause material damage, does not initiate unless the surface of the metal can be polarized temporarily more positive than the critical pitting potential, which is about –0.75 V_{SCE} in seawater [8]. The value varies somewhat depending on the composition of various alloying elements [9]. Once initiated, however, such pits can propagate at potentials appreciably more negative than the pitting potential. This type of pitting is represented in Fig. 9.2 by the pitting zone above the zone of passivity.

Susceptibility to pitting and crevice corrosion may increase with chloride content, temperature [1] and pressure [10,11]. Added presence of heavy metal ions and dissolved CO_2 is not beneficial, since unexpected negative synergy of these species, together with Cl^-, dissolved oxygen and elevated temperature and pressure may cause high corrosion rates [12]. Dissolved H_2S is an effective corrosion inhibitor for aluminum alloys as reviewed and further documented in Ref. [13].

The microgalvanic coupling between the intermetallic phases and the solid-solution aluminum matrix has long been recognized [14]. Corrosion potentials of different phases found in various aluminum alloys in chloride media have been widely mapped out and correlated with pitting corrosion susceptibility, as reviewed in Ref. [15]. The information has been utilized in the development of corrosion-resistant alloys over the years. However, the application of the data and the know-how about mechanisms of pitting summarized above to corrosion protection purposes is relatively little and recent.

9.3 Effect of flow on corrosion rate and morphology

Increasing flow rates in seawater reduces the possibility of the pitting observed in stagnant environments and low flow rates. However, the rate of uniform corrosion increases [16]. It is not possible to specify a flow rate for this transition because it depends on the alloy and the hydrodynamic conditions. e.g. In laboratory testing by use of small samples, the transition occurred above 8 cm/s for alloys Al99.5 and AlMgSi1, while the seawater-resistant alloy AlMg3 did not suffer any significant pitting in the flow range tested, as shown in Fig. 9.5. The scatter in the data at low flow rates is due to pitting. With increasing flow rate the data can be correlated by a single straight line on a log–log plot, indicating that the mechanism of uniform corrosion is similar for all alloy types. The corrosion rate does not decrease with time in the uniform corrosion regime in contrast to the decreasing rates generally observed in the case of pitting. The uniform corrosion rate remains nearly constant as a function of time, and it is not affected by elevated pressures up to the test limit of 30 bar. The mechanism of this flow-dependent uniform corrosion will be discussed further below, together with the effect of cathodic protection.

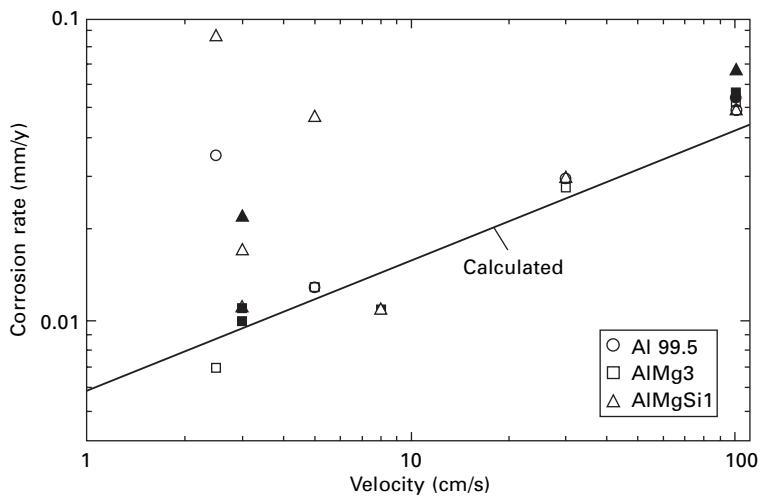

9.5 Corrosion rate of sheet specimens under open-circuit conditions (open) and cathodic protection at –1.0 V_{SCE} (solid) as a function of seawater flow rate. Specimen surfaces lie in the direction of flow. The data are based on weight loss measurements and an immersion period of two months. See reference [16] for experimental details. The line corresponds to the predicted uniform corrosion rate based on the mass-transfer considerations discussed in the text.

It should be emphasized that the transition velocity from pitting to uniform corrosion depends on the shear stress exerted by the flowing seawater on the aluminum surface. The shear stress exerted by the solution on small size specimens in the lab is high at low velocities. Similar shear stresses will be attained at significantly higher flow velocities past large aluminum structures. The scale-up from laboratory to practice can be obtained in the usual manner by use of universal friction factor correlations for flow past a specified structure geometry [17].

Corrosion of aluminum alloys under exposure to one-phase flow, even under highly turbulent conditions, is a mass transfer controlled phenomenon, as will be discussed further. Cavitation, impingement, or multiphase flow is required for erosion–corrosion to occur. Under such circumstances, aluminum alloys are susceptible to erosion–corrosion. Several comprehensive experimental studies are available for corrosion of aluminum alloys in seawater at high flow rates [18–21]. Our analysis of the available data [22] indicated that the transition from localized to a more uniform etching type of corrosion, in which the cavitation and multiphase flow are apparently not present, is a result of the type of transition discussed above and not erosion–corrosion in almost all cases. The transition often corresponds to laminar to turbulent transition in the experiments. It should be reiterated that this type of flow-dependent corrosion is a mass transfer limited phenomenon, whereas erosion–corrosion involves mechanical removal of material from the surface in addition to chemical and electrochemical corrosion. In the case of mechanical material removal, it is not possible to estimate corrosion rates from pure mass transfer considerations as discussed above and demonstrated in Fig. 9.5. A large amount of literature is available on erosion–corrosion of aluminum alloys in multiphase flow. However, review of this subject is outside the scope of this chapter.

9.4 Cathodic protection

Two important issues distinguish aluminum alloys from steel in terms of cathodic protection. Firstly, the oxide is amphoteric as seen in Fig. 9.1, i.e. it is not stable in acid or alkaline environments. If the metal surface becomes alkaline during cathodic protection, because the rate of the cathodic reaction is too high, then, the protective oxide may become destabilized. The transition between passivity and cathodic pitting in Fig. 9.2 can be used as a rough guideline for the negative limit of the potential applied during cathodic protection, although the limit actually also depends on the flow rate. Thus, protection is achieved by maintaining the passivity of the surface rather than by bringing the potential close to or into the range of immunity, as is the case for steel. In principle, therefore, we are talking about anodic rather than cathodic protection. Moreover, it should suffice to maintain the potential

sufficiently more negative than the critical pitting potential, e.g. at –0.85 V_{SCE}, to achieve the necessary protection. Cathodic (or more correctly anodic) protection is an effective way of preventing pitting corrosion of aluminum alloys [23].

The other issue is the requirement for very low current relative to the cathodic protection of steel. This is related again to the fact that the cathodic process is restricted to the cathodic intermetallic sites, which constitute a small fraction of the total exposed area while, in contrast, the entire exposed surface of a steel structure is uniformly accessible. Figure 9.6 shows cathodic polarization curves obtained on three aluminum alloys and carbon steel in flowing seawater [23]. These were obtained on small size (10 × 19 cm) plate specimens in an experimental flow channel at a linear flow rate of 8 cm/s, and the data were measured on freshly-exposed specimens before the onset of calcareous scale deposition. The cathodic current density measured on steel does not vary significantly with increasing cathodic potential because it is given by the limiting current for oxygen reduction on a uniformly accessible surface, which can be predicted by use of universal Nusselt number correlations for mass transfer. In contrast, the rate of cathodic reaction on the aluminum specimens is about an order of magnitude smaller, and it varies as a function of applied potential. Moreover, the current depends on the type of aluminum alloy. No flow dependence of the data for aluminum was detected [23]. The small current level and its alloy dependence indicate that the cathodic reaction is confined to microscale cathodic sites on the aluminum surface.

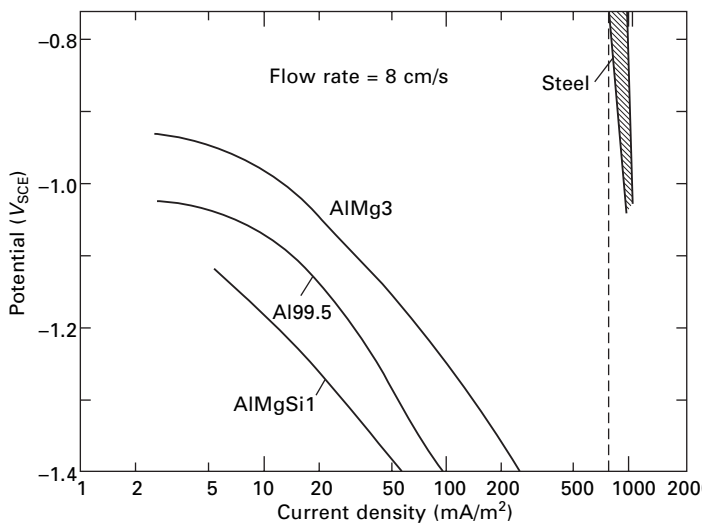

9.6 Cathodic polarization curves of freshly exposed aluminum and steel specimens at a flow rate of 8 cm/s. The dashed line is the calculated limiting current for oxygen reduction on steel [23].

The type and area of these cathodic intermetallic particles vary from one alloy to another. Because of their microscopic size, moreover, their mass-transfer properties are governed by the electrode size rather than by the stirring conditions in the bulk of the solution.

The current requirement for aluminum under cathodic protection in seawater is further reduced by an order of magnitude with time relative to the freshly exposed surface. This reduction is not only due to coverage of the cathodic particles by calcareous deposits, but is caused more by the detachment of the particles from the surface as a result of the cathodic etching phenomenon described above (see Figs 9.3 and 9.4), as also sketched in Fig. 9.7. The current requirement may in fact become a few mA/m^2 positive [23] or oscillate around essentially zero current, thus the appropriateness of anodic rather than cathodic protection for aluminum.

The foregoing considerations of cathodic protection apply to low flow rates where pitting is the predominant corrosion mode. As uniform corrosion

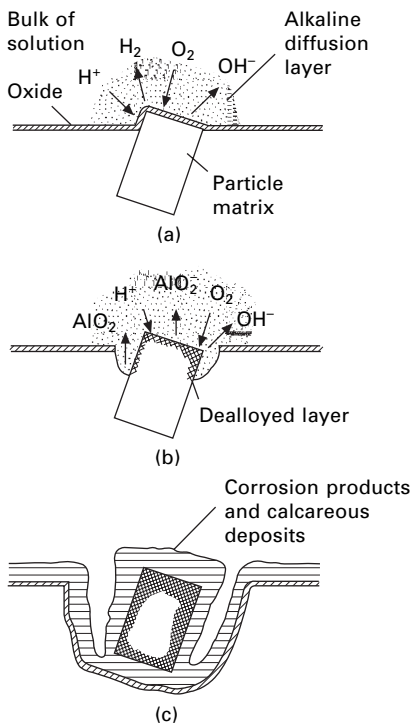

9.7 Schematic description of the mechanism of cathodic protection of aluminum alloys in seawater: (a) development of alkaline diffusion layer; (b) crevicing of the matrix around the particle and selective dissolution of the particle; (c) repassivation of the surface after detachment of particle [23].

becomes dominating with increasing flow rate as discussed above, cathodic (or anodic) protection becomes ineffective [16]. In fact, cathodic protection may increase the corrosion rate rather than reduce it, as shown in Fig. 9.5, because the corrosion rate is controlled by the chemical dissolution of the oxide rather than by an electrochemical process. The dissolved oxide is replaced by anodic formation of new oxide at the metal–oxide interface.

In cases where the uniform corrosion under flow conditions is intolerable or erosion–corrosion is possible, the most effective corrosion protection is to use corrosion-resistant coatings. The technology of applying organic coatings on an aluminum surface is again quite different from the technology for steel. Since proper chemical cleaning and the use of a conversion coating are normally required, it is appropriate to use sheets or extrusions already coated at the plant in constructing aluminum marine structures. However, the subject of surface treatment of aluminum alloys is outside the scope of this chapter, and the reader is referred to an authoritative treatise on the subject [24].

9.5 Summary

As long as galvanic contact with more noble metals is avoided, most structural alloys, such as those in the AA1000 (commercially pure), 3000 (AlMn), 5000 (AlMg) and 6000 (AlMgSi) series, are resistant to corrosion in seawater, especially the so-called seawater-resistant alloys in the 5000-series. In stagnant waters or in the presence of low flow rates, pitting may occur, with the possible exception of seawater-resistant alloys. However, pitting corrosion, driven by the Fe-rich cathodic intermetallic compounds, is often of a superficial nature. The pits tend to passivate as a result of etching or passivation of the intermetallics with time. Although thermodynamic calculations suggest possible instability of the oxide in slightly alkaline solutions, such as seawater, the protective nature of the oxide in practice is attributed to the presence of alloying elements such as Mg and Mn. Thus, the passivity of both the aluminum matrix alloy (the anode) and the intermetallics (cathodes) has to be considered in evaluating the corrosion and protection of aluminum alloys. The presence of acid or alkaline pH, heavy metal ions such as Cu^{2+} and Hg^{2+}, dissolved CO_2, or high temperatures, in addition to the presence of Cl^-, may cause unexpectedly high corrosion rates, while H_2S acts as a corrosion inhibitor.

With increasing flow rate, the possibility of pitting corrosion reduces with increase in the rate of uniform corrosion, which is controlled by the flow-dependent chemical dissolution of the oxide. In multiphase flow, aluminum alloys may become susceptible to erosion–corrosion, and they should not be used without a coating.

Cathodic protection is an effective way of preventing pitting. It also requires low current densities since the cathodic area, defined by the Fe-rich intermetallics, is small in contrast to steel, which is uniformly accessible to

the cathodic reaction. Application of too negative potentials will cause cathodic corrosion resulting from reduced passivity of the oxide with increasing pH at the surface. Cathodic protection does not stop uniform corrosion at high flow rates, and use of a coating may again be necessary.

9.6 References

1. K. Ni ancıo lu, H. Sigurdsson, O. Lunder, J. Drugli, 'Korrosjonshåndbok for aluminium,' SINTEF Report STF34 F87032, Trondheim, Norway (1987).
2. A. Pourbaix, *Proc. Eurocorr 2003*, paper no. 306, Budapest, Hungary, 28 Sept.–2 Oct. 2003.
3. P. Gimenez, J.J. Rameau, M.C. Reboul, *Corrosion*, **37** (1981) 673–682.
4. A.P. Bond, G.F. Bolling, H.A. Domian, *J. Electrochem. Soc*., **113** (1966) 773–778.
5. G.C. Wood, W.H. Sutton, J.A Richardson, T.N.K. Riley, A.G. Malherbe, *Proc. U. R. Evans Conference on Localized Corrosion*, NACE International, Houston, TX, 1971, 526.
6. O. Seri, M. Imaizumi, *Corr. Sci*., **30** (1990) 1121–1133.
7. K. Ni ancıo lu, K.Y. Davanger, Ø. Strandmyr, H. Holtan, *J. Electrochem. Soc*., **128** (1981) 1523–1526.
8. K. Ni ancıo lu, H. Holtan, *Wekst. Korros*., **30** (1979) 105.
9. E.H. Hollingsworth, H.Y. Hunsicker, in *Metals Handbook*, 9th edn, Vol. 13: *Corrosion*, Metals Park, OH, ASM International, 1987, 583.
10. W.H. Ailor, *J. Hydronautics*, **2**(1) (1968) 26.
11. J.F. Jenkins, F.M. Reinhart, *Corrosion/74*, paper no. 82, NACE International, Houston, TX, 1974.
12. A. Bjørgum, H. Sigurdsson, K. Ni ancıo lu, *Corrosion*, **51** (1995) 544.
13. A. Bjørgum, H. Sigurdsson, K. Ni ancıo lu, *Corrosion*, **51** (1995) 631.
14. R.B. Mears, R.H. Brown, *Ind. Eng. Chem*., **33**(8) (1941) 1001.
15. R.G. Buchheit, *J. Electrochem. Soc*., **142** (1995) 3994.
16. T. Wenn, K. Ni ancıo lu, *Proc. 3rd International Conference on Aluminium Alloys*, **2**, Trondheim, Norway, 22–26 June, 1992, 491.
17. D.C. Silverman, *Corrosion*, **59** (2003) 207.
18. J.A. Davis, G.A. Gehring, *Corrosion/74*, paper no. 78, NACE International Houston, TX, 1974; *Mater. Perform*., p. 32 (April 1975); *Corrosion/75*, paper no. 123, NACE International Houston, TX, 1975.
19. G.A. Gehring, Jr, M.H. Peterson, *Corrosion*, **37** (1981) 232.
20. R.L. Dillon, R.S. Hope, USAEC R & D Report No. HW-74359, Richland, WA, General Electric Hanford Laboratories, April 1963.
21. J. Symonds, *Proc. 5th OTEC Conference*, CONF-780236, **4**, VIII–222, Miami Beach, FL, February, 1978.
22. K. Ni ancıo lu, SINTEF Report STF34 F86047, Trondheim, Norway, 1986.
23. R. Gundersen, K. Ni ancıo lu, *Corrosion*, **46** (1990) 279–285.
24. O.B.E. Wernick, R. Pinner, P.G. Sheasby, *The Surface Treatment and Finishing of Aluminium and Its Alloys*, 5th edn, Teddington, Finishing Publications Ltd, 1987.

Part V

Aluminium-based anode material

10

Electrochemical behavior of new ternary aluminum alloys as sacrificial anodes

R. OROZCO-CRUZ, Universidad Veracruzana, México;
J. GENESCA, and J. A. JUAREZ-ISLAS,
Universidad Nacional Autonoma, México

10.1 Introduction

Since 1975, aluminum anode technology in the marine environment has emphasized the indium- and mercury-activated alloy chemistry [1]. Since around 1980, the predominant alloy has been the generic indium-containing alloy. Activation of the aluminum surface is the process of transition from the naturally passive state to the active state by removal or weakening of the passivating film. Activation may be achieved by cathodic currents, by a reduced substance in the adjacent solution, or by an alloying element added at a low quantity having a suitable negative potential [1]. Unalloyed aluminum adopts a relatively noble corrosion potential in saline media as a result of its protective oxide film. The oxide is the cause of polarization when aluminum is placed under anodic load in a cathodic polarization circuit. Numerous alloying combinations have been made to aluminum to reduce anodic polarization traits. With a few exceptions, the alloying approaches used to eliminate passivation, and hence promote surface activation, have been largely empirical.

The most widely accepted aluminum anode alloys contain mercury or indium as elements responsible for surface activation. Indium is second to mercury in this application followed by tin, magnesium, cadmium, and bismuth, with the latter elements not necessarily listed in their order of importance [1]. Aluminum alloys suitable for cathodic protection have been developed in recent years, and the influence of alloying elements such as zinc (Zn), titanium (Ti), mercury (Hg), and indium (In) has been studied by several researchers [2,3]. Many works refer to the addition of Hg, gallium (Ga), tin (Sn), and In to aluminum alloys. Each of these elements has been demonstrated to improve aluminum activation in neutral chloride media; however, the good results obtained in this field clash with the increased sensitivity to environmental protection. The use of Hg in particularly (which may be dangerous during the manufacture of the sacrificial anodes) pollutes sea life, thus giving rise to great concern about the environment. Research towards

the substitution of dangerous elements such as Hg involves the scientific knowledge of solidification processes, the kinetics of precipitation of primary binary/ternary intermetallics, the distribution of intermetallics and/or precipitates in α-Al solid solution after heat treatment, and the corrosion mechanisms involved during the dissolution of this kind of anode.

Technical knowledge involves the melting/casting of aluminum alloys with ternary additions of elements belonging to the groups IA, IIA, and IIB from the periodic table, and the implementation of electrochemical techniques which are adequate for the evaluation of the current efficiency of the anode.

It has been reported that in the Al–IIB–IIA system, the α-Al solid solution and the τ-phase with a composition close to the $Al_2IIB_3IIA_3$ are present [4]. In the as-cast condition the main microstructure is formed by the α-Al solid solution and the second phase τ [5]. The eutectic formed by a fine dispersion of the α + τ is segregated at grain boundaries and, to some extent, the τ-phase is partially dispersed in the core of the aluminum grains. To promote further fine dispersion of the τ-phase in the matrix, thermal treatments can be carried out on the resulting ingots by taking advantage of the fast kinetic reactions occurring in the solid state. The addition of a combination of IIA and IIB elements in Al is carried out with the aim of assuring that the aluminum oxide does not develop protective properties against dissolution, being the amount and distribution of intermetallic compounds relevant to the electrochemical and corrosion behavior of the alloy.

With reference to the Al–IIB–IIA ternary phase diagram [6], in the isotherm at 400 °C (720 °F), there is present the α-Al solid solution plus eutectics of the IIA_2Al_3 and Al_2IIA_3IIB, which ensure via aging treatments a fine dispersion of those eutectics which help the non-passivation of the anode. In order to make the Al–Zn–Mg ternary system more efficient with respect to the superficial activation of the anode (preventing the formation of superficial aluminum oxide films) additions of IA are convenient [7] with the precipitation of the Al_3IA (δ′) in grain boundary and matrix, by taking advantage of the facts that the Zn lowers the solid solubility of IA in the α-Al phase and that it can be incorporated into the δ′ phase.

This research has as its main objective the substitution of Al–Zn–In and Al–Zn–Hg alloys used as aluminum sacrificial anodes for alloys of the Al–IIB–IIA type in order to avoid pollution of the sea life by elements such as Hg, without at the same time decreasing the current efficiency of the resulting anodes. The choice of the alloy system has as its basis the precipitation and distribution of fine intermetallic phases belonging to the ternary Al–IIB–IIA system, in the α-Al matrix, with the aim of achieving two ends: (i) a good surface activation of the anode and (ii) corrosion products similar to those found in the salts of the seawater, thus preventing the pollution of sea life.

10.2 Experimental

An Al-5 at. % Zn-5 at. % Mg-0.1 at. % Li alloy was prepared with commercially available Al, Zn, and Mg with purities of 99.98 %. Li was used as a wire of 3.2 mm in diameter and 99.9 % purity with 4.5 mg/cm of sodium (Na). Initially, the Al was placed in an alumina/graphite-coated crucible and melted in a resistance furnace under an argon atmosphere. Once the Al was melted, the liquid bath was overheated 150 °C and the Al-capsules containing Zn and Mg were added. The bath was stirred with argon for 10 min in order to obtain a uniform distribution of Zn and Mg. Immediately after this operation, the Al-capsule containing Li was added to the liquid bath, which was stirred with a flux of argon for another 5 min, after which time the liquid alloy was poured into a copper mold of dimensions $8 \times 8 \times 50$ cm. The top and bottom of the ingot were cut off for chemical analysis thus obtaining a nominal composition of Al-4.8 at. % Zn-5.1 at. % Mg, and 0.09 at. % Li.

A representative microstructure observed in the as-cast ingot (Fig. 10.1) consisted of α-Al dendrites with sizes between 130 and 150 μm. In the interdendritic regions, the presence of a eutectic and black spherical particles was observed. The eutectic showed a white color with a maximum width of 10 μm, always following the contour of the dendritic arms. This eutectic, instead of presenting a platelet morphology such as the one reported [4], showed the presence of rows formed by gray spherical particles.

Al, Zn, and Mg elements of commercial purity (99.5 %), previously weighed, were placed into a SiC crucible and melted in a resistance furnace under an

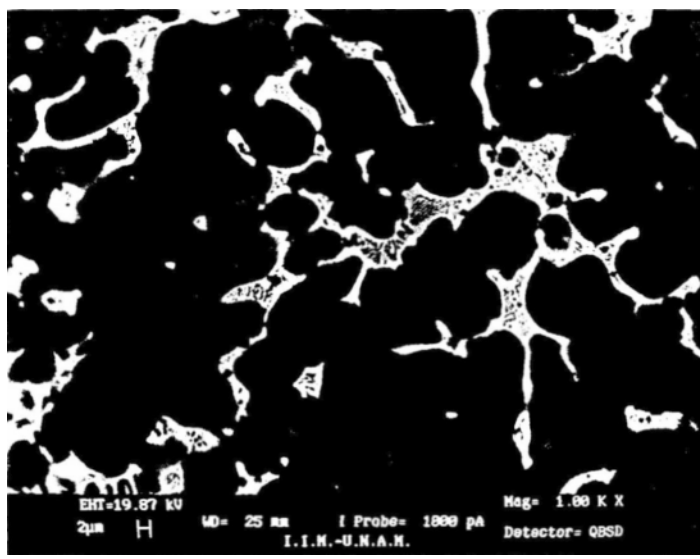

10.1 Microstructure of the Al-Zn-Mg-Li anode in the as-cast condition.

argon protective atmosphere. The liquid melt was gravity cast into a steel chill mold of dimensions 3.08 × 3.08 cm. The resulting alloys showed compositions (shown in Table 10.1), which lie in the maximum concentration of solute at equilibrium (C_{max}^{eq}) and in the α + τ field. The resulting ingots were cut out in sections parallel to the heat flow. The microstructure was revealed by electroetching the samples (25 V, –10 °C, 20 s) in a solution containing 10 % perchloric acid in ethanol. The samples were observed under an optical (Zeiss-Olympus), and a scanning electron (Stereoscan 440) microscope.

The structure observed in chill-cast ingots showed the presence of dendrites and eutectic in interdendritic regions, as shown in Fig. 10.2. During solidification of the alloys, the first phase to growth was the α-Al, which

Table 10.1 Chemical composition of the test alloy under study

Alloy	Field	Zn % at.	Mg % at.	Si % at.	Cu % at.	Al % at.	Electrochemical efficiency, %
1	(C_{max}^{eq})	5.3	5.3	0.168	0.003	bal.	68
2	α + τ	5.3	6.7	0.160	0.002	bal.	73
3	α + τ	5.3	7.2	0.125	0.008	bal.	73
4	α + τ	5.3	11.3	0.152	0.002	bal.	78

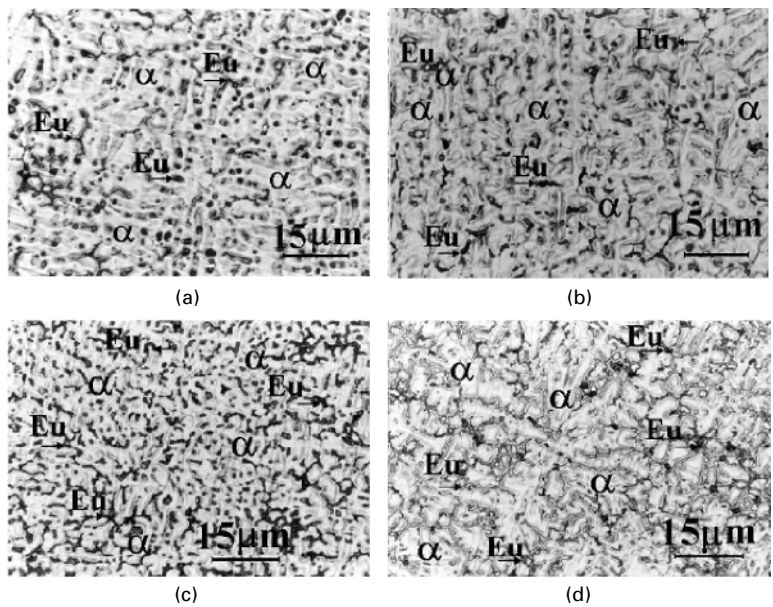

10.2 As-cast Al-Zn-Mg alloys; (a) Al-5.3 at. % Zn-5.3 at. % Mg; (b) Al-5.3 at.% Zn-6.7 at. % Mg; (c) Al-5.3 at. % Zn-7.2 at. % Mg; (d) Al-5.3 at. % Zn-11.3 at. % Mg.

developed a dendritic pattern. As the solidification continued, the liquid surrounding the advancing solid/liquid interface was enriched with solute (Zn and Mg + Si as impurity) and, as the temperature dropped and reached a phase transformation, phases such as the eutectic (α-Al + Si), the τ-phase, and the eutectic (α + τ) were formed. Regarding the τ-phase (reported previously [3] to be a key factor in promoting a good surface activation of the anode avoiding the formation of the continuous, adherent, and protective oxide film on the alloy surface, once in service), this was mainly observed in the specimens with 5.3 at. % Zn + 6.7, 7.2 and 11.3 at. % Mg.

A short-term electrochemical test [8] was performed on the Al–Zn–Mg–Li alloy anode, corresponding approximately to Al–5Zn–5Mg–0.1Li. Cubic anodes were machined from the ingot, thus eliminating the structure formed by direct contact with the mold wall.

The accelerated electrochemical test was carried out to determine anode efficiency and working potential [8]. All potentials were measured relative to a saturated calomel reference electrode (SCE). Samples were held galvanostatically at different current density levels. Each level was applied during a 24 h period, and the total duration of the test was 96 h. During the test, the anode potential and electrochemical impedance spectroscopy (EIS) were measured at the beginning and at the end of each current density level period (every 24 h). This could reveal any tendencies to passivation. The test solution was aerated substitute ocean water with an initial pH of 8.3 according to ASTM D1141 [9]. Electrochemical impedance was conducted using the CMS300 EIS system (Gamry Instruments, Inco, Warminister, PA) over a frequency range of 10 kHz–100 mHz (10 points per decade), superimposing a 10 mV AC signal, and interpreted in terms of equivalent circuit with frequency-dependent components.

10.3 Experimental results and discussion

The calculated electrochemical efficiency [8] for the as-cast Al anode samples was 61.43 %, corresponding to 1832 A-h/Kg. The closed-circuit potentials measured were in the range between –1.05 V (SCE) at 0 mA/cm^2 and –0.86 V (SCE) at 4.0 mA/cm^2. An active closed-circuit potential is desirable because a relatively noble potential could indicate the presence of passivation. Anodes must also possess high faradic efficiency to prevent frequent anode replacement. The NACE [10] and DNV [8] tests specify that an Al anode should have a closed-circuit potential active to –1.0 V (SCE) and an electrochemical efficiency (current efficiency of the anode) between 2300 and 2700 A-h/Kg. Then the anode analyzed met the potential criterion, but appeared to exhibit only moderate efficiency. Theoretically, uniform anode dissolution will give maximum efficiency. Either secondary cathodic reaction on the same interface and/or mechanical grain loss due to local macro or microcorrosion cells will

reduce the anode efficiency [11]. In Al–Zn alloys, Zn tends to be rejected to interdendritic zones or grain boundaries. This effect is favored by the cooling rate and the alloying element characteristics (lower melting point than aluminum). Under polarization, this local composition variation will favor the initiation and propagation of macro- and micro-local events (galvanic corrosion and pitting for example). These events are responsible for lowering anode efficiency by electrochemical or mechanical mass loss [11]. The low efficiencies shown by the studied anodes are similar to those obtained by Salinas *et al*. [11] for Al–5%Zn alloy. A possible explanation is that the main efficiency loss can be ascribed to the secondary reactions, since they are produced by the relatively high content of impurities, particularly Fe and Cu, that cause local cell action.

EIS measurements were performed during the DNV test [12]. The shape of the diagrams presents important differences. At high and medium frequencies two depressed capacitive loops are evident, probably due to the oxide and to the aluminum faradic dissolution. At low frequencies an inductive loop was detected. These results are in agreement with those obtained by Barbucci *et al*. [13] and other authors [14–16], although in their research unalloyed aluminum was studied. The capacitive behavior at high and medium frequencies might be due to the oxide passive film and the metal/oxide interface, whereas for the inductive behavior, an oxide/solution interface could be ascribed to the faradic processes.

It is evident from the electrochemical impedance data [12] that the current density condition plays a critical role on the resistive property of the corrosion products, suggesting a significant change on the corrosion product property formed on the Al anode. Dark gray corrosion products were formed. The surface dissolution morphology exhibited a rough, pitted surface. The EIS diagrams showed evidence of both passivation and pitting. The lower electrochemical activity exhibited by the Al anode samples strongly suggests that secondary reactions may be the fundamental cause of this behavior. In our experiments, the EIS diagrams obtained at higher current densities show an inductive semicircle which could be attributed to pitting corrosion. The preferred dissolution morphology is general attack rather than pitting, since pitting attack has been correlated to less than optimal performance.

Regarding the Al–Zn–Mg alloys, it is reported in the literature that a τ-phase exists in equilibrium with a solid solution of Mg and Zn in Al (α-solid solution). The $Al_2Mg_3Zn_3$ phase exists in a range of compositions which could be useful in obtaining the depolarization feature of the alloys. The structure of the studied aluminum alloys has been recognized as being composed of two phases: the α-Al matrix in which Mg and Zn are present to some extent, and the ternary intermetallic compound (phase τ). The formation and distribution of the intermetallic phase in the aluminum matrix in the form of many small crystals have been promoted as a key factor in achieving good

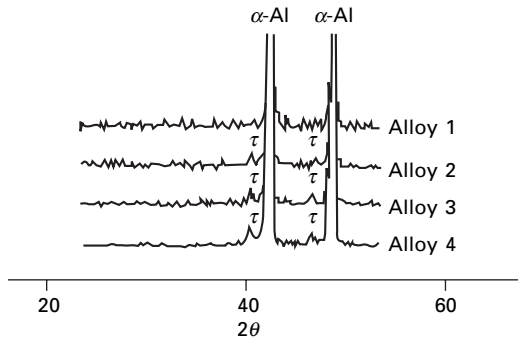

10.3 X-Ray diffractograms of alloys under study.

surface activation of the anode. Then, electrochemical efficiency must increase when the volume content of τ-phase increases. The investigation of the effect of this intermetallic on the activation capability of Al–Zn–Mg alloys when exposed to an aggressive environment containing chlorides has been carried out. The electrochemical efficiency (Table 10.1) clearly shows how these aluminum alloys are strongly affected by the presence and amount of this type of intermetallic. From X-Ray phase analysis (Fig. 10.3) it has been possible to demonstrate that τ-phase can be formed on the alloys whose composition exceeds the maximum concentration of solute at equilibrium $(C_{\max}^{\text{eq}})$.

10.3.1 Effect of Mg content on the anodic behavior

Zinc as a simple additive to aluminum sacrificial alloys has very limited activation properties. Zn has a high solid solubility with aluminum, and use is made of this property with the addition of Mg. Electrochemically, Zn has a combination effect upon anode current capacity when alloyed with Mg. Zinc provides a weight advantage to aluminum anodes in the commercial sense and also provides resistance to anaerobic bacteria in sediments, thus permitting improved anode behavior [1].

Magnesium is used in this work as the element responsible for surface activation of aluminum. The primary reason that a certain metal is beneficial is because it comes into intimate contact with aluminum but is not sufficiently dissolved in it to affect the potential [1]. The effect of Mg content on the polarization behavior of these alloys is shown in Fig. 10.4. Addition of Mg to the anode alloy shifts the corrosion potential to more negative values, which is desirable for cathodic protection systems. Employing the 'mixed potential theory' it can be concluded that the potential of any anode is the result of anodic and cathodic contributions of the metals involved. The contributions will be increased by depolarization or, conversely, decreased

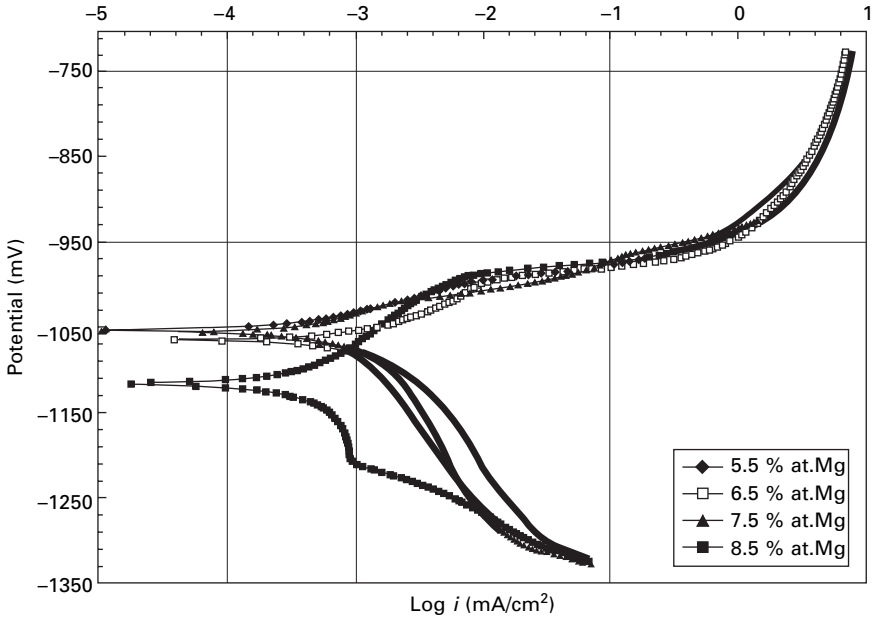

10.4 Potentiodynamic polarization curves of Al-5.3% at. Zn-*x* % at. Mg (*x* = 5.5–8.5 %) in 3 % NaCl solution at room temperature.

by polarization of the reactions. Studies indicate that anodic depolarization is necessary, and it occurs with almost every low melting point addition to about the same extent. Improved potentials are the result of this anodic depolarization coupled with polarization of the cathodic reactions [17]. Cathodic polarization is caused by adding elements with a high hydrogen overvoltage. They are also metals with low melting points.

The potentiodynamic polarization plots of Al–Zn–Mg alloys show that the anodic behavior looks very similar and, in all the cases, a net anodic current resulted at potentials positive to about –0.95 V (SCE), where a passive plateau is apparent, although anodic current density increased as anodic polarization progressed, whereas the cathodic behavior presents some important differences as a function of Mg content.

The cathodic behavior seems to be interpreted as follows: a first activation region near E_{corr}, followed by a diffusion area, possibly due to oxygen reduction at intermediate potentials, and finally a new activation region at higher potentials due to the water reduction. It is clear that the Al-5.3% at. Zn-8.5% at. Mg alloy shows an important catalytic effect of the surface elements on oxygen reduction reaction. At 8.5% at. Mg, more negative potential and lowering in O_2 reduction limiting current can be observed.

Polarization curves for the four alloys are shown in Fig. 10.4 for the experimental conditions studied. These polarization curves were obtained in

a 3 % NaCl solution at 20 °C. The polarization curves shown in Fig. 10.4 indicate that, in general, a good reproducibility was obtained in the experimental results. Referring to the anodic branch of the polarization curves, three main regions can be observed:

- a first region developing from the E_{corr} to potential values of –0.99 V (SCE);
- a second region in which a sudden change in the slope of the anodic current occurs, between –0.99 and –0.95 V (SCE);
- finally, a third region at higher anodic potentials, where another change in the slope of the anodic curve can be observed – this region can be seen above –0.95 V (SCE).

These features can be explained in a qualitative manner as follows. As the potential of the working electrode increases from E_{corr}, an anodic reaction on the Al alloy surface occurs and a linear relationship between the applied potential and the logarithm of the current density can be observed which corresponds to a charge-transfer process known as Tafel region, characterized by a slope, Tafel slope, which contains mechanistic information about the corrosion reaction. In the region in which a sudden change in the slope of the anodic polarization curve occurs with a plateau in the anodic current, this behavior can be attributed to the formation of a pseudo-passivating film. This film could be due to the formation of an Al_2O_3 layer on the metal surface. At higher anodic potentials the resulting anodic current density increases again. This may be attributed to the growth of the film previously formed.

Aluminum reacts readily with Cl^- in aqueous solutions containing NaCl. Hence one might hypothesize that the native barrier oxide is gradually converted to a hydrated salt film at the oxide solution interface. Figure 10.4 illustrates dc polarization results on Al–Zn–Mg alloy as a function of Mg content. All data are IR corrected. For 8.5% at. Mg content the polarization behavior seems to be consistent with the notion that the native Al_2O_3 is converted to a non-protective $AlCl_3 \cdot xH_2O$ film. A white gel-like film was observed. After 336 h of immersion time, the morphology of the corrosion products formed on the surface of Al alloys was observed in the MEB. X-Ray microanalysis clearly showed the formation of a possible aluminum hydroxychloride, $Al_2O_3 \cdot xAlCl_3 \cdot yH_2O$ [18].

10.3.2 Electrochemical impedance spectroscopy measurements

With EIS it is possible to monitor the conversion of the native oxide-covered metal to $AlCl_3$-covered with both exposure time and increasing Mg content. EIS also provides a means to verify the presence of oxide at the lowest Mg

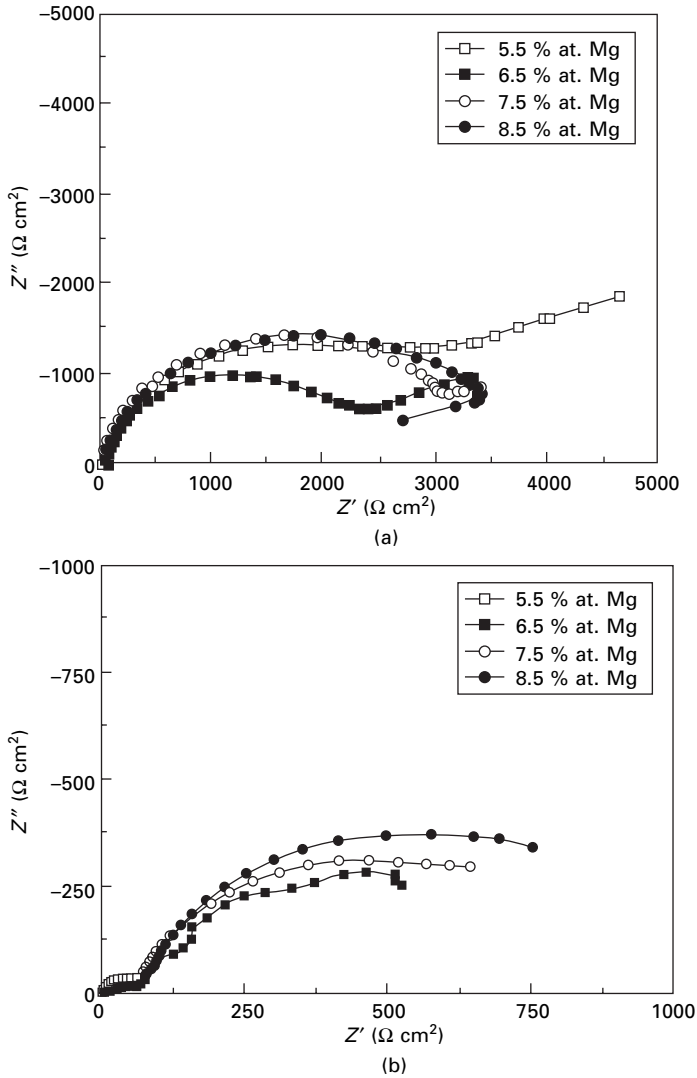

10.5 EIS diagrams of Al-5.3% at. Zn-*x* % at. Mg (*x* = 5.5–8.5% at.) anode samples in 3% NaCl at room temperature; (a) after immersion; (b) after 336 h of immersion.

content. Figures 10.5a and b illustrate the experimental impedance response at E_{corr} potential. EIS measurements were performed as a function of immersion time. The shape of the diagrams shows, independent of Mg content, the presence of one capacitive semicircle. By increasing immersion time (Fig. 10.5b) a second time-constant at high frequency begins to develop, that could be due to the formation of a layer of corrosion products. The capacitive

behavior at high and medium frequencies might be due to the corrosion products film and the metal/oxide interface. EIS fit was obtained assuming the equivalent circuit model illustrated in Fig. 10.6, which corresponds to the classic mass transfer control. According to this model, oxides are characterized by a high frequency parallel RC network consisting of the oxide capacitance in parallel with the oxide resistance and a low-frequency diffusional impedance, Z_D, associated with anion and cation transport across the oxide. The oxide impedance is proportional to oxide thickness and inversely proportional to the ability of the oxide to support both electronic and ionic charge transfer across the oxide. The low-frequency EIS response associated with the diffusional impedance of the oxide depends on the Warburg coefficient for both anions and cations, σ. The justification for choosing this particular model is based upon previous work on oxide-covered metals in the literature [19,20].

Concerning the high frequency EIS response, the capacitance obtained by EIS is, in principle, given by the oxide film capacitance, C_{ox}, in series with the double-layer capacitance at the oxide/solution interface, C_{dl} [19,21]:

$$\frac{1}{C_t} = \frac{1}{C_{ox}} + \frac{1}{C_{dl}} \qquad [10.1]$$

where C_{ox} is given by

$$C_{ox} = \varepsilon\varepsilon_0 \frac{1}{d_{ox}} \qquad [10.2]$$

where d_{ox} is the oxide thickness and other terms have their usual meaning. C_{ox} is approximately 16.42 μF/cm^2 just after exposure, which yields a 0.54-nm-thick Al_2O_3 film from Equation [10.2] assuming ε = 5–10. Since C_{dl} is normally 40–60 μF/cm^2, C_t is dominated by C_{ox} in Equation [10.1] for a homogeneous oxide-covered surface.

R_{ox} and C_t are shown in Fig. 10.7 and 10.8 as a function of exposure time

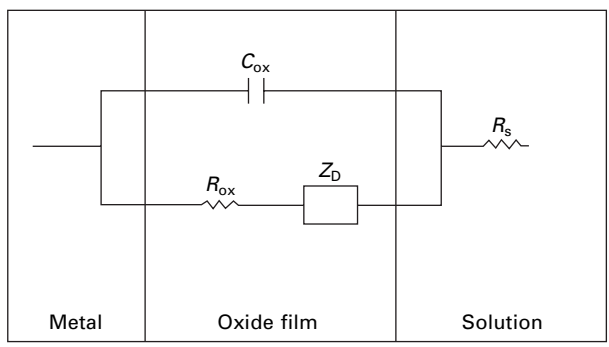

10.6 Electric equivalent circuit.

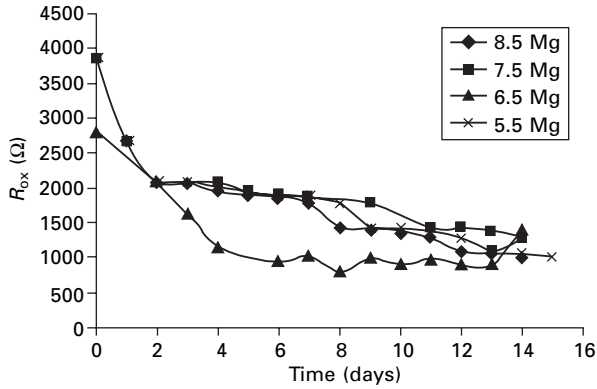

10.7 Corrosion products resistance, R_{ox}, as a function of immersion time.

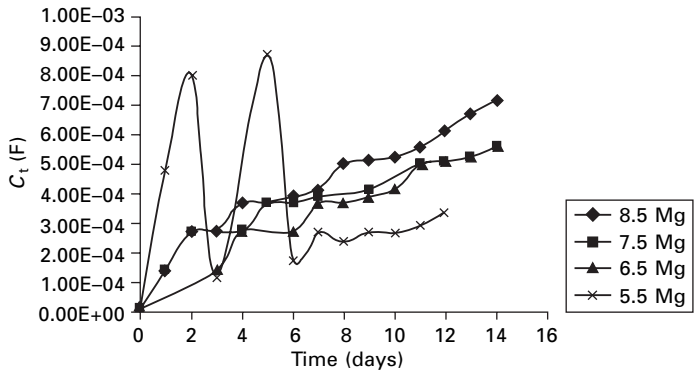

10.8 Capacitance, C_t, as a function of immersion time.

at E_{corr} potential for the different Mg content indicated. Capacitance data indicate thinning of the native barrier oxide with increasing exposure time since:

- C_t at short exposure times is in good agreement with initial oxide thicknesses calculated using Equation [10.2], and
- C_t increases with exposure time indicative of oxide thinning and exposure of bare metal.

Note that C_t increases with increasing Mg content (Fig. 10.8) while R_{ox} decreases (Fig. 10.7) and that the low frequency diffusional impedance is no longer observed at 7.5% at. Mg (Fig. 10.5a) These results further substantiate the claim that the low-frequency EIS response observed in Fig. 10.5a is indeed attributed to a diffusional impedance associated with the oxide since the conversion of the oxide to a gel-like salt resulted in the suppression of the

low-frequency diffusional impedance response. The data in Fig. 10.7 indicate that the native oxide is dissolved and converted to a salt film within about 12 days.

10.4 Conclusions

- As-cast Al-5.3% at. Zn-x% at. Mg alloys showed a microstructure that consisted of α-Al dendrites and eutectic α + τ in interdendritic regions. This alloy reached values of electrochemical efficiency up to 78 %.
- Magnesium addition helps in improving the anode current capacity when present to the extent of 8.5 %.
- From X-Ray phase analysis it has been possible to demonstrate that τ-phase can be formed on the alloys which composition is away from equilibrium.
- The morphology of the corrosion products formed on the surface of Al alloys was observed in the MEB. X-Ray microanalysis clearly showed the formation of a possible aluminum hydroxychloride, $Al_2O_3 \cdot xAlCl_3 \cdot yH_2O$.
- EIS has been demonstrated to be a useful tool in monitoring surface changes on the anode.

10.5 Acknowledgements

This work was supported by a grant from CONACYT (Mexico) (Project NC-204) and (MARINA-2002-C01-1553).

10.6 References

1. C.F. Schrieber, in *Designing Cathodic Protection Systems for Marine Structures and Vehicles*, Harvey P. Hack (Ed.), STP 1370, Baltimore, ASTM, OH, 1999, 39–51.
2. A.R. Despic, D.M. Drazic, M.M. Purenovic, N. Cikovic, *J. Appl. Electrochem.*, 1976, **6**, 527–542.
3. M. Salleh, Ph. D Thesis, UMIST, Manchester, UK, 1978.
4. A. Barbucci, G. Cerisola, G. Bruzzone, A. Saccone, *Electrochim. Acta*, 1997, **42**, 2369–2380.
5. R.J. Kilmer, G.E. Stonere, in *Light Weight Alloys for Aerospace Applications II,* E. W. Lee, N. J. Kim (eds), Warrendale, PA, Minerals, Metals and Materials Society, 1991, 3–18.
6. D.A. Petrov, in *Ternary Alloys*, G. Petzow, G.E. Effemberg (eds), VCH Weinheim, Germany, 1995, vol. 7, 57–68.
7. X. Zhand, Y. Wang, *Corr. Sci. Protec.*, 1995, **7**, 53–59.
8. DNV Recommended Practice RP B401 (1993): 'Cathodic Protection Design', Hovik, Det Norske Veritas Industry AS, 1993.
9. ASTM D1141-98(2003): *Standard Practice for the Preparation of Substitute Ocean Water*, West Conshohocken, PA, American Society for Testing and Materials.
10. NACE Standard Test Method 'Impressed Current Laboratory Testing of Aluminum

Alloy Anodes', NACE Standard TM0190-98, Houston, TX, NACE International, 1998.
11. D.R. Salinas, S.G. Garcia, J.B. Bessone, *J. Appl. Electrochem*., 1999, **29**, 1063–1071.
12. M.A. Talavera, S. Valdez, B. Mena, J.A. Juarez-Islas, J. Genesca, *J. Appl. Electrochem*., 2002, **32**, 897–903.
13. A. Barbucci, G. Cerisola, P.L. Cabot, G. Bruzzone, *Mater. Sci. Forum* 1998, 289–292, 529–535.
14. J.B. Bessone, D.R. Salinas, C.E. Mayer, M. Ebert, W.J. Lorenz, *Electrochim. Acta*, 1992, **37**, 2283–2290.
15. J.B. Bessone, C.E. Mayer, K. Juttner, W.J. Lorenz, *Electrochim. Acta*, 1983, **28**, 171–175.
16. J.H.W. DeWitt, H.J.W. Lenderink, *Electrochim. Acta*, 1996, **41**, 1111–1119.
17. J. Uruchurtu, *Corrosion*, 1991, **47**, 472–479.
18. R. Orozco, J. Genesca, J.A. Juarez-Islas, *J. Mater. Eng. Perform*., 2005 (to be published).
19. J.R. Scully, in *Electrochemical Impedance: Analysis and Interpretation*, J.R. Scully, D.C. Silverman, M.W. Kendig (eds) (STP 1188), Philadelphia, PA, ASTM, 1993, 276–296.
20. D.D. MacDonald, R.Y. Liang, B.G. Pound, *J. Electrochem. Soc*., 1987, **134**(12), 2981–2986.
21. J.W. Diggle, *Oxides and Oxide Films*, Vol. I, New York, Marcel Dekker, 1972, 319–517.

11

Low-voltage aluminium anodes – optimization of the insert–anode bond

HERVÉ LE GUYADER, VALÉRIE DEBOUT and ANNE-MARIE GROLLEAU, DCN Cherbourg, France;
JEAN-PIERRE PAUTASSO, DGA/CTA, France

11.1 Introduction

Aluminium sacrificial anodes are used for corrosion protection of various marine structures, components and systems, such as offshore platforms, ship hulls or ballast tanks to cite but a few. The Al–Zn–In alloy and Zn are the most widely used sacrificial materials and their open-circuit potentials range from –1 V vs Ag–AgCl for Zn anodes to –1.1 V vs Ag–AgCl for Al–Zn–In. The recent development of high-performance marine structures has led to the use of new materials with high mechanical properties but with an increased susceptibility to stress corrosion cracking or hydrogen embrittlement when excessively electronegative potentials are encountered.

In the 1990, DGA (Délégation Générale pour l'Armement) and DCN studied a new cathodic protection system and pursued the development of a low-voltage anode for use in cathodic protection of high-strength steels [1]. Determination of the cathodic protection criteria was first performed and indicated that applied potentials on Ni-alloyed and C–Mn steels between –0.730 and –0.850 V vs Ag–AgCl provided both acceptable Stress Corrosion Cracking (SCC) resistance and uniform corrosion rates, as well as protection against potential galvanic couplings. The structure and anode potential criteria determined are given in Table 11.1. Extensive laboratory tests and full-scale marine tests led to the selection of the Al–0.1% Ga alloy, which shows a working potential of –0.80 to –0.83 V vs Ag–AgCl and a current capacity around 1500 Ahr/Kg. The specified chemical composition of Al–0.1%Ga and electrochemical characteristics of the anodes are presented in Tables 11.2 and 11.3 respectively.

Measurements of open circuit potentials (OCP) during long-term experiments showed that severe OCP fluctuations could occur. However, steady potentials were obtained by applying low current densities between 0.01 and 0.1 A/m^2. As a result, two additional bare steel washers were included in the final design of the anode, as shown in Fig. 11.1, so that the maximum

Table 11.1 Criteria for a low-voltage anode

Potential of the protected structure	E_k	$-850\ mV \leq E_k \geq -730\ mV$
Required anode potential	E_a	$-850\ mV \leq E_k \geq -800\ mV$
Anode current density	I_a	$\geq 2\ A/m^2$
Anode area	S_a	$\approx 7\ dm^2$
Anode resistance	R_a	$0.3 \leq R_a \geq 0.4\ \Omega$

Table 11.2 Specified chemical composition of Al–0.1% Ga anodes

Elements	Al	Ga	Zn	In	Hg	Cu	Fe	Si	Ni	Mg	Mn	Others
Content (%)	balance	≥0.092 ≤0.110	≤0.15	≤0.005	≤0.005	≤0.005	≤0.08	≤0.10	≤0.005	≤0.010	≤0.010	≤0.005

Table 11.3 Specified electrochemical characteristics of Al–0.1% Ga anodes

	Potential mV vs Ag/AgCl	Efficiency %
NACE test	$-830 \leq E \geq -780$ mV	≥ 60
DNV test	$-830 \leq E \geq -780$ mV	≥ 60

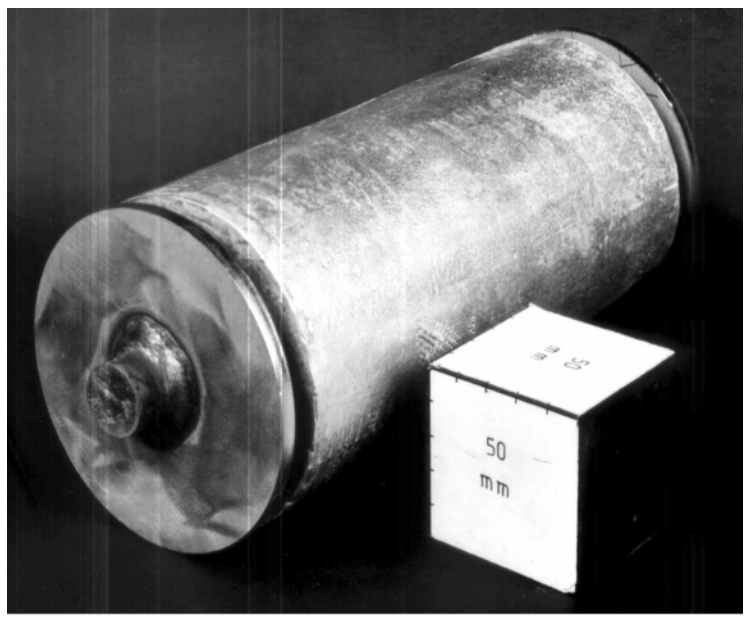

11.1 Al–0.1% Ga anode original design.

performance of the anode and the required range of potentials could be reached.

As most of the full-scale tests had been carried out at a temperature varying from 15 to 19 °C, questions regarding the performance of the alloy with temperature and especially at colder temperatures were raised. Some short-term tests were performed at 2 °C in natural seawater on the industrial casting of the anode, and these indicated that, although a decrease in the current output was observed at 2 °C as compared to 20 °C, there was no indication of any passivation of the alloy at the selected temperature (Table 11.4). Lemieux *et al*. [3] reported that the anode current output correlates directly with electrolyte temperature, increases in water temperatures inducing increases in anode current output and vice versa for temperatures in the range 16–31 °C.

Following the first evaluations, more than 500 cylindrical anodes were installed on a submerged marine structure, replacing the classical zinc anode. A first inspection was carried out after four months of service and showed that some of the anodes had not performed as expected. Further investigations indicated that the problem was due to a bad metallurgical compatibility between the insert and the sacrificial materials resulting in a poor bond between the anode and the plain rod insert. Progressive loss of contact between the anode and the structure to be protected was then induced by penetration of seawater at the anode–insert interface (Fig. 11.2). This was also evidenced by electrical resistance measurements between anodes and inserts that were carried out on additional anode samplings after 9 and 11 months of operation. In some cases values significantly higher than the acceptance criterion ($R < 0.1\ \Omega$) were measured as listed in Tables 11.5 and 11.6. It became clear also that seawater pressure may have been responsible for or contributed to the anode failure and that qualification tests had to be toughened regarding this particular issue.

This chapter describes the additional studies that were subsequently launched with two aims: (i) find temporary remedies for the anodes already installed on the structure; (ii) correct the anode original design and/or manufacturing process to achieve the maximum performance on new anode lots. Field experience regarding the use of these anodes is also given.

Table 11.4 Anode performance in cold seawater

Specimen	Anode current density at –800 mV vs SCE at 2 °C (A/m^2)	Anode current density at –800 mV vs SCE at 20 °C (A/m^2)
Al–0.1 %Ga industrial casting	1.5	3.5

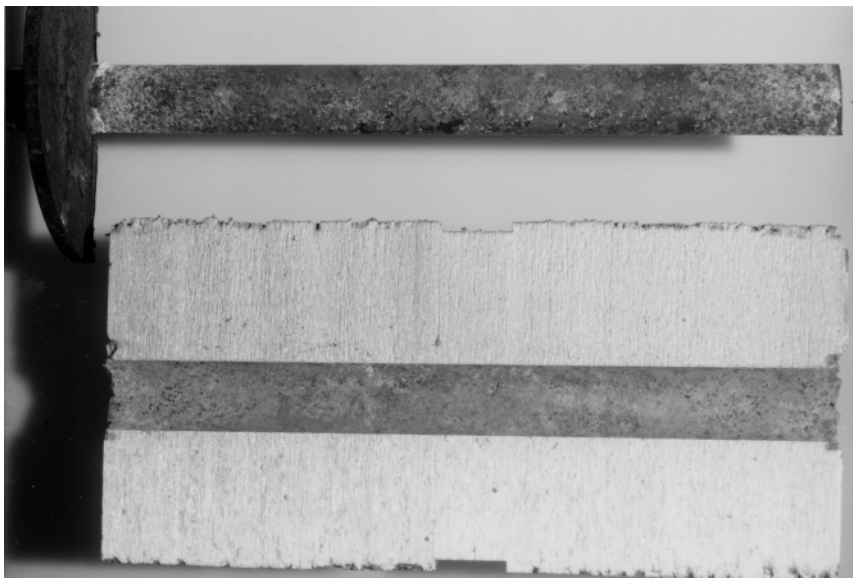

11.2 Decohesion and corrosion between anode and insert after four months of operation.

Table 11.5 Typical resistance measurements after nine months of operation (acceptance criterion $R < 0.1\ \Omega$)

	$R\ \Omega$
AG2.1	0.025
AG2.2	3.6
AG2.3	1.17
AG2.4	17
AG2.5	0.16
AG2.6	0.005
AG2.7	0.67
AG2.8	0.014
AG2.9	0.006
AG2.10	400
AG2.11	227

Table 11.6 Defective anodes on a sampling investigated after 11 months of operation

Working duration	11 months	
Anode type	AG2	AG1
Total no. examined	63	10
Results	53 defective (73%)	

11.2 Experimental procedure

11.2.1 Specimens

For obvious cost-saving and time-related reasons, the first phase of the study consisted of finding a suitable solution that could be easily applied for existing anodes modification. Some anodes were then adapted according to the principle shown in Fig. 11.3. Electrical connection was ensured between anodes and inserts by a braid both bolted to the sacrificial material using stainless steel fittings and welded to one of the steel washers, which in turn was welded to the insert. Protection against seawater penetration was maintained using a sealing polymer compound.

The second phase of the present work focused on the modification of the anode original design or manufacturing process, investigating new orientations such as surface preparation, nature, shape or dimensions of the insert, use of bimetallic materials, use of post-casting heat treatments, or replacement of rod inserts by tube inserts. A first set of anodes was produced specifically for this study by continuous casting and supplied by Pechiney-Hermillon*. The various parameters taken into account are presented in Table 11.7. The anode diameter was 94 mm with diameter for the inserts varying from 20 to 30 mm. In order to eliminate porosities and obtain a more homogenous bond some of the anodes were sent to TCS** to be treated by Hot Isostatic Pressure.

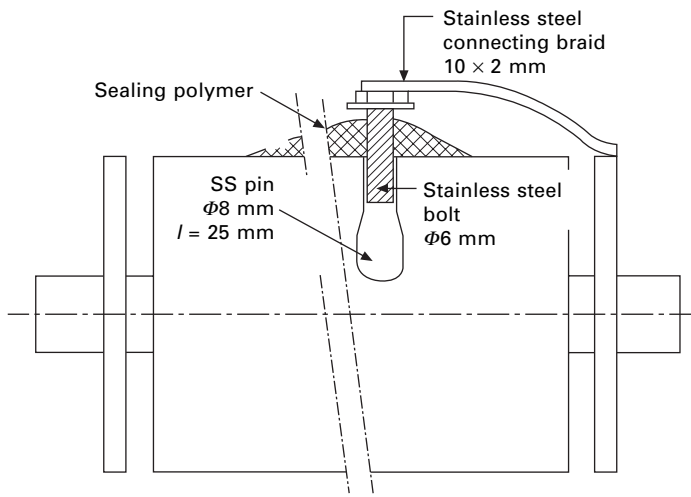

11.3 Principle used for modification of existing anodes.

*Pechiney Hermillon 73302 St Jean de Maurienne.
** Traitements Compression Service 58470 Magny-Cours.

Table 11.7 Characteristics of first anodes set investigated

Anode characteristics		Insert characteristics				Heat treatment
Material	Diameter (mm)	Material	Geometry	Diameter (mm)	Roughness	
Al–Ga	94	Steel	bar	30	knurled	–
Al–Ga	94	Steel	bar	20	R_a = 30 µ	–
Al–Ga	94	Steel	bar	20	R_a = 75 µ	–
Al–Ga	94	Steel	bar + dovetail	30	R_a = 30 µ	–
Al–Ga	94	Steel	bar + regular throttling	20		–
Al–Ga	94	Bimetal: steel–aluminium bronze	bar	20		–
Al–Ga	94	Bimetal: steel–aluminium bronze	bar	30		–
Al–Ga	94	Bimetal: stainless steel–aluminium	prismatic 42 * 13 mm			–
Al–Ga	94	Aluminium bronze	bar + regular throttling	20		–
Al–Ga	94	Steel	bar	20	R_a = 30 µ	Hot Isostatic Pressure
Al–Ga	94	Bimetal: stainless steel–aluminium	prismatic 42 * 13 mm			Hot Isostatic Pressure
Al–Ga	94	Steel	bar + dovetail		R_a = 30 µ	Hot Isostatic Pressure

While the latter set of anodes concentrated on the rod insert modification, a new approach with no insert was also considered as described in Figs 11.4, 11.5 and 11.6. In this particular case, the anode was tapered at each end and electrical contact was ensured by two stainless steel bolts. Seawater penetration was avoided using a double barrier system comprising an O-ring associated with a sealing gasket. The anodes were supplied by BAC France***.

***BAC France 78960 Voisins Le Bretonneux.

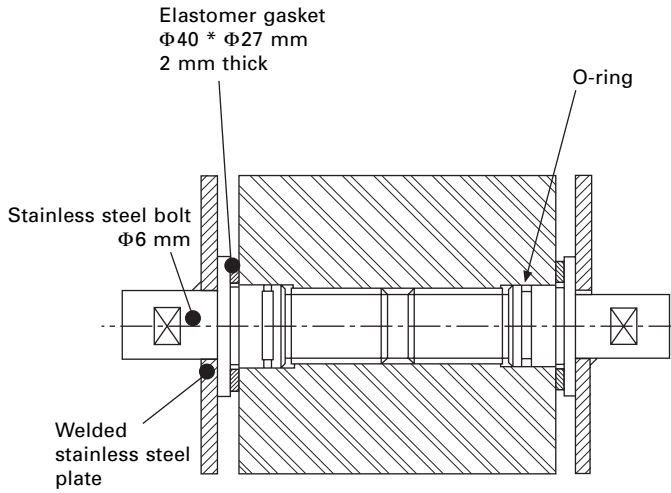

11.4 Principle of new anode design using a double-barrier system.

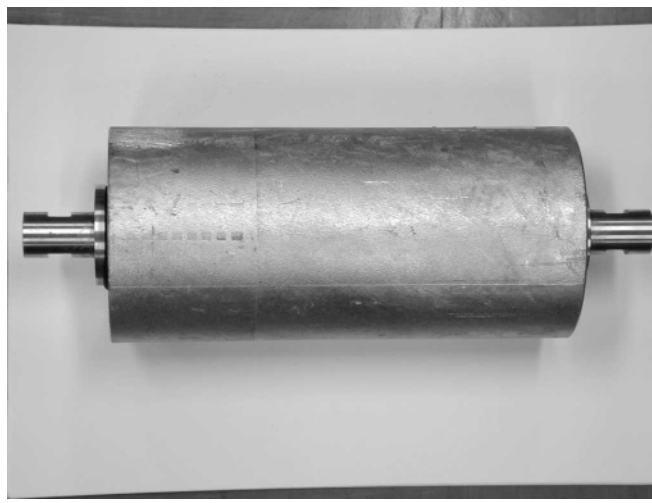

11.5 New Al–Ga anode.

Finally, further studies were performed on Al–Zn–In anodes that were cast by Ampères Industries****, replacing the plain rod insert by a tube insert. The anodes were then machined to their final dimensions at DCN Cherbourg with external diameters ranging from 94 to 160 mm as listed in Table 11.8. As the aim of the present work was not to investigate the sacrificial material but the bond between aluminium and steel, Al–Zn–In specimens

****Ampères Industries 69360 Serezin Du Rhône.

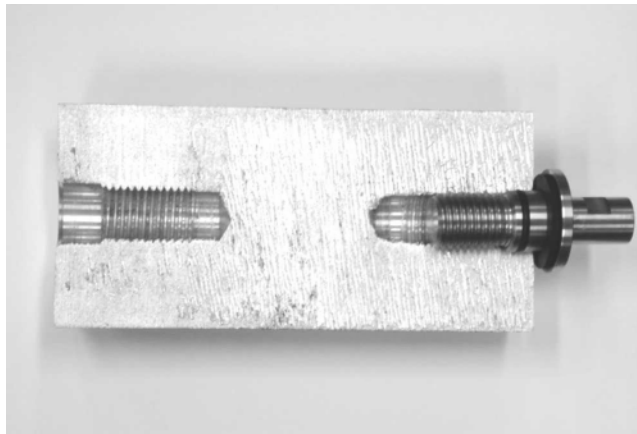

11.6 Longitudinal section of the anode showing the sealing gasket and O-ring.

were used for economical reasons and assumed to behave similarly to Al–0.1%Ga anodes for this specific topic of interest. A total of 30 anodes was tested including a version for which the inserts were water-cooled during casting. Comparisons were also carried out on Al–Zn–In anodes treated by hot isostatic pressure, Al–Zn–In anodes cast on plain rod inserts as well as cast-in strap-type Al–Zn–In Hydral 2C® anodes (Ampères Industries) and cast-in strap zinc anodes.

11.2.2 Tests

To evaluate the integrity between anodes and inserts, comparative pulling tests were performed using an Amsler 400 KN 699 type tensile testing machine (Zurick GmbH © Co. KG, Ulin, Germany). The anode was mounted on the first grip of the machine frame whereas the insert was placed in the opposite grip. Maximum tearing loads reached were then recorded and allowed for comparisons from one anode version to the other.

Toughened cyclic pressure tests in seawater were defined and implemented according to the cycle shown in Fig. 11.7. A total number of 2000 cycles was applied to each set of anodes, which corresponds to a test duration of around one month. Electrical resistances between anodes and inserts were measured before and after cyclic pressure testing, with a precision ohmmeter. Anodes displaying electrical resistances above 0.1 Ω were considered as defective and rejected. Following cyclic pressure tests completion, the anodes were visually examined and sectioned longitudinally. Further investigations of the insert–anode bond were performed by optical and scanning electron microscopy in conjunction with X-Ray analyses. In addition, long-term full-scale marine

Table 11.8 Characteristics of Al–Zn–In specimens

Anode characteristics				Insert characteristics		
Sacrificial	label	Length (mm)	Diameter (mm)	External diameter (mm)	Internal diameter (mm)	Observation
H2C	H2C1-1111-1	100	94	21	16.3	tube insert
H2C	H2C1-1111-2	100	94	21	16.3	tube insert
H2C	H2C2-1111-1	200	94	21	16.3	tube insert
H2C	H2C2-1111-2	200	94	21	16.3	tube insert
H2C	H2C2-1111-3	200	94	21	16.3	tube insert
H2C	H2C1-1131-1	100	110	27	20.5	tube insert
H2C	H2C1-1131-2	100	110	27	20.5	tube insert
H2C	H2C2-1131-1	200	110	27	20.5	tube insert
H2C	H2C2-1131-2	200	110	27	20.5	tube insert
H2C	H2C2-1131-3	200	110	27	20.5	tube insert
H2C	H2C1-1151-1	100	150	34	24.5	tube insert
H2C	H2C1-1151-2	100	150	34	24.5	tube insert
H2C	H2C2-1151-1	200	150	34	24.5	tube insert
H2C	H2C2-1151-2	200	150	34	24.5	tube insert
H2C	H2C2-1151-3	200	150	34	24.5	tube insert
H2C	H2C1-1141-1	100	160	48	41.3	tube insert
H2C	H2C1-1141-2	100	160	48	41.3	tube insert
H2C	H2C2-1141-1	200	160	48	41.3	tube insert
H2C	H2C2-1141-2	200	160	48	41.3	tube insert
H2C	H2C2-1141-3	200	160	48	41.3	tube insert
H2C	H2C1-1161-1R	100	150	34	24	tube insert water-cooled during casting
H2C	H2C1-1161-2R	100	150	34	24	tube insert water-cooled during casting
H2C	H2C2-1161-1R	200	150	34	24	tube insert water-cooled during casting
H2C	H2C2-1161-2R	200	150	34	24	tube insert water-cooled during casting
H2C	H2C2-1161-3R	200	150	34	24	tube insert water-cooled during casting
H2C	H2C1-1121-A1	100	94	20	–	Plain rod insert + Hot Isostatic Pressure
H2C	H2C1-1121-A2	100	94	20	–	Plain rod insert + Hot Isostatic Pressure
H2C	H2C2-1121-A1	200	94	20	–	Plain rod insert + Hot Isostatic Pressure
H2C	H2C2-1121-A2	200	94	20	–	Plain rod insert + Hot Isostatic Pressure
H2C	H2C2-1121-A3	200	94	20	–	Plain rod insert + Hot Isostatic Pressure

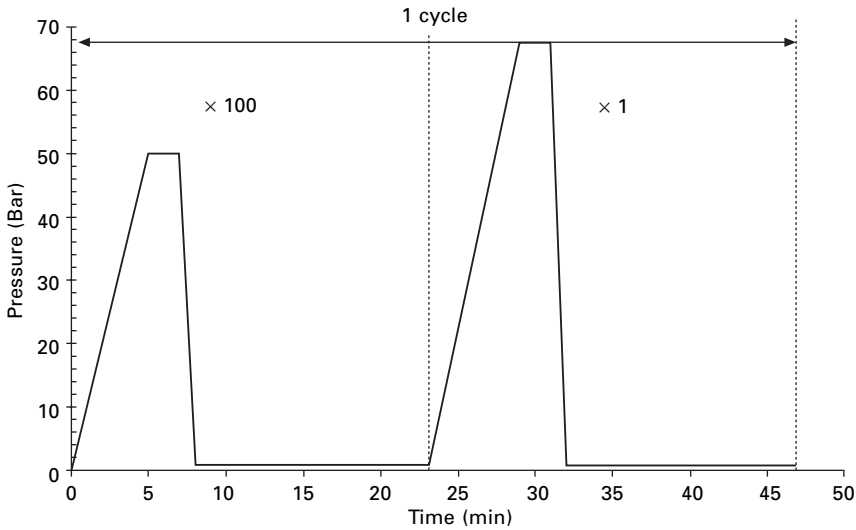

11.7 Parameters used for cyclic pressure testing.

tests already described in [1] were performed on the most promising versions of the anode. The test consisted of connecting the anode to a 18 m^2 stainless steel plate (type AISI 316) and measuring both the resulting potentials and current outputs.

11.3 Results and discussion

11.3.1 Modification of in-service anodes

Three defective anodes with electrical resistances well above the acceptance criteria were modified according to Fig. 11.3 and later assessed by cyclic pressure testing in seawater. Measurements of the electrical resistance between inserts and Al–Ga alloy after testing showed that the continuity on the three of them was still good with values under 0.1 Ω. In addition, no penetration of seawater was observed in the fittings. The decision was thus made to repair the existing anodes following this particular procedure. Subsequent regular detailed inspections by maintenance operators confirmed the overall good condition of the system and indicated that the anodes operated at their expected performance. No additional anode failure was reported afterwards and anodes were replaced in agreement with their specified utilization factor. Figure 11.8 presents a modified anode after more than five years of operation, showing the uniform dissolution of the Al–Ga sacrificial alloy. A cross-section of the area where the braid was fixed is also shown in Fig. 11.9.

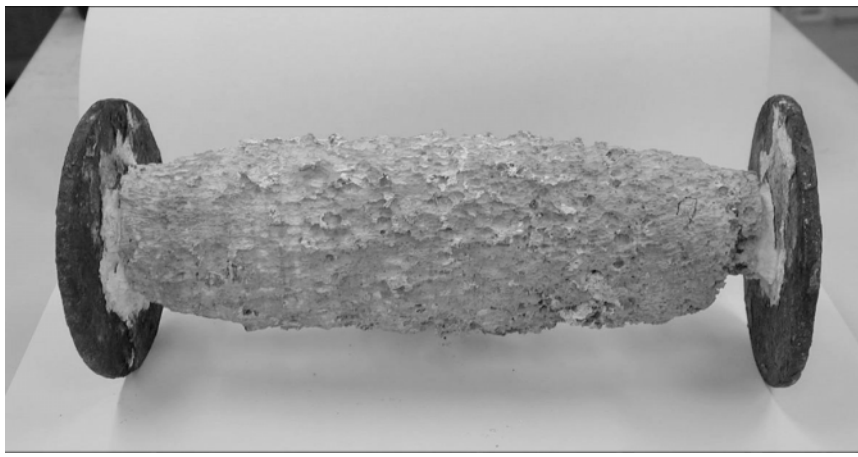

11.8 Modified Al–Ga anode after more than five years of operation.

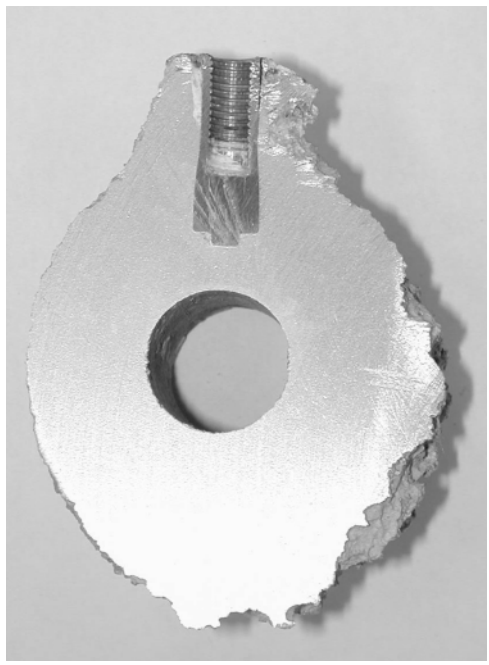

11.9 Modified Al–Ga anode cross–section.

11.3.2 Search for new anode design or manufacturing process

The first phase of the study focused on the surface preparation of the steel plain insert, its shape or dimension. Potential improvements of the chemical

bond were also explored with the use of bimetallic inserts such as aluminium–steel or aluminium–stainless steel. Figure 11.10 gives the results of the pulling tests carried out on seven new versions of the anode. Maximum loads reached were found to be in the same order, ranging from 40 000 to 60 000 N for most of the specimens. A significantly higher value was found on the anode treated by Hot Isostatic Pressure, suggesting a better bond between anode and insert. This was confirmed by X-Ray microanalyses performed at the interface and revealing aluminium enrichment on the insert side as shown in Fig. 11.11. After completion of the cyclic pressure tests, the anodes were examined and rust was found in all the insert-alloy interfaces except for the Hot Isostatic Pressure specimen. As an illustration, pictures of some of these anodes are given in Figs 11.12–11.14. Comparable results were obtained for the classical Hydral 2C ® cast-in strap anode. Also presented in Fig. 11.15 for comparison purposes is the classical 1Z-type zinc anode with cast-in strap galvanized insert, which was found to have a good behavior during pressure testing with no onset of corrosion at the insert–anode interface. In view of the results obtained in this first evaluation, the search for improvements on plain inserts was soon abandoned, with the exception of the Hot Isostatic Pressure version, which will be reconsidered later on.

The new design with replacement of the insert by two stainless steel bolts at each extremity of the anode was then studied. Five AG2-type anodes were

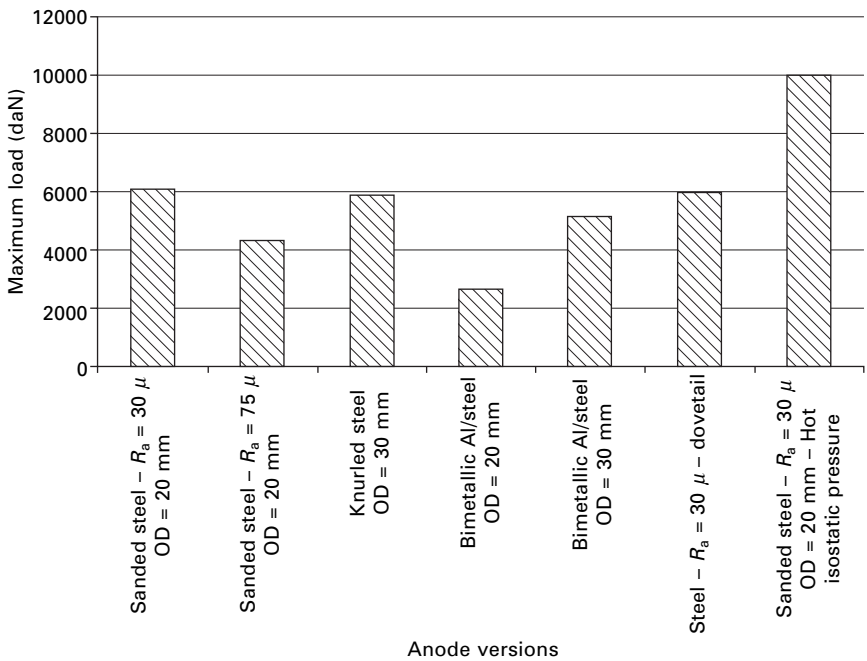

11.10 Plain rod inserts – results of the pulling tests.

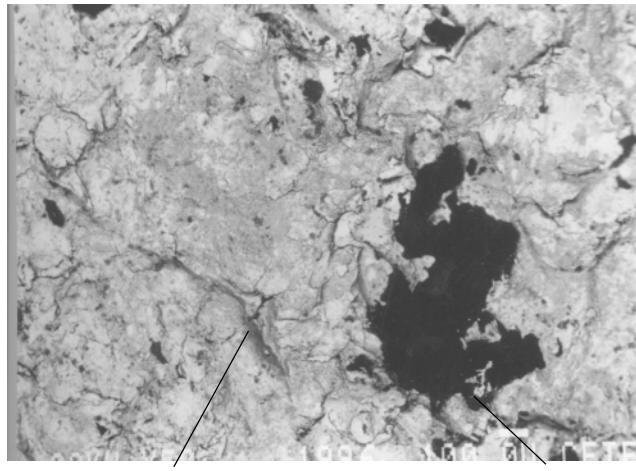

(a)

Elements	Global analysis of steel aluminium bond	Zone 1	Zone 2
Aluminium	5–10%	90–95%	<5%
Steel 90–95%	90–95%	5–10%	<95%

(b)

11.11 (a) Image obtained by backscattered electron microscopy; (b) results of X-Ray microanalyses.

11.12 Steel–aluminium plain insert after pressure testing.

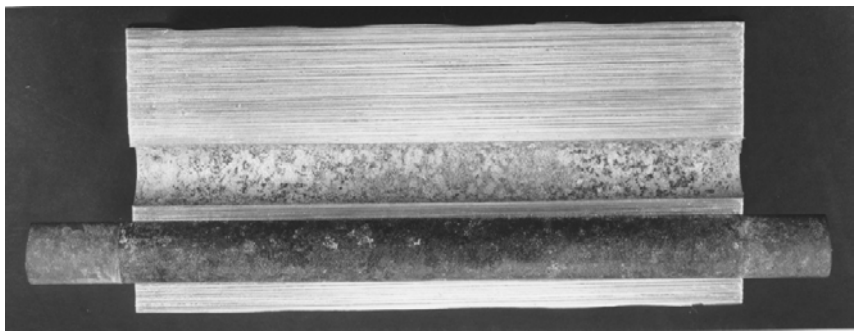

11.13 Sand blasted steel plain insert after pressure testing.

11.14 Plain steel insert with regular throttling after pressure testing.

manufactured in accordance with Fig. 11.4 and assessed by cyclic pressure testing in seawater. Detailed visual examinations after the tests indicated that there was no penetration of seawater within the fittings. Sealing gaskets and O-rings were intact with no sign of deterioration or deformation during the test. X-Ray microanalyses confirmed the efficiency of the double-barrier

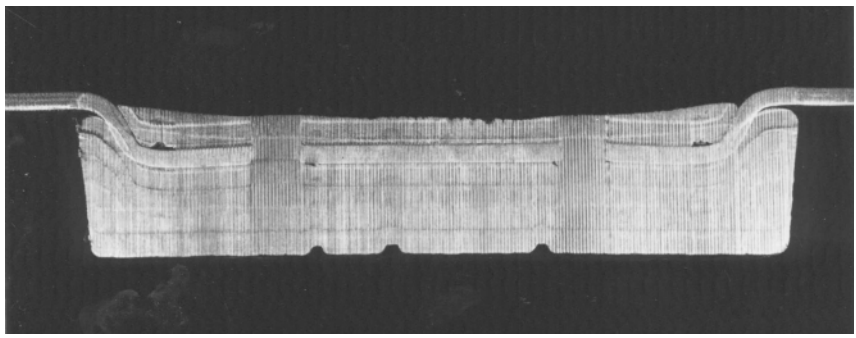

11.15 Type 1Z zinc anode – cast-in strap galvanized steel insert.

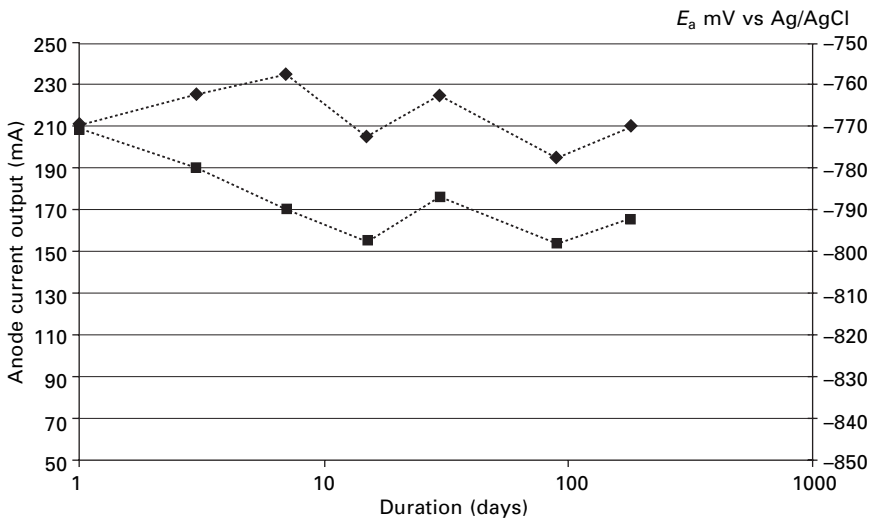

11.16 Results of full-scale marine test on new AG2-type anode.
■ = E_a (mV vs Ag/AgCl), ♦ = anode current output (mA).

system as no chloride traces were detected on the threads of the anodes and associated fittings. This new design was thus regarded as a promising option and long-term full-scale marine tests were then performed in order to verify the working parameters of such anodes. The results obtained are presented in Fig. 11.16 and are in good agreement with the required parameters, that is a current output in the order of 200 mA associated with a working potential around –800 mV vs Ag/AgCl. As these data gave confirmation of the adequate performance of the anodes in service conditions, the decision was made to use them on a new marine structure. More than 500 cylindrical new anodes were installed and are currently in use. Regular detailed inspections have been carried out and no failure has been reported after more than five years of operation.

The final phase of this study consisted in investigating the possible use of tube inserts on a set of Al/Zn/In anodes. Figure 11.17 shows the electrical resistance measurements before and after cyclic pressure tests. Comparable data were found irrespective of the anode diameter, insert diameter or use of water-cooled inserts during casting, and resistance levels were under 0.1 Ω both before and after testing. Results obtained with the plain insert plus Hot Isostatic Pressure version are also given in the same chart and confirm the good performance already noted for this process. The conclusions of the ensuing examinations are listed in Table 11.9. Seawater penetration was observed at each extremity on all the anodes, with length affected by corrosion varying from 2–47 mm at the most. Although it is difficult to identify any trend, it seems from Fig. 11.18 that the total length affected by corrosion varies in proportion with the anode diameter. Cyclic pressure tests did not reveal any significant difference between inserts water-cooled during casting and other specimens. Despite the good results previously mentioned, the plain rod insert plus Hot Isostatic Pressure specimen displayed larger corroded areas with an average value as high as 36 mm.

11.4 Conclusion

DGA and DCN have developed a new Al–Ga low voltage anode that is currently in use to protect marine structures. After the development of the first industrial anode version with plain rod inserts, additional studies were launched with the aim of optimizing the insert–anode bond. The following conclusions were reached, both from laboratory studies and field experience.

- Use of plain rods as inserts has proved to be unsatisfactory as penetration of seawater at the insert–anode interface occurs, thus reducing the performance of the cathodic protection system. All the attempts regarding modification of the insert surface preparation, nature or geometry did not improve the behavior of such anodes used in severe cyclic pressure conditions.
- Although expensive, treating the anodes with plain inserts by Hot Isostatic Pressure could be a promising orientation. However, more tests are necessary to reach a final conclusion.
- A new anode design with stainless steel fittings replacing the insert was developed, qualified and installed on a new marine structure. Adequate continuity between the anode and the structure to be protected was achieved, thus ensuring a good protection level. If this option has proved to be an efficient one, it is, however, a costly solution.
- Laboratory tests have shown that the use of tube inserts is a promising option. Further investigations on Al–Ga industrial versions as well as supplier qualification are necessary before any use in service.

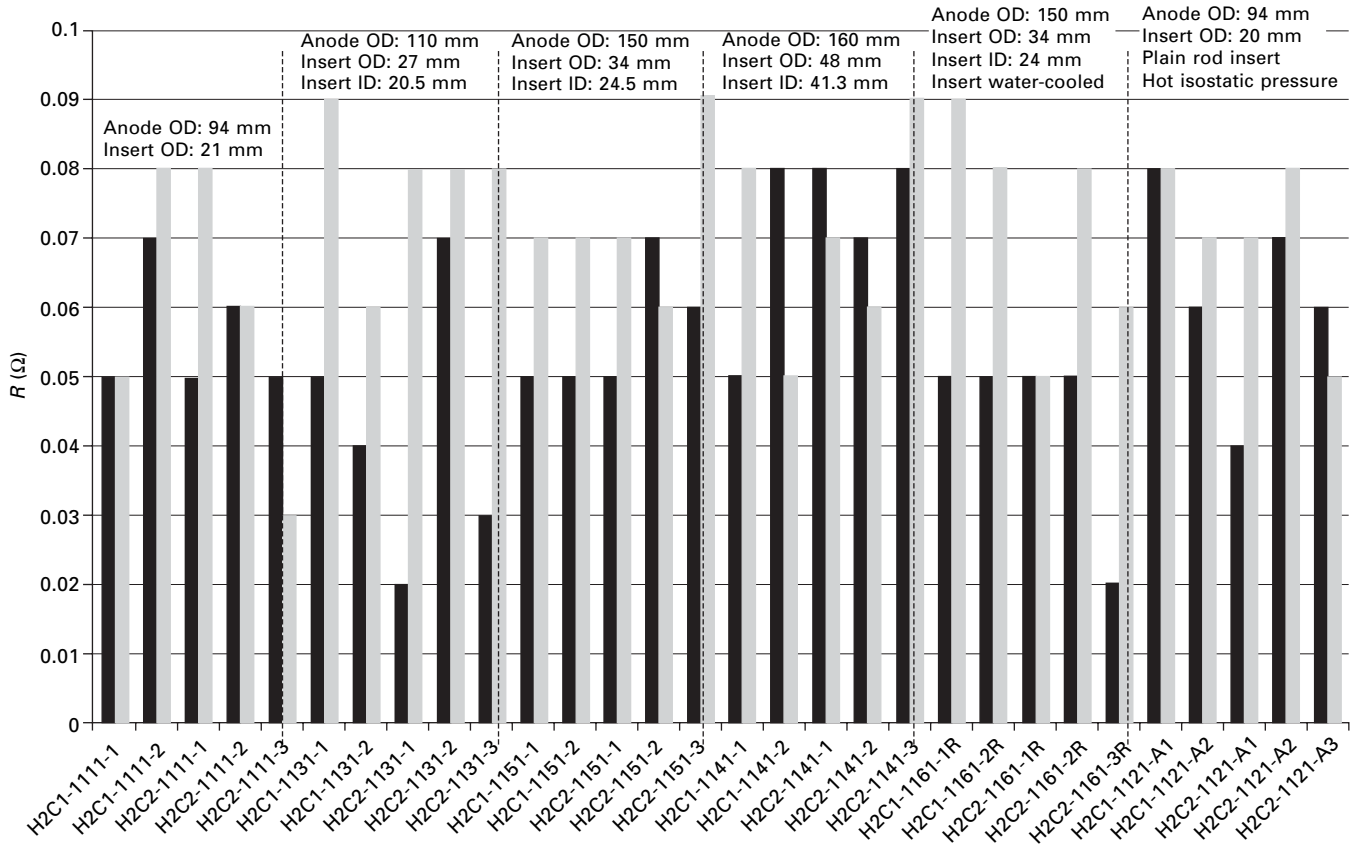

11.17 Electrical resistance measurements before (black bars) and after (gray bars) pressure testing of Al–Zn–In anodes.

Table 11.9 Al–Zn–In specimens – measurements of corroded areas after pressure testing

Anode label	Length of corroded area (seawater penetration) (mm) Side 1	Length of corroded area (seawater penetration) (mm) Side 2
H2C1-1111-1	7	8
H2C1-1131-1	7	12
H2C1-1151-1	15	20
H2C1-1141-1	8	12
H2C1-1161-1R	2	35
H2C2-1111-1	2	19
H2C2-1131-1	5	6
H2C2-1151-3	25	12
H2C2-1141-3	36	31
H2C2-1161-1R	26	12
H2C1-1121-A1	25	47
H2C2-1121-A1	20	33

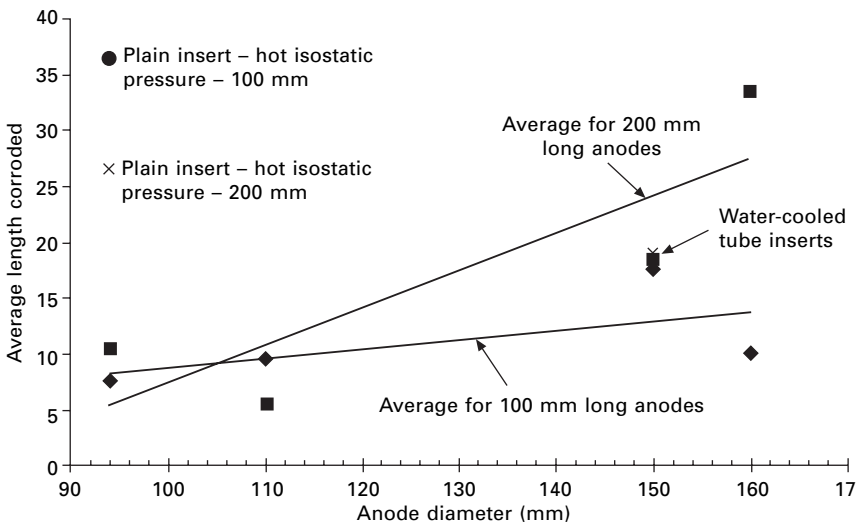

11.18 Tube insert specimens – length of corroded area versus anode diameter.

- Provided that a good anode–insert bond is kept, the Al–0.1% Ga low-voltage anodes meet the specified cathodic protection requirements. They have shown excellent results in service, satisfactorily protecting the structure against uniform corrosion and possible galvanic couplings while keeping potentials and susceptibility to environmentally induced cracking at the required levels.

- Both the sacrificial material itself and the new anode design have proved to be successful. New studies will be launched in the future in order to find cost-saving anode designs or manufacturing processes.

11.5 References

1. J.P. Pautasso, H. Le Guyader, V. Debout, *Corrosion 98*, Paper no. 275, NACE International, Houston, TX, 1998.
2. Patent granted in France No. 2 713 244, 12 January 1996 and in the USA, No. 5 547 560, 20 August 1996.
3. E. Lemieux, K.E. Lucas, E.A. Hogan, A.M. Grolleau, *Corrosion 2002*, paper no. 2016, NACE International, Houston, TX, 2002.

Index